Politecnico di Milano

| Concrete Structures | Costruzioni in Calcestruzzo |
| "Fratelli Pesenti" | "Fratelli Pesenti" |

Studies and Researches
Annual Review of Structural Concrete
Volume 30

Editorial Board

Antonio Migliacci,
Pietro G. Gambarova, Paola Ronca

Scientific Committee

STUDIES AND RESEARCHES

Annual Review of Structural Concrete

Volume 30 – December 2010

Technical Papers

Technical Notes

News of the School "Fratelli Pesenti"

Foreword

The long recession we are leaving behind and the timid recovery taking place in a few countries are forcing all the actors of the building process to look for new opportunities in terms of conceptual design, structural optimization, enhanced or new materials, higher-quality building components and improved building technologies. All the efforts have – or should have – a common denominator, "green thinking", a rather abused term, which – however – expresses an unquestionable necessity for the future of any human activity and for the survival of the mankind itself.

Green thinking refers not only to the production of goods with no or minimal requirements in terms of fossil-fuel consumption, but also to the improvement of existing goods to make their use less dependent on fossil fuels, in order to leave the environment as pristine as possible. In both cases, "energy" is involved. Hence, the first step implied by green thinking is towards both renewable and low-impact sources, with no or limited consumption of Earth's resources, no or limited emission of green-house gases, and the least possible soil occupation, to mitigate visual impact and environmental disruption.

Within this context, the role of Civil and Materials Engineering – and particularly of Structural Engineering – is fundamental from at least three different points of view:

- repairing/rehabilitating/strengthening/upgrading existing buildings and infrastructures to minimize their energy needs, by producing and using better materials and building components, with enhanced thermo-mechanical properties and durability;

- designing and constructing innovative buildings and infrastructures, characterized by energy-conscious production processes, low maintenance and improved durability;

- contributing to the design and construction of more efficient plants for the production of electric energy, in order to guarantee high quality in each stage of the building process, the reliability during the service life and the safety in accidental conditions.

With reference to existing buildings and infrastructures, the first point indicates one of the major goals to be pursued in the next few years, namely that of developing a common set of technical provisions (within the Eurocodes) to help each actor in the repairing, rehabilitating, strengthening and maintenance field to work in a more rational and reliable way. Among the many open issues, the evaluation of the actual safety levels and the definition of the safety targets stand out. To give an answer, "safety indices" should be quantified, in order to take into account all existing flaws and their possible development. In this way, priority levels could be established, something that is badly needed for the consolidation and renovation of many socially-valuable buildings and infrastructures.

The second point refers to both large structures, like tall buildings and bridges, and infrastructures aimed to meet strategic social and economical needs. Talking about tall buildings, several recent outstanding projects have proved that concrete is the best technological choice as a structural material, thanks to the properties of the "new" mixes (high strength, workability, durability, ...). Using these materials and taking advantage of prestressing, large-span bidirectional slabs can be designed and rapidly built, with the plus of an increased in-plane stiffness, a better resistance to lateral loads (wind and earthquake)

of the whole structure and fewer problems in the slab-column connections, where high workability is required by the highly-congested reinforcement.

With reference to the third point, nuclear power plants stand out as a challenge for cement and construction industry, as well as for structural designers and materials experts. As a matter of fact, in today's plants and even more in future advanced plants a variety of cementitious materials is needed, as each step of the fuel cycle - from uranium mines to waste repositories – requires specific materials exhibiting excellent properties in terms of resistance, durability and radiation-shielding capabilities.

Ordinary concrete and shotcrete are extensively used in uranium mines (as it is usual in tunnels); heavy concrete is suitable for fuel-processing plants and primary-containment shells; high-performance temperature- and fire-resistant fiber-reinforced concrete for secondary-containment shells; and heavy durable concrete for the shielded facilities destined to reprocessing the spent fuel to be fed to both thermal and fast reactors. Finally, durable high/ultra high-performance impact- and fire-resistant concrete should be used for multi-barrier waste storage, which requires the production of casks, canisters and caissons, as well as the construction of dry-storage pads and underground waste repositories.

All the above-mentioned cementitious composites, except shotcrete and heavy concrete, may have self compacting/consolidating properties, which bring in higher standards of workability, homogeneity, durability and labor safety.

This is good news for Civil Engineers, Architects, Structural Designers and Materials Scientists, and for the Building Industry as a whole, on condition that the governments, the institutions and the public opinion understand that investing on strategic high-quality structures and infrastructures is a smart way to favor the economy, to save job positions and to create new job opportunities.

Several topics related to high-level Structural Engineering are addressed in the eight technical papers (1-8) and four technical notes (9-12) published in this volume.

Five papers are aimed at understanding – through modelling and testing – the structural behavior of: SCC beams (1) or R/C beams affected by cover delamination (4); R/C columns strengthened by steel cages (2) or FRP (3); and R/C walls subjected to shrinkage (5).

Two papers are about concrete triaxial and fatigue behavior (6,8), and a third about concrete sustainability and innovation (7).

Among the notes, the first (9) is about the re-examination of the static behavior of a rather interesting folded-plate structure designed fifty years ago in Sardinia (Italy), while the last three are focused on Structural Fire Engineering (open-section P/C girders - 10, composite girders – 11, and general problems of R/C sections in fire – 12).

As usual, the news of the School "Fratelli Pesenti" ends this volume.

Milan, December 2010

Pietro G. Gambarova, Antonio Migliacci and Paola Ronca

Premessa

La lunga recessione che ci stiamo lasciando alle spalle e che solo in alcuni paesi mostra segni di ripresa obbliga tutte le parti interessate al processo costruttivo a cercare nuove opportunità riguardo a filosofia progettuale, ottimizzaizoone strutturale, materiali avanzati ed innovativi, migliore qualità della componentistica ed affinamento delle tecnologie costruttive. Peraltro, tutti gli sforzi vanno orientati al rispetto dell'ambiente, concetto abusato, ma che esprime un' inderogabile necessità per la sopravvivenza dell'Umanità.

Il rispeto dell'ambiente riguarda sia la produzione di beni richiedenti un uso minimale di combustibili fossili, sia il miglioramento dei beni esistenti in modo da renderne l'uso meno dipendente dai suddetti combustibili, nell'ottica di limitare il più possibile le alterazioni al patrimonio ambientale. Essendo in ambedue i casi coinvolta la produzione di energia, il primo passo verso il rispetto dell'ambiente riguarda sia le fonti rinnovabili, che quelle a ridotto impatto ambientale, con consumi molto limitati delle risorse naturali, emissioni molto ridotte dei gas responsabili di effetto serra ed occupazione minimale del suolo.

In tale contesto, il ruolo dell'Ingegneria Civile e dei Materiali – ed in particolare dell'Ingegneria Strutturale – è fondamentale da almeno tre diversi punti di vista:

- restauro statico / ricupero / rafforzamento / aggiornamento di edifici ed infrastrutture esistenti per minimizzare i consumi di energia, tramite produzione ed uso di materiali e componenti di migliori prestazioni termomeccaniche e di più elevata durabilità;

- progettazione e costruzione di edifici ed infrastrutture innovative, caratterizzate da processi produttivi improntati al risparmio energetico, da limitata manutenzione e da elevata durabilità;

- contributo alla progettazione ed alla realizzazione di impianti di produzione dell'energia elettrica più efficienti, in modo da favorirne la qualità in ogni fase del processo costruttivo, l'affidabilità durante la vita utile e la sicurezza in condizioni incidentali.

Con riferimento agli edifici ed alle infrastrutture esistenti (primo punto), uno dei principali obiettivi da raggiungere nei prossimi anni è lo sviluppo – nell'ambito degli Eurocodici - di un insieme di regole che permettano a chi si occupa di restauro statico, ricupero e manutenzione di lavorare in modo più razionale e professionale. Fra i molti problemi tuttora aperti, la valutazione dell'effettivo livello di sicurezza e la definizione degli obiettivi della sicurezza sono di particolare rilevanza. A tal fine occorre quantificare gli indici di sicurezza per tener conto dell'effettivo livello di degrado e della sua possibile evoluzione temporale. Sarà così possibile definire dei livelli di priorità, il che è necessario per gli interventi di consolidamento e ristrutturazione in molte opere di grande rilevanza socio-economica.

Il secondo punto riguarda le grandi opere strutturali sviluppate sia in altezza (edifici alti), che in lunghezza (ponti), nonchè le opere strutturali nel territorio (infrastrutture di trasporto ed impianti speciali per le esigenze della collettività). In tema di edifici alti, ad esempio, varie recenti e straordinarie realizzazioni hanno dimostrato che il materiale "calcestruzzo" risulta essere la scelta tecnologica migliore in virtù delle caratteristiche dei nuovi conglomerati cementizi (alta resistenza, lavorabilità, durabilità, ...). Infatti, l'impiego di tali calcestruzzi, abbinato o meno alla precompressione, permette di realizzare campi di piastra

di grande luce, con ciò conferendo all'intera opera migliore resistenza alle azioni orizzontali (vento e sisma), riducendo i tempi di costruzione e facilitando la realizzazione dei nodi colonna-impalcato, dove la congestione dell'armatura richiede elevata lavorabilità.

Con riferimento al terzo punto, l'argomento molto "caldo" delle centrali nucleari per la produzione di energia elettrica rappresenta una sfida per l'industria del cemento e delle costruzioni, così come per i progettisti strutturali e per gli esperti di materiali. Non v'è infatti dubbio che nei più moderni impianti oggi esistenti, e a maggior ragione negli impianti avanzati del prossimo futuro, è richiesta una straordinaria varietà di conglomerati cementizi, in quanto vi sono esigenze specifiche per ogni passo del ciclo del combustibile.

I calcestruzzi ordinari e proiettati sono impiegati nelle miniere di uranio (come daltronde nelle gallerie), mentre i calcestruzzi pesanti sono richiesti dagli impianti di produzione degli elementi di combustibile e dalle strutture primarie di contenimento del nocciolo; i calcestruzzi ad alte prestazioni con/senza fibre metalliche resistenti all'alta temperatura ed all'incendio dai gusci di contenimento secondario; ed i calcestruzzi pesanti ad alta durabilità dalle strutture schermate per la ricarica degli elementi di combustibile da riutilizzare nei futuri reattori veloci. Infine, i calcestruzzi ad alta durabilità, ad alte/altissime prestazioni, resistenti all'impatto ed all'incendio (come richiesto anche dai nuclei controventanti degli edifici alti) si prestano ad essere utilizzati nei contenitori singoli e multipli, nei cassoni, nei piastroni per l'immagazzinaggio all'aperto e nei depositi sotterranei.

Occorre aggiungere che tutti i calcestruzzi suindicati – ad eccezione di quelli pesanti e proiettati – si prestano ad essere realizzati con proprietà autocompattanti, che assicurano migliore lavorabilità e durabilità, oltre ad aumentare la sicurezza del lavoro in cantiere.

Si tratta di buone notizie per Ingegneri Civili, Architetti, Progettisti Strutturali ed Esperti di Materiali – ed in generale per l'Industria delle Costruzioni - purchè i Governi, le Istituzioni e l'opinione pubblica capiscano che investire in strutture ed infrastrutture strategiche di qualità è una via primaria per favorire l'economia e creare nuove opportunità di lavoro.

Un contributo significativo viene da questo 30° volume di Studi e Ricerche, ove vengono trattati vari temi di Ingegneria Strutturale in otto memorie e quattro note.

Cinque memorie riguardano il comportamento strutturale di : travi armate realizzate in calcestruzzo autocompattante (1) oppure soggette a delaminazione del ricoprimento dell'armatura (4), colonne in c.a. rinforzate con angolari e traversi (2) oppure con polimeri fibrorinforzati-FRP (3), e pareti in c.a. soggette a ritiro (5).

Il comportamento triassiale e a fatica del calcestruzzo è trattato in altre due memorie (6,8), mentre l'ultima memoria ha per tema la sostenibilità e l'innovazione nell'ambito del materiale strutturale "calcestruzzo" (7).

Fra le note, la prima (9) riesamina in chiave "moderna" il progetto di una interessante copertura a lastre piane realizzata in Sardegna, mentre le altre tre hanno in comune l'incendio (travi precompresse a sezione aperta – 10, travi composite – 11 e problemi generali delle sezioni in c.a. – 12).

Come d'uso, le notizie della Scuola Master "Fratelli Pesenti" concludono il volume.

Milano, Dicembre 2010

Pietro G. Gambarova, Antonio Migliacci and Paola Ronca

Technical Papers

EXPERIMENTAL INVESTIGATION ON THE STRENGTH AND DUCTILITY OF HSC AND SCC BEAMS SUBJECTED TO MONOTONIC AND CYCLIC LOADING

Franco Angotti[1], Luciano Galano[2], Andrea Vignoli[1]

ABSTRACT

The results of an experimental campaign concerning eighteen beams made of normal-strength and high-strength self-consolidating or vibrated concrete are presented and discussed in this paper. The beams were subjected to 4-point bending. Six beams were tested under monotonic loading and the remaining twelve under cyclic loading. Concrete cylindrical compressive strength covered the range 40 - 115 N/mm^2.

On the whole, the tests show that the ultimate strength and ductility of SCC beams are comparable with those of the beams made of vibrated concrete. Some differences emerge in the crack pattern and in the type of damage. In the beams made of either normal-strength self-consolidating concrete or vibrated concrete the cracks mostly formed in the constant-bending zone, with more concentrated cracks in the latter case, for the same concrete strength. Negligible differences were detected among the HSC beams made of either self-consolidating or vibrated concrete.

KEYWORDS: high-strength concrete, self-consolidating concrete, R/C beams, bending tests, compressive strength, ductility.

---

[1] Professor, Department of Civil and Environmental Engineering, Università degli Studi di Firenze, Florence (Italy).
[2] Assistant Professor, Department of Civil and Environmental Engineering, Università degli Studi di Firenze, Florence (Italy).

1. INTRODUCTION

In the last decades, improvements in materials technology led to the development and application of high-strength concrete (HSC) and self-consolidating concrete (SCC). HSC (or HPC = high-performance concrete, this denomination being preferred in Europe) are cementitious composites with a cylindrical compressive strength larger than 60 N/mm^2. SCC is a rather recent development that allows concrete elements to be cast without mechanical vibration (ACI, 237-03, 2003; EFNARC, 2002). Studies and researches on these materials are required to make structural designers more comfortable in the use of SCC in concrete structures. Hence, experimental tests are necessary to investigate the mechanical properties of these concretes and to collect useful information in order to improve the design methods (Sonebi et al., 2003; Das et al., 2005; Cattaneo et al., 2007). In addition, knowing the mechanical behavior of SCC is instrumental in improving the analytical models.

In this paper the results of the flexural tests on eighteen reinforced-concrete beams with rectangular cross section are presented for extending the data bank on beams made of HSC and SCC. Attention is focused on their ultimate flexural strength and ductility. The beams were tested under both monotonic and cyclic loading, in 4-point bending, i.e. with constant bending in the central zone of the specimens. All beams have the same geometry and reinforcement (length, cross section and reinforcement layout). Six different concrete mixes were used in order to cover the range 40-115 N/mm^2. Three mixes concerned as many concretes to be vibrated, while the remaining three mixes were devised for self-consolidating concretes. For each mix, three beams were cast to be tested according to a displacement-controlled procedure, with the first beam under monotonic loading and the other two under cyclic loading. Some results of these tests were synthetically treated in two previous papers (Angotti et al., 2007; Angotti et al., 2009). Here, the same results are presented and discussed in a more extended form and in more details.

The aim of this study is to investigate the ultimate flexural strength, the ductility and the cracking patterns of the beams for various concrete mixes. The differences and similarities between SCC and vibrated beams are stressed as well.

2. EXPERIMENTAL SETUP

2.1 Beams

Eighteen beams each with constant rectangular cross section (b × h = 150 mm × 200 mm; length l = 2400 mm) were tested (Fig. 1). The same arrangement of the reinforcement was adopted in all beams. The longitudinal bottom reinforcement consisted of four hot-rolled deformed bars FeB44k (f_{yk} = 435 N/mm^2; 2∅10 + 2∅12 mm). The longitudinal top reinforcement consisted of three deformed bars

of the same grade (3∅10 mm). Consequently, the steel ratio of the tension bars ρ_s = $A_s/(b \times h)$ was equal to 1.28 % (A_s = total area of the bottom reinforcement).

The transverse reinforcement consisted of 2-leg ∅8 mm stirrups spaced by s = 80 mm close to the supports, and of 2-leg ∅6 mm stirrups spaced by s = 120 mm at mid-span. The transverse reinforcement was designed to obtain a flexural collapse in the central zone. Additional stirrups were provided at the two ends of the specimens, to prevent undesired failures in these zones. All stirrups were anchored in the concrete core with 60 mm-long bends.
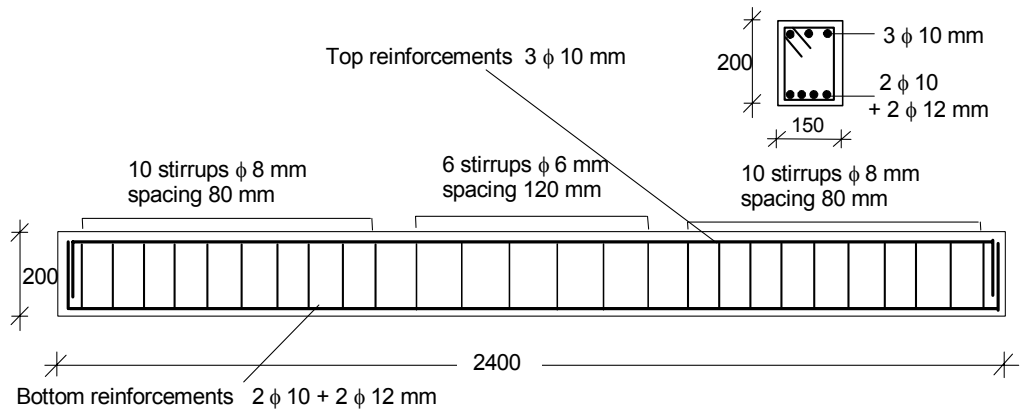
Figure 1 – Geometry and reinforcement of the beams (dimensions in mm).

2.2 Mix designs, concrete samples and structural specimens

The concretes used in this study were based on six mixes with different target compressive strengths:

- Mixes HSCB and HSCC: vibrated high-strength concretes with target cylindrical compressive strengths at 28 days of 80 and 100 N/mm², no silica fume (HSCB), with silica fume (HSCC), max. aggregate size d_a = 10 mm;

- Mix NSCD: vibrated normal-strength concrete with target strength at 28 days of 40 N/mm², no silica fume, max. aggregate size d_a = 10 mm;

- Mixes SCCE and SCCF: self-consolidating high-strength concretes with target strengths of 80 and 95 N/mm², respectively, with silica fume, max. aggregate size d_a = 10 mm;

- Mix SCCG: self-consolidating normal-strength concrete with target strength of 40 N/mm², with silica fume, max. aggregate size d_a = 15 mm.

An appropriate amount of superplasticizer was added to all mixes to guarantee the workability. The details of the mix designs and of other properties of the mixes measured in the fresh state are listed in Table 1.

From each mix, three identical beams were manufactured (for instance, HSCB-T1, HSCB-T2 and HSCB-T3 = beams made from Mix HSCB). The six beams indicated with T1 were tested under monotonic loading, while the other twelve beams - indicated with T2 and T3 - were tested under cyclic loading.

The specimens were cast horizontally in recoverable steel moulds, with the compressive side of the beams upward. The concrete was vibrated by means of an internal vibrator (SCC specimens of course - were not vibrated). Plastic sheets were used to cover the beams for one day.

Later, the moulds were removed and the beams were left for two days at 20 ± 2 °C and RH ≥ 90 %. Then the beams were exposed to the ordinary environmental conditions typical of a laboratory, prior to be tested. The same procedure was used for curing the control specimens.

The actual net cover was accurately measured in the mid-span cross section of each beam after testing. Values close to 16 mm were obtained for all the beams, except for the beams of Mix SCCG, where the net cover was larger (close to 20 mm).

Concrete cylinders (h = 200 mm and $\varnothing$ = 100 mm) and cubes (side = 100 mm) were used to determine the compressive strengths at 28 days and at the time of testing (these strengths are denoted by $f_{c28,cyl}$, $f_{c,cyl}$, $f_{c28,cube}$, $f_{c,cube}$). The splitting tensile strength $f_{c,split}$, the tensile strength in bending f_r and the secant modulus of elasticity E_{cs} were also measured at the time of testing (E_{cs} was determined according to the Italian norm UNI 6556, 1976, ensuing from the ISO norms).

Table 2 gives the mechanical properties of the hardened concretes (average values of three specimens; γ is the density or mass per unit volume). As reported in Table 2, no control cylinders were available for Mix SCCG (only cubes were available; hence, in this case the usual ratio 0.83 was introduced for the evaluation of $f_{c,cyl}$, i.e. $f_{c,cyl} = 0.83 \, f_{c,cube} = 40.16$ N/mm^2 at the time of testing).

The properties of the reinforcement were measured by means of standard tensile tests carried out using an Instron universal testing machine. Table 3 lists the yield strength f_{sy}, the ultimate strength f_{su} and the ultimate ductility A_5 evaluated according to the Italian Recommendations on R/C structures (Ministry of Public Works, January 9, 1996). The stress-strain diagrams were obtained by measuring the strains over a gauge length of 50 mm by means of an electronic extensometer.

2.3 Test setup and instrumentation

The experimental setup is shown in Fig. 2. The load P was applied by means of a MTS hydraulic press (max. capacity 350 kN). As already mentioned, the beams were tested in 4-point bending; the central zone subjected to pure bending was 700 mm-long, while the shear span was 750 mm-long.

Mix	HSCB	HSCC	NSCD	SCCE	SCCF	SCCG
Portland cement type	I 52.5 R	I 52.5 R	I 52.5 R	I 52.5 R	I 52.5 R	II/A-LL 42.5 R
Water [kg/m^3]	139	130	184	138	155	200
Cement [kg/m^3]	537	594	337	517	609	340
Silica-fume [kg/m^3]		21		43	43	140 (filler)
Sand I [kg/m^3]	300	292	316	302	278	620 (0-3 mm)
Sand II [kg/m^3]	527	511	526	517	481	440 (0-12 mm)
Crushed stone [kg/m^3] [d_a = 0 - 5 mm]	207	208	210	215	203	
Crushed stone, [kg/m^3] [d_{amax} = 10 mm]	734	709	736	722	673	710 (8-15 mm)
Superplasicizer [kg/m^3]	7.0	11.7	1.7	11.3	13.3	3.5
Viscofluid, [kg/m^3]				0.43	0.32	1.0
Slump, mm	260	280	175	750[1]	800[1]	650[1]
Air, [%]	1.2	1.0	2.4	0.3	0.3	–
W/C	0.26	0.22	0.55	0.27	0.25	0.59
W/(C+SF)	0.26	0.21	0.55	0.25	0.24	0.42
Density, [kg/m^3] (fresh concrete)	2448	2466	2322	2412	2420	–

[1] Slump flow test; – = not measured items.

Table 1 – Mix designs and properties of the concretes in the fresh state.

Concrete	$f_{c28,cyl}$ [N/mm^2]	$f_{c28,cube}$ [N/mm^2]	$f_{c,cyl}$ [N/mm^2]	$f_{c,cube}$ [N/mm^2]	$f_{c,split}$ [N/mm^2]	f_r [N/mm^2]	E_{cs} [N/mm^2]	$\gamma_{28,cyl}$ [kg/m^3]
HSCB	80.56	96.63	86.95	101.34	5.53	11.27	39971	2401
HSCC	98.06	120.27	113.32	130.50	6.71	10.78	49810	2410
NSCD	39.28	47.36	43.11	50.65	3.24	8.31	31835	2263
SCCE	82.57	111.65	88.83	110.72	4.92	10.90	40351	2394
SCCF	92.66[1]	115.22	100.11	121.64	4.18	9.76	42654	2427
SCCG	–	49.76	–	48.38	3.63	8.58	29998	2321

[1] Mean value of two specimens; – = not measured items.

Table 2 – Properties of the hardened concretes at 28 days and at the time of testing.

All beams except SCCG			
Size	f_{sy} [N/mm^2]	f_{su} [N/mm^2]	A_5 [%]
ϕ 6	604.1	638.4	10.9
ϕ 8	549.3	614.1	25.9
ϕ 10	519.7	619.8	25.7
ϕ 12	541.3	641.7	22.2
Beams SCCG			
Size	f_{sy} [N/mm^2]	f_{su} [N/mm^2]	A_5 [%]
ϕ 6	642.5	657.5	10.2
ϕ 8	603.9	627.3	18.8
ϕ 10	501.5	579.4	29.3
ϕ 12	555.1	652.7	23.1

Table 3 – Mechanical properties of the reinforcement.

During the tests, the load P was measured by means of the pressure transducer of the press, and both the mid-span displacement and the settlements at the supports were monitored by means of linear transducers (F1, F2 and F3). One strain gauge glued to the concrete surface (Ω type) measured the compressive strain in the mid-span cross section (D1 in Fig. 2). Five deformometers (Ts1, Ts2, Ts3, Ts4 and Ts5) were located along the intrados (bottom face in tension) to check the crack pattern in the zone subjected to constant bending and to measure the average curvature of the beam. As an example, Fig. 3 shows the Beam SCCG-T1 before being tested.

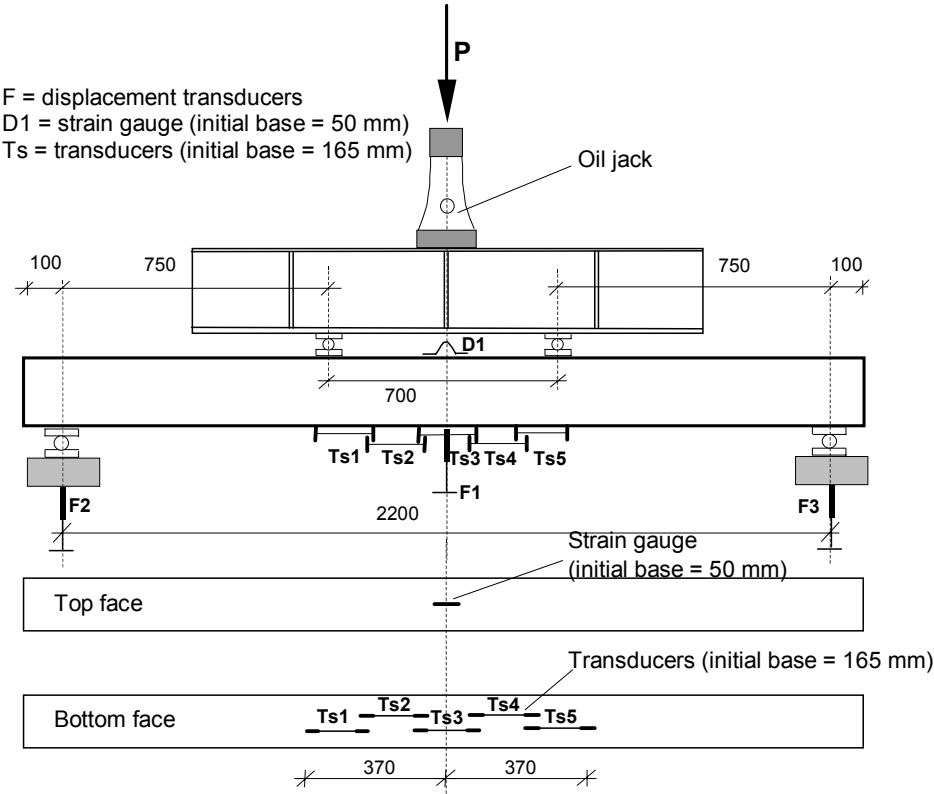Figure 2 – Test setup of the beams and details of the instrumentation (dimensions in mm).

The monotonic tests were carried out by increasing the mid-span displacement at a constant rate of 3 mm/minute; a constant rate of approximately 18 mm/minute was used in the cyclic tests. Fig. 4 shows the loading history of the cyclic tests; d_y denotes the mid-span displacement corresponding to the yielding of the bottom reinforcement.
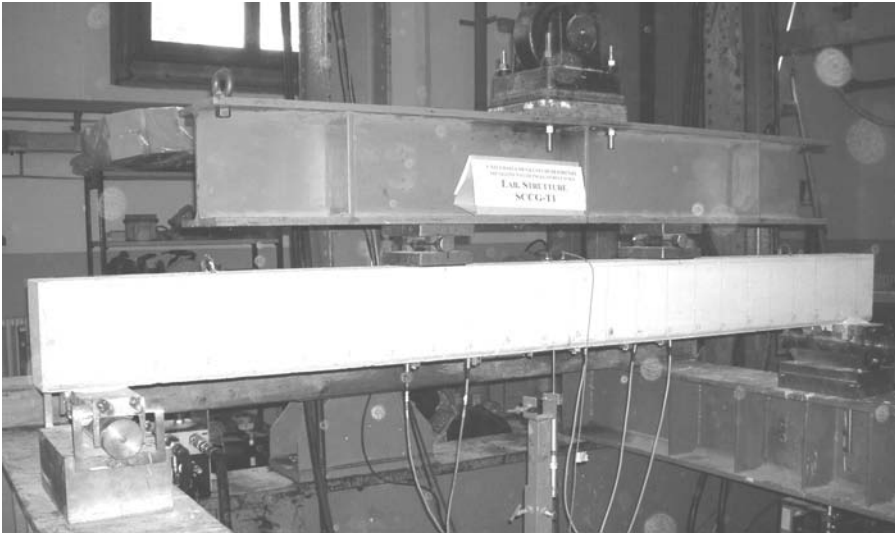
Figure 3 – Beam SCCG-T1 before the test.
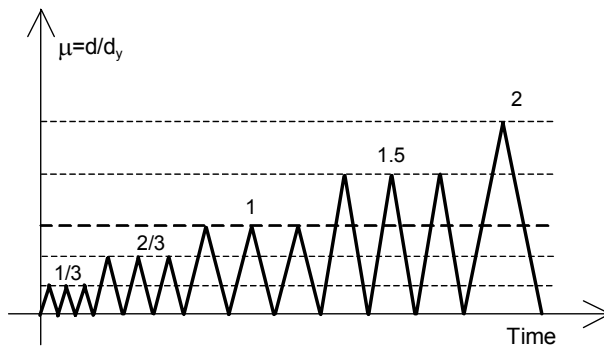
Figure 4 – Loading history of the cyclic tests.

For each beam, d_y was first evaluated according to the monotonic test results; then the actual values were determined from the results of each cyclic test. As shown in Fig. 4, three pulsating load-cycles (no reversal of the curvature) were applied for each ductility level $\mu = d/d_y$. The tests were protracted until a significant level of damage was detected in the specimens.

3. MONOTONIC TESTS

3.1 Load–displacement relationship

The monotonic tests were carried out by increasing the mid-span displacement d up to approximately 80 mm. The value of d was obtained from the difference between the value measured by transducer F1 and the average value of the displacements measured by transducers F2 and F3. In all experiments the beams were severely damaged and the concrete cover close to the mid-span section exhibited extensive spalling.

The plot of the load P vs. the mid-span displacement d allows to identify the typical "points" of the response curve of a beam in bending (Fig. 5): the load P_{cr} corresponding to the formation of the first crack, the yielding load P_y, the maximum load P_{max} and the ultimate load P_u. Generally, these points can be conventionally identified by means of calculus. As an example, both d_y and P_y can be determined by applying the so-called "¾ rule" (Fig. 5). In the present study, P_{cr} and P_y were manually determined according to the load-displacement response (see Beam HSCB-T1 in Fig.6). The ultimate load P_u was the load at the maximum applied displacement d_u. All these results are collected in Tables 4 and 5, whereas the diagrams of the load vs. the mid-span displacement are reported in Figs. 7 and 8. Unfortunately, because of some malfunctioning of the acquisition data-system, not all the results concerning Beam NSCD-T1 are available.

Beam	P_{cr} [kN]	P_y [kN]	P_{max} [kN]	M_y [kNm]	M_{ru} [kNm]
HSCB-T1	24.04	95.44	107.06	35.79	33.44
HSCC-T1	20.00	93.86	103.34	35.20	34.09
SCCE-T1	18.80	94.76	103.22	35.54	33.48
SCCF-T1	23.02	96.58	101.92	36.22	33.75
SCCG-T1	12.52	85.08	95.64	31.91	31.01

Table 4 – Results of the monotonic tests.

Beam	$K_0 = P_y/d_y$ [kN/mm]	d_y [mm]	d_u/d_y	P_u/P_{max}
HSCB-T1	7.22	13.2	6.1	0.89
HSCC-T1	7.26	12.9	6.2	0.91
SCCE-T1	7.32	12.9	6.2	0.85
SCCF-T1	7.34	13.2	6.4	0.92
SCCG-T1	5.74	14.8	4.6	0.73

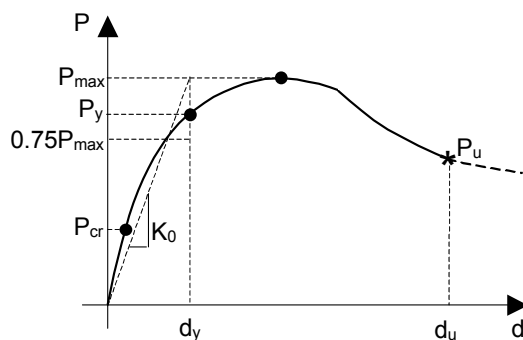Table 5 – Results of the monotonic tests.

Figure 5 – Definition of the characteristic points of the load-displacement curves under monotonically-increasing displacement.

The first part of the ascending branches is almost linear and the first cracks appear approximately in the mid-span section along the intrados of the beams. The second part of the ascending branches is still rather linear until the yielding of the main reinforcement. In this phase, any small increase of the load favors the formation of thin cracks in the central zone of each specimen (crack spacing comprised between 50 and 100 mm).

After yielding, the hardening of the tension reinforcement becomes very evident in all tests. Finally, because of concrete-cover splitting, a sudden decrease of the load occurs (in Beam SCCG-T1 the cover splitting occurred in two subsequent phases).

The beams made with the Mixes HSCB, HSCC, SCCE and SCCF produced comparable loads P_y and P_{max}; slight differences were detected for the load P_{cr}. All these beams exhibited a residual ultimate capacity of at least 0.85 P_{max} and a displacement ductility ratio d_u/d_y close to 6. The normalized diagrams of the load vs. the mid-span displacement differ only after yielding (Fig. 8).

Beam SCCG-T1 exhibited the lowest ductility and the lowest values of the loads at first cracking, at yielding, at the peak of the response curve and during the unloading phase (residual load), probably because of the lower value of the internal lever arm due to the larger concrete cover. (Beam SCCG-T1 is the only one manufactured with normal-strength concrete).

These qualitative comments apply to all beams, as the overall behavior of SCC beams was similar to that of vibrated-concrete beams. Furthermore, Table 4 shows that the experimental values of the moment M_y at yielding are very similar to the theoretical values of the ultimate moment M_{ru} calculated according to Eurocode 2 (CEN-EN 1992-1-1, 2004). The moment M_{ru} was evaluated using the actual strengths of the materials and the parabola-rectangle law for the concrete in compression. The constitutive law of the reinforcement was assumed to be perfectly elastic-plastic (stress at yielding = f_{sy}).
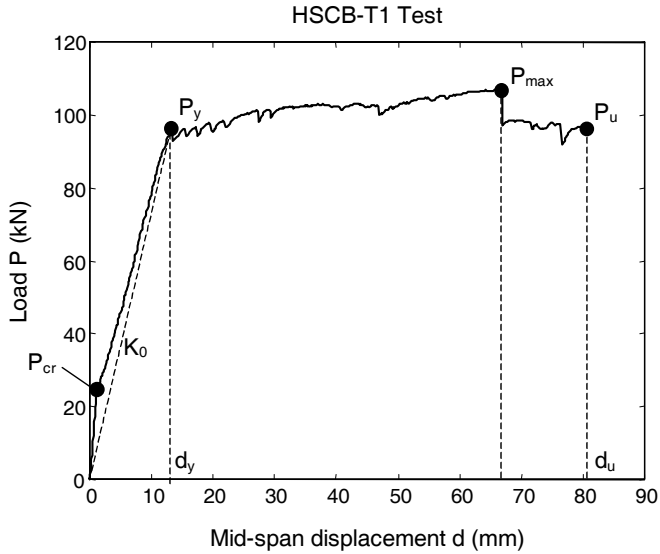
Figure 6 – Beam HSCB-T1: characteristic points of the load-displacement curve.
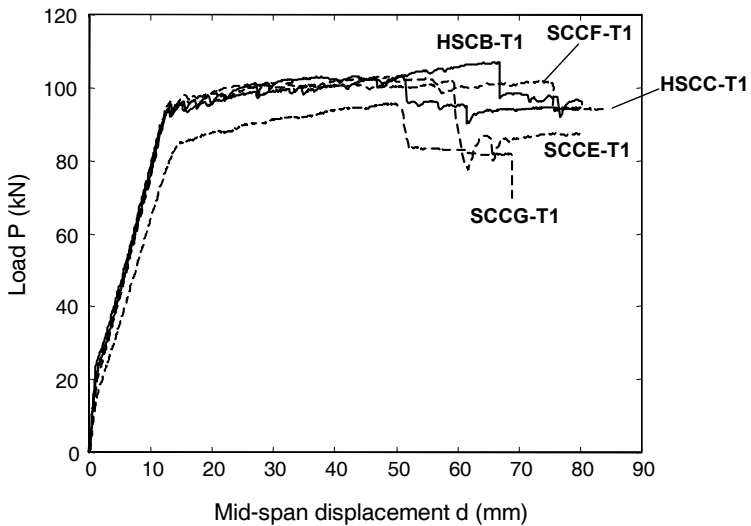

Figure 7 – Load vs. displacement curves under monotonic loading.

3.2 Bending moment–curvature relationship

A useful parameter to describe the behavior of a beam in bending is the concrete strain ε_c measured in the mid-span section at the compressive side. In the tests ε_c
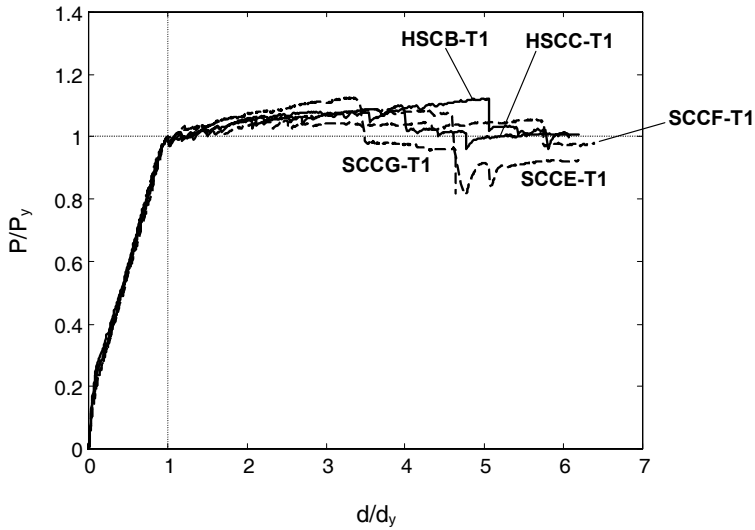
Figure 8 – Normalized load vs. mid-span displacement under monotonic loading.

was measured by means of the strain gauge D1, up to the occurrence of cover spalling (at the onset of spalling the strain is denoted as ε_{cu}). Note that Beam SCCF-T1 ε_c was measured only in the first part of the test, approximately up to the peak load. The values of the ultimate strain ε_{cu} are reported in Table 6. All are larger than 0.35% (with the exception of Beam SCCF-T1), which indicates that the limit of 0.35% for ε_{cu} is valid - for design purposes - also for SCC members.

Beam	$\varepsilon_{cu} \times 10^3$	χ_y [1/mm]	χ_{crush} [1/mm]	μ_s
HSCB-T1	6.0	2.87×10^{-5}	1.96×10^{-4}	6.83
HSCC-T1	4.5	2.54×10^{-5}	1.42×10^{-4}	5.58
SCCE-T1	6.6	2.75×10^{-5}	1.72×10^{-4}	6.24
SCCF-T1[1]	2.7	2.81×10^{-5}	0.64×10^{-4}	2.26
SCCG-T1	7.6	3.54×10^{-5}	1.62×10^{-4}	4.58

[1] ε_{cu}, χ_{crush}, μ_s = maximum values.

Table 6 – Results of the monotonic tests.

The values of the tensile strains in the concrete at the intrados of the beams ε_t were the mean of the values indicated by the 5 transducers. Thus, the average curvature χ of each beam is defined as:

$$\chi = \frac{|\varepsilon_c| + \varepsilon_t}{h} \tag{1}$$

where h is the depth of the cross section.

The strains are plotted as a function of time in Fig. 9, separately for Beams HSCB-T1, SCCE-T1 and SCCG-T1, and for Beams HSCC-T1 and SCCF-T1. Prior to yielding, the differences are negligible, and even past yielding there are only slight differences. These results show that – in terms of deformations - the flexural behavior of SCC beams is comparable to that of vibrated beams. Similar conclusions can be drawn by considering the plots of the bending moment vs. the curvature of the five beams (Fig. 10). Prior to concrete spalling, the bending moment of the beams is almost independent of the concrete mix-design, with the only exception of Beam SCCG-T1.

Further experimental results are shown in Table 6, where χ_y, χ_{crush} and μ_s are the average curvature at yielding, the average curvature corresponding to ε_{cu} and the sectional ductility, respectively, with:

$$\mu_s = \frac{\chi_{crush}}{\chi_y} \tag{2}$$

The sectional ductility's ranges from 4.58 to 6.83 (with the only exception of Beam SCCF-T1). In spite of this spread, no significant differences between SCC and vibrated beams emerged.


3.3 Damage and crack patterns

Figure 11 shows the central zone of the beams at the end of the tests (the spacing of the vertical lines is 100 mm and the cracks have been marked). The part of the concrete that exhibited more or less severe spalling at the extrados was larger in Beams SCCG-T1 and SCCE-T1. The spalling was less severe in the other beams. Again, no significant differences were detected between SCC and vibrated beams.

Different crack patterns were detected in the two beams made of normal-strength concrete (NSCD-T1 and SCCG-T1). In the first beam, the length of the cracked-concrete zone was 380 mm, whereas in the second the same zone had a 910 mm length (6 and 11 main cracks developed, respectively). Hence, in Beam SCCG-T1 the whole zone with constant bending was damaged, whereas more concentrated cracking was exhibited by Beam NSCD-T1.

With reference to HSC beams, the crack pattern exhibited no sizable differences in SCC and vibrated beams. The full results concerning the length of the cracked zone after testing, the number of the cracks and their average spacing are given in Table 10, together with the results of the cyclic tests.
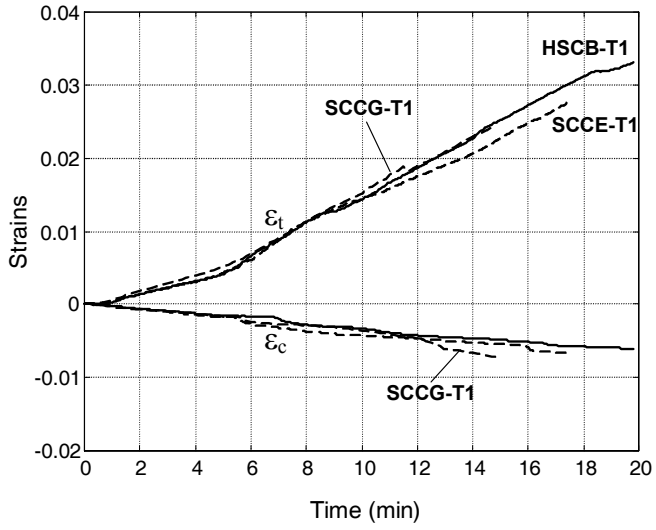
(a)
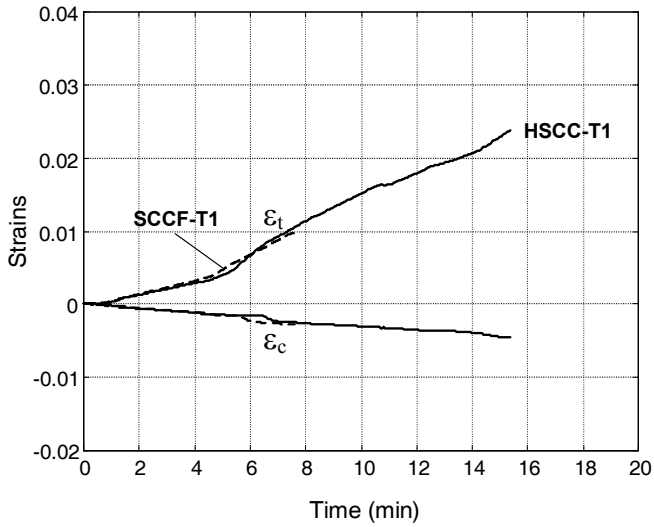
(b)

Figure 9 – Plots of the strains ε_c at the extrados and ε_t at the intrados for Beams HSCB-T1, SCCE-T1 and SCCG-T1 (a); and HSCC-T1 and SCCF-T1 (b).
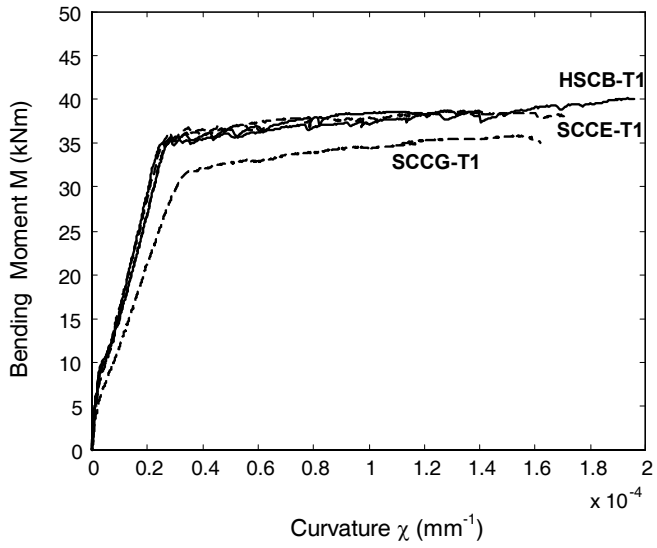
(a)
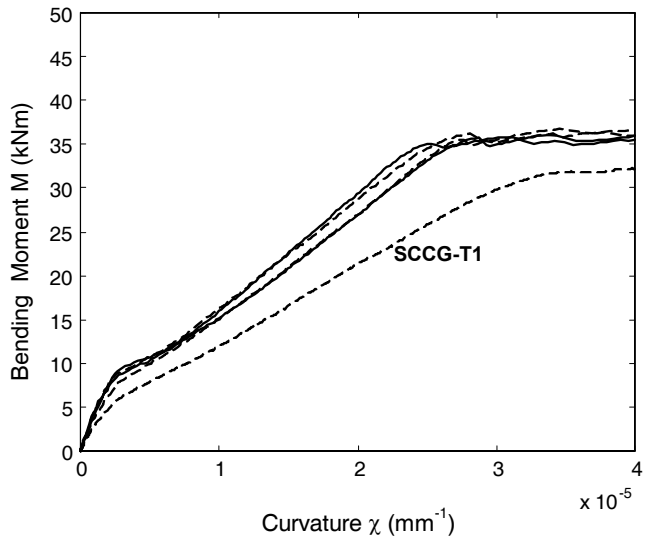
(b)

Figure 10 – Monotonic tests: plots of the bending moment as a function of the curvature for Beams HSCB-T1, SCCE-T1 and SCCG-T1 (a); and SCCG-T1 (b).
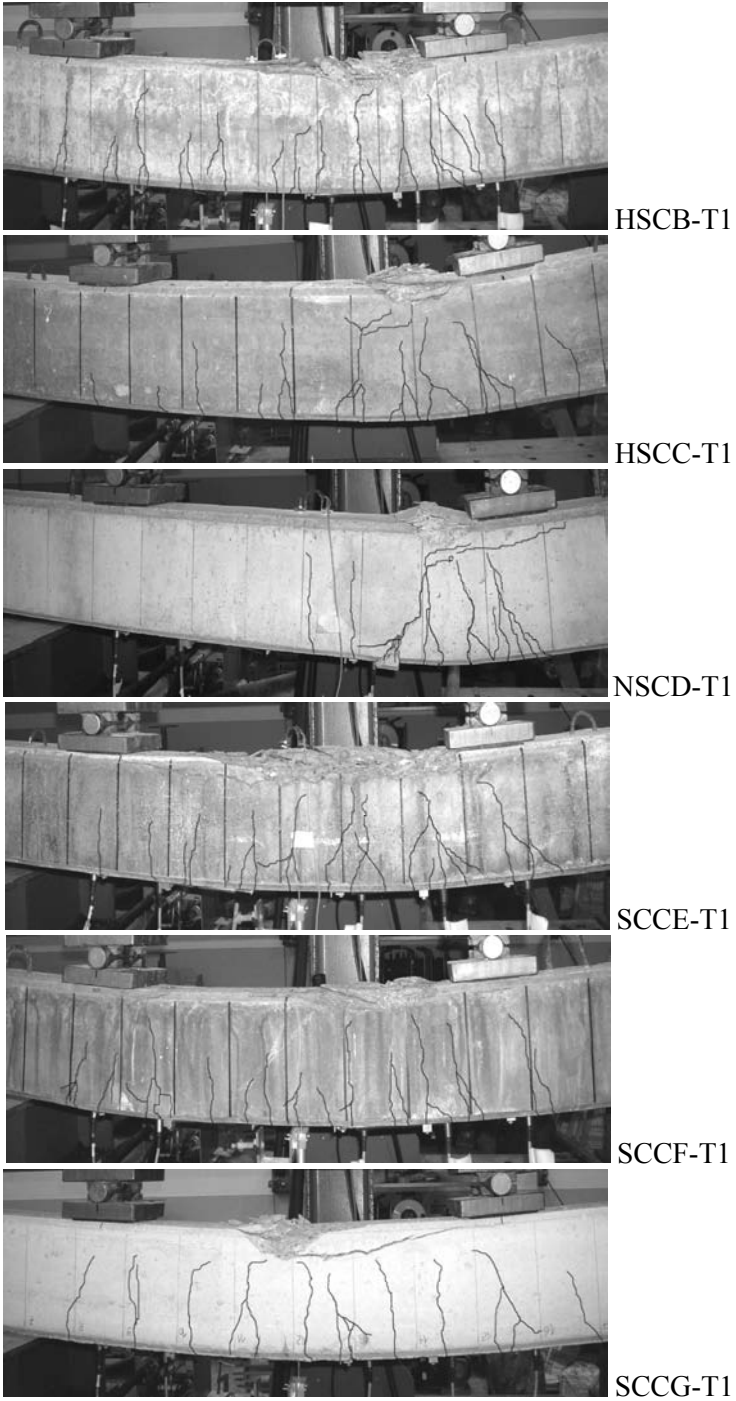
HSCB-T1

HSCC-T1

NSCD-T1

SCCE-T1

SCCF-T1

SCCG-T1

Figure 11 – Residual crack patterns.

4. CYCLIC TESTS

4.1 Load–displacement relationship

The cyclic tests were carried out according to the load history of Fig. 4, up to a maximum displacement d greater than 80 mm. One exception is Beam SCCG-T2, that was subjected to a single load cycle for each ductility level. At the end of each test, all the beams were severely damaged and the concrete cover along the extrados exhibited extensive spalling.

The flexural behavior was similar in all beams: the flexural strength was governed by the tension reinforcement and the ductility was limited by concrete crushing along the extrados. On the whole, the results of the cyclic tests were hardly different from those of the monotonic tests.

Figure 12 shows the load-displacement response of Beam HSCB-T2, which exhibits the same characteristic points already defined under monotonic loading: the first-cracking load P_{cr}, the load P_y at yielding, the maximum load P_{max} and the ultimate load P_u. The loads P_{cr} and P_y, as well as the displacement d_y were determined by hand calculations; yielding generally occurred during the 7th load cycle. These results are reported in Tables 7 and 8, while the curves enveloping the load-displacement responses are shown in Figs. 13 and 14 (dashed curves for SCC beams).

The envelope curves confirm the behavior exhibited during the monotonic tests: the first part of the ascending branches is almost linear and the first cracks appear close to the mid-span section at the intrados. The second part of the ascending branches is linear up to the yielding of the tension reinforcement. The hardening phase ends up with concrete spalling. As an example, Beam SCCG-T2 exhibited severe and sudden spalling in the concrete cover, when the displacement d reached 50 mm (Fig. 13a).

The tests on HSC beams, made either of SCC or vibrated concrete, exhibited very similar loads P_y and P_{max}. Small differences occurred for P_{cr}. These beams had a residual capacity (after testing) never below 0.80 P_{max}, and the displacement ductility d_u/d_y always exceeded the value 6. Only in Beams SCCE-T2 and SCCF-T2 the ratio P_u/P_{max} was slightly lower than 0.80 (0.79 and 0.76, respectively). The tests on the beams made of normal-strength vibrated concrete (NSCD) revealed a greater load capacity than that of their counterparts made of SCC (SCCG).

As in the case of monotonic tests, the normalized load-displacement curves are rather different in the various tests only beyond the yielding point (Fig. 14). The agreement between M_y and M_{ru} is reasonably satisfactory (Table 7).

Additional information on the response under cyclic loading is given by the secant-stiffness decay and by the amount of dissipated energy due to hysteretic phenomena. The secant stiffness corresponding to the ith cycle was calculated as $K_i = P_i/d_i$, where d_i is the maximum displacement in the same cycle and P_i the corresponding load (Fig. 12). The growing hysteretic energy E_h is given by the

area enveloped by the P – d diagram. K_i and E_h are reported in Figs. 15 and 16 for the beams T2 (E_{hEPP} is the energy dissipated by an elastic perfectly-plastic SDOF system in a half cycle with a displacement ductility equal to the actual maximum ductility).

Needless to say, the behavior of SCC beams is equivalent to that of the vibrated beams. Similar conclusions can be drawn for the Beams T3.

Beam	P_{cr} [kN]	P_y [kN]	P_{max} [kN]	M_y [kNm]	M_{ru} [kNm]
HSCB-T2	26.70	98.42	103.92	36.91	33.44
HSCB-T3	25.44	100.18	108.62	37.57	33.44
HSCC-T2	24.86	92.20	99.46	34.58	34.09
HSCC-T3	23.56	93.22	97.66	34.96	34.09
NSCD-T2	16.78	99.80	102.18	37.43	32.09
NSCD-T3	15.30	96.42	99.78	36.16	32.09
SCCE-T2	21.26	99.04	105.20	37.14	33.48
SCCE-T3	16.84	96.16	103.28	36.06	33.48
SCCF-T2	23.86	94.26	104.10	35.35	33.75
SCCF-T3	24.98	97.62	105.60	36.61	33.75
SCCG-T2	11.80	85.28	96.18	31.98	31.01
SCCG-T3	14.78	85.92	95.60	32.22	31.01

Table 7 – Cyclic tests : loads and moments at first cracking (cr), at yielding of the bottom reinforcement (y), at the peak of the load-displacement curve (max) and according to EC-2 (ru).

Beam	n_{cycles}	$K_0 = P_y/d_y$ [kN/mm]	d_y [mm]	d_u/d_y	P_u/P_{max}
HSCB-T2	37	7.46	13.2	6.2	0.85
HSCB-T3	37	7.50	13.4	6.0	0.89
HSCC-T2	37	7.32	12.6	6.4	0.81
HSCC-T3	37	7.08	13.2	6.1	0.86
NSCD-T2	34	7.01	14.2	5.8	0.91
NSCD-T3	34	6.31	15.3	5.4	0.95
SCCE-T2	36	7.77	12.7	6.4	0.79
SCCE-T3	37	7.69	12.5	6.6	0.82
SCCF-T2	36	7.09	13.3	6.3	0.76
SCCF-T3	39	8.14	12.0	7.4	0.90
SCCG-T2	9	5.65	15.1	5.3	0.83
SCCG-T3	29	6.10	14.1	5.7	0.81

Table 8 – Cyclic tests : number of cycles necessary to reach the maximum preset displacement (n_{cycles}), secant stiffness in the monotonic test (K_0), displacement at reinforcement yielding (d_y), displacement ductility (d_u/d_y), and ratio of the load at the maximum displacement to the maximum load (P_u/P_{max}).
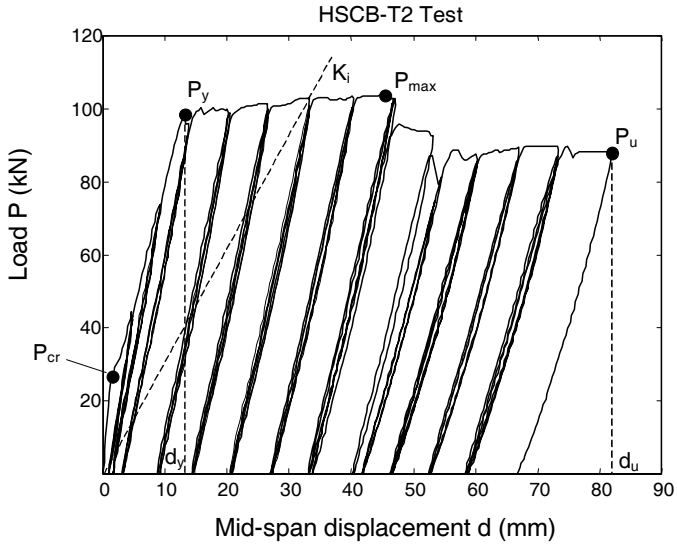
Figure 12 – Cyclic tests - Beam HSCB-T2: characteristic points of the load-displacement response.

Figure 13a – Cyclic tests : envelope curves of the load-displacement responses for Beams NSCD-T2, NSCD-T3, SCCG-T2 and SCCG-T3.
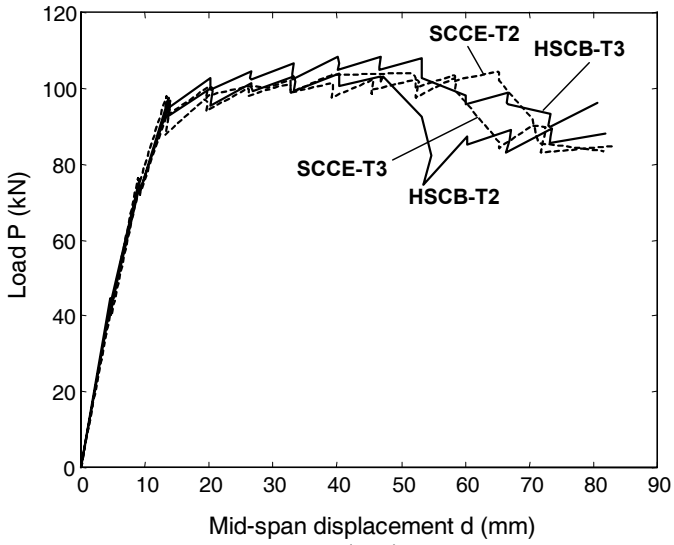
(b)
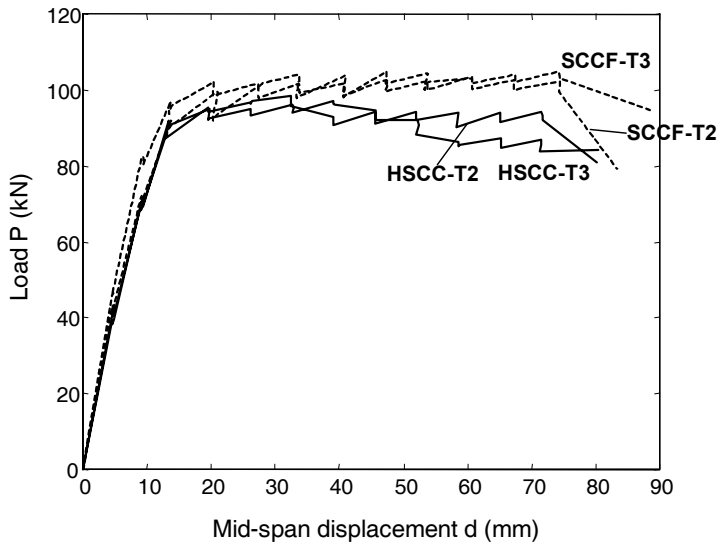
(c)

Figures 13b,c – Cyclic tests : envelope curves of the load-displacement responses for Beams SCCE-T2, SCCE-T3, HSCB-T2 and HSCB-T3 (a); and SCCF-T2, SCCF-T3, HSCC-T2 and HSCC-T3 (b).
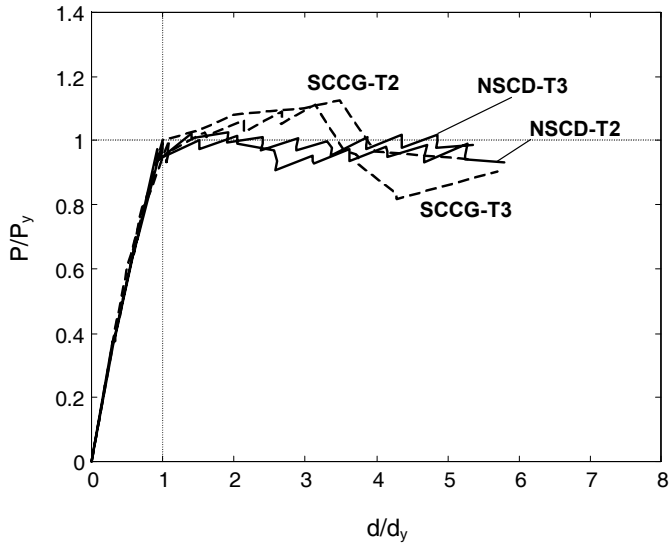
(a)
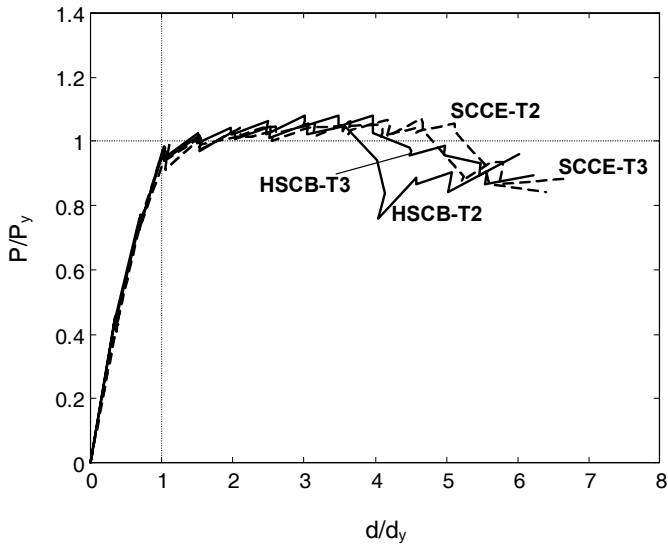
(b)

Figures 14a,b – Cyclic tests : envelope curves of the normalized load-displacement responses for Beams SCCE-T2, SCCE-T3, HSCB-T2 and HSCB-T3.
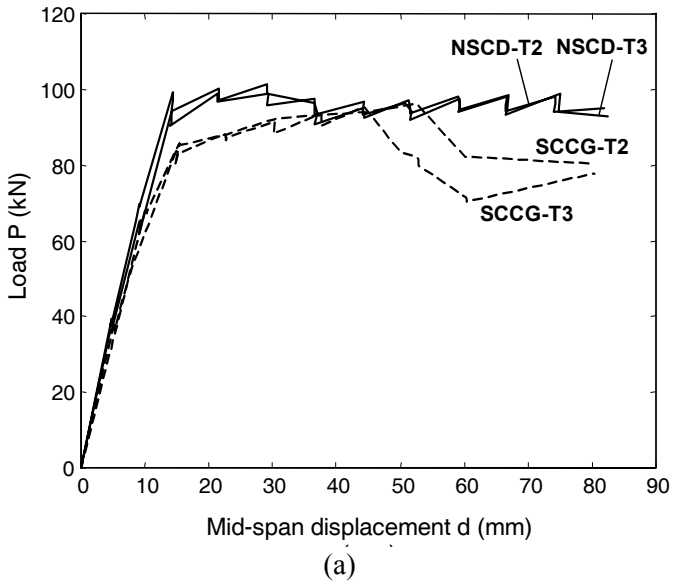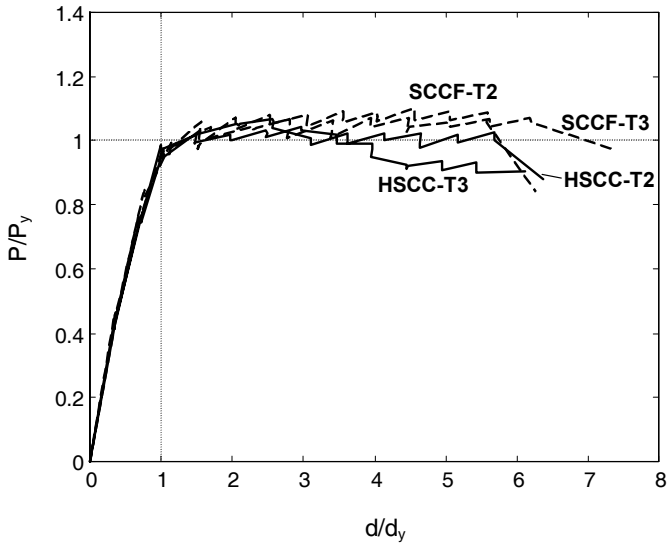
(c)

Figure 14c – Cyclic tests : envelope curves of the normalized load-displacement responses of Beams SCCF-T2, SCCF-T3, HSCC-T2 and HSCC-T3..
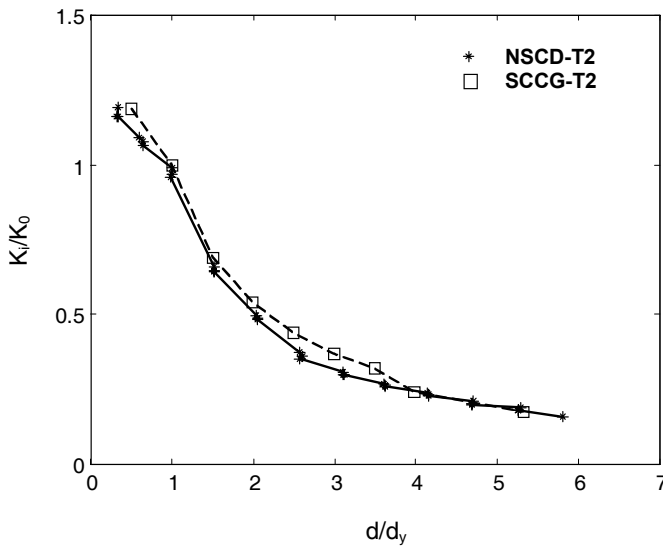
Figure 15a – Cyclic tests – Beams NSCD-T2 and SCCG-T2 : normalized secant stiffness (K_i/K_0) as a function of the displacement ductility $\mu = d/d_y$.
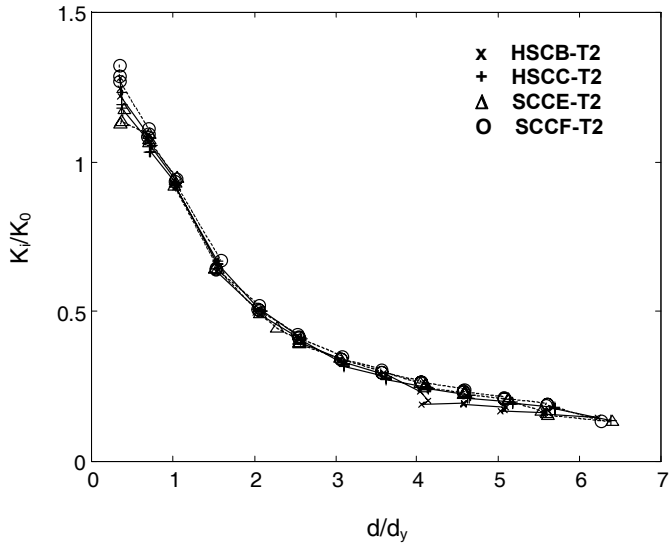
Figure 15b – Cyclic tests – Beams HSCB-T2, HSCC-T2, SCCE-T2 and SCCF-T2: normalized secant stiffness (K_i/K_0) as a function of the displacement ductility $\mu = d/d_y$.
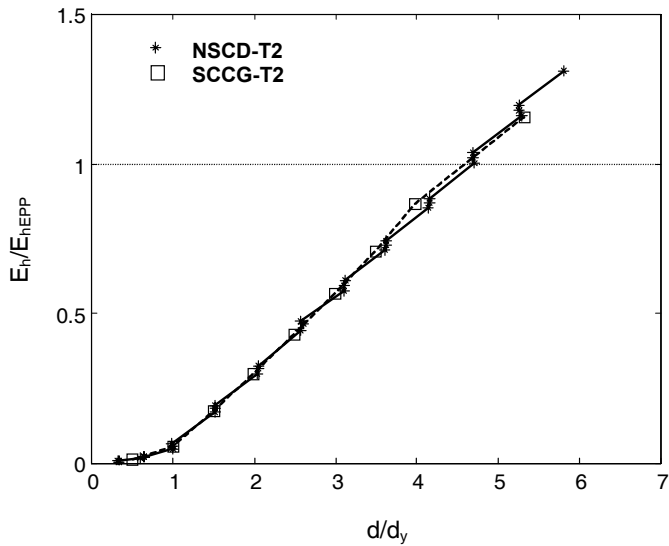
Figure 16a – Cyclic tests – Beams NSCD-T2 and SCCG-T2 : normalized hysteretic energy (E_h/E_{hEPP}) as a function of the displacement ductility $\mu = d/d_y$.
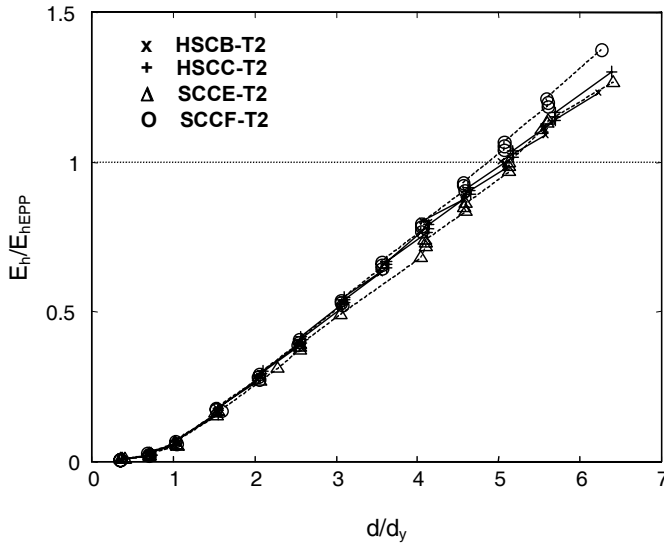
Figure 16b – Cyclic tests – Beams HSCB-T2, HSCC-T2, SCCE-T2 and SCCF-T2: normalized hysteretic energy (E_h/E_{hEPP}) as a function of the displacement ductility $\mu = d/d_y$.

4.2 Bending moment–curvature relationship and deformations

The compressive and tensile strains ε_c and ε_t in the concrete at mid-span were measured (as in the monotonic tests), in order to obtain the average curvature in the central zone.

Two examples of the strain vs. time curves are presented in Fig. 17 for Beams HSCB-T3 and SCCE-T3, and for Beams NSCD-T3 and SCCG-T3.

No significant differences between SCC and vibrated beams emerge from these plots. Hence, even at large strains the behaviors are similar.

Complete information on the deformations in the cyclic tests is given in Table 9 (the symbols are the same as in the case of monotonic tests).

Note that for Beams NSCD and SCCF the ultimate values refer to a situation immediately preceding cover spalling. The ultimate concrete compressive strain is always greater than 0.35%, as a further confirmation that this limit is safe for the computation of sectional ductility, even in the case of SCC.

The sectional ductility ranged from 2.88 up to 7.24 for all cyclic tests. In spite of this large spread, no significant differences between SCC and vibrated beams appeared.

The lowest measured ductility (< 5) is that of Beams SCCG and HSCC.
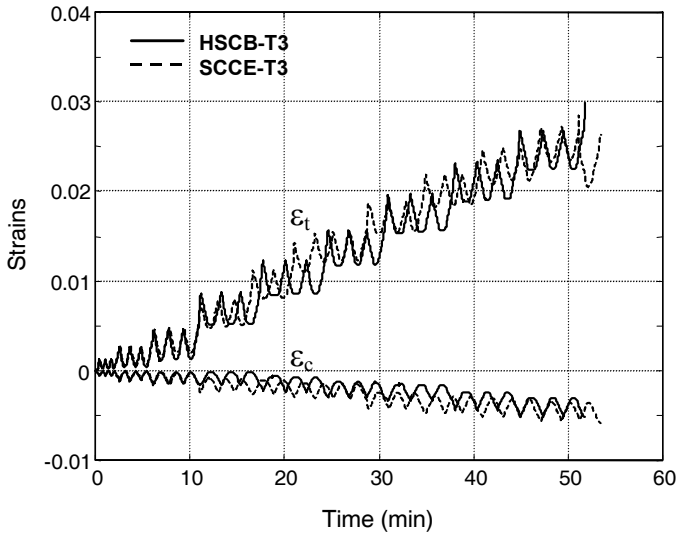
(a)
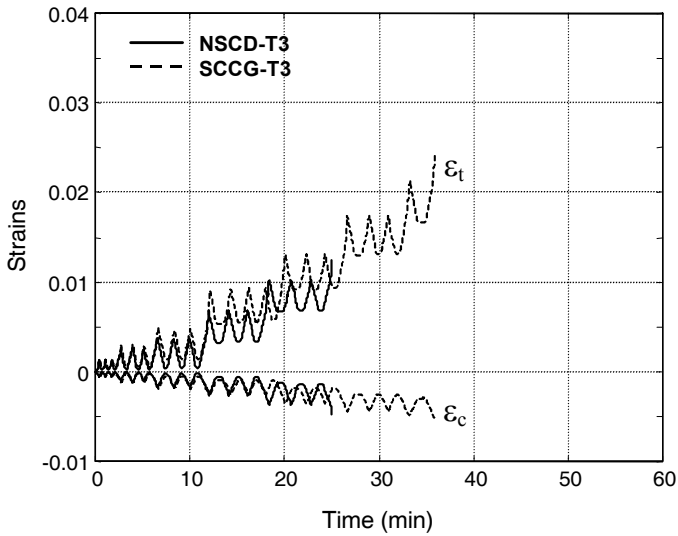
(b)

Figure 17 – Plots of the strains ε_c along the extrados (in compression) and ε_t along the intrados (in tension) in the tests on Beams HSCB-T3 and SCCE-T3 (a); and on Beams NSCD-T3 and SCCG-T3 (b).

Beam	$\varepsilon_{cu} \times 10^3$	χ_y [1/mm]	χ_{crush} [1/mm]	μ_s
HSCB-T2	3.8	2.60×10^{-5}	1.39×10^{-4}	5.35
HSCB-T3	5.2	2.81×10^{-5}	1.75×10^{-4}	6.22
HSCC-T2	3.8	2.71×10^{-5}	1.03×10^{-4}	3.80
HSCC-T3	4.0	2.92×10^{-5}	1.34×10^{-4}	4.60
NSCD-T2[1]	5.0	2.96×10^{-5}	9.95×10^{-5}	3.36
NSCD-T3[1]	4.7	2.96×10^{-5}	8.53×10^{-5}	2.88
SCCE-T2	6.0	3.39×10^{-5}	2.26×10^{-4}	6.65
SCCE-T3	5.9	2.56×10^{-5}	1.61×10^{-4}	6.31
SCCF-T2[1]	5.7	3.01×10^{-5}	1.89×10^{-4}	6.27
SCCF-T3[1]	6.7	2.58×10^{-5}	1.87×10^{-4}	7.24
SCCG-T2	6.8	3.03×10^{-5}	1.45×10^{-4}	4.77
SCCG-T3	5.2	3.00×10^{-5}	1.47×10^{-4}	4.88

[1] $\varepsilon_{cu,}$ $\chi_{crush},$ μ_s = maximum values.

Table 9 – Results of the cyclic tests.

4.3 Damage and crack patterns

Figures 18 and 19 show the central zone of the beams after testing. The spacing between two adjacent vertical lines is 100 mm as in monotonic tests. The crack patterns are very similar in all tests; the number of cracks ranges from 8 to 13 (average spacing 60 – 80 mm, see Table 10).

Beams HSCB-T2, HSCC-T3 and SCCE-T3 exhibited a damaged zone close to the right support, and the damage was more concentrated than in the other beams. However, these differences do not imply any clear trend related to concrete mix design.

Some differences were observed between Beams SCCG and HSCC. In the first case, several cracks spaced at 90 mm appeared in the central zone at the beginning of the tests. Later, the width of these cracks increased up to 1-3 mm. In the second case, prior to reinforcement yielding, only two cracks appeared at the intrados; later, the crack pattern became concentrated in a 500 mm-zone located at the right of the mid-span section.

Also in beams HSCC the crack width was smaller than in beams SCCG. Intermediate crack patterns were detected in the other eight beams. The cyclic tests revealed a rather marked brittleness in all HSC beams (either vibrated or made of SCC).

On the whole, the beams subjected to cyclic loading were damaged very similarly to those tested under monotonic loading. Hence, the tests confirm the sizable brittleness of HSC even under cyclic loading.

The maximum load and the ductility were similar to those evaluated by means of theoretical formulae.
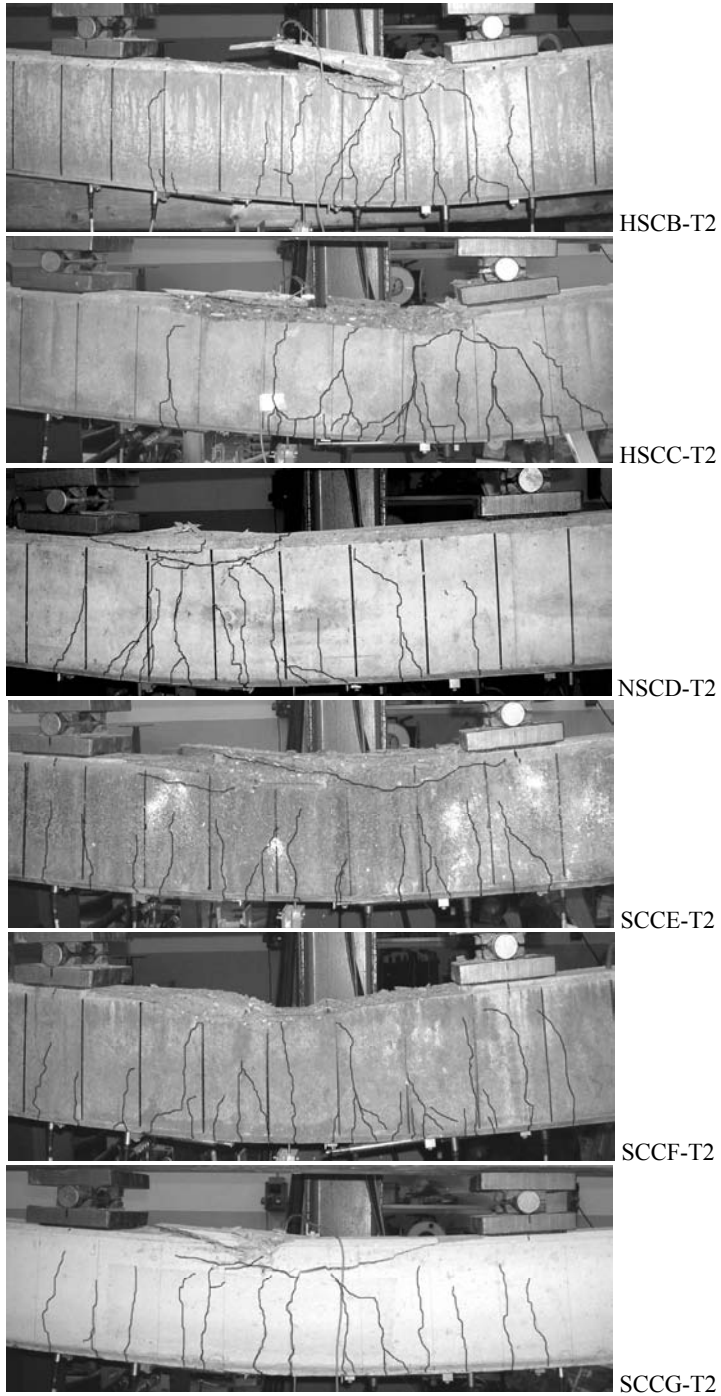
HSCB-T2

HSCC-T2

NSCD-T2

SCCE-T2

SCCF-T2

SCCG-T2

Figure 18 – Cyclic tests – Tests T2 : residual crack patterns.

HSCB-T3

HSCC-T3

NSCD-T3

SCCE-T3

SCCF-T3

SCCG-T3
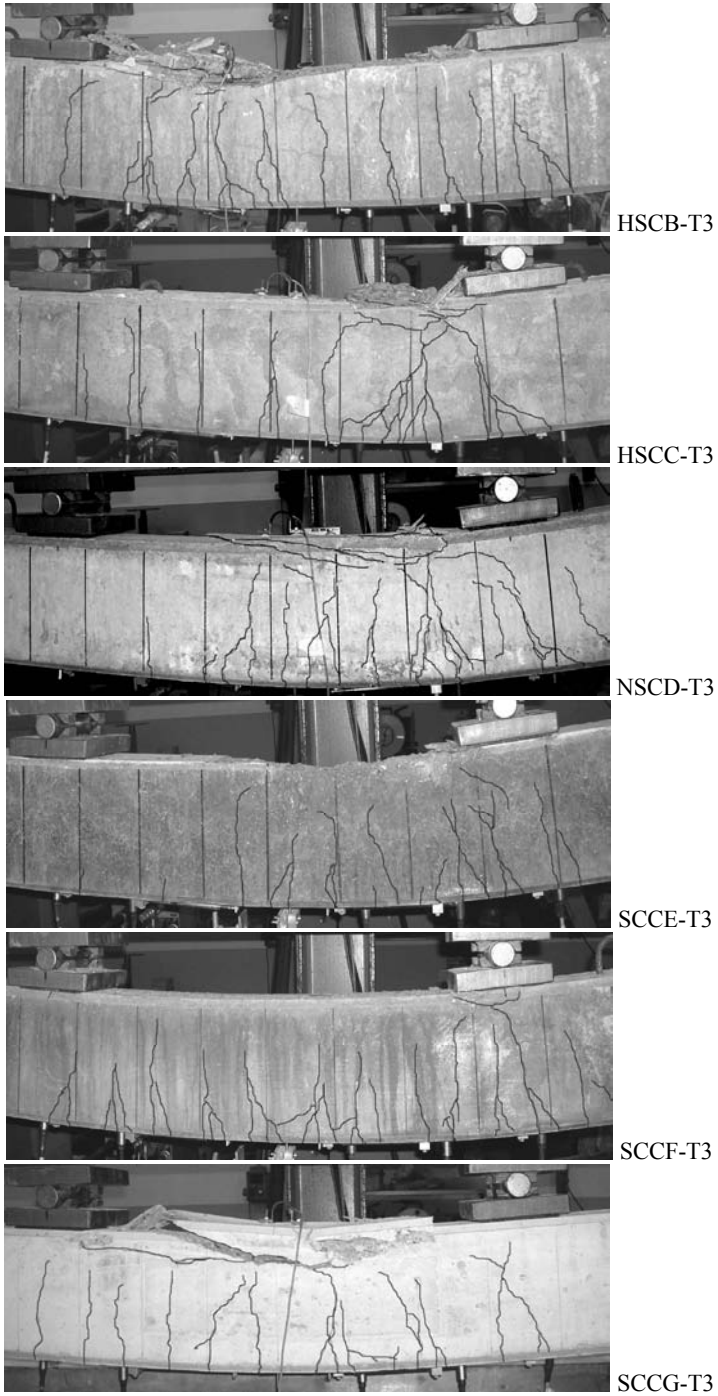
Figure 19 – Cyclic tests – Tests T3 : residual crack patterns.

Beam	l_{f1} [mm]	l_{f2} [mm]	n_{f1}	n_{f2}	s_1 [mm]	s_2 [mm]
HSCB-T1	770	770	12	10	64.2	77.0
HSCB-T2	620	620	9	9	68.9	68.9
HSCB-T3	730	730	11	11	66.4	66.4
HSCC-T1	820	510	9	6	91.1	85.0
HSCC-T2	630	630	10	10	63.0	63.0
HSCC-T3	660	600	10	9	66.0	66.7
NSCD-T1	380	380	6	5	63.3	76.0
NSCD-T2	620	620	8	8	77.5	77.5
NSCD-T3	700	600	10	9	70.0	66.7
SCCE-T1	780	450	10	6	78.0	75.0
SCCE-T2	750	750	12	12	62.5	62.5
SCCE-T3	600	470	8	7	75.0	67.1
SCCF-T1	830	330	12	4	69.2	82.5
SCCF-T2	810	610	11	8	73.6	76.3
SCCF-T3	830	700	12	10	69.2	70.0
SCCG-T1	910	910	11	10	82.7	91.0
SCCG-T2	750	750	13	13	57.7	57.7
SCCG-T3	750	750	11	11	68.2	68.2

Table 10 – Parameters concerning the crack patterns: length of the cracked zone; number of the cracks; and crack spacing.

5. CONCLUDING REMARKS

The experimental tests carried out on eighteen beams made of normal-strength and high-strength concrete, either vibrated or self-consolidating, lead to the following remarks.

The ultimate flexural capacity and the sectional ductility of SCC and vibrated beams are comparable for the same concrete grade. This conclusion is based on the maximum load, on the maximum mid-span deformation at the extrados and at the intrados, and on the average curvature of the specimens tested under monotonic loading. The cyclic tests revealed that the decays of both the secant stiffness and dissipated hysteretic energy are similar in SCC and vibrated beams.

Some qualitative differences were observed with reference to the crack pattern and damage of the beams. These differences, however, were mainly caused by the different concrete grade rather than by the properties ensuing from the self-consolidation capability. A rather slight difference between SCC and vibrated beams was detected by examining the residual crack patterns. The vibrated beams showed a more concentrated damaged zone compared to that of the SCC beams. These differences, however, are hardly relevant in design applications.

On the whole, these experimental campaign reveals that the mechanical

performance of R/C beams in bending does not depend on whether self-consolidating or vibrated concrete is used. However, it should be noted that – being the beams tested in this research project lightly reinforced - their bending behavior is mainly governed by the mechanical properties of the reinforcement. Hence, further experiments on heavily-reinforced beams should be performed.

ACKNOWLEDGEMENTS

REFERENCES

ACI Committee 237-03 (2003). "*Emerging Technology Series on Self-Consolidating Concrete*", American Concrete Institute, Farmington Hills, MI, USA.

Angotti F., Galano L. and Vignoli A. (2007). "Strength and Ductility of Beams Made of High-Strength and Self-Consolidating Concrete" (in Italian), *Proc. of 24th Nat. Conf. of AICAP (Italian Soc. for R/C and P/C Structures),* ed. and pub. by AICAP, October 2007, Salerno (Italy), pp. 3-8.

Angotti F., Galano L. and Vignoli A. (2009). "Strength and Ductility of HSC and SCC Beams Subjected to Oligocyclic Loading" (in Italian), *Proc. of 25th Nat. Conf. of AICAP (Italian Soc. for R/C and P/C Structures),* ed. and pub. by AICAP, May 2009, Pisa (Italy), pp. 41-48.

Cattaneo S., Mola F. and Rosati G. (2007). "Shear Strength in Self-Compacting Reinforced-Concrete Beams", *Proc. of 4th Int. Conf. on the Conceptual Approach to Structural Design*, 28-29 June 2007, Venice (Italy).

CEN-EN 1992-1-1 (2004). *"Eurocode 2: Design of Concrete Structures - Part 1-1: General Rules and Rules for Buildings"*, Bruxelles, Belgium, December 2004.

Das D., Kaushik S. K. and Gupta V. K. (2005). "Shear Resistance of Self-Compacting Concrete", *Proc. of SCC 2005 Conf. Center for Advanced Cement-Based Materials*, Northwestern University, Evanston, Illinois, USA.

Italian Ministry of Public Works - Decree 9-01-1996 (1996). *"Technical Provisions for the Design, Manufacture and Certification of R/C and P/C Structures, and of Metallic Structures"* (in Italian), Official Gazette 5-2-1996, No. 29.

EFNARC - European Federation of National Trade Associations (2002). *"Specification and Guidelines for Self-Compacting Concrete"*, Surrey, UK, February 2002.

Sonebi M., Tamini A. K. and Bartos P. J. M. (2003). "Performance and Cracking Behavior of Reinforced Beams Cast with Self-Consolidating Concrete", *ACI Material Journal*, Vol. 100, No. 6, pp. 492-500.

UNI 6556 (1976). *"Concrete Testing: Determination of the Secant Elastic Modulus in Compression"* (in Italian), Italian Normalization Institute.

NOTATION

A_s = area of the tension reinforcement in the mid-span section
A_5 = ultimate ductility of the reinforcement
E_{cs} = concrete secant modulus of elasticity
E_h = hysteretic energy
E_{hEPP} = energy dissipated by an elastic perfectly-plastic single-degree-of-freedom system
K_i = secant stiffness at the ith cycle (= P_i/d_i)
K_0 = secant stiffness at yielding of the load-displacement curve under monotonic loading
M_{ru} = bending moment evaluated with the analytical procedure suggested by EC2
M_y = bending moment at yielding
P = load applied during a test
P_{cr} = first-crack load
P_i = load corresponding to the displacement d_i
P_{max} = maximum load
P_u = ultimate load
P_y = load at yielding
b = width of the cross section
d = mid-span displacement
d_a = aggregate size
d_{amax} = maximum aggregate size
d_i = maximum mid-span displacement at the ith cycle
d_u = ultimate mid-span displacement
d_y = mid-span displacement at yielding
$f_{c,cube}$ = concrete cube compressive strength at the onset of testing
$f_{c,cyl}$ = concrete cylindrical compressive strength at the onset of testing
$f_{c28,cube}$ = concrete cube compressive strength at 28 days
$f_{c28,cyl}$ = concrete cylindrical compressive strength at 28 days
$f_{c,split}$ = concrete splitting tensile strength at the onset of testing

f_r = concrete flexural tensile strength at the onset of testing
f_{su} = ultimate strength of the reinforcement
f_{sy} = yield strength of the reinforcement
h = section depth
l = total length of the specimen
l_{f1} = total length of the cracked zone after testing
l_{f2} = as l_{f1} but including only the cracks propagated above $h/2$
n_{f1} = total number of the cracks
n_{f2} = as n_{f1} but including only the cracks propagated above $h/2$
s = stirrup spacing
s_1 = average spacing of the cracks
s_2 = as s_1 but including only the cracks propagated above $h/2$
ε_c = concrete strain at the extrados in the mid-span section
ε_{cu} = ultimate concrete strain at the extrados in the mid-span section
ε_t = average concrete strain at the intrados
$\varnothing$ = bar diameter
γ = concrete density / concrete mass per unit volume
χ = average curvature
χ_y = average curvature at yielding
χ_{crush} = average curvature at cover spalling
ρ_s = steel ratio of the tension reinforcement
μ = displacement ductility
μ_s = sectional ductility

extrados = top side, belonging to the compression zone in a simply-supported beam
intrados = bottom side, belonging to the tension zone in a simply-supported beam.

R/C COLUMNS STRENGTHENED BY MEANS OF STEEL ANGLES AND BATTENS: TESTING, MODELING AND DESIGN

Giuseppe Campione[1]

ABSTRACT

An experimental investigation on the compressive behavior of eight short, confined, reinforced-concrete columns, externally strengthened by means of steel angles and battens with different spacing, is presented in this paper, together with an analytical model, which considers the strengthened column as a composite member. The model describes the favorable confining effect exerted by both the battens and the angles on concrete core, and takes care of the contribution of the angles to the load-carrying capacity of the column. (The angles are primarily subjected to an axial force, but some bending occurs because of the lateral angle-concrete pressure).

The two cases of directly- and indirectly-loaded angles are addressed. The numerical results are compared with the experimental results available in the literature and with those provided by other analytical models. The fitting of the experimental results and the agreement with those obtained by using other models is satisfactory, for both directly- and indirectly-loaded angles.

The proposed model allows to check and comment the available code provisions concerning structural strengthening via angles and battens.

---

[1] Associate Professor, Department of Aerospace, Structural and Geotechnical Engineering, University of Palermo, Palermo, Italy.
<campione@diseg.unipa.it>

1. INTRODUCTION

Several systems aimed to increase the bearing capacity and the ductility of R/C columns take advantage of the lateral confinement exerted by: (a) traditional steel stirrups; (b) FRP wrapping; (c) steel jacketing; (d) longitudinal angles and pre-tensioned steel ribbons [6]; and (d) light-weight or normal-weight concrete jacketing, to quote some of the available technologies.

Within such a context, the focus of this paper is on steel-jacketing techniques applied to R/C columns. According to Eurocode 8 [2] steel jackets around square (or rectangular) columns usually consist of four corner angles connected by means of continuous welded steel plates, or by rather thick discrete horizontal battens welded to the angles. The angles may be epoxy-bonded to the concrete, or may simply adhere to the corners. The battens may be pre-heated prior to welding, in order to increase at a later stage the confinement exerted by the angles.

A typical case of a column strengthened by means of angles and battens is shown in Fig.1. Angles and battens exert a confinement pressure on concrete core, when concrete expands laterally (under compressive loading), to the advantage of the load-carrying capacity. This technique brings in two favorable side effects: more ductility (because of the multi-axial state of stress in compression in the concrete core) and less risk of buckling in the longitudinal bars [1, 3, 5-12].

Depending on the structural details adopted in the beam-column joints, the angles act as (a) tension and compression members, (b) compression members or (c) confining devices.

Fig. 1 - R/C columns strengthened by means of angles and battens.

Angles and battens are extensively used in many countries of the Mediterranean area, mainly because they do not increase significantly the cross-section, and are both handy and durable (once adequate protection against fire and corrosion is provided). As for the design of the strengthened members, including the evaluation of their load carrying capacity, several tests and theoretical models are available [1, 2, 4]. Only few studies, however, takes care of the increased load-carrying capacity ensuing from the coupling of the confinement effect and of the load directly carried by the angles [10, 11, 14].

In this paper, an experimentally-validated analytical model is presented and discussed. The tests were carried out on R/C square columns externally strengthened with angles at the corners and battens welded to the angles.

2. EXPERIMENTAL INVESTIGATION

Eight R/C square columns externally strengthened with four steel angles connected by a number of battens [12] were tested in compression. The geometry and the details of the internal reinforcement are shown in Fig. 2.

δ=25mm: a=215mm, a'=415mm, b=246mm
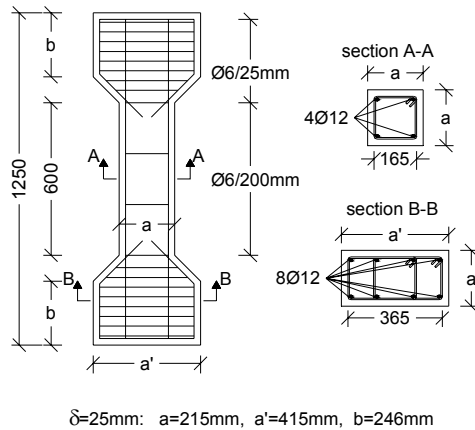
Fig. 2 – Geometry and reinforcement of the specimens tested in this project.

The columns were cast horizontally (total length = 1250 mm; mid-portion length = 600 mm; side of the square cross-section = 215 mm). All specimens were reinforced with four ∅ 12-mm longitudinal bars and ∅ 6-mm closed stirrups spaced by 200 mm. The specimens had dog bone-shaped end portions, which were reinforced with eight ∅ 12-mm longitudinal bars and ∅ 6-mm stirrups spaced by 65 mm, this additional reinforcement being aimed to avoid any premature failure of the end portions during the tests. The steel ratio of the transverse reinforcement

was ρ_{st} = A_{st}/(s·a) = 0.131%, where A_{st} is the total area of the stirrups over the spacing s, and a is the side length of the section. The steel ratio of the longitudinal reinforcement was ρ_{fl} = A_{fl}/a^2 = 0.98%, where A_{fl} is the total area of the longitudinal bars. (The geometric percentage of the longitudinal reinforcement adhere to neither the European nor the American design codes, but is typical of many columns designed only for gravity loads).

Some of the columns were also externally strengthened with angles and battens welded to the angles. The geometry of the angles was: length = 600 mm, width = 30 mm, and thickness = 3 mm, while the geometry of each batten was: length = 185 mm, width = 30 mm and thickness = 3 mm. The ends of the columns were laterally expanded to localize the failure in the central portion of the shank and to have the angles directly loaded in compression.

The battens at the end sections of the central zone of each specimen (length = 600 mm, see Fig.3 for details) were wider (width = 40 mm) and thicker (thickness = 5 mm). The angles were glued to the concrete by means of an epoxy mortar, while the battens were externally welded to the angles (no epoxy mortar between each batten and the concrete).

In more details (Fig.3), the experimental program included 8 R/C specimens: 2 without angles and battens; 2 reinforced with angles and battens placed only at the ends of the central part; 2 as in the previous case, but with an extra batten in the mid-height section; and 2 reinforced with angles and equally-spaced battens (4 battens spaced by 200 mm).

The stiffer battens adopted at the ends of the central part of each specimen were aimed to increase locally the confining action and to guarantee the transmission of the load to the angles.
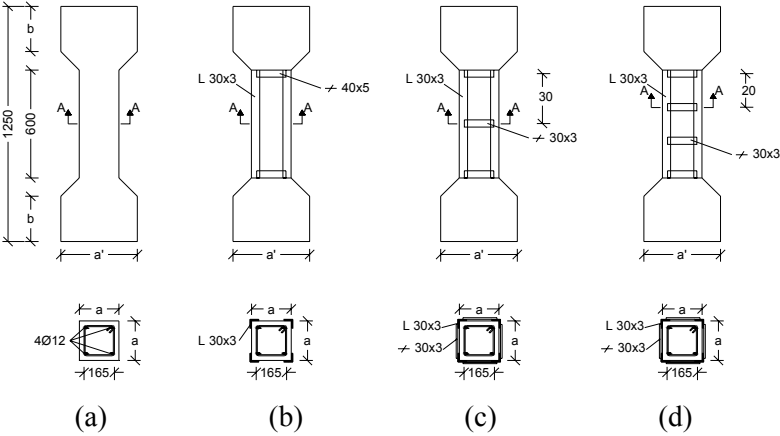

Fig. 3 – R/C specimens without external reinforcement (a), and with angles and battens (b,c,d).

The spacing of the stirrups adopted in the central part of the columns provided a low confinement level and was chosen in such a way that the yielding of the longitudinal bars, the spalling of their concrete cover and their buckling occurred simultaneously. One of the objectives was to evaluate the influence of both angles and battens in preventing (or delaying) the buckling of the longitudinal bars.

The mix design of the concrete included Portland cement (ASTM Type I) and a water/cement ratio equal to 0.57 (Table 1). This mix design is not the best for a structural concrete (f_c = 15-20 MPa, and even 10 MPa). Such a strength, however, is often found in many constructions built after the 2nd World War in the Mediterranean area. Since the required strength for design purposes may be higher than the effective strength (measured in situ), the strengthening technique based on angles and battens appears to be well suited to increase the safety level of these low-quality structures.

For the mechanical characterization of concrete, four 100x200 mm cylinders were tested in compression (to measure f_c) and four in tension (splitting tests, $f_{t,sp}$) at 28 days, see Table 1.

Table 1 – Mix design and mechanical properties of concrete.

Constituents	Mass per unit volume (kg/m^3)	Mechanical properties (MPa)	
Cement	300	f_c	$f_{t,sp}$
Water (w/c)	170 (0.57)	10.3	1.87
Sand	1040		
Natural gravel (d_a = 20 mm)	980		

For the mechanical characterization of the longitudinal bars (Ø = 12mm) and of the transverse reinforcement (Ø = 6mm), direct tensile tests were carried out. The values of the strength at yielding f_y are given in Table 2. The steel used for both the battens and the angles is classified as S 235 according to Eurocode 3 [15] (f_y = 239 MPa).

Table 2 – Mechanical properties of the reinforcement.

Diameter (mm)	f_y (MPa)
12	461
6	480

To perform the displacement-controlled tests, a 4000 kN-press manufactured by Zwick/Roell & Toni Technik was utilized. The vertical load was applied to the columns by interposing two 20 mm-thick steel plates between the specimen and the loading platens. Only the vertical displacement (axial shortening) was recorded by means of four LVDTs (base-length = distance between the steel plates).

Fig.4 shows the load-axial shortening (P-δ) curves recorded during the tests (2 curves for each of the four specimen types).

All the response curves are characterized by an initial linear-elastic branch up to a value of approximately 30% of the peak load. (For any combination of angles and battens, the initial stiffness is very close to that of R/C columns = no angles and battens).

After this first – and rather limited - stage, a progressive loss was observed for the axial stiffness, with a nonlinear behavior up to the peak-load. (This loss was more pronounced in R/C specimens).

As should be expected, the load-carrying capacity of the columns markedly increases if angles and battens are introduced. As a matter of fact, the angles contribute directly to the load-bearing capacity by increasing the resisting section, and indirectly – together with the battens – by improving concrete strength via lateral confinement.

The effect of the battens depends on their spacing, as the smaller the spacing, the larger the contribution to the load-bearing capacity.

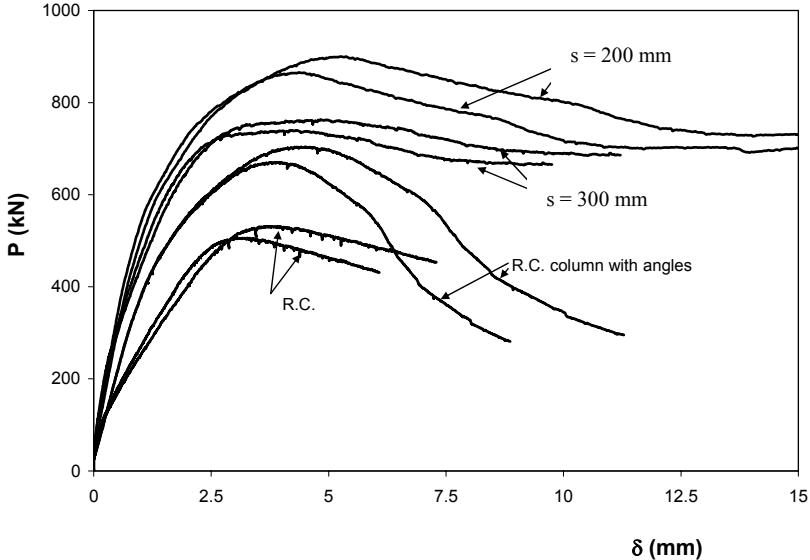In all cases, past the load peak there is a prolonged softening.

Fig. 4 - Load-axial shortening curves (P-δ): R/C = no angles and battens.

In R/C specimens, the strength degradation measured in the softening phase is due first to concrete crushing and then to the buckling of the longitudinal bars (Fig.5a). When angles are introduced, the cover contribution becomes more effective because of the delayed spalling process. If there are no battens in the central part of the specimen, the angles buckle in the softening phase because of their large slenderness and of the loss of stiffness due to steel yielding (see Fig.5b). When battens are placed in the central part of the specimen, a more ductile behavior is observed, because of the increased confinement (Fig.5c). Furthermore, the angles and the distributed battens prevent the longitudinal bars from buckling, and allow the axial shortening to attain higher values.

| (a) | (b) | (c) |
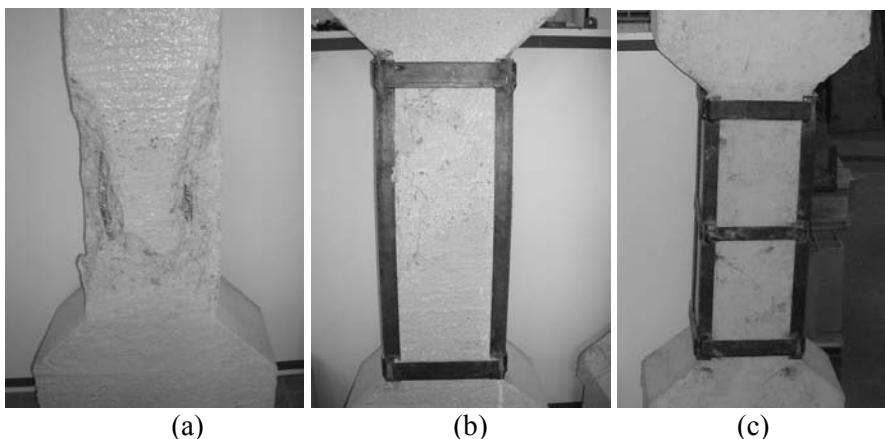
Fig. 5 – Typical failure of the specimens: (a) no angles and battens; (b) with angles and 2 end battens; and (c) with angles and 3 battens.

To have indications on structural ductility, the ductility factor μ was calculated. This factor is the ratio between the displacement measured in the softening branch at 0.85 P_{max} , and the displacement corresponding to P_{max}.

In the specimens devoid of angles and battens, the value of the ductility factor was 1.48, while in the specimens provided with angles a slightly higher value was reached (1.5). In the specimens with angles and battens (spacing = 300 and 200 mm), the ductility factor was 2.20 in the former case and 2.44 in the latter case. Summing up, as should be expected, the ductility factor increases if the battens are more densely spaced, and so the overall ductility of the column.

3. MODEL FORMULATION AND APPLICATION TO A REFERENCE CASE

The case examined theoretically refers to a column with a square cross-section (side b, Fig.6) strengthened with steel angles (side L_1, thickness t_1) and battens

(length s_2, thickness t_2 and spacing s). Moreover, f_{yb} and f_{ya} are the strengths at yielding (battens and angles, respectively). The steel is assumed to have an elastic-plastic behavior. Possible failures in the welded sections are not considered. The angles are assumed to be in contact with, but not bonded to the concrete.

Indirectly- and directly-loaded angles (Figs.6a,b) are considered, including 2nd-order effects.

To take into account the confinement exerted by the traditional reinforcement (longitudinal bars and stirrups), the model proposed in [13] was adopted. Moreover, as already mentioned the contribution of the longitudinal bars to the load-carrying capacity was evaluated by assuming an elastic-plastic behavior for the steel (buckling was disregarded, since angles reduce the risk of bar buckling).
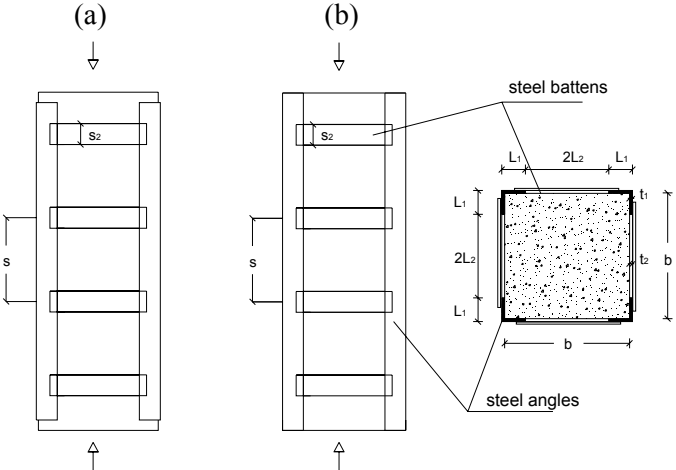
Fig. 6 – (a) Indirectly- and (b) directly-loaded angles.

The model proposed in the following is aimed to describe the behavior in compression of a concrete column strengthened with steel angles and battens, with reference to two cases (steel angles directly and indirectly loaded). The strength of the angles and their 2nd-order effects are taken care of as well.

The response of the columns is determined on the basis of the responses of the confined core and of the steel angles.

3.1 Calculation of the equivalent uniform confinement pressure

To calculate the confinement pressure in the transverse planes containing the battens and in the concrete volume between two contiguous battens, the starting point is the transverse expansion of the axially-loaded column, which depends on the value of the Poisson's ratio and on the transverse size of the structural member.

Cross-sections are assumed to be in a biaxial state of deformation, characterized by a lateral expansion $\delta = \nu \, \varepsilon \, b/2$ along each side. To determine the confinement pressure at batten level, the procedure proposed by Campione [14] in the case of concrete columns provided with stirrups and longitudinal bars is adopted. Reference is made to a quarter of the transverse cross-section (Fig.7a). As a further simplification, a one-dimensional model is assumed for the lateral expansion [14] (Fig.7b).
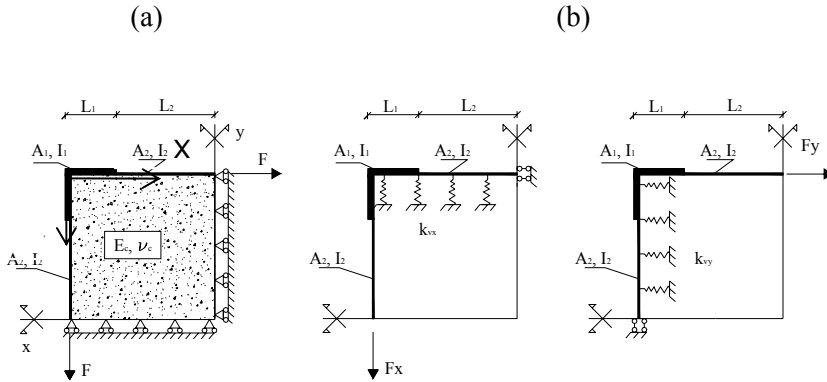
Fig. 7 – Simplified model for concrete-reinforcement interaction: (a) 2-D model; and (b) 1-D model.

The stiffness of the springs (acting in the direction perpendicular to beam axis) has the following formulation [14]:

$$k_v = \frac{E_c}{b \cdot (1 - \nu)} \qquad \text{where } \nu = \nu_c = \text{concrete Poisson's ratio} \qquad (1)$$

The flexural stiffness of the battens depends on the moment of inertia of their cross-section I:

$$I = \frac{s_2 \cdot t_2^{\,3}}{12} \qquad (2)$$

The equation of the deflection curve for a batten resting on the cohesionless soil represented by the springs is governed by the following differential equation, where w is the lateral displacement and δ is the transverse deformation of the unconfined concrete column:

$$\frac{d^4 w}{dx^4} + \frac{k_v}{E_s \cdot I} \cdot (\delta - w) = 0 \qquad (3)$$

The solution of Eq. 2 has the following well-known formulation:

$$w(x) = \delta + A \cdot \cosh\beta x \cdot \cos\beta x + B \cdot \text{senh}\beta x \cdot \text{sen}\beta x + $$
$$+ c \cdot \text{senh}\beta x \cdot \cos\beta x + D \cdot \cosh\beta x \cdot \text{sen}\beta x \tag{4}$$

where the parameter β ($\cong$ relative stiffness) has the following expression:

$$\beta = \sqrt[4]{\frac{k_v \cdot A_2}{4 \cdot E_s \cdot I_2}} \tag{5}$$

Being $A_2 = t_2 \cdot s_2$ the area of the battens, Eq.5 can be written as:

$$\beta = \sqrt[4]{\frac{3}{b \cdot t_2{}^2} \cdot \frac{E_c}{E_s \cdot (1-\nu)}} \tag{6}$$

It is clear from Eq.6 that the stiffness of the system batten+concrete depends on the Young's moduli of the materials and on the geometry of the batten. To calculate the four constants A, B, C, D the boundary conditions should be enforced for the batten.

As previously mentioned, the angle (which is span-wise continuous and whose thickness is larger than or equal to that of the batten) has a flexural stiffness that is much larger than that of the batten. Therefore, the displacement $w_1(x)$, for the entire stretch L_1, is roughly constant and tends to coincide with the displacement δ_1 corresponding to the elongation induced in the batten by the tensile force F acting during the restrained lateral expansion. The displacement $w_1(x)$ can be formulated as follows:

$$w_1(x) = \delta_1 = F \cdot \left(\frac{L_1}{E_{s1} \cdot s \cdot t_1} + \frac{L_2}{E_{s2} \cdot s_s \cdot t_2} \right) \tag{7}$$

where E_{s1} and E_{s2} are the Young's moduli of the angles and of the battens, respectively (in case of steel $E_{s1} = E_{s2} = E_s$).

For the beam of length L_2 (Fig. 7b) subjected to the displacement $w_2(x)$, the following boundary conditions have to be enforced:

$$w_2(x)\big|_{x=0} = \delta_1 \qquad \frac{dw_2(x)}{dx}\bigg|_{x=0} = 0;$$
$$\frac{d^3 w_2(x)}{dx^3}\bigg|_{x=L_2} = 0; \quad \frac{dw_2(x)}{dx}\bigg|_{x=L_2} = 0; \tag{8}$$

where the origin of the coordinate x is at the connection between the batten and the angle (x = 0) and $2L_2$ is the clear length of the batten. By using Eq.8, the following expressions can be worked out for A, B, C, D:

$$A = \delta_1 - \delta$$

$$B = (\delta_1 - \delta) \cdot \frac{[Sen(\beta L_2) \cdot Cos(\beta L_2) - Senh(\beta L_2) \cdot Cosh(\beta L_2)]}{[Sen(\beta L_2) \cdot Cos(\beta L_2) + Senh(\beta L_2) \cdot Cosh(\beta L_2)]}$$

(9)

$$C = (\delta_1 - \delta) \cdot \frac{[Cos^2(\beta L_2) - Cosh^2(\beta L_2)]}{[Sen(\beta L_2) \cdot Cos(\beta L_2) + Senh(\beta L_2) \cdot Cosh(\beta L_2)]}$$

$$D = -C$$

3.1.1 Evaluation of the uniform equivalent confining pressure

According to [14], the confining pressure $q(x)$ can be assumed as a linear function of the stiffness k_v of the concrete and of the effective displacement, the latter being the difference between δ and w:

$$q(x) = k_v \cdot [\delta - w(x)] \cdot s_2$$ (10)

It should be observed that Eqs.9 contain also the unknown δ_1 (= effective elongation of the steel batten, that is a function of the unknown axial force F).

Moreover, the confinement-induced pressure $q(x)$ at batten level does not reflect the variability of the pressure between two contiguous battens; therefore, an "effectiveness" coefficient $A(z)$ has to be introduced. As proposed by Campione [12], at any given point at the distance z from the batten the value of the pressure can be expressed by multiplying the pressure $q(x)$ by $A(z)$:

$$p(x,z) = q(x) \cdot A(z)$$ (11)

The confinement pressure exerted by the angles is accompanied by shear friction, which is proportional to $q(x)$ as shown in Fig.8, via the frictional coefficient μ (for instance, $\mu = 0.5$, see Adam et al. [9]).
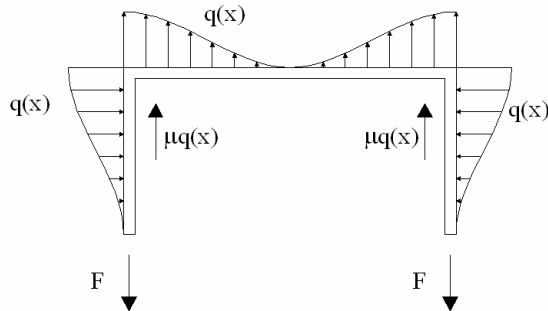

Fig. 8 – Plot of the confining pressure at batten level.

Therefore, the resultant of the confining pressure is:

$$R = \int_v p(x,z)\cdot dx \cdot dz = 2\cdot(1+\mu)\cdot \int_0^{L/2} q(x)dx \cdot \int_0^{s/2} A(z)dz = 2\cdot(1+\mu)\cdot k_{sv}\cdot s_2 \cdot \int_0^{L/2} q(x)dx \quad (12)$$

where k_{sv} has been introduced by Campione [14] in the following form:

$$k_{sv} = \int_{-\frac{s}{2}}^{\frac{s}{2}} A(z)\cdot dz = e^{-\frac{3}{2}\frac{s}{b}} \quad (13)$$

Finally, equilibrium requires that the resultant of the confining pressure acting in the plane of the batten and in the space between two contiguous battens be equal to the axial force acting in the legs of the battens:

$$(14)$$

$$F = \cfrac{v\cdot\varepsilon\cdot b\cdot k_{sv}}{(1+\mu)\cdot\left\{\cfrac{1}{E_s}\cdot\left(\cfrac{L_1}{s\cdot t_1}+\cfrac{L_2}{s_s\cdot t_2}\right)+\cfrac{1}{s_2\cdot k_v\cdot L_1+\cfrac{k_v}{\beta}\cdot\left(\cfrac{\cosh^2\beta L_2-\cos^2\beta L_2}{\text{sen}\beta L_2\cdot\cos\beta L_2+\text{senh}\beta L_2\cdot\cosh\beta L_2}\right)}\right\}}$$

Should the influence of the confinement pressure acting along the battens be disregarded (for instance because there is no contact between the concrete and the battens), Eq.14 would assume the following simplified expression:

$$F \cong \cfrac{v\cdot\varepsilon\cdot b\cdot e^{\left(-1.5\cdot\frac{s}{b}\right)}}{(1+\mu)\cdot\left\{\cfrac{1}{E_s}\cdot\left(\cfrac{L_1}{s\cdot t_1}+\cfrac{L_2}{s_s\cdot t_2}\right)+\cfrac{b\cdot(1-v_c)}{E_c\cdot s_2\cdot L_1}\right\}} \quad (15)$$

Therefore, the uniform equivalent confining pressure, defined as $f_1(\varepsilon)=\dfrac{2\cdot F}{b\cdot s}$

(see Mander *et al.* [13]) has the following formulation :

$$f_1(\varepsilon) = \cfrac{2\cdot v\cdot\varepsilon\cdot e^{\left(-1.5\cdot\frac{s}{b}\right)}}{(1+\mu)\cdot s\cdot\left\{\cfrac{1}{E_s}\cdot\left(\cfrac{L_1}{s\cdot t_1}+\cfrac{L_2}{s_2\cdot t_2}\right)+\cfrac{b\cdot(1-v_c)}{E_c\cdot s_2\cdot L_1}\right\}} \quad (16)$$

where E_s is the elastic modulus of the steel, E_c and $v = v_c$ are the elastic modulus and the Poisson's ratio of the concrete, and μ is the frictional coefficient at the

steel-concrete interface. Eq. 16 shows that the equivalent uniform confining pressure is variable during the loading process (E_c, ν, ε) and depends on: (a) thickness (t_2), length (s_2) and spacing (s) of the battens; and (b) side (L_1) and thickness (t_1) of the angles.

The confining pressure given by Eq. 16 is variable with the axial strain and reaches its maximum value when the battens are at yielding. (Note that in Eq. 16, F reaches its maximum value for $f_{yb} = E_s \, \varepsilon_{yb}$ and $\varepsilon_{yb} = \nu \, \varepsilon$). If the concrete core is assumed to be perfectly stiff ($E_c = \infty$) and the design strength f_{yd} of the battens is introduced in Eq. 16, one obtains:

$$f_{1max} = \frac{1.33 \cdot f_{yd} \cdot e^{\left(-1.5 \cdot \frac{s}{b}\right)}}{s \cdot \left(\frac{L_1}{s \cdot t_1} + \frac{L_2}{s_2 \cdot t_2}\right)} \tag{17}$$

Eq.17 can be simplified by neglecting the stiffness of the battens compared to that of the angles ($t_1 = \infty$) and by assuming $L_2 \approx b$:

$$f_{1max} = 0.33 \cdot \rho_s \cdot f_{yd} \cdot e^{\left(-1.5 \cdot \frac{s}{b}\right)} \tag{19}$$

where ρ_s (= steel ratio of the battens) is defined as follows:

$$\rho_s = \frac{4 \cdot t_2 \cdot s_2}{b \cdot s} \tag{20}$$

3.1.2 Strength of confined concrete

To evaluate concrete compressive strength in confined conditions, the analytical relationship given in Eurocode 8 [2], is used, but the confining pressure is assumed to be a function of the axial strain. Therefore, the maximum compressive strength at each axial-strain level has the following formulation:

$$f_{cc} = f_c \left[1 + 3.7 \cdot \left(\frac{f_1(\varepsilon)}{f_c} \right)^{0.87} \right] \tag{21}$$

The load carried by the core is given by the product of the compressive strength f_{cc} time the cross-sectional area (b^2).

The corresponding strain according to Mander *et al.* [13] model is:

$$\varepsilon_{cc} = \varepsilon_{co} \cdot \left[1 + 5 \cdot \left(\frac{f_{cc}}{f_c} - 1 \right) \right] \tag{22}$$

3.2 Contribution of the steel angles to the bearing capacity

The contribution of indirectly- and directly-loaded angles to the bearing capacity of the column (2nd-order effects included) should be considered as well [10, 11].

3.2.1 <u>Strength contribution due to the yielding of the steel angles</u>

The angles are subjected to the coupled effects of the axial force and of the bending moment (Fig.9), the latter resulting from the lateral expansion of concrete core.
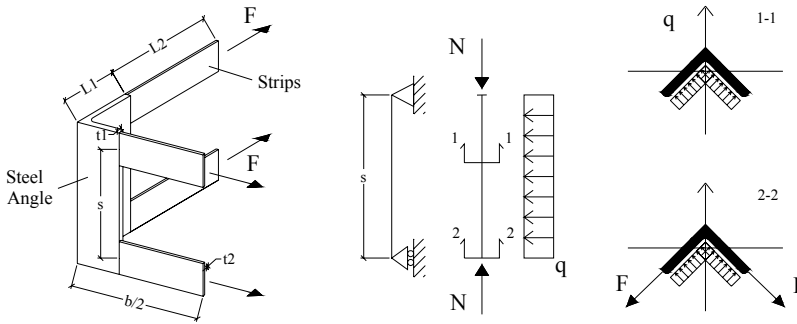
Fig. 9 – Simplified modeling of the angles.

The axial force is related to the shortening of the column in the case of directly-loaded angles, and to the interfacial friction occurring at the contact between each angle and the concrete in the case of indirectly-loaded angles (Fig.9). Each part of an angle (comprised between two contiguous battens) is modeled as a fixed-end beam subjected (along its symmetry plane) to the distributed force resulting from the confining pressure ($q = 2 \cdot \sqrt{2}/2 \cdot f_1 \cdot L_1$) and to the force N_{ds} (induced by the axial shortening in directly-loaded angles) or to the force N_{df} (induced by shear friction in indirectly-loaded angles):

$$N_{ds} = \left(2 \cdot L_1 \cdot t_1\right) \cdot \varepsilon \cdot E_s \tag{23}$$

$$N_{df} = \left(2 \cdot L_1 \cdot s\right) \cdot \mu \cdot f_1 \tag{24}$$

The maximum design moment M_{dmax} is a function of the confining pressure acting along the angle and can be calculated on the basis of a simplified model (fixed-end beam). Assuming for the confinement pressure an even distribution from batten to batten (in fact, it is larger near the batten-angle connections and smaller at midspan between two contiguous battens), the maximum moment has the following expression:

$$M_{dmax} = \frac{1}{12} \cdot q \cdot s^2 \tag{25}$$

Assuming (as already mentioned) for the steel an elastic-plastic behavior, the ultimate strength envelope (M_u^*, N_u^*) can be worked out.

The ultimate axial force in a steel angle has the following expression:

$$N_u = (2 \cdot L_1 \cdot t_1) \cdot f_y \tag{26}$$

while the ultimate bending moment in pure bending is:

$$M_u = \frac{L_1^2 \cdot t_1}{4} \cdot f_y \tag{27}$$

If an axial force is applied, the ultimate bending moment is given by Eq.28 [11]:

$$M_u^* = M_u - M_u^d \tag{28}$$

where

$$M_u^d = N_u^* \cdot d \qquad \text{with} \qquad d = \frac{N_u^*}{16 \cdot f_y \cdot t_1} \tag{29,30}$$

By replacing Eq.27 and Eq.29 in Eq.28, the following relationship is obtained:

$$M_u^* = \frac{L_1^2 \cdot t_1 \cdot f_y}{4} - \frac{\left(N_u^*\right)^2}{16 \cdot f_y \cdot t_1} \leq M_u \tag{31}$$

In directly-loaded angles, by imposing $M_u^* = M_{dmax}$ and $f_l = f_{lmax}$, it is possible to obtain from Eq.31 the ultimate axial force taking into account the bending moment in the angle:

$$N_u^* = \sqrt{4 \cdot f_y \cdot t_1 \cdot \left(t_1 \cdot f_y \cdot L_1^2 - 4 \cdot M_u^*\right)} \leq N_u \tag{32}$$

Figure 10 shows a set of typical strength envelopes obtained from Eq.31 for three geometries of the steel angles (50x5 mm; 50x8 mm; and 50x10 mm), steel grade S 275 (Eurocode 3 [15]).

It is interesting to observe that in both directly- and indirectly-loaded angles the ultimate axial force is significantly lower than the ultimate axial force.

In the case of directly-loaded angles, and for the spacing of the battens adopted in this study, the maximum axial load is almost constant, as indicated by the small squares in Fig.10.
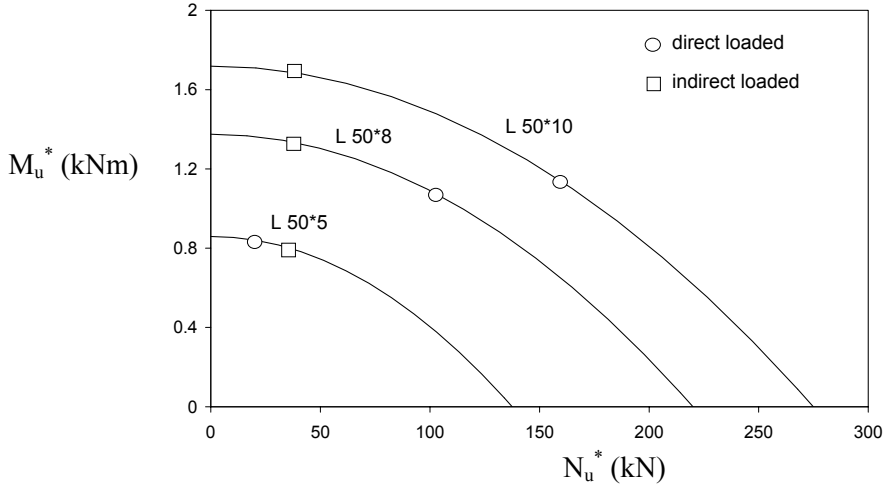
Fig. 10 - Axial force – bending moment envelopes for angles loaded along their symmetry plane.

3.2.2   Check of the stability (buckling) of the angles

With regard to the stability conditions of the angles subjected to an eccentric axial force, a simplified model is shown in Fig.11. The proposed model refers to a buckled fixed-end angle (s = batten spacing). Two rigid bars are connected by means of an elastic-plastic hinge, under the coupled effect of the axial force N and of the transverse confinement-induced load (q).

Let us now write the equilibrium conditions for the buckled angle:

$$N_c \cdot w_h - 2 \cdot M_u^* + q \cdot L_1 \cdot \frac{s^2}{8} = 0 \tag{33}$$

The compatibility condition can be formulated as follows:

$$\delta_v = s - 2 \cdot \left(\frac{s}{2} \right) \cdot \cos \theta = s \cdot (1 - \cos \theta) \tag{34}$$

where w_h = lateral displacements, δ_v = axial shortening and θ = angle defining the configuration after buckling.

Fig. 11 - Failure mechanism of buckled angles.

Therefore, a further relation between w_h, s and θ with $\varepsilon = \delta/s$ can be written:

$$w_h = \frac{s}{2} \cdot sen\theta = \frac{s}{2} \cdot \sqrt{1 - \cos^2\theta} = \frac{s}{2} \cdot \sqrt{2 \cdot \frac{\delta_v}{s} - \frac{\delta_v^{\,2}}{s^2}} = \frac{s}{2} \cdot \sqrt{2 \cdot \varepsilon - \varepsilon^2} \quad (35)$$
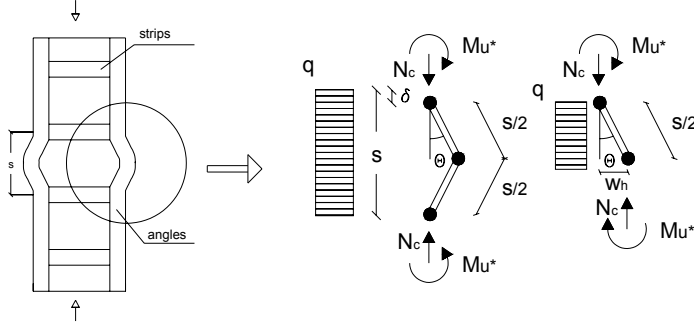
Finally, introducing w_h (see Eq. 35) into Eq. 33 makes it possible to obtain the following relationship:

$$N_c = \frac{2}{w_h} \cdot \left(M_u^{\,*} - q \cdot \frac{s^2}{8} \cdot L_1 \right) \leq N_u \quad (36)$$

For any value of the ultimate moment, Eq.36 provides the critical axial load. If (a) N_c is divided by the area of the steel angle, (b) the expressions of q and M_u^* are introduced into Eq.36, and (c) Eq.36 is divided by the area of a single angle, the critical stress has the following form:

$$\sigma_c = \frac{1}{s \cdot L_1 \cdot t_2} \cdot \frac{1}{\sqrt{2 \cdot \varepsilon - \varepsilon^2}} \cdot \left[2 \cdot \left(\frac{L_1^{\,2} \cdot t_1 \cdot f_y}{4} - \frac{\left(N_u^*\right)^2}{16 \cdot f_y \cdot t_1} \right) - \sqrt{2} \cdot f_l \cdot L_1 \cdot \frac{s^2}{4} \right] \quad (37)$$

Furthermore, M_u^* is given by Eq.31 and q is assumed as $q = 2 \cdot \sqrt{2}/2 \cdot f_l \cdot L_1$ with f_l given by Eq.19. If in Eq.37 N_u^* is assumed to be variable with the axial strain (see the relationship: $N = \varepsilon \cdot 2 \cdot L_1 \cdot t_1 \cdot E_s \leq N_u$), the stress-strain curve of the buckled angle can be obtained, as shown by the plots in Fig.12, where the normalized stress-strain curves include the elastic-plastic behavior of the angles, without buckling. The previously-examined cases refer to the following geometry: for the angles width 50 mm and thickness 8 mm; for the battens: spacing = b/2, b, 2b (where b = 300 mm), width 50 mm and thickness 8 mm.

It is evident that for s = b and b/2 buckling occurs after steel yielding, while for s = 2 b buckling occurs in the elastic range. Finally, should the thickness of the angles be smaller (for instance 3 mm), buckling would always occur within the elastic range.
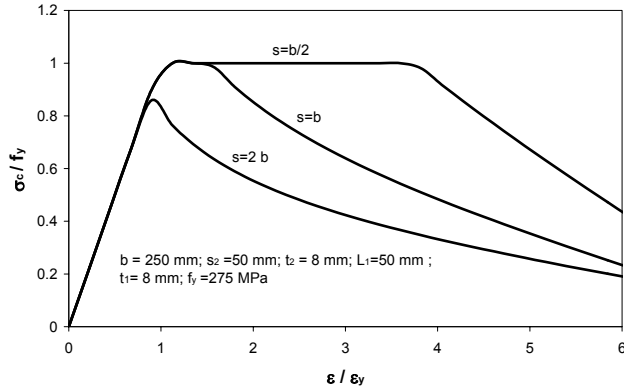
Fig. 12 - Stress-strain curves for the angles in compression, buckling included.

4. STRESS-STRAIN CURVES OF CONFINED CONCRETE AND NUMERICAL INCREMENTAL PROCEDURE

To work out the stress-strain curve (and therefore the axial load-shortening curve) of a composite column, including the lateral confinement, a suitable numerical procedure is proposed in the following.

The starting point is the equation introduced in [13] to describe the stress-strain curve. This equation is extended to take care of the confining pressure corresponding to the current axial and lateral strain values.

The above-mentioned procedure is based on the following steps:

- assume an initial value for the axial strain ε;
- compute the lateral displacement $\delta = \nu \cdot \varepsilon \cdot b/2$ by adopting for ν a formulation as a function of ε [16]); calculate the effective confinement pressure f_l, the peak strength f_{cc} and the corresponding strain ε_{cc} via Eqs.25, 27, 28;
- evaluate σ by means of the equation introduced in [13] (on the basis of concrete actual secant elastic modulus);
- repeat this procedure for various values of the axial strain; and
- work out the complete stress-strain curve.

The stress σ was multiplied by b^2 to evaluate the axial load P and the strain ε was multiplied by H (height of the column) to work out the average shortening δ. The total external load was determined by including the contribution of the angles, with their nonlinearity and buckling.

5. EXPERIMENTAL VALIDATION OF PROPOSED MODEL

Several studies have been published on columns externally strengthened by means of angles and battens [1, 6, 7, 9]. In most studies information was limited to the load-carrying capacity, and only in a few cases the information concerned the load-shortening curve [6,9], as required for the sake of comparison.

The tests by Adam *et al.* [9] (Fig.13a) refer to full-size columns loaded in uniaxial compression (length = 2500 mm; section = 300x300 mm). The columns were strengthened by means of angles (L 80x8 mm) and battens (270x160x8 mm; spacing 475 mm). The steel type was S 275 (f_y = 275 MPa, Eurocode 3, 1993) and concrete compressive strength was comprised between 11 and 16 MPa.

Two types of similarly-strengthened columns were tested. In Type A columns (two specimens), the indirectly-loaded angles were mutually connected only by means of welded end-battens. In Type B columns (two specimens), the angles were directly loaded, since they had end capitals (80x80x8 mm), but no end battens.

The model proposed in this study is shown to efficiently describe: (a) the contribution of the confinement to both the bearing capacity and the ductility, and (b) the contribution of the angles to the bearing capacity. The tests show also that the columns provided with directly-loaded angles (Specimens B) have a slightly lower bearing capacity than the columns provided with indirectly-loaded angles (Specimens A). This fact is taken care of by the proposed model through the buckling of the angles (Fig.13b) when the angles are directly loaded. Since buckling does not occur in indirectly-loaded angles, the confining pressure is higher, to the advantage of the load-bearing capacity. The model fits very satisfactorily the experimental results, and confirms that in both cases the full axial resistance of the steel angles is not reached (and so the maximum confinement effect), because of the state of stress in the angles (moment and axial force with 2nd-order effects).

The tests by Dolce *et al.* [6] refer to shorter columns (length = 800 mm; section = 300x200 mm). Two types of columns with the same indirectly-loaded angles (L 50x5 mm; length 750 mm), but different battens were tested. Columns SJ (Fig.14a) had traditional carbon-steel battens (260x50x5 mm/160x50x6 mm, along the longer and shorter side, respectively; spacing = 200 mm). The steel type was Fe 360 (f_y = 235 MPa, according to Eurocode 3) and concrete compressive strength was close to 13 MPa. Columns CAM (Fig.14b) had high-strength stainless-steel battens manufactured from ribbons (width 19 mm; thickness 0.8 mm; spacing 40 mm; f_y = 780 MPa; each batten was mechanically fixed to the angles).

In the analytical model, an equivalent square section (side = 245 mm) was adopted (same area as in the actual 200x300 mm section). Fig.14 shows that in both cases (SJ and CAM Systems) the fitting of the test results is satisfactory, and that the bearing capacity predicted by the proposed model is in good agreement

with Eurocode 8 [2]. It should be observed that in the case of the CAM System (Fig.14b) a reduction factor was applied to the strength of the ribbon-like battens, to take care of the stress concentration at the corners of the cross-section.

The CAM System is not only very effective, but can be applied more easily than the SJ System. However, because of the brittleness of the stainless-steel ribbon-like battens and because of the nature of their connections to the angles, the occurrence of a brittle failure in the battens or in their connections to the angles may nullify the contribution of the system angles + battens, because the confinement disappears once the angles buckle, something that does not occur in the SJ System.
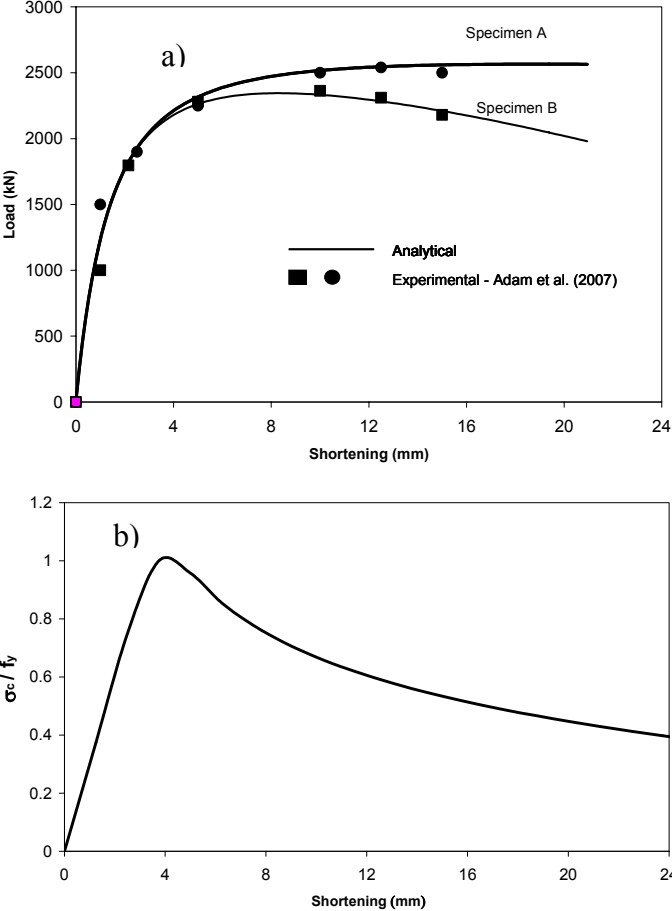
Fig. 13 – (a) Load-shortening curves for the columns tested by Adam *et al.* [9] (indirectly-loaded angles in Specimens A; directly-loaded angles in Specimens B); and (b) stress-strain diagram for a single directly-loaded angle.
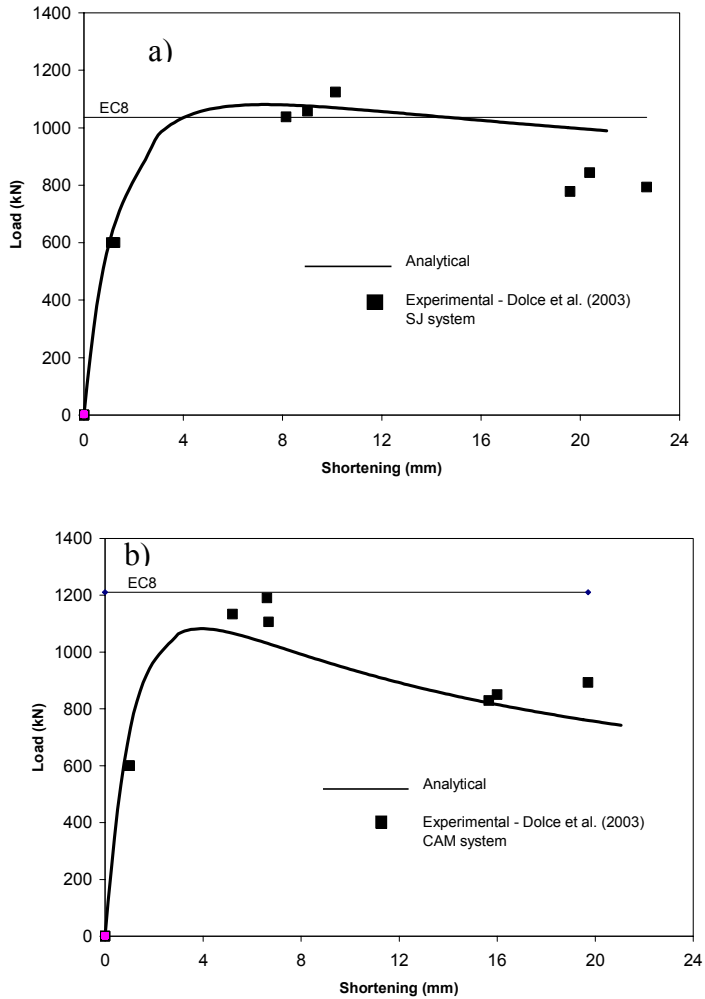
Fig. 14 – Load - shortening curves for the columns tested by Dolce *et al.* [6]; all specimens were provided with angles and battens: (a) traditional carbon-steel battens (SJ System); and (b) stainless – steel ribbon-type battens (CAM System).

6. DESIGN CONSIDERATIONS AND SIMPLIFIED PROCEDURE TO PREDICT THE LOAD-CARRYING CAPACITY

Eurocode 8 [2] has specific design provisions for R/C columns strengthened by means of battens and angles. For instance, the spacing between two successive battens should not be larger than b/2. In the case of rectangular columns with rather oblong sections, steel ties crossing the member should be provided in order to reduce the free length of the angles between the battens.

Eurocode 8 [2] prescribes also that the minimum mechanical ratio of the battens ω_s (referred to the spacing s) should be at least 0.07, 0.11 and 0.13 with reference to the ductility classes L, M, H (low, medium, high), respectively.

The mechanical ratio of the battens ω_s is defined as follows:

$$\omega_s = \rho_s \cdot \frac{f_{yd}}{f_{cd}} \tag{38}$$

where f_{cd} and f_{yd} are concrete and steel design strengths (Eurocode 2 [17] and Eurocode 3 [15]). These values are a function of concrete cylindrical compressive strength (unconfined concrete, f_c) and of steel strength at yielding (f_{ya}, battens), respectively.

According to Eurocode 8 [2], both angles and battens contribute to column bearing capacity through their confining action, but the angles (assumed to be indirectly loaded) do not contribute directly with their resisting section.

Hence, the only resisting section is that of the concrete core, whose area (b^2 for a square section having side b) should be multiplied by the compressive strength of the confined concrete (f_{cc}).

Being:

$$\frac{f_{cc}}{f_{cd}} = 1 + 3.7 \cdot \left(\frac{f_{1max}}{f_{cd}} \right)^{0.87} \tag{39}$$

f_{1max} is the equivalent confining pressure expressed, according to Eurocode 8 [2]:

$$f_{1max} = 0.5 \cdot \rho_s \cdot f_{yd} \cdot \left(1 - \frac{2}{3} \cdot \frac{(b - 2 \cdot L_1)^2}{b^2} \right) \cdot \left(1 - \frac{s}{2 \cdot b} \right)^2 \tag{40}$$

Eq.40, which was worked out independently in [5], and in [18], provides the average confinement pressure.

If Eq.40 is introduced into Eq.39, the load-carrying capacity of the confined concrete has the following expression:

$$P_u = f_{cd} \cdot b^2 \cdot \left[1 + 2.02 \cdot \left(\omega_s \cdot \left(1 - \frac{2}{3} \cdot \frac{(b - 2 \cdot L_1)^2}{b^2} \right) \cdot \left(1 - \frac{s}{2 \cdot b} \right)^2 \right)^{0.87} \right] \tag{41}$$

Contrary to Eurocode 8 [2], Eurocode 4 [4] considers the R/C column strengthened by means of battens and angles as a composite column. In this case, the load-carrying capacity results from the combined contributions of the unconfined concrete core, of the angles and of the longitudinal bars (assumed to be yielded). Should the bars be neglected and angle buckling ruled out (because of the battens), the following expression would apply:

$$P_u = 0.85 \cdot f_{cd} \cdot b^2 + 8 \cdot L_1 \cdot t_1 \cdot f_{yd} \tag{42}$$

Should the battens be replaced by a full steel jacketing (s = 0), the factor 0.85 in Eq.6 may be put equal to unity.

In order to model the strengthened R/C column as a composite member, certain minimum and maximum values for the reinforcement ratio of the angles should be respected, as specified in Eurocode 4 [4]:

$$0.2 \leq \frac{8 \cdot L_1 \cdot t_1 \cdot f_{yd}}{0.85 \cdot f_{cd} \cdot b^2 + 8 \cdot L_1 \cdot t_1 \cdot f_{yd}} \leq 0.9 \tag{43}$$

If the mechanical ratio of the angles ω_a is introduced:

$$\omega_a = \frac{8 \cdot L_1 \cdot t_1}{b^2} \cdot \frac{f_{yd}}{f_{cd}} \tag{44}$$

and reference is made to ω_a in Eq.43, the following limitations come out:

$$0.222 \leq \omega_a \leq 2.33 \tag{45}$$

Eurocode 4 [4] prescribes that the spacing of the battens be reduced to avoid angle buckling and the normalized slenderness be lower than two.

In agreement with Eurocode 8 [2], in [1] the increased load-carrying capacity of strengthened R/C columns is justified through the passive confinement induced by both the battens and the angles (the use of equilateral angles is suggested with: side $\geq$ 50 mm; thickness $\geq$ 5 mm; $L_1 \geq 0.2 \cdot b$; $t_1 \geq 0.1 \cdot L_1 = 0.02 \cdot b$; $H_{ang} = H - 0.05$ [m]).

Analogously, for steel battens it should be:

- $0.4 \leq \dfrac{s}{b} \leq 0.75$;

- $t_2 \leq t_1$;

- $s_2 \geq \dfrac{0.004 \cdot b^2}{t_2}$.

Following the indications contained in [1] and choosing $t_2 = 0.02 \cdot b$; $\dfrac{s}{b} = 0.4$; $s_2 = \dfrac{0.004 \cdot b^2}{t_2}$; f_{yd} =250 MPa and f_{cd} = 15 MPa (steel grade S275 and concrete grade C18/25 MPa, see Eurocode 3 [15] and Eurocode 2 [17]) the minimum value of ω_s turns out to be 0.18. Therefore the strengthened member is in the high-ductility class according to Eurocode 8 (2003).

Adopting $t_1 = 0.02 \cdot b$; $L_1 = 0.2 \cdot b$ (as suggested in [1]), $f_{yd} = 250$ MPa and $f_{cd} = 15$ MPa (steel grade S275 and concrete grade C18/25 MPa), the minimum value of ω_a turns out to be 0.48. This value is comprised betwen 0.2 and 0.9; hence, the strengthened member is a composite column in accordance with Eurocode 4 [4].

On the basis of the previous comments, following the indications contained in [1] (which are very reliable whenever the evaluation of the increased load-bearing capacity and the avoidance of angle buckling are at issue in a strengthened R/C column), composite action and passive confinement characterize the structural behavior of a column. Therefore, it is necessary to develop a unified analytical model able to include (a) the confinement effect induced by both the angles and the battens (Eurocode 8), and (b) the direct contribution of the angles (Eurocode 4).

By using the proposed model and by introducing Eq.19 into Eq.39, the normalized load-carrying capacity of the confined concrete core can be written in the following form:

$$n = \frac{f_{cc}}{f_{cd}} = 1 + 1.42 \cdot \left(\omega_s \cdot e^{\left(-1.5 \cdot \frac{s}{b}\right)} \right)^{0.87} \tag{46}$$

Hence, the load carrying capacity of the confined core P_{uc} is:

$$P_{uc} = f_{cd} \cdot b^2 \cdot \left[1 + 1.42 \cdot \left(\omega_s \cdot e^{\left(-1.5 \cdot \frac{s}{b}\right)} \right)^{0.87} \right] \tag{47}$$

The capacity N_u^* (Eq.33) may be put in a normalized or dimensionless form, by introducing N_u (= maximum axial force developed by directly-loaded angles); the expression of $n_a = N_u^*/N_u$ is as follows:

$$n_a = \sqrt{1 - 0.63 \cdot \frac{1}{t_1} \cdot \frac{s}{b} \cdot \frac{1}{\dfrac{L_1}{s \cdot t_1} + \dfrac{(0.5 \cdot b - L_1)}{s_2 \cdot t_2}} \cdot e^{\left(-1.5 \cdot \frac{s}{b}\right)}} \tag{48}$$

The use of Eq.48 confirms that when R/C strengthened columns behave as composite members, a sizable share of the load-carrying capacity is developed by the directly-loaded angles. However, should the passive confinement increase, the load carried by the angles would decrease. Similar effects are observed in concrete-filled steel tubes (Eurocode 4 [4], Part 4.8.3.3).

Should buckling effects be absent (for instance, because the indications on the spacing of the battens given in [1], or the provisions of Eurocodes 8 [2] and 4 [4] have been adopted in the design), the load-carrying capacity of the composite

member may be calculated by merely considering the contributions of the confined core and of the directly-loaded angles:

$$P_u = f_{cd} \cdot b^2 \cdot \left[1 + 1.42 \cdot \left(\omega_s \cdot e^{\left(-1.5 \cdot \frac{s}{b}\right)} \right)^{0.87} \right] +$$

$$+ 8 \cdot L_1 \cdot t_1 \cdot f_{yd} \cdot \sqrt{1 - 0.63 \cdot \frac{1}{t_1} \cdot \frac{s}{b} \cdot \frac{1}{\dfrac{L_1}{s \cdot t_1} + \dfrac{(0.5 \cdot b - L_1)}{s_2 \cdot t_2}} \cdot e^{\left(-1.5 \cdot \frac{s}{b}\right)}}$$

(49)

Of the two terms appearing in Eq.49, the first brings in the favorable effect that the confinement has on the load-carrying capacity, and the second takes care of the contribution of the steel angles (composite action).

7. PREDICTION OF THE LOAD CARRYING CAPACITY

A comparison among the experimental results available in the literature [1, 6, 7, 9] (see Table 1), and the numerical results obtained by means of the proposed model and of other models available in the literature (see [1,3,4], EC4 [4] and EC8 [2]) is carried out in this section. More recent papers, however, may give fresh and useful information (like [19], whose results are not included in this study).

Fig.15a refers to the influence that the spacing of the battens has on the normalized axial force $n_a = N_u^*/N_u$ in strengthened R/C columns (the cross-sectional area of the battens is assumed to be constant). As should be expected, the closer the battens, the larger the load-carrying capacity (+20-70% for s/b = 0.40-0.75). The analytical model fits very well the test results by Cirtek [1].

Fig.15b refers to the influence that the cross-section area of the battens has on the load carrying-capacity. The spacing of the battens is assumed to be constant. In this case too the analytical results fit very well the test results by Cirtek [1]. Increasing the area of the battens brings in an increase of the load-carrying capacity (up to +80% within the range investigated in this project).

Finally, in Figs.16a,b the experimental results and the analytical values predicted by the above-mentioned models are compared.

In the application of the models, the contribution of the directly-loaded angles is included.

Figs.16a,b refer to indirectly-loaded angles (i.e. the angles are shorter than the columns) and directly-loaded angles, respectively.

The fitting of the test results clearly shows that the majority of the models examined in this project provide acceptable and conservative predictions, with Eurocode 8 [2], Cirtek [1] and the proposed model giving the best predictions
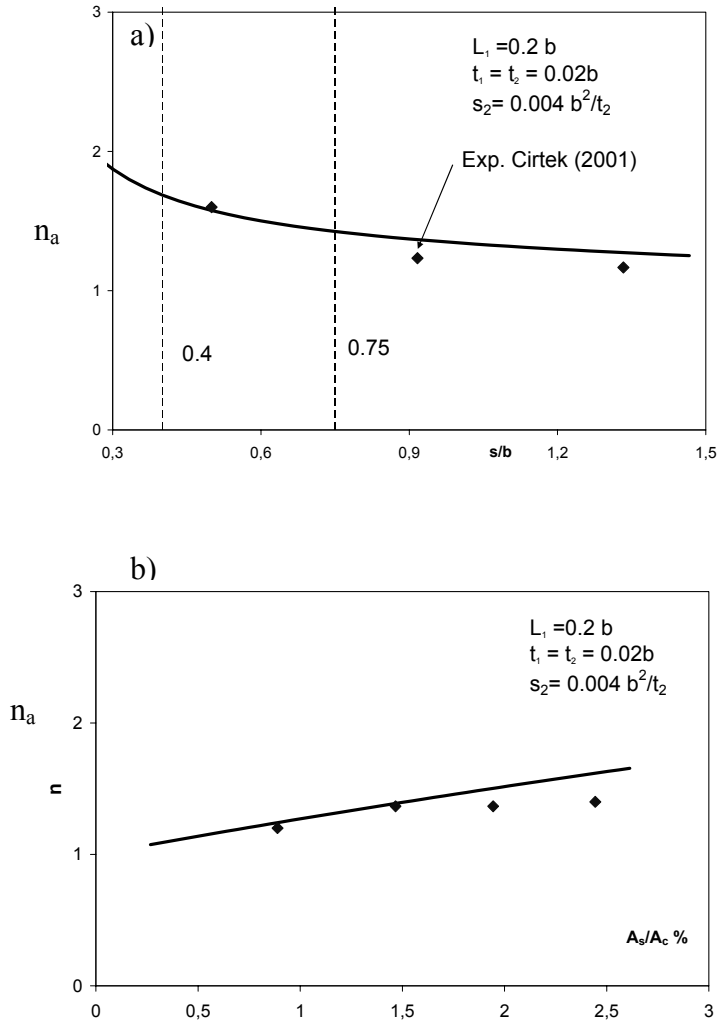
Fig. 15 – Diagrams of the normalized axial force versus: (a) the ratio between the batten spacing and the section side; and (b) the normalized area of the battens. (tests by Cirtek [1]).

(Fig.16a), and Braga *et al.* [3] giving the most conservative predictions. Eurocode 4 [4] is too conservative (the confinement is ignored). On the contrary, Fig.16b shows that Eurocode 4 [4] is more accurate than Eurocode 3 [15]. However, the best fitting is provided by the model proposed by the authors.

In Table 3 the values of the mean ratio between the experimental results and the analytical predictions, and the values of the standard deviation are given.
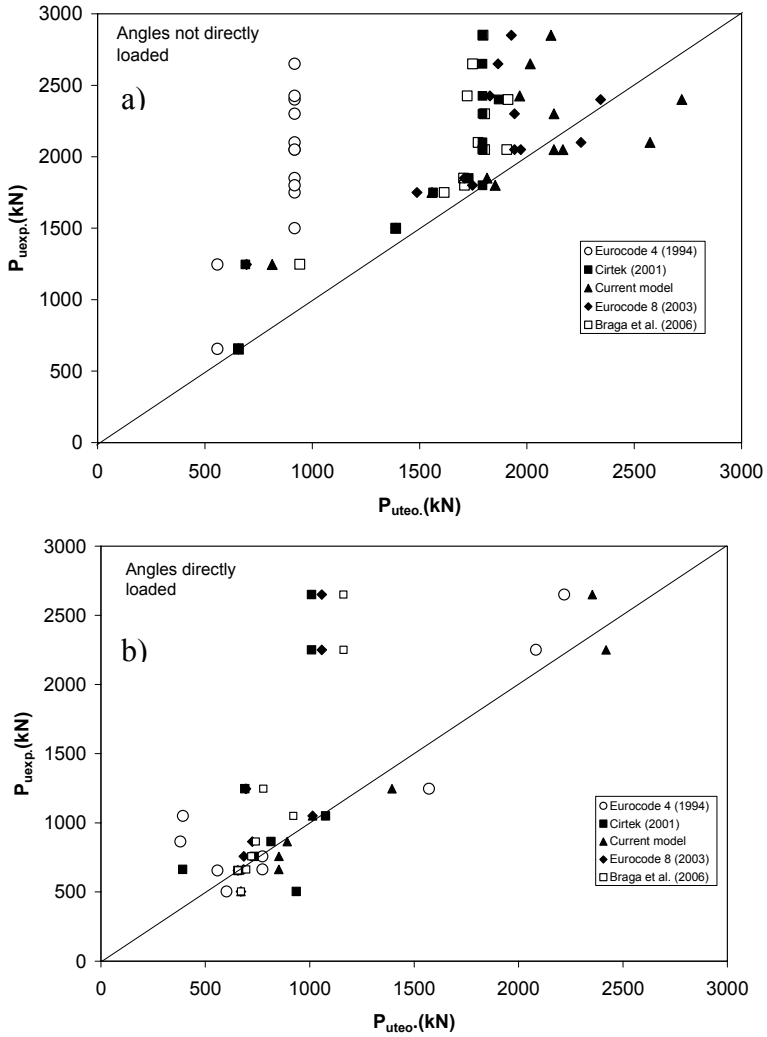
Fig 16 – Fitting of the test results: (a) indirectly-loaded angles; and (b) directly-loaded angles.

8. CONCLUSIONS

In this project, a number of tests on confined R/C columns externally strengthened by means of steel angles and battens was carried out, in order to have first-hand experimental evidence to validate a new analytical model. Comparisons were also made with a number of analytical models and experimental results available in the literature.

TABLE 3 – Load-carrying capacity: experimental and numerical results.

Reference	P_{exp}/P_{th}		Standard Deviation	
	Directly-loaded angles	Indirectly-loaded angles	Directly-loaded angles	Indirectly-loaded angles
Cirtek [1]	1.44	1.25	0.68	0.23
Braga *et al.* [3]	1.32	1.21	0.50	0.18
Eurocode 8 [2]	1.38	1.18	0.60	0.23
Eurocode 4 [4]	1.31	2.38	0.67	0.89
Proposed model	0.93	1.09	0.11	0.20

According to the existing design-oriented literature, R/C strengthened columns with angles and battens exhibit a higher load-carrying capacity and ductility, provided that the confining reinforcement is properly designed and detailed. Furthermore, should the angles be directly loaded, the behavior of the columns would be a "composite behavior", with the plus of the favorable confinement effect exerted by the system of the angles and of the battens.

The analytical model developed in this project proves to be able to realistically describe the favorable effects of the following two factors:

(a) the confinement pressure exerted by the angles and by the battens; and
(b) the load-bearing capacity of the angles subjected to an eccentric axial force.

In the model, the roles of the geometrical and mechanical properties of the angles and of the battens (side-length and thickness of the angles; width and thickness of the battens) and those of the concrete core are clearly justified, as well as their relationship with the load-bearing capacity of the column.

The experimental results show that steel angles and battens significantly increase the load-carrying capacity of R/C columns, provided that the spacing of the battens is properly chosen. Furthermore, angles and battens prevent the longitudinal bars from buckling.

The contribution of the angles to the load-bearing capacity of the columns is shown to be sizable up to the peak load, but the full yielding of the angles in pure compression cannot be reached, because of the interaction between the axial force and the bending moment in the same angles.

Finally, the proposed model appears to be very effective in fitting the test results, and more effective than other models proposed in the literature, which are often too conservative.

REFERENCES

[1] Cirtek L. (2001). "RC Columns Strengthened with Bandage - Experimental Programme and Design Recommendations". *Construction and Building Materials*, 15 (8), pp. 341-349.

[2] Eurocode 8 (2003) - Part 3. *Design of Structures forEearthquake Resistance - Part 3 - Strengthening and Repair of Buildings*. Doc CEN TC250/SC8/N343.

[3] Braga F., Gigliotti R. and Laterza M. (2006). "Analytical Stress-Strain Relationship for Concrete Confined by Steel Stirrups and/or FRP Jackets", *ASCE - Journal of Structural Engineering*, 132 (9), pp. 1402-1419.

[4] Eurocode 4 (1994). *Design of Composite Steel and Concrete Structures. Part 1-1: General Rules and Rules for Buildings*. ENV 1994-1-1

[5] Monturi R. and Piluso V. (2009). "Reinforced - Concrete Columns Strengthened with Angles and Battens Subjected to Eccentric Load", *Engineering Structures*, 31, pp. 539-550.

[6] Dolce M., Masi A., Cappa T., Nigro D. and Ferrini M. (2003). "Experimental Evaluation of the Effectiveness of Local Strengthening on Columns of R/C Existing Structures". CD-Rom of Fib-Symposium on Concrete Structures in Earthquake Regions, May 6-9, Athens (Greece).

[7] Ramirez J.L. (1996). "Ten Concrete-Column Repair Methods". *Construction and Building Materials* , 10 (3), pp. 195-202.

[8] Ramirez J.L., Barcena J.M., Urreta J. I. and Sanchez J.A. (1997). "Efficiency of Short Steel-Jackets for Strengthening Square-Section Concrete Columns". *Construction and Building Materials*, 11 (5-6), pp. 345-352.

[9] Adam J.M., Ivorra S., Gimenez E., Moragues J.J., Miguel P., Mirgall C. and Calderon P.A. (2007). "Behaviour of Axially-Loaded R/C Columns Strengthened by Steel Angles and Battens". *Steel and Composites Structures*, 7 (5), pp. 405-419.

[10] Campione G. (2007). "On the Compressive Behaviour of R/C Members Strengthened by means of Steel Angles and Battens" (in Italian). *Ingegneria Sismica* , 4, pp. 7-19.

[11] Badalamenti V., Campione G. and Mangiavillano M.L. (2010). "Simplified Model for Compressive Behavior of Concrete Columns Strengthened by Steel Angles and Battens". *ASCE-Journal of Engineering Mechanics*, 136 (2), pp. 230-238.

[12] Campione G. (2010). "R/C Columns Strengthened with Steel Angles and Battens: Confined R.C. or Composite Members?", *submitted to ASCE-Journal of Structural Engineering*.

[13] Mander J.B., Priestley M.J.N. and Park R.(1988). "Theoretical Stress-Strain Model for Confined Concrete", *ASCE-Journal of Structural Engineering*, 114 (8), pp. 1804-1826.

[14] Campione G. (2008), "Analytical Model for High-Strength Concrete Columns with Square Cross-Section". *Structural Engineering and Mechanics*, 28 (3), pp. 295-316.

[15] Eurocode 3 (1993). *Design of Steel Structures. Part 1: General Rules and Rules for Buildings.* , ENV 1993-1-1.

[16] Elwi A.A. and Murray D.W. (1979). "A 3D Hypoelastic Concrete Constitutive Relationship", *ASCE - Journal of Engineering Mechanics,* 105, pp. 623-641.

[17] Eurocode 2 (1992). *Design of Concrete Structures, Part 1.: General Rules and Rules for Buildings*.

[18] Nagaprasad P., Sahoo D. R. and Rai D.C. (2009). "Seismic Strengthening of RC Columns Using External Steel Cages". *Earthquake Engineering and Structural Dynamics*, 38, pp. 1536-1586.

[19] Gimenez E., Adam J. M., Ivorra S., Calderon P.A. (2009)," Influence of Strips Configuration on the Behaviour of Axially-Loaded R.C. Columns Strengthened by Steel Angles and Strips", *Material and Design*, 30, pp. 4103-4111.

BEHAVIOR OF FULL-SCALE REINFORCED-CONCRETE COLUMNS EXTERNALLY CONFINED WITH FRP LAMINATES

Antonio De Luca[1], Fabio Nardone[2], Gian Piero Lignola[3],
Andrea Prota[4] and Antonio Nanni[5]

ABSTRACT

The external confinement of reinforced-concrete columns by means of externally-bonded fiber-reinforced polymer (FRP) laminates is a well-established technique for strengthening and retrofitting purposes. This paper presents a research project that includes laboratory testing of prismatic R/C columns externally confined with glass and basalt-glass FRP laminates, and subjected to pure axial load. Specimens that are representative of full-scale building columns were designed according to dated design codes for gravity loads only. The study was conducted to investigate how peak axial strength and deformation of an R/C column are affected by FRP confinement.

The results show that the FRP confinement increases concrete axial strength, but it is more effective in enhancing concrete strain capacity, as in the case of R/C columns confined by steel ties. .

---

[1] Post-Doctoral Associate, University of Miami, Miami (Florida, USA).
[2] Post-Doctoral Associate, University of Naples-Federico II (Naples, Italy).
[3] Assistant Professor, University of Naples-Federico II.
[4] Assistant Professor, University of Naples-Federico II.
[5] Lester and Gwen Fisher Endowed Scholar and Professor, University of Miami; Professor, University of Naples-Federico II.

1. INTRODUCTION

Over the second half of the twentieth century, many existing reinforced-concrete buildings and bridges were found to be in need of repair and strengthening due to several causes, among them the deterioration caused by environmental effects such as corrosion initiated by water and salt solutions, damages and change in use of the structures, higher load capacity demand as a consequence of more severe code requirements, and higher strength and ductility demand to correct design or construction errors.

During the same period, the need to satisfy aerospace industry demand not met by traditional materials induced researchers and scientists to look for new solutions. The answer was found in developing new material systems by combining together two or more constituents. Composites – also known as fiber reinforced polymers (FRPs) – consisting of a reinforcing phase (fibers) embedded into a matrix (polymer), offered several advantages with respect to conventional monolithic materials (Kaw, 2005). High specific modulus and strength together with other beneficial properties (such as corrosion resistance and transparency to electromagnetic fields) made FRP also suitable for use as a construction material in structural engineering (Nanni, 1993).

During the 1980s, strengthening of concrete members with externally-bonded FRP laminates or near-surface mounted (NSM) bars gained relevant attention. FRP was used for strengthening bridge girders and piles, parking garages, office buildings and silos (Nanni, 2001). In particular, the external confinement of concrete columns became one of the most attractive applications of FRP laminates for repair and upgrading. This new technology found in the ease and flexibility of installation the most remarkable driver for its development, and became soon a competitive option to steel jackets and welded-wire fabrics (Nanni and Bedford, 1995).

Among the various types of columns, hollow-core R/C columns are an economically-attractive solution in concrete bridges (a) to maximize the structural efficiency (by increasing the strength-mass and stiffness-mass ratios), (b) to reduce the mass contribution of the column to seismic response, and (c) to limit the carrying demand on foundations. At present, many R/C bridges incorporate hollow-core piers, especially in areas where natural constraints require high-elevation infrastructures, such as tall buildings and bridges with tall piers (often found in Europe, United States and Japan). In case of seismic events, however, bridge piers designed in accordance with old design codes may suffer severe damage, because of their low ductility. Unfortunately, modern codes of practice oriented to seismic design do not address any specific problem related to hollow sections.

As the piers of many bridges represent a threat in regions under high seismic risk (because of their insufficient shear or flexural strength, low ductility or inadequate seismic detailing) and are in need of retrofitting, many studies have

been carried out on FRP-confined R/C circular and prismatic solid columns in the past years, and several analytical models have been proposed. On the other hand, the behavior of FRP-jacketed R/C hollow columns has been much less investigated (Lignola et al., 2010).

When considering column confinement, glass fibers are particularly attractive. First, they have the highest ultimate strain of any "high-modulus" fiber; second, their low fatigue and creep-rupture resistance are not a detrimental factor in this type of application. In addition, the shortage of carbon fiber that recently affected the market, as well as the development of high-performance glass fibers with lower manufacturing costs made GFRP laminates cost-competitive with CFRP laminates, thereby inducing an important increase in the demand of glass fibers over the last years. At the same time, continuous basalt fibers started to become commercially available. Basalt fibers offer an alternative to glass fibers due to their desirable characteristics, including - for example - thermal stability (Sim et al., 2005).

In FRP-confined concrete, the interaction between the two materials allows for the enhancement of concrete strength and deformability. Several experimental studies have been carried out and several analytical models have been proposed to describe the behavior of FRP-confined concrete. These models satisfactorily capture the mechanics of the phenomenon for circular columns. The same cannot be said for prismatic columns, for which these models are definitely less reliable and are still in need of validation for full-scale columns (Rocca et al., 2008).

In the early years of the twenty-first century, the publication by the American Concrete Institute (ACI) of design guidelines about the use of FRP for external strengthening of concrete members accelerated their adoption. To date, FRP systems have gained considerable acceptance in construction, and their use is poised to become as routine as the use of conventional structural materials such as masonry, wood, steel, and concrete (Bank, 2006).

This paper presents the experimental results of a research project that includes laboratory testing of R/C columns externally confined with glass and basalt-glass FRP laminates, subjected to pure axial load. The specimens were intended to represent real-size building columns designed according to dated design codes (i.e., prior to 1970) for gravity loads only. The condition of pure axial load is atypical for R/C columns given that they always sustain axial compressive loads together with bending moments, but this condition represents a critical step to understand the mechanics of FRP confinement.

2. RESEARCH SIGNIFICANCE AND OBJECTIVES

In FRP-confined concrete, the interaction between the two materials allows for the enhancement of concrete strength and ultimate strain. In the case of small plain-concrete cylinders, the properties of the two materials are used in the most desirable and successful way: (a) the transverse FRP is loaded in tension due to concrete dilation, thus containing concrete (after its internal cracking) and

providing lateral confining pressure; and (b) the concrete is loaded in triaxial compression due to the restraining action of the FRP laminate, thus leading to a substantial improvement in strength and ultimate strain. The behavior of confined plain-concrete cylinders subjected to pure axial loads has been extensively studied, and confinement effectiveness has been experimentally proven since the late 1970's (e.g., Kurt, 1978; Fardis and Khalili, 1981; Nanni and Bradford, 1994; Mirmiran and Shahawy, 1996; Karbhari and Gao, 1997; Spoelstra and Monti, 1999; Fam and Rizkalla, 2001; Shehata et al., 2002; Campione and Miraglia, 2003; Lam and Teng, 2003; Matthys et al., 2005; Matthys et al., 2006; Harajli, 2006; Saenz and Pantelides, 2007; Wu et al., 2009; Toutanji et al., 2010).

In concrete columns with circular cross-section, the confining effectiveness of FRP jackets is optimal since the geometrical configuration allows the fibers to be effective on the entire cross section (Lam and Teng, 2003).

Prismatic cross-sections, however, behave differently: as it is well recognized, the confining pressure is high at the corners and low along the sides, and the cross-section is only partially confined (Mander et al., 1988; Lam and Teng, 2003b). Confining rectangular cross-sections still enhances concrete strength and ultimate strain, but its effectiveness is not as tangible as that on a circular cross-section (Rocca et al., 2006; Rocca et al., 2008). Confinement effectiveness is even less tangible in the case of wall-like columns (Prota et al. 2006), i.e. in columns having rectangular sections characterized by a side aspect ratio larger than 3.

An important feature of this experimental program is the size of the column specimens. Full-scale experiments are limited by high cost and low availability of high-capacity testing equipment. Most of the time, the design of real concrete structures relies on the extrapolation from experimental results of laboratory tests carried out on scaled members. However, as quasi-brittle failures of concrete structures exhibit a large statistical scatter (Bažant and Yavari, 2005), full-scale experiments are critical to ensure that design equations are truly representative of the actual behavior of full-scale members.

Furthermore, the nominal concrete compressive strength does not represent the actual strength of the concrete in the columns to be tested due to several phenomena: the difference in cross-section sizes of the columns and the companion cylinders; the partial confinement provided by the ties; the fact that bars promote longitudinal splitting cracks; and the brittle or quasi-brittle failure which is governed mainly by the rate of release of the stored–strain energy (Bažant and Kwon, 1994).

All these phenomena are influenced by the size of the column. In particular, (a) the brittleness in tension is characterized by the concentration of the deformation into narrow zones (whose size is comparable with that of the aggregate), and the energy accumulated in the structure is dissipated through these narrow zones; and (b) the brittleness in compression develops in zones of dimensions comparable to those of the structure (Nemecek and Bittnar, 2003).
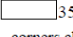
The work presented is this paper was set-up with the following objectives:

- exploring the effectiveness of FRP confinement on the axial strength and deformation of a prismatic R/C column under pure compressive load;

- evaluating whether the confinement is able to prevent or to delay the buckling of the longitudinal bars;

- understanding the possible limitations due to the cross-sectional shape; and

- providing experimental evidence to remedy the lack in the specific literature.

3. EXPERIMENTAL PROGRAM

The test matrix, summarized in Table 1, was designed considering different factors, namely: shape factor (side-aspect ratio), volume factor (volume-aspect ratio based on a benchmark volume of $610\times610\times3050$ mm^3 [$24\times24\times120$ in^3]), FRP volumetric ratio (ratio between the total volume of confining FRP and volume of confined concrete), type and amount of FRP plies.

Table 1: Test matrix

Specimen code	Cross-section Geometry	Internal steel reinforcement	Shape factor	Volume factor	FRP vol. ratio (%)	Type of fibers	No. of plies
S-1-control	610 × 610 corners chamfered with a radius of 20 mm	8 Ø25.4-mm longitudinal bars and Ø12.7-mm bars at a spacing of 406 mm			-	-	-
S-1-5GA			1.0	1.0	1.57	GLASS A	5
S-1-2GB					1.67	GLASS B	2
S-1-8H					1.49	HYBRID	8
R-1-control	508 × 737 corners chamfered with a radius of 20 mm				-	-	-
R-1-5GA			1.45	1.0	1.60	GLASS A	5
R-1-8H					1.51	HYBRID	8
R-0.5-control	356 × 508 mm corners chamfered with a radius of 20 mm	4 Ø25.4-mm longitudinal bars and Ø12.7-mm ties at a spacing of 356 mm			-	-	-
R-0.5-5GA			1.43	0.5	2.29	GLASS A	5
R-0.5-2GB					2.43	GLASS B	2
R-0.5-5GB					6.07	GLASS B	5
R-0.5-8H					2.18	HYBRID	8
WL-1-control	356 × 1041 mm corners chamfered with a radius of 20 mm	4 Ø25.4-mm longitudinal bars and Ø12.7-mm ties at a spacing of 356 mm			-	-	-
WL-1-5GA			2.92	1.0	1.60	GLASS A	5
WL-1-8GA					2.52	GLASS A	8
HR-0.6-control	508 × 737 corners chamfered with a radius of 20 mm	8 Ø25.4-mm longitudinal bars and Ø12.7-mm bars at a spacing of 406 mm			-	-	-
HR-0.6-5GA			1.45	0.6	2.67	GLASS A	5
HR-0.6-8GA					3.56	GLASS A	8

Note: 25.4 mm = 1 in; Ø25.4-mm bar = #8 bar; Ø12.7-mm bar = #4 bar.

Five series of column specimens were considered:

- Series S-1 corresponds to a shape factor of 1.0 and a volume factor of 1.0;

- Series R-1 to a shape factor of 1.45 and a volume factor of 1.0;

- Series R-0.5 to a shape factor very close to 1.45 (actually 1.43) and a volume factor of 0.5;

- Series WL-1 to a shape factor very close to 2.90 (actually 2.92) and a volume factor of 1.0; and

- Series HR-0.6 to a shape factor of 1.45 and to a volume factor of 0.6.

Three different types of fiber fabrics were used: two types of conventional glass fiber sheets from two different manufacturers (which are denoted herein as "Type A" and "Type B"); and a hybrid glass-basalt fiber sheet (glass-to-basalt fiber ratio 2:1). For each series, one specimen was kept as-built and used as benchmark. For the first series (S-1), three specimens were confined with both the glass FRP systems (Types A and B) and with the HFRP system; for the second series (R-1), one specimen was confined with Type A glass FRP and the other with the HFRP; for the third series (R-0.5), one specimen was confined with Type A glass FRP, two specimens with Type B glass FRP (with different number of plies), and one specimen with the HFRP system; for the fourth and the fifth series (WL-1 and HR-0.6, respectively), both specimens were confined with Type A glass FRP.

A three-part denomination is used to identify each specimen. The first part identifies the cross-sectional geometry: "S" stands for square (shape factor of 1.0); "R" for rectangular (shape factor of 1.45); "WL" stands for wall-like (shape factor of 2.90); and "HR" stands for hollow-core rectangular. The digits of the second part indicate the volume factor (1, 0.6, or 0.5). The third part identifies type and number of plies: GA for Type-A glass, GB for Type-B glass and H for hybrid, with 2, 5 or 8 plies.

3.1 Specimen design

The column specimens belonging to Series S-1, R-1, R-0.5, and WL-1 were designed using the ACI 318-63 code-mandated minimum amount of longitudinal reinforcement and minimum tie area at maximum spacing. ACI 318-63 requires that the total area of longitudinal bars be larger than 1.0% of the gross section area, A_g, and that the vertical spacing of the ties be the smallest of 16 longitudinal bar diameters (to prevent bar buckling), 48 tie diameters (to ensure sufficient tie area to restrain the lateral displacement of the longitudinal bars), and the least lateral dimension of the column (to develop the maximum strength of the concrete core).

The total cross-sectional area of the longitudinal bars was kept at 1.0% using eight 25.4-mm diameter (No. 8) bars for Series S-1, R-1, and WL-1, and four 25.4-mm diameter (No. 8) bars for Series R-0.5. For Series S-1 and R-1, 12.7-mm diameter (No. 4) ties were used, spaced at 406 mm (16 in.) on-center, which

corresponds to the requirement to prevent bar buckling. For Series R-0.5 and WL-1, 12.7-mm diameter (No. 4) ties were spaced at 356 mm (14 in.) on-center, which corresponds to the requirement to develop the maximum strength of the concrete core.

Hollow-core specimens (Series HR-0.6) were intended to represent scaled R/C bridge piers designed according to a dated code (i.e. prior to 1970) for gravity loads only. The longitudinal reinforcement was designed based on the requirements of the AASHTO code used in 1969. The tie spacing was defined as mandated by the ACI code effective at the same time. The longitudinal steel reinforcement was given by a total of eight 25.4-mm diameter (No. 8) bars, corresponding to a geometric steel percentage equal to 1.7 %. For the transverse reinforcement 12.7-mm diameter (No. 4) steel ties spaced at 410 mm on center (which corresponds to the code requirement for preventing bar buckling) were used.

The specimens' dimensions were also selected to ignore slenderness effects. At the two ends of the specimens, 12.7-mm diameter (No. 4) steel ties spaced at 50.8 mm on-center (2 in.) were used to prevent failure in these zones.

The FRP plies were applied by manual lay-up in the transverse direction. Prior to the application of the FRP, all corners were rounded with a radius of about 25.4 mm (1 in). The number of FRP plies was five in the case of the Type A glass fiber sheets, two in the case of the Type B glass fiber sheets, and eight in the case of the hybrid glass-basalt fiber sheets. Given that the fiber types were all of comparable quality, the number of plies was designed in order to have the same FRP volume ratio for all column specimens, with the exception of specimen R-0.5-5GB.

In typical field applications, the number of plies ranges between 3 and 6 in the case of 600 grams per square meter (1.1 lb/sq.yd) yield, and between 2 and 3 in the case of 900 grams per square meter (1.7 lb/sq.yd) yield. Specimens R-0.5-5GB, and WL-1-8GA were designed to have data points at a high FRP confinement ratio.

3.2 Materials

The specimens were fabricated at a precast plant one at a time using the same concrete mix design. The average concrete compressive strength, f'$_c$, is reported in Table 2. Concrete strength is based on the results of compression tests on 150 mm diameter by 304 mm (6 by 12 in.) cylinder samples, 100 mm diameter by 202 mm (4 by 8 in.) cylinder samples, or 92.7 mm diameter by 114 mm (3.71 by 7.50 in.) core samples, per ASTM C 39.

For specimens S-1-2GB, R-1-5GA and R-1-8H, concrete cylinder samples were delivered to the laboratory at different times. This could have caused inconsistent results; therefore concrete cores were taken from the cast specimens and used to define concrete strength.

According to ASTM C39, if the concrete core length to diameter ratio is higher than 1.75, the concrete compressive strength can be taken as is and no correction factor has to be applied. ASTM Grade 60 steel bars and ties were used for all

specimens. Unidirectional continuous fiber sheets were used for the FRP systems, where the properties of the fiber sheets are summarized in Table 3 as provided by the manufacturers.

Table 2: Concrete strength

Specimen code	Concrete sample (diameter and height are in mm)	No. of tests	Average strength, f'_c [MPa]
S-1-control	152 by 304	6	37.3
S-1-5GA	152 by 304	3	48.6
S-1-2GB	94.2 by 190 (core)	3	37.1
S-1-8H	152 by 304	3	44.4
R-1-control	152 by 304	3	48.0
R-1-5GA	94.2 by 190 (core)	3	56.4
R-1-8H	94.2 by 190 (core)	3	47.6
R-0.5-control	102 by 203	3	34.7
R-0.5-5GA	102 by 203	3	53.8
R-0.5-2GB	102 by 203	6	46.4
R-0.5-5GB	102 by 203	6	49.7
R-0.5-8H	102 by 203	3	46.8
WL-1-control	152 by 304	3	56.1
WL-1-5GA	152 by 304	3	48.5
WL-1-8GA	152 by 304	3	52.7
HR-0.6-control	102 by 203	3	43.5
HR-0.6-5GA	94.2 by 190 (core)	3	44.8
HR-0.6-8GA	94.2 by 190 (core)	3	45.9

Note: 6.895 MPa = 1,000 psi; 25.4 mm = 1 in.

Table 3: FRP system properties

Filament yarn properties	Glass A fabric	Glass B fabric	Hybrid fabric
Type of fibers	Glass	Glass	Basalt – Glass
Ratio in volume	100%	100%	33.3% – 66.6%
Tensile modulus (MPa)	76,948	72,397	88,945 – 76,948
Tensile strength (MPa)	3,399	3,241	4,840 – 3,399
Tensile strain (%)	4.7	4.5	3.15 – 4.7
Sheet properties	**Glass A fabric**	**Glass B fabric**	**Hybrid fabric**
Ply thickness (mm)	0.246 [0.480]	0.589 [1.27]	0.120 [0.284]
Weight (g/m^2)	600	900	340

Note: 6.895 MPa = 1 ksi; 25.4 mm = 1 in; 0.542 g/m2 = 1 lb/yd2; gross laminate properties are in square brackets.

3.3 Test setup and procedure

The instrumentation in all the specimens consisted of electrical strain gauges located on the longitudinal and transverse steel reinforcement at the level of the mid-height cross section, and on the external surface of the specimen: onto the concrete surface at the mid-height section for the control specimens, and on the FRP jacket at critical locations (corner areas and mid-section on each face of the specimens) along the perimeter of the cross-section at mid-height of the strengthened specimens. Additionally, linear variable differential transformers (LVDT) were used to measure the total shortening of the specimens, and to evaluate the horizontal dilation at the mid-height section, along the two sides and in the diagonal directions.

The stroke of the LVDTs ranged between ±12.25 mm (±0.5 in.) and ±490 mm (±20 in.). The control specimens were tested using a 22 MN (5 million lbf) press, while the tests of the strengthened specimens were carried out using a 53 MN (12 million lbf) press. The control specimens and the strengthened ones were tested five and eighteen months after casting, respectively. Special care was taken in aligning each specimen with the axis of the press. The specimens were capped with thin layers of high-strength grout. The load was applied at a displacement rate of 0.5 mm/min (0.02 in/min). The same rate was maintained when the concrete cylinders and cores were tested. The loading sequence included five subsequent load cycles, with increments of one fifth of the expected capacity.

4. EXPERIMENTAL RESULTS

The test results are summarized in Table 4. For each specimen, the following is reported: average concrete compressive strength, f'_c (as defined in the section "Materials"); maximum applied load, P_{peak}; load at failure, P_u, (in most cases close to 75% of the peak load); ratio between load at failure and maximum load, P_u/P_{peak}; axial deformation when the maximum load was reached, Δ_{peak}; ultimate axial deformation, Δ_u (defined as the axial deformation corresponding to P_u); ratio between the ultimate axial deformation and the axial deformation at peak, Δ_u/Δ_{peak}; concrete axial stress at peak, $\sigma_{c,peak}$, normalized with respect to the average concrete compressive strength, f'_c, ($\sigma_{c,peak}/f'_c$); ratio between normalized concrete axial stress at peak and corresponding value of the control specimen for the reference series, $[(\sigma_{c,peak}/f'_c)/(\sigma_{c,peak}/f'_c)_{control}]$. The axial deformation is rendered as the average of the measurements from the LVDTs.

The concrete axial stress at the peak, $\sigma_{c,peak}$, was computed as the difference between the peak load (P_{peak}) and the load carried by the reinforcement (P_{bar}), divided by the net area of concrete (A_c), where P_{bar} is given as the total area of the reinforcing steel (A_s) times the nominal yield stress (f_y). The plots of the normalized concrete axial stress versus the axial deformation for all the specimensare shown in Figs.1-5.

4.1 Strength and failure modes

Failure of the control specimens initiated with vertical cracks followed by lateral displacement of the longitudinal bars (that contributed to the splitting of the concrete cover) and later by crushing of the concrete core accompanied by buckling of the longitudinal bars.

All FRP-confined columns failed due to the rupture of the FRP jacket; cracking of the concrete core developed after the maximum load was attained, and longitudinal-bar buckling was visible after the post-mortem removal of the ruptured FRP jacket and of the concrete cover.

Table 4: Test results

Spec. ID	f'_c [MPa]	P_{peak} [MN]	P_u [MN]	$\dfrac{P_u}{P_{peak}}$	Δ_{peak} [mm]	Δ_u [mm]	$\dfrac{\Delta_u}{\Delta_{peak}}$	$\dfrac{\sigma_{c,peak}}{f'_c}$	$\dfrac{\sigma_{c,peak}/f'_c}{\left(\sigma_{c,peak}/f'_c\right)_{control}}$
S-1-control	37.3	12.5	9.87	0.789	6.53	8.94	1.37	0.779	1.00
S-1-5GA	48.6	17.8	N/A	N/A	7.01	N/A	N/A	0.893	1.15
S-1-2GB	37.1	13.0	9.79	0.753	9.07	15.93	1.76	0.821	1.05
S-1-8H	44.4	15.6	12.1	0.775	6.10	28.1	4.61	0.843	1.09
R-1-control	47.9	16.5	16.3	0.987	7.09	7.72	1.09	0.826	1.00
R-1-8H	56.4	17.0	12.8	0.750	8.64	14.63	1.69	0.870	1.05
R-0.5-control	34.7	5.52	5.05	0.915	8.00	8.38	1.06	0.746	1.00
R-0.5-5GA	53.8	8.66	6.49	0.750	7.70	15.32	1.99	0.847	1.13
R-0.5-2GB	46.4	7.11	5.36	0.754	6.83	18.21	2.66	0.748	1.00
R-0.5-5GB	49.7	8.73	6.86	0.785	9.14	30.73	3.36	0.879	1.18
R-0.5-8H	46.8	7.97	6.04	0.758	8.00	27.69	3.46	0.844	1.13
WL-1-control	56.1	17.1	16.4	0.964	7.815	8.24	1.05	0.749	1.00
WL-1-5GA	48.5	14.6	10.9	0.750	9.26	26.1	2.82	0.757	1.01
WL-1-8GA	52.7	15.9	11.9	0.749	7.73	23.7	3.07	0.767	1.02
HR-0.6-control	43.5	7.89	7.79	0.987	5.59	5.91	1.06	0.697	1.00
HR-0.6-5GA	44.8	9.21	6.93	0.756	6.30	13.8	2.19	0.719	1.03
HR-0.6-8GA	45.9	9.04	6.81	0.753	5.08	10.5	2.07	0.775	1.11

Note: 6.895 MPa = 1,000 psi; 4.448 MN = 1,000 kip; 25.4 mm = 1 in; $\sigma_{c,peak}$ = $(P_{peak} - P_{bar}) / A_c$

Series S-1 — In Figure 1 the normalized axial stress in the concrete (defined as the ratio between $\sigma_{c,peak}$ and f'_c) is plotted as a function of the axial deformation of the specimens. The failure of the benchmark Specimen S-1-control was brittle and occurred at the center of the upper half of the specimen. The peak capacity was attained when the average concrete axial stress was equal to about 78% of the average concrete compressive strength, f'_c. The load stabilized at the level of the

peak load before it suddenly dropped. Cracking of the concrete was observed before splitting of the concrete cover and buckling of the longitudinal bars. The ultimate axial deformation recorded, Δ_u, was about 137% the value at the peak load, Δ_{peak}, while the load dropped to 78% of P_{peak}. Crushing of the concrete core and buckling of the longitudinal bars are documented in Fig. 2. The confined specimens behaved similarly with respect to each other: upon attaining the peak load, the load steadily decreased while the axial deformation continued increasing due to the confining action of the FRP wrap. Failure occurred by rupture of the FRP laminates. In particular, fiber rupture always initiated in the proximity of a corner and then propagated towards the sides. The average concrete axial peak stress, $\sigma_{c,peak}$ ranged between 82 and 89% of the average concrete compressive strength, f'_c, when the peak capacity was reached. The increment in concrete strength due to confinement was 15%, 9% and 5% for S-1-5GA, S-1-8H and S-1-2GB, respectively. A remarkable improvement in the post-peak deformability was experienced by the confined specimens. The ultimate axial deformation recorded, Δ_u, was about 461% and 176% of Δ_{peak} for S-1-8H and S-1-2GB, respectively. While testing Specimen S-1-5GA, a problem on the data acquisition system caused the loss of the data in the post-peak phase. Figure 1 also shows the failure of the FRP wrap in Specimen S-1-8H.
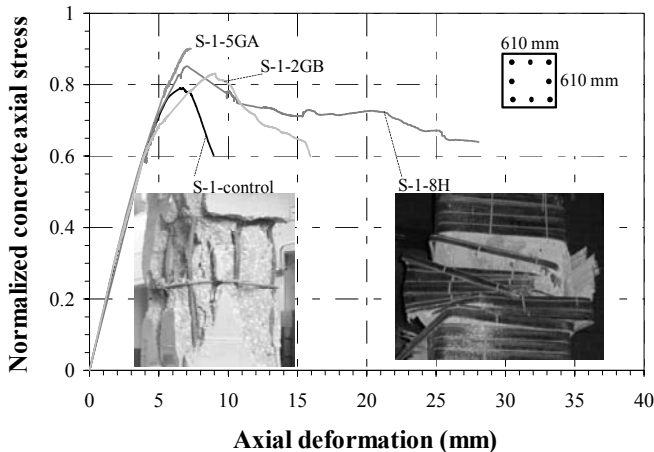

Figure 1 - Normalized axial stress vs. axial deformation (Series S-1). Failed Specimens S-1-control and S-1-8H are also shown.

Series R-1 — In Figure 2 the normalized axial stress in the concrete is plotted as a function of the axial deformation of the specimens. Failure of the benchmark Specimen R-1-control was sudden and accompanied by an explosive noise. The peak capacity was attained at an average concrete axial stress equal to about 83% of f'_c. Once the peak load was attained, the load dropped almost instantly without early warning, as no cracking of the concrete was observed until the final crushing.

Failure occurred when the load was about 99% of P_{peak}. The ultimate axial deformation recorded, Δ_u, was only about 109% of Δ_{peak}. Failure occurred at the lower half of the specimen, as shown in Fig. 3. Specimen R-1-5GA experienced a premature failure localized at the top of the specimen due to stress concentration and has not been taken into account in this study. A 102-mm (4-inch) wide strip at the top end of Specimen R-1-5GA was left unconfined: the splitting of the concrete cover in this region caused the premature rupture of the FRP jacket. Failure of Specimen R-1-8H occurred due to rupture of the FRP laminate. Failure started at one of the corners in the higher half of the specimen and then propagated to the adjacent sides (Fig. 2). The peak load was reached when the average concrete axial stress was about 87% of f'_c. The increment of concrete strength due to confinement was about 5%, while the ultimate axial strain was about 169% of Δ_{peak}.
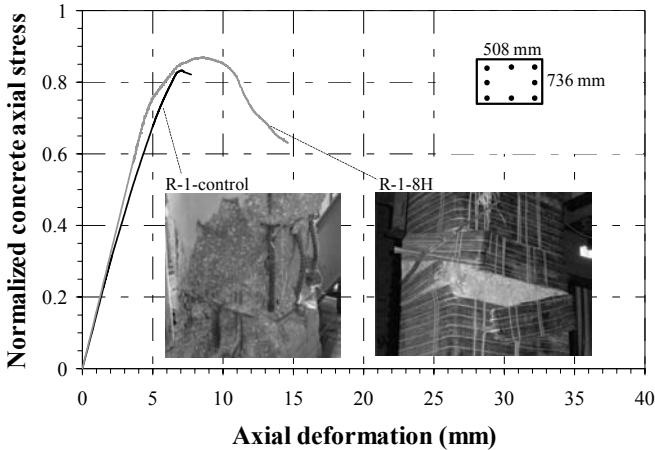

Figure 2 - Normalized axial stress vs. axial deformation (Series R-1). Failed Specimens R-1-control and R-1-8H are also shown.

Series R-0.5 — In Figure 3 the normalized axial stress in the concrete is plotted as a function of the axial deformation of the specimens. Specimen R-0.5-control failed similarly to Specimen S-1-control. The failure affected the entire upper half of the column. Concrete cracking was heard before concrete-cover spalling and rebars buckling. The peak load was reached when the average concrete axial stress was about 75% of f'_c. The failure was brittle (failure occurred when the load was about 92% of P_{peak}), with a measured ultimate axial strain of 106% of Δ_{peak}. Specimens R-0.5-5GA, R-0.5-8H and R-0.5-5GB behaved similarly to each other. The average concrete axial stress ranged between 84% and 88% of f'_c when the peak load was reached. The increment in concrete strength was 13% for both R-0.5-5GA and R-0.5-8H, and 18% for R-0.5-5GB, as result of a higher FRP confinement ratio. After the peak load was attained, for both R-0.5-5GA and R-

0.5-8H the load gradually decreased with increasing axial deformations. R-0.5-5GA failed when the axial deformation almost doubled the value at the peak. In the case of Specimen R-0.5-8H, instead, the load stabilized at about 80% of the peak load, and the specimen failed when the axial deformation was about 346% of Δ_{peak}. For Specimen R-0.5-5GB, the load remained nearly constant after reaching the peak load, with increasing axial deformations; then, the load decreased quite suddenly and stabilized at about 90% of the peak load. The specimen failed when the axial load was about 78% of P_{peak} and the axial deformation was about 336% of Δ_{peak}. The failure mode was similar to that of the specimens of Series S-1 and R-1, as documented in Fig. 4 for Specimens R-0.5-5GB and R-0.5-8H. Specimen R-0.5-2GB did not experience any gain in concrete strength. The peak load was reached when the average concrete axial stress was about 75% of f'_c and the ultimate axial deformation was about 266% of Δ_{peak}. Factors contributing to this strength result may include those affected by preparation, setup and execution of the test itself.
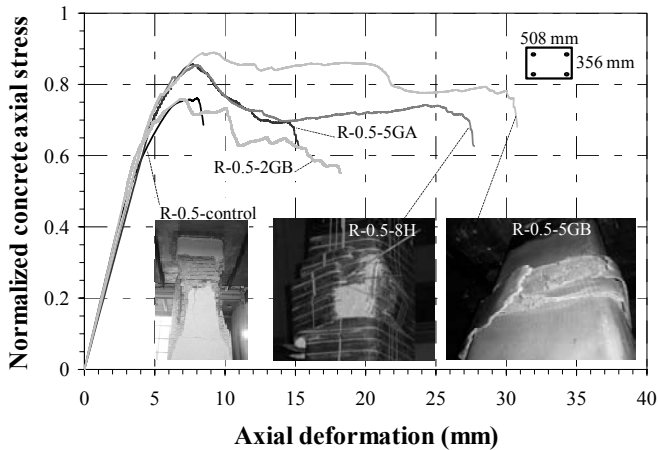

Figure 3 - Normalized axial stress vs. axial deformation (Series R-0.5). Failed Specimens R-0.5-control, R-0.5-5GB and R-0.5-8H are also shown.

Series WL-1 — No significant increment in concrete strength due to confinement was observed. The normalized axial stress at the peak is 0.749 for the control specimen and varies between 0.757 and 0.767 for the confined specimens. The increment in concrete strength due to confinement, evaluated with respect to the corresponding control specimen, ranges between about 1.01 and 1.02. On the other hand, a significant improvement in post-peak deformability was experienced by the two confined specimens, as the ratio between the axial deformation at failure and the peak axial deformation is 2.82 and 3.07 for Specimens WL-5G and WL-8G, respectively. In Figure 4 the normalized axial stress in the concrete is plotted as a function of the axial deformation of the specimens. The control specimen

failed suddenly due to rebars buckling and concrete cover splitting. Failure happened after the longitudinal steel reinforcement reached the yield point. Both the FRP-confined specimens exhibited high axial deformations. They failed due to the rupture of the FRP jacket localized in a limited region close to a corner. Bulging of the FRP wrapping also occurred. Details of the failure of the specimens are shown in Fig. 4.
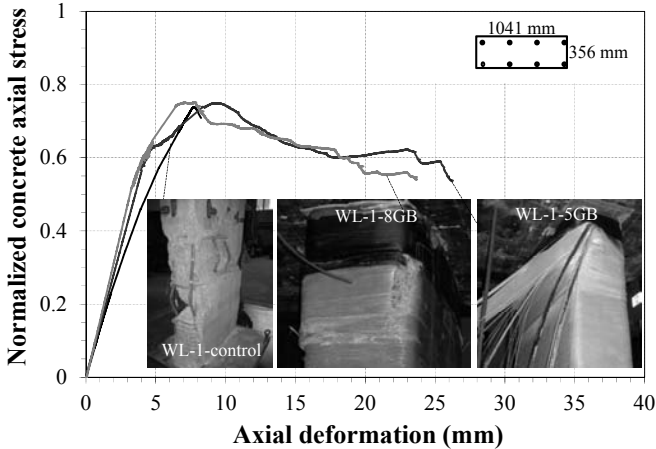

Figure 4 - Normalized axial stress vs. axial deformation (Series WL-1). Failed specimens are also shown.

Series HR-0.6 — No significant increment in concrete strength due to confinement was observed. The normalized axial stress is 0.697 for the control specimen and varies between 0.719 and 0.775 for the confined specimens. The increment in concrete strength due to confinement, evaluated with respect to the corresponding control specimen, ranges between about 1.03 and 1.11. A noteworthy improvement in deformability in the post-peak behavior was experienced by the two confined specimens. The ratio between the axial strain at ultimate and the peak load ranges from 2.19 to 2.07 for Specimens HR-0.6-5GA and HR-0.6-8GA, respectively. In Figure 5 the normalized axial stress in the concrete is plotted as a function of the axial deformation of the specimens. It can be noticed that increasing the number of GFRP plies brings in a slight enhancement of concrete strength and almost no significant variations in the corresponding axial strain. The control specimen failed suddenly due to the buckling of the longitudinal steel and to the spalling of the concrete cover. The failure occurred close to the upper side of the column, before the longitudinal steel reinforcement reached the yield point. The longitudinal steel bars buckled between two consecutive stirrups and determined the spalling of the concrete cover; at that stage the column became unable to carry further loads. Both FRP-confined specimens failed due to the

rupture of the FRP jacket which was localized in a limited region close to a corner, located in the upper side of the column. The peak load was reached at a strain level close to the yielding of the reinforcing bars. Cracking of the concrete core was heard during the post-peak phase. Both longitudinal bar buckling and concrete cover splitting were significantly restrained by the GFRP-jacket. Details of the failure of the specimens are shown in Fig. 5.
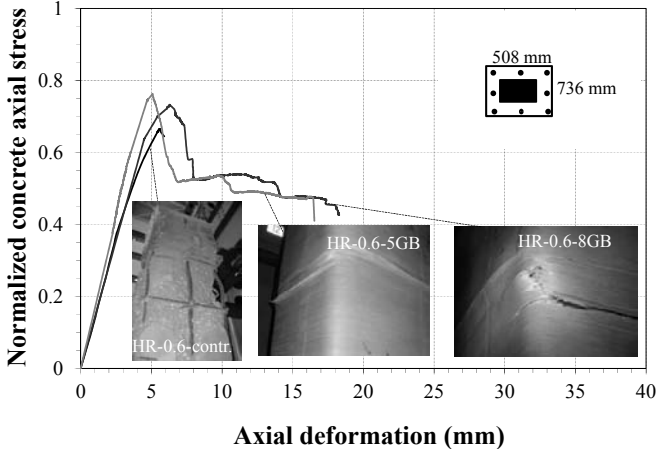

Figure 5 - Normalized axial stress vs. axial deformation (Series HR-0.6). Failed specimens are also shown.

4.2. Vertical strain in reinforcing bars

Strain gages were attached to the longitudinal steel bars in the mid-height section, between two adjacent ties. The axial strain in the bars recorded for the unstrengthened specimens was either close to or exceeded the yield strain, and was slightly higher than that measured in the confined specimens. This can be explained as follows. In the case of unconfined specimens, the strain gages stopped reading immediately after concrete cover splitting since they were located at the interface between bar and concrete cover. The compressive strain recorded on the steel bars by the strain gages was not affected by the lateral displacement of the bars since concrete failure and bar buckling occurred simultaneously. For confined specimens, instead, the confining action provided by the FRP jacket delayed column failure and the strain gages continued reading after concrete cover splitting. Strain readings were affected by the lateral deflection of the steel bars. The compressive strain was therefore reduced by the tensile strains induced by the lateral bending of the bars, since the strain gages were located on the exterior side of the rebars. Experimental measurements were not used for the analysis, and, given also the small percentage of the steel reinforcement, the assumption of yielded steel was considered reasonable for the analysis.

5. VOLUMETRIC STRAIN AND DILATION RATIO

In this section, the volumetric strain and dilation ratio of column specimens belonging to Series S-1 and Series R-0.5 is discussed. The impact of the external confinement provided by the FRP jacket on column strength enhancement and post-peak deformability is analyzed with respect to the volumetric response. It has been widely recognized (Park and Paulay, 1975; Pantazopoulou and Mills, 1995; Neville, 1996; Spoelstra and Monti, 1999) that axially-loaded unconfined concrete contracts in volume up to about 90% of its peak strength; then, the volume change reverses and results in dilation when the peak strength is reached. Beyond this point, the volume expansion grows at a higher rate as the softening branch develops, until failure occurs.

When concrete is confined with FRP jackets, the volume expansion may be effectively constrained, and the unstable crack growth controlled. Provided that the jacket is sufficiently thick, concrete expansion can be curtailed (Mirmiran et al., 1998; Spoelstra and Monti, 1999; Pessiki et al., 2001; Harries and Kharel, 2002; Carey and Harries, 2003; Lam and Teng, 2003a-b). Plain-concrete dilation ratio (defined as the ratio of transverse to axial strain) has an initial value (Poisson's ratio) generally found to be about 0.20, begins to increase non-linearly when concrete starts cracking and grows uncontrollably until failure.

The presence of the FRP jacket affects the concrete dilation ratio before and after the peak load is reached, by significantly restraining the growth in volume and allowing large axial deformations (Mirmiran et al., 1998; Pessiki et al., 2001).

The axial strain was measured as the LVDT-measured axial deformation averaged along the entire height of the column. The volumetric strain (change in volume per unit volume of concrete) was calculated as the sum of the axial strain and the two transverse strains at the mid-height cross-section (measured along the two orthogonal directions in the plane of the cross-section). A positive volumetric strain indicates a volume reduction, whereas a negative value indicates an expansion. The volumetric strain represents an indicator of the response of the cross-section in its entirety, unlike the dilation ratio which indicates how the cross-section tends to deform along different directions. The dilation ratio is defined as the ratio between the average transverse strain along each of the two orthogonal directions in the plane of the cross-section and the axial strain. The mid-height cross section is less affected by the boundary conditions and, even though failure may occur elsewhere, it is taken as representative of the behavior of the column.

Series S-1 — Figures 6a,c show the plots of the volumetric strain and of the dilation, respectively, as a function of the axial strain of the specimens of Series S-1 (with the exception of Specimen S-1-5GA, for which the data for the post-peak branch were not available). The initial slope of all the curves in Fig.6a is close to $(1-2\nu)$ - where ν is the Poisson's ratio of the concrete assumed equal to 0.20 - and corresponds to the elastic behavior. The curves deviate from this line and reach
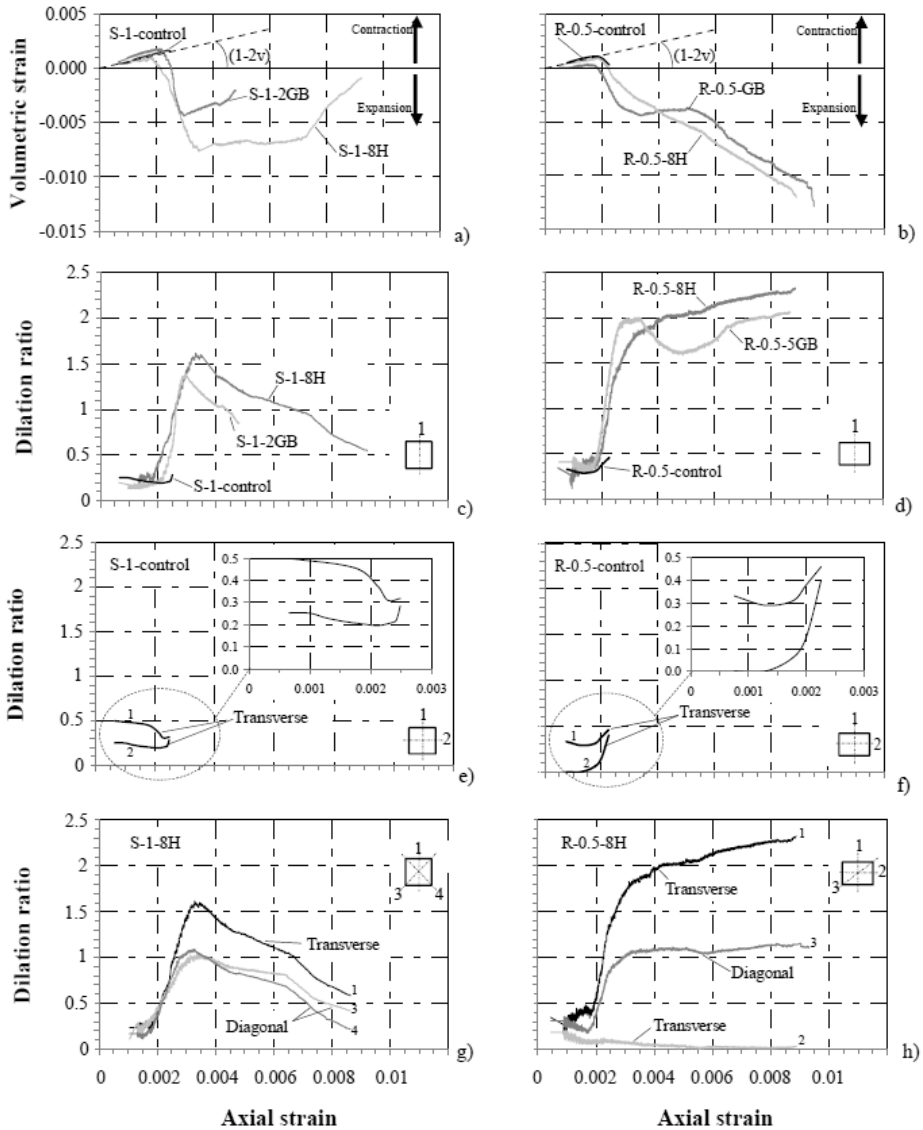
Figure 6 - Plots of the volumetric strain and of the dilation ratio versus the axial strain [Series S-1 (a, c, e, g) and R-0.5 (b, d, f, h)].

their maximum (point of reversal of the volumetric strain) as the load approaches its peak value. This point corresponds to the onset of uncontrolled crack growth leading to the failure of the control specimen (S-1-control), whose post-peak branch had a limited extent and rapidly developed into failure. In the case of the externally confined specimens (S-1-2GB and S-1-8H), the larger development of

the post-peak branch clearly shows that the external FRP jacket provides a lateral constraint for the cracked concrete and reverses the dilation process of the concrete. In Fig.6c, for the control specimen the dilation ratio along direction 1 has an average value of about 0.2 for axial strains up to 0.0028, past which it rapidly increases. No readings are available in the post-peak zone because confinement loss, concrete crushing and bar buckling occurred almost instantaneously. For Specimens S-1-2GB and S-1-8H (Fig.6c), the dilation ratio along direction 1 ranges between 0.15 and 0.25 up to axial strains of about 0.002. Past this level, the dilation ratio for both specimens increases rapidly and reaches a limit value of about 1.5 when the axial strain is about 0.0035. Beyond this point, both curves begin to decrease almost with the same slope. Specimen S-1-2GB failed when the axial strain was about 0.005 and the dilation ratio dropped to about 0.8. Specimen S-1-8H reached an axial strain at failure of about 0.009 with a dilation ratio dropping to about 0.5. Fig.6e shows the plot of the dilation ratio of Specimen S-1-control measured along the two transverse directions (directions 1 and 2), whereas Fig.6g shows the dilation ratio of Specimen S-1-8H measured along direction 1 and along the two diagonals (directions 3 and 4). For the control specimen, the dilation ratios along directions 1 and 2 are similar, that is, the cross-section deforms symmetrically along these axes. For Specimen S-1-8H, after reaching its peak capacity, the concrete tends to expand much more along the transverse directions (direction1) rather than along the two diagonals (directions 3 and 4). As expected for a square column, the dilation ratio is symmetrical along the two diagonals.

Series R-0.5 — To describe the volumetric response of the specimens of Series R-0.5, Specimens R-0.5-control, R-0.5-5GB and R-0.5-8H were selected. Figs.6b,d show the volumetric strain-axial strain and the dilation ratio-axial strain relations, respectively. The volumetric response of Specimen R-0.5-control is similar to that experienced by Specimen S-1-control. In the case of the confined specimens, the FRP jacket constrains the volume dilation of the concrete, but its effectiveness is not sufficient to reverse the volumetric expansion as for the square columns. For specimen R-0.5-5GB, given the higher FRP amount compared to Specimen R-0.5-8H, a reversal point is reached but not maintained. The dilation ratio along direction 1 for the control specimen has a constant average value of about 0.30 until failure occurs (Fig.6d). The dilation ratio along direction 1 for Specimens R-0.5-5GB and R-0.5-8H (Fig.6d) ranges between 0.30 and 0.45 up to axial strains of about 0.0015. Past this level, the dilation ratio for both specimens increases at a high rate until a value of about 2, for axial strains close to 0.003. Beyond this point, the dilation ratio continues to increase at a lower rate until failure. Specimen R-0.5-5GB failed when the axial strain was about 0.009 and the dilation ratio was close to 2.1. Specimen R-0.5-8H reached an axial strain at failure of about 0.008 with a dilation ratio close to 2.3, whereas its square counterpart (S-1-8H) reached an axial strain at failure of about 0.009 with a dilation ratio close to 0.5. In

Figs.6f,h the dilation ratios of the Specimen R-0.5-control (measured along the two transverse directions 1 and 2) and of the Specimen.R-0.5-8H (measured also along direction 3) are plotted. The dilation ratio along the long side (direction 2) is much smaller than that along the short side (direction 1) for both the control and the confined specimens. In the case of the control specimen, because of the development of unstable cracks the dilation ratio along the long side (direction 2) increases rapidly until failure.

6. DISCUSSION

The definition of the lateral confining pressure exerted by the FRP jacket on the concrete is key to the prediction of the increment in concrete strength. The lateral pressure depends on the strain in the FRP and varies depending on the cross-sectional shape (circular or prismatic). For circular cross-sections, the lateral pressure is in principle uniformly distributed around the perimeter of the cross-section, and can be uniquely determined considering force equilibrium and radial displacement compatibility between the concrete and the FRP jacket. In circular RC columns, the confining effectiveness of the FRP jacket is optimal since the geometrical configuration allows the fibers to be effective on the entire cross section. The final point in the stress-strain curve of the column generally defines both the peak load and the ultimate axial strain. The peak stress is reached when the lateral confining pressure reaches its maximum (Fig.7a) and soon later the FRP fails.

Several analytical models have been developed to describe the behavior of FRP-confined concrete circular columns. The majority of them (Mirmiran and Shahawy, 1997; Spoelstra and Monti, 1999; Fam and Rizkalla, 2001; Harries and Kharel, 2002; Teng et al., 2009) are based on the assumption that the axial stress and the axial strain of FRP-confined concrete at any given lateral strain are the same as those of the same concrete actively confined with a constant confining pressure equal to that supplied by the FRP-jacket (Teng and Lam, 2004). These models calculate the axial stress and the axial strain of FRP-confined concrete at a given confining pressure by using an active confinement model for concrete. In other words, if the lateral strain – axial strain relationship is known, for a given axial strain the corresponding lateral pressure provided by the FRP jacket can be derived. The axial strain and the lateral pressure can then be used together with a model based on active confinement to evaluate the corresponding axial stress in the column. This incremental approach ultimately leads to the definition of the entire stress-strain curve (Teng et al. 2009).

Many experimental studies have been carried out on FRP-confined RC square columns in the past years (Pessiki et al., 2001; Shehata et al., 2002; Mirmiran et al., 1997; Rocca et al., 2006; Rocca et al., 2008; De Luca et al., 2010). It has been widely recognized that the lateral pressure provided by the FRP jacket is not uniformly distributed along the cross-sectional perimeter, since it is high close to

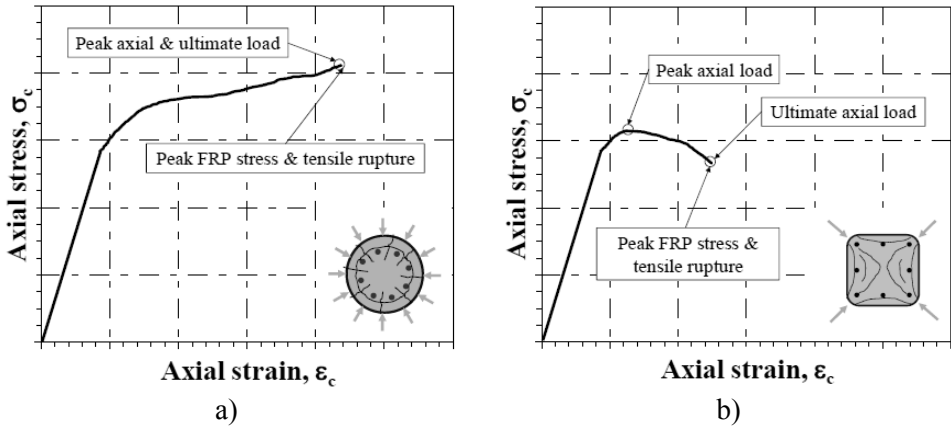a)   b)

Figure 7 - Typical axial stress – axial strain diagrams showing the different behaviors of FRP-confined circular (a) and square (b) columns.

the corners and low along the sides, so that the cross-section is only partially confined (Mander et al., 1988; Lam and Teng, 2003b). Also the distribution of the lateral strain along the FRP jacket is not uniform and the shape of the section changes while concrete grows in volume. FRP confinement still enhances concrete strength and ultimate strain, but its effectiveness is not as tangible as that of jacketing a circular cross-section. While ultimate column failures coincide with the rupture of the FRP, the peak capacity of the column occurs at a FRP strain much lower than its ultimate value (Fig.7b). Several theoretical models to predict the peak axial stress for square and rectangular columns have been developed and proposed (Mirmiran et al., 1998; Wang and Restrepo, 2001; Campione and Miraglia, 2003; Lam and Teng, 2003b; Kumutha et al., 2007; Wu and Wang, 2009). However, the equations of these models do not yield the same values, their validity for full-scale columns has still to be proven, and their limitations come from their being derived from the models created for circular shapes and modified by means of factors intended to account for the change in the sectional shape and for the ensuing effect on the confining pressure (De Luca et al. 2010).

Figs.8a-d show the change in volume of a representative one-quarter unit element of Specimens S-1-8H and R-0.5-8H, respectively, when the peak load is reached (a,c) and at failure (b,d). To make the change in volume visible, all changes in length are amplified using the same magnification factor. Given the symmetry, only one quarter of the cross-section is drawn. For both square and rectangular shapes, when the peak load of the column is reached no significant cross-sectional shape changes are noted (Figs.8a,c), as the displacements of the mid-points of the two sides are of the same order of magnitude and the displacement of the corner is smaller, but comparable to the transverse displacements. For the square column, the transverse expansion at failure is significantly higher than the diagonal expansion (Fig.8b). This experimental
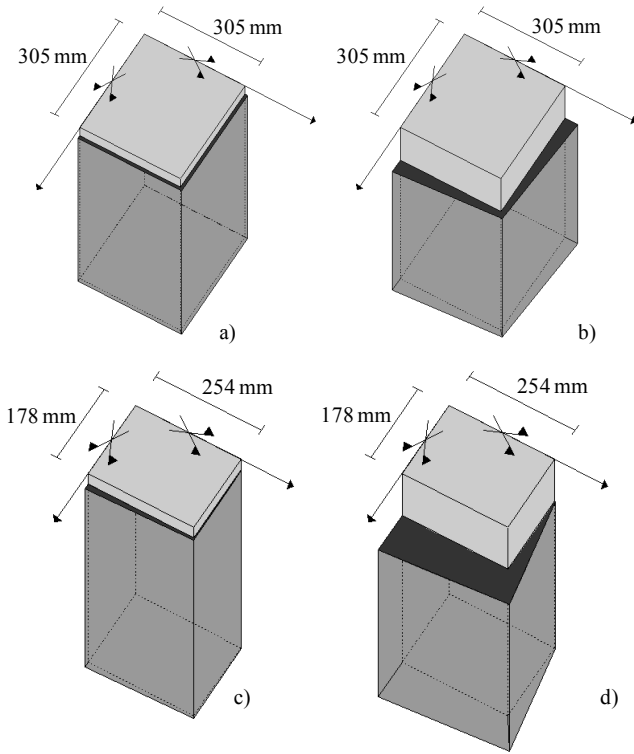
Figure 8 - Change in volume of a one-quarter unit element for Specimens S-1-8H and R-0.5-8H at the peak load (a,c) and at failure (b,d).

observation confirms the generally-accepted assumption that in prismatic cross-sections the confining pressure is higher at the corners than along the sides. For rectangular columns at the onset of failure (Fig.8d), instead, the displacements of the mid-point on the long side and of the corner are of about the same magnitude and much larger than the displacement at the mid-point of the short side, respectively. The commonly accepted assumption is that the confined area is defined by four parabolas, which envelop the fully confined concrete (the external concrete is assumed to be unconfined). Based on this experimental evidence, it appears that the two parabolas along the short sides may be disregarded, since the dilation in the direction orthogonal to the short side is small. Furthermore, as the rectangular column has more FRP than the square column (but the jacket is less effective), the performance level depends on the cross-sectional shape. Moreover, it appears that for a prismatic cross-section, the maximum load is reached when the concrete contracts in volume.

Fig. 9 shows a typical plot of the axial stress versus the volumetric strain for a FRP-confined prismatic column (Specimen S-1-8H). FRP confinement allows the reversal in volume change, and - during the process of volume dilation - concrete experiences large axial deformations without sizable increases of its axial strength.
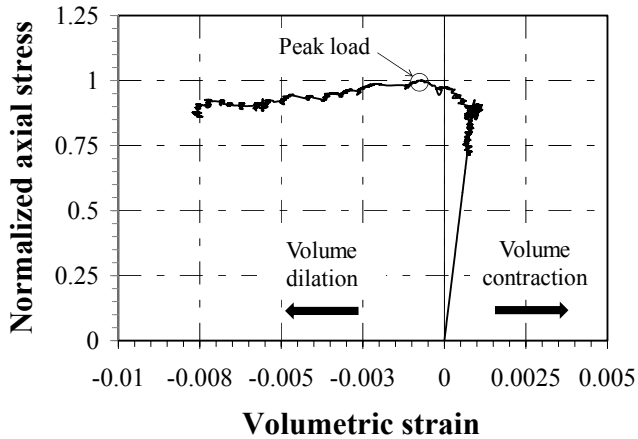
Figure 9 - Typical plot of the volumetric strain versus the normalized axial stress for FRP-confined prismatic columns (Specimen S-1-8H).

7. CONCLUSIONS

Based upon the experimental evidence gained through the full-scale experiments presented in this paper, the following conclusions are drawn.

1. The axial load-axial deformation behavior of a prismatic concrete column laterally confined by means of a FRP jacket of thickness representative of field applications is characterized by a linear elastic branch almost up to the peak load, and by a descending post-peak branch until failure. In prismatic columns, the effectiveness of the FRP confinement is more significant in terms of enhancement of concrete axial deformation rather than increment in axial strength. The presence of the FRP jacket allows a "growth" in volume of the concrete core by offsetting buckling of the longitudinal bars and by delaying unstable crack propagation.

2. The shape of the cross-section influences the effectiveness of the confinement, which is higher for square than for rectangular shapes, and decreases as the side aspect-ratio of a rectangular cross-section increases. The transverse expansion of the concrete core, defined by means of the dilation ratio, changes with the direction along which it is evaluated. For square cross-sections the dilation ratio is smaller along the diagonals than along the two transverse directions, whereas for rectangular cross-sections the dilation ratio is high if measured along the short transverse direction and along the diagonals, and low along the long transverse direction.

3. Existing semi-empirical prediction models do not yield similar predictions for the ultimate axial capacity of full-scale FRP-confined prismatic concrete columns. The increment in strength due to the FRP confinement is based on

the strength of a control concrete cylinder, f'_c, and not on concrete strength of the as-built unconfined column. The maximum stress reached by concrete in columns is only about 85% of the cylinder strength; hence, theoretical models should use $0.85 \cdot f'_c$, not just f'_c.

4. Differences in the FRP materials produced by different manufacturers do not affect performance when confining materials are of comparable quality. The contribution to column confinement of the hybrid glass-basalt FRP laminates is similar to that of the GFRP laminates.

5. Significant increases of the ductility can be achieved by confining wall-like and hollow-core rectangular R/C columns with GFRP laminates. The number of GFRP plies does not play a major role in boosting the axial strength, but gives remarkable improvements in terms of axial ductility. The failure is controlled by the shape of the cross section and determines the bulging of the FRP laminates that occurs at fiber strains far below the ultimate value guaranteed by the manufacturer.

The condition of pure axial loads is hardly found in R/C columns, which are typically subjected to compressive loads combined with bending moments that may also be produced by lateral loads. Hence, more evidence is needed to evaluate the effects of realistic loading scenarios.

NOTATION

A_g	gross area of the section
A_c	net concrete area
A_s	total area of reinforcing steel
f'_c	average compressive strength measured on cylinders
f_y	nominal steel stress at yielding
P_{peak}	maximum applied load
P_{bar}	load carried by the reinforcement
P_u	load at failure
P_u / P_{peak}	ratio between the load at failure and the maximum load
ν	Poisson's ratio of the concrete (assumed equal to 0.20)
Δ_{peak}	axial deformation when the maximum load is reached
Δ_u	ultimate axial deformation
Δ_u / Δ_{peak}	ratio between the ultimate axial deformation and the axial deformation at the maximum load
σ_c	concrete axial stress
$\sigma_{c,peak}$	concrete axial stress at the maximum load

σ_c / f'_c	normalized concrete axial stress
$\sigma_{c,peak} / f'_c$	normalized concrete axial stress at the maximum load
$\dfrac{\left(\sigma_{peak} / f'_c\right)}{\left(\sigma_{peak} / f'_c\right)_{control}}$	ratio between the normalized concrete axial stress at the maximum load and the corresponding value of the control specimen for the reference series

ACKNOWLEDGEMENTS

REFERENCES

American Concrete Institute – ACI (1963). *Building Code Requirements for Reinforced Concrete*. ACI 318-63, Detroit, Michigan (USA).

American Association of State Highway and Transportation Officials – AASHTO (1969). *Standard Specifications for Highway Bridges*. 10th ed., Washington, D.C.

Bank L.C. (2006). *Composites for Construction: Structural Design with FRP Materials*. John Wiley & Sons, New York, NY.

Bažant Z. P. (1984a). "Size Effect in Blunt Fracture: Concrete, Rock, Metal". *ASCE - Journal of Engineering Mechanics*, 110(4), 518–535.

Bažant Z. P. and Kwon Y. K. (1994). "Failure of Slender and Stocky Reinforced Concrete Columns: Tests of Size Effect". *Materials and Structures*, 27, 79–90.

Bažant Z. P. and Yavari A. (2005). "Is the Cause of Size Effect on Structural Strength Fractal or Energetic-Statistical?". *Engineering Fracture Mechanics*, 72, 1–31.

Blanks R.F. and McNamara C.C. (1935). "Mass Concrete Tests in Large Cylinders". *ACI Journal Proceedings*, Paper JL31-12, 280-303.

Campione G. and Miraglia N. (2003). "Strength and Strain Capacities of Concrete Compression Members Reinforced with FRP". *Cement and Concrete Composites*, 25, 31–41.

Carey S. A. and Harries K. A. (2005). "Axial Behavior and Modeling of Confined Small-, Medium-, and Large-Scale Circular Sections with Carbon Fiber-Reinforced Polymer Jackets". *ACI Structural Journal*, 102(4), 596–604.

De Luca A., Nardone F., Matta F., Nanni A., Lignola G. P. and Prota A. (2010a). "Structural Evaluation of Full-Scale FRP-Confined Reinforced-Concrete Columns". *ASCE - Journal of Composites for Construction*, 10.1061/ (ASCE)CC.1943-5614.0000152.

De Luca A. and Nanni A. (2010b). "Single–Parameter Methodology for the Prediction of the Stress-Strain Behavior of FRP Confined RC Square Columns". *ASCE - Journal of Composites for Construction*, 10.1061 /(ASCE)CC.1943-5614.0000152 (in press).

Fam A. Z. and Rizkalla S. H. (2001). "Confinement Model for Axially-Loaded Concrete Confined by Circular Fiber-Reinforced Polymer Tubes". *ACI Structural Journal*, 98(4), 451–461.

Fardis M. N. and Khalili H. (1982). "FRP-Encased Concrete as a Structural Material". *Magazine of Concrete Research*, 34(121), 191–202.

Harajli M. H. (2006). "Axial Stress-Strain Relationship for FRP-Confined Circular and Rectangular Concrete Columns". *Cement and Concrete Composites*, 28(10), 938–948.

Harries K. A. and Kharel G. (2002). "Behavior and Modeling of Concrete Subject to Variable Confining Pressure". *ACI Materials Journal*, 99(2), 180–189.

Hassan M. and Chaallal O. (2007). "Fiber-Reinforced Polymer Confined Rectangular Columns: Assessment of Models and Design Guidelines". *ASCE - Journal of Composites for Construction*, 104(6), 693-702.

Jiang T. and Teng J.G. (2007). "Analysis-Oriented Stress–Strain Models for FRP–Confined Concrete". *Engineering Structures*, 29, 2968-2986.

Kaw A. K. (2005). *Mechanics of Composite Materials* (Second Edition). Taylor and Francis, Boca Raton (Florida, USA).

Karbhari V. M. and Gao, Y. (1997). "Composite Jacketed Concrete under Uniaxial Compression - Verification of Simple Design Equations". *ASCE – Journal of Materials in Civil Engineering*, 9(4), 185–193.

Kumutha R., Vaidyanathan R. and Palanichamy M. S. (2007). "Behaviour of Reinforced-Concrete Rectangular Columns Strengthened using GFRP". *Cement and Concrete Composites*, 29(8), 609–615.

Kurt C. E. (1978). "Concrete-Filled Structural Plastic Columns". *ASCE – Journal of the Structural Division*, 104(1), 55–63.

Lam L. and Teng, J. G. (2003a). "Design-Oriented Stress-Strain Model for FRP-Confined Concrete". *Construction and Building Materials*, 17, 471–489.

Lam L. and Teng, J. G. (2003b). "Design-Oriented Stress-Strain Model for FRP-Confined Concrete in Rectangular Columns". *Journal of Reinforced Plastic Composites*, 22(13), 1149–1186.

Lignola G. P., Nardone F., Prota A. F., De Luca A. and Nanni, A. (2010). "Analysis of RC Hollow Columns Strengthened with GFRP". *ASCE – Journal of Composites for Construction* (submitted for possible publication).

Lyse I. and Kreidler L. (1932). "Fourth Progress Report on Column Tests at Lehigh University". *ACI - Journal of the American Concrete Institute Proceedings*, 28(1) 317-346.

Lyse I. (1933). "Fifth Report on Column Tests at Lehigh University". *ACI - Journal of the American Concrete Institute Proceedings*, 29, 433-442.

Mander J.B., Priestley M. J. N. and Park R. (1988). "Theoretical Stress-Strain Model for Confined Concrete". *ACI – Journal of Structural Engineering*, 114(8), 1804–1826.

Matthys S., Toutanji H., Audenaert K. and Taerwe L. (2005). "Axial-Load Behavior of Large-Scale Columns Confined with Fiber-Reinforced Polymer Composites". *ACI Structural Journal*, 102(2), 258–267.

Matthys S., Toutanji H. and Taerwe L. (2006). "Stress–Strain Behavior of Large-Scale Circular Columns Confined with FRP Composites". *Journal of Structural Engineering*, 132(1), 123-133.

Mirmiran A. and Shahawy M. (1997). "Behavior of Concrete Columns Confined by Fiber Composite". *Journal of Structural Engineering*, 123(5), 583–590.

Mirmiran A., Shahawy M., Samaan M., Echary H. E., Mastrapa J. C. and Pico O. (1998). "Effect of Column Parameters on FRP-Confined Concrete". *ASCE - Journal of Composites for Construction*, 2(4), 175–185.

Nanni A. (1993). "Flexural Behavior and Design of Reinforced Concrete Using FRP Rods". *Journal of Structural Engineering*, 119(11), 3344-3359.

Nanni A. and Bradford N. M. (1995). "FRP-Jacketed Concrete under Uniaxial Compression". *Construction and Building Materials*, 9(2), 115–124.

Nanni A. (2001). "Relevant Applications of FRP Composites in Concrete Structures." *Proceedings of Composites in Construction (CCC 2001)*, ed. by J Figueiras, L. Juvandes and R. Furia, Porto (Portugal), 661-670.

Nemecek J. and Bittnar Z. (2004). "Experimental Investigation and Numerical Simulation of Post-Peak Behavior and Size Effect of Reinforced-Concrete Columns". *Materials and Structures*, 37, 161- 169.

Neville A. (1996). *Properties of Concrete*. John Wiley and Sons, Inc, New York.

Pantazopoulou S. J. and Mills R. H. (1995). "Microstructural Aspects of the Mechanical Response of Plain Concrete". *ACI Materials Journal*, 92(6), 605–616.

Park R. and Paulay T. (1975). *Reinforced Concrete Structures*. John Wiley and Sons, Inc, New York (USA).

Pessiki S., Harries K. A., Kestner J., Sause R. and Ricles J. M. (2001). "The Axial Behavior of Concrete Confined with Fiber Reinforced Composite Jackets". *ASCE – Journal of Composites for Construction*, 5(4), 237-245.

Richart F.E. (1933). "Reinforced-Concrete Column Investigation". *ACI - Journal of the American Concrete Institute Proceedings*, 29(2), 275-284.

Richart F.E. and Brown R.L. (1934). *An Investigation of Reinforced-Concrete Columns*. University of Illinois Engineering Experiment Station, Bulletin No. 267, 91 pp.

Rocca S., Galati N. and Nanni A. (2006). *Experimental Evaluation of FRP Strengthening of Large-Size Reinforced-Concrete Columns*. Center for Infrastructure Engineering Studies (CIES), Report No. 06-63, University of Missouri-Rolla, Rolla (Missouri, USA).

Rocca S., Galati N. and Nanni A. (2008). "Review of Design Guidelines for FRP Confinement of Reinforced Concrete Columns of Noncircular Cross Sections". *ASCE - Journal of Composites for Construction*, 12(1), 80-92.

Saenz N. and Pantelides C. P. (2007). "Strain-Based Confinement Model for FRP-Confined Concrete". *Journal of Structural Engineering*, 133(6), 825–833.

Shehata L. A. E. M., Carneiro L. A. V. and Shehata L. C. D. (2002). "Strength of Short Concrete Columns Confined with CFRP Sheets". *Materials and Structures*, 35, 50–58.

Sim J., Park C. and Moon D. Y. (2005). "Characteristics of Basalt Fiber as a Strengthening Material for Concrete Structures". *Composites*, 36, 504-512.

Teng J. G. and Lam L. (2004). "Behavior and Modeling of Fiber-Reinforced Polymer-Confined Concrete". *Journal of Structural Engineering*, 130(11), 1713–1723.

Teng J. G., Yu T., Wong Y. L. and Dong S. L. (2007). "Hybrid FRP-Concrete-Steel Tubular Columns: Concept and Behavior". *Constructions and Building Materials*, 21(4), 846–854.

Teng J. G., Jiang T., Lam L. and Luo Y. Z. (2009). "Refinement of a Design-Oriented Stress–Strain Model for FRP-Confined Concrete". *ASCE – Journal of Composites for Construction*, 13(4), 269-278.

Toutanji H., Han M., Gilbert J. and Matthys S. (2010). "Behavior of Large-Scale Rectangular Columns Confined with FRP Composites". *ASCE - Journal of Composites for Construction*, 14(1), 62-71.

Wang Y. C.and Restrepo J. I. (2001). "Investigation of Concentrically-Loaded Reinforced-Concrete Columns Confined with Glass Fiber-Reinforced Polymer Jackets". *ACI Structural Journal*, 98(3), 377–385.

Wu Y. F. and Wang L. M. (2009). "Unified Strength Model for Square and Circular Concrete Columns Confined by External Jacket". *ASCE – Journal of Composites for Construction*, 135(3), 253-261.

Wu H. L., Wang Y. F., Yu L. and Li X. R. (2009). "Experimental and Computational Studies on High-Strength Concrete Circular Columns Confined by Aramid Fiber-Reinforced Polymer Sheets". *ASCE – Journal of Composites for Construction*, 13(2), 125-134.

ASSESSMENT OF CONCRETE STRUCTURES AFFECTED BY COVER DELAMINATION PART 2 : BOND-SHEAR INTERACTION

Paul E. Regan [1] , Iain L. Kennedy Reid [2]

ABSTRACT

Tests are reported of beams with main bars either exposed to mid-barrel (i.e. with only half the lateral surface bonded to the concrete) or flush with the concrete surface, in all or parts of their spans, to simulate the effects of delamination induced by corrosion. Assessment of ultimate load capacities in such circumstances, where bond and anchorage are critical, depends on the modelling of internal behaviour and the estimation of bond strengths. Relevant models are developed here and used with limiting bond stresses derived previously in a companion paper, to provide estimates of ultimate loads, which are shown to agree satisfactorily with experimental values.

[1] Professor, formerly Head of the Architecture and Engineering Dept. at the University of Westminster, London, UK.
[2] Atkins Highways and Transportation, London, UK.

1. INTRODUCTION

A previous paper (Regan and Kennedy Reid, 2009) has reported research on the assessment of reinforced concrete affected by delamination of cover due to corrosion of reinforcement. The topics included were (a) the bond strengths of bars with cover affected by delamination, (b) the resistance to shear cracking and (c) the performance of beams with the bond completely lost along a sizeable part of the span.
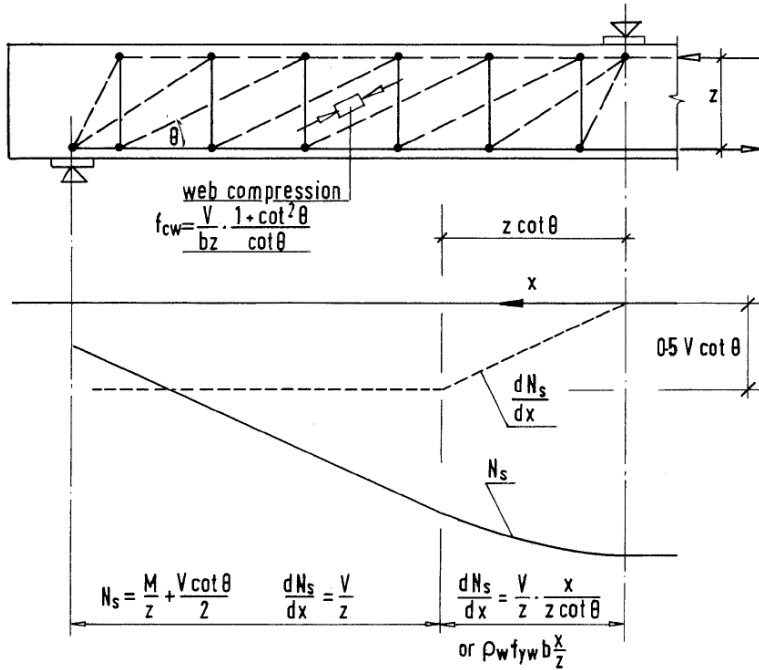

Figure 1 – Typical truss model. Limits for $\cot\theta$: $1 \leq \cot\theta \leq 2.5$ (EC2) or 3.0 (MC90). Limit ofr f_{cw}: $f_{cw} \leq 0.48\ f_{cu}\ (1- f_{cu}/300)$. Characteristic shear resistance (assuming yield of stirrups) = $\rho\ f_{yw}\ b\ z\ \cot\theta$. Note that in flanged beams b is replaced by b_w.

   The tests reported in the present paper were of the same type as most of the earlier work, in the sense that delamination was simulated by casting concrete either to mid-barrel level of the main bars or so that the bars were flush with the concrete surface. The present beams are more complex in two respects. The influence of shear and bond resistance interact in them, and the main steel includes bars in different situations acting together at the sections of maximum moment.

The differences concern the length and the restraints provided by stirrups and/or transverse pressure.

Circumstances such as these require the use of structural models of member behaviour and this paper illustrates the use of truss models in combination with the recommendations of the previous paper for limiting bond stresses. The results obtained are compared with the experimental strengths of the beams. The basic form of truss from which variants are derived is illustrated by Fig 1.

2. SUMMARY OF RECOMMENDATIONS FROM REGAN AND KENNEDY REID, 2009

2.1 Limiting bond stresses for Type 2 deformed bars

Bond stresses for ULS design (= rate of change of bar force/ $\pi\phi$) are:

- For bars with normal cover

$$f_{b1} = 0.7 \sqrt{f_{cu}} \tag{1}$$

- For bars flush with the surface of sound concrete

$$f_{b2} = (0.3 + 15\ A_{ss}/s\phi) \sqrt{f_{cu}} \le 0.7 \sqrt{f_{cu}} \tag{2}$$

or $\quad f_{b3} = 0.6 \sqrt{f_{cu}} + 2p \le 0.7 \sqrt{f_{cu}} \tag{3}$

- For bars in concrete delaminated to mid-barrel level

$$f_{b4} = (0.1 + 15\ A_{ss}/s\phi) \sqrt{f_{cu}} \le 0.7 \sqrt{f_{cu}} \tag{4}$$

or $\quad f_{b5} = 0.25 \sqrt{f_{cu}} + p \le 0.7 \sqrt{f_{cu}} \tag{5}$

A_{ss} = effective area of a link restraining a main bar (see Fig. 2)

$s\quad$ = spacing of links along a main bar

$\phi\quad$ = diameter of main bar

$p\quad$ = transverse pressure (pressure normal to surface of delamination) $\ge 0.05 \sqrt{f_{cu}}$

These bond stresses may be treated as plastic except that the 0.1 from Eq. (4) for Ass/s = 0, should not be used in combination with other values of fb. Either all bars should be treated as having a bond resistance of 0.1 , or the bars with Ass/s = 0, should be discounted except in lengths where p $\ge$ 0.05 .

2.2 Reduction of shear cracking resistance due to delamination

The delamination of cover and the consequent reduction of bond of the main steel can reduce a member's resistance to shear cracking. The reduced characteristic resistance can be estimated as

$$Vk,red = 0.19 \sqrt[3]{f_{cu} \cdot 100A_s / bd} \quad \sqrt[4]{500 / d} \qquad (6)$$

with d in mm.

Shear cracking is unlikely if the bond strength is very low, i.e. if

$$\sum fb\, u \leq \frac{V_{k,red}}{z} \qquad (7)$$

where u is the perimeter of a bar.
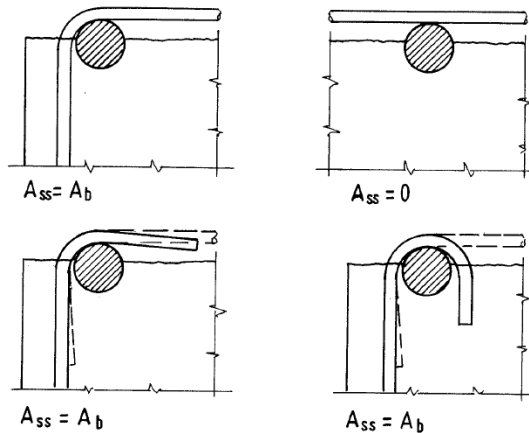
Figure 2 – Assessment of the effective area A_{ss} of a link restraining a main bar; A_b is the area of a stirrup leg. Bars shown by broken lines are required at corner main bars.

3. SERIES "F" - CANTILEVER BEAMS WITH DISTRIBUTED LOADS

The tests of Series F were made to study the behaviour of combinations of main steel in which some bars were restrained by transverse pressure from loads and others were unrestrained.

The beams cantilevered either side of a central support. The shorter cantilever was subjected to four concentrated forces, which simulated uniform loading and provided the restraints to main bars. The longer cantilever was simply a tie-down arrangement. Details of the beams are shown in Figure 3.
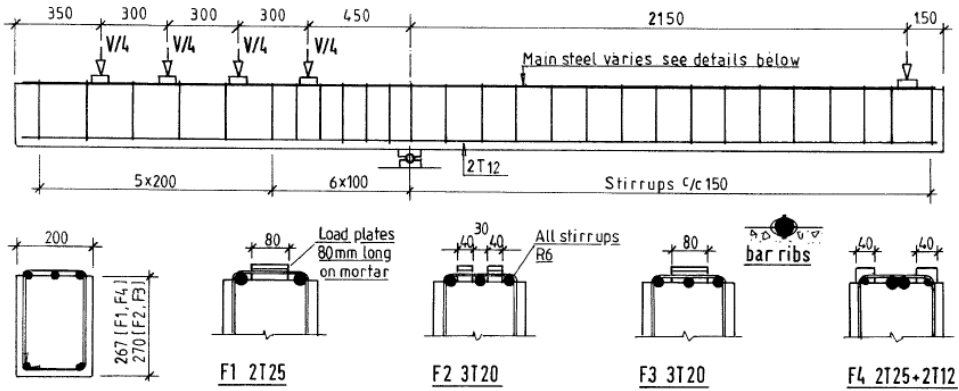
Figure 3 – Example of cantilever beam (top); and different modes to simulate the delamination of the cover (bottom).

In Beam F1 the two main bars run outside the loading plates avoiding any clamping action by the loads. In the critical cantilever, two flexure-shear cracks developed fully - one from the section of the innermost load and one from midway between this and the support. Mean bond stresses over the three lengths A, B and C shown in Figure 4 were determined from strain measurements and their evolutions are plotted in the same figure.

At low loads the bond was highest in length C nearest to the support, lower in the next length B and very small in the length A near the beam end. At high loads the bond in C peaked and then reduced, that in B continued to increase steadily and that in A rose at a rapidly increasing rate. At failure the bond was practically uniform from the outer shear crack to the beam end.

The failure was a bond failure running all the way from the shear crack closest to the support to the ends of the bars.

Beam F2 had three main bars, two of which were in stirrup corners and none of which was clamped by loads. The strain-gauged sections were increased by one at the support and the average bond stresses for the four lengths are shown with the crack pattern in Fig 5. For the additional length D , the bond was assumed to be concentrated in the outer 3/4 of the length, i.e. f_b - $4\Delta N/31\sum u$.

There is a clear difference between the centre bar and the bars in the stirrup corners. The behaviour of the bars in the stirrups is similar to that of beam F1, while the bond stresses of the middle bar are much lower. For the middle bar the maximum force at the support peaked at a load of 72 kN and had decreased by 50% at the failure load of 94 kN.
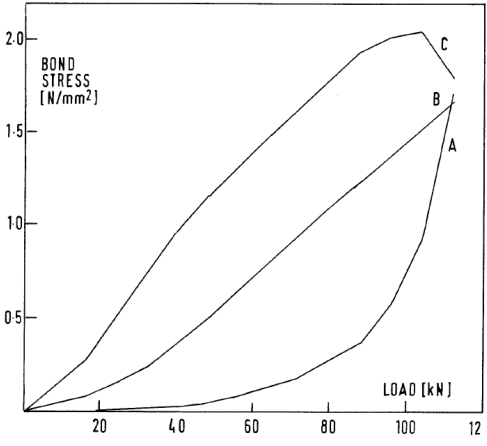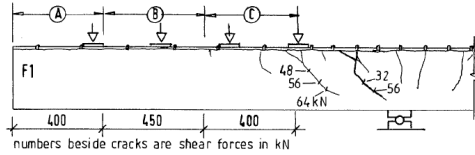
Figure 4 – Beam F1: Evolution of the mean bond stress in the zones A, B and C, as a function of the load level.
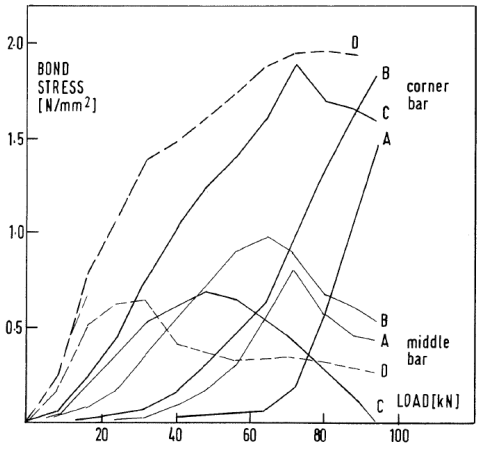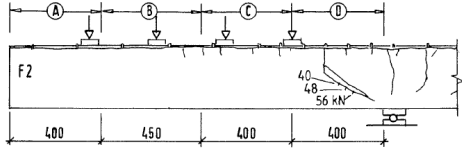

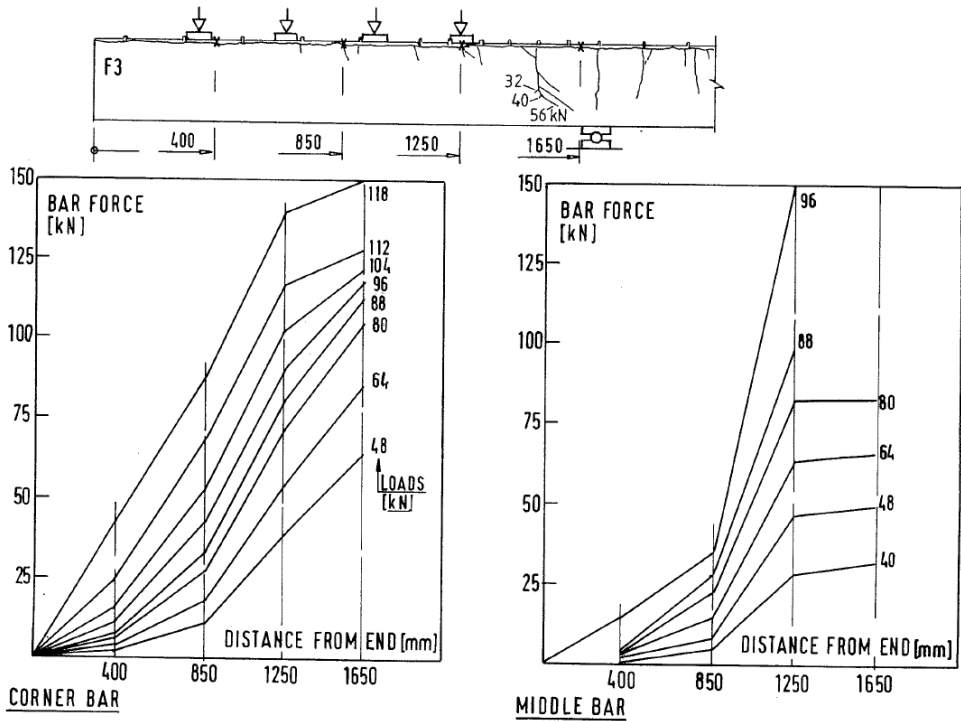Figure 5 - Beam F2: Evolution of the mean bond stress in the zones A, B,C and D, as a function of the load level

Figure 6 – Beam F3: Crack pattern (top); plots of the forces in the corner bars (left); and in the middle bars (right).

The failure was by rotation at the flexure-shear crack, with slip of the middle bar and the outer bar without gauges and yield of the gauged outer bar. The end slip of the middle bar was 4 mm when the ultimate load was reached.

Beam F3 was similar to F2 but with the loads applied over widths that included the middle bar. The side face cracking was very similar to that of F2. In Fig.6 the plots of the forces in the middle bar and one corner bar are shown. The presentation for the middle bar is not ideal as the large change of bar force between 850 and 1250 mm from the end, was not distributed but concentrated to the loading points. Beyond the load closest to the support, the middle bar showed practically no bond and the tensile force was almost fully anchored by the section 850 mm from the beam end, showing that the clamping forces provided a bond more effective than that obtained from the stirrups. The ultimate load of 118 kN was 25% above that of beam F2. The ultimate moment at the support was equal to the flexural capacity, although the outer bar without gauges probably slipped without yielding.

Beam F4 contained a pair of 25 mm bars not in stirrup corners and not below the load plates and two 12 mm bars in the stirrup comers but embedded to a depth

less than $\phi/2$. These outer bars were below the load plates. The cracking of the shear span was very limited.

At low loads, the maximum strains were similar for the corner and middle bars. At later stages the clamped corner bars were more highly strained and yielded in the process of failure although not until the maximum load had been passed. As in beam F2, the bond stresses of the middle bars were initially highest near the support but decreased before failure, while the stresses toward the beam end increased rapidly. The redistribution of this bond was however less pronounced than in F2. The corner bars were very poorly anchored in the concrete except at loads, but the anchorage provided by the transverse pressure at the loads allowed them to yield while at their outer ends they were just in compression.

Failure occurred because (a) of a rotation in a crack by the support, (b) full-length slip of the inner bars and (c) of the yielding of the corner bars under decreasing load.

In an assessment of these beams, the first issue is whether or not shear cracking should be expected. In view of the major delamination, the resistance to flexure-shear cracking can be estimated by equation (6). Shear cracking should however be avoided if $\sum uf_b z$ for the region in question is below $V_{k,red}$. The calculations are summarised in Table 1. Exact shear cracking loads are difficult to define but a value of $V = 56$ kN would be reasonable for Beams F1 to F3 (see Figs 3-5) and the predicted shears are from 93 to 99% of it. F4 is correctly predicted to suffer no shear cracking.

In the absence of shear cracking, the ultimate main steel force of Beam F4 is predicted as the greater of the forces corresponding to:

i)   zero force in the middle bars and the maximum resistance given by equation (4) $\leq F_y$ for the outer bars.

ii) forces in all bars corresponding to stresses given by equation (4) for the middle bars, i.e. $f_{b1} = 0.1\sqrt{f_{cu}}$.

The latter is the higher and gives $N_s = 274$ kN and $V_{calc} = 75$ kN, which is 94% of the actual ultimate moment.

Models for the other beams are given in Fig 7. The internal actions are shown in detail for the region close to the supports. Beyond the lengths with shear cracks, the thrust lines in the concrete follow whatever shape is required to maintain equilibrium between the applied moment M and the product $N_s z$ with the steel force defined by the conditions of bond. In the transition zone between the fan and the second load, there may or may not be shear cracks but this is of no importance as the limit bond stresses apply in any case and the applied shear reduces after the first load.

The length z cot θ of the zone close to the support, within which the web compression radiates, is governed by the bond force required by the truss action reaching the bond capacity of the main bars. Assuming the stirrups to yield, for truss action:
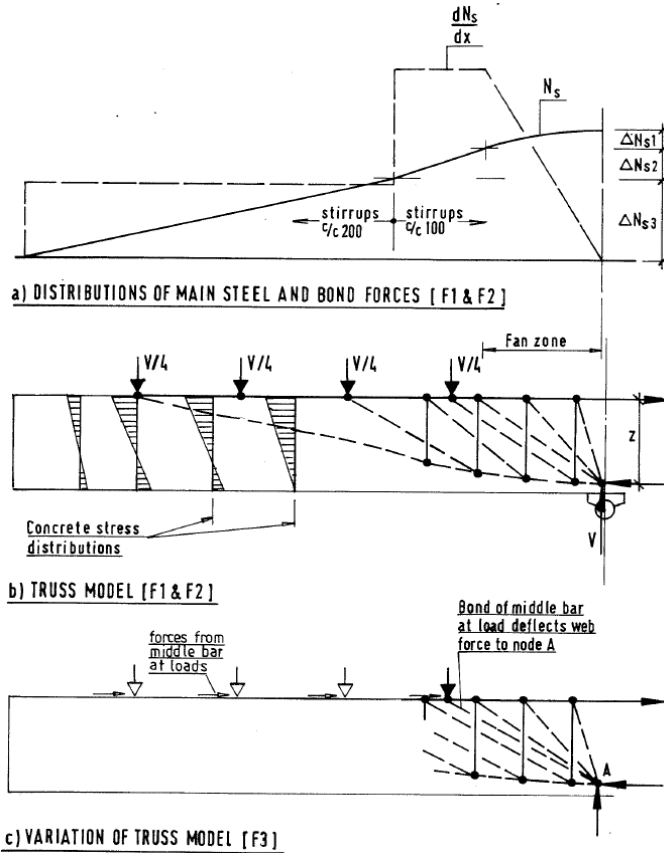

Figure 7 – Distributions of main steel and bond forces in Beams F1 and F2 (a); and truss models (b, c).

$$\rho_w f_{yw} \, b \, z \cot \theta = V \tag{8}$$

$$\cot \theta = V / \rho_w f_{yw} \, b \, z \tag{9}$$

The bond capacity of the main is $\sum f_b \, u$ and is equal to V/z.
  Substituting for V/z in equation (9):

$$\cot \theta = \sum f_b u / (b \, \rho_w f_{yw)} \tag{10}$$

Using the uls flexural value for z, the distance x to the end of the fan zone is:

$$x = z \cot \theta \qquad (11)$$

and within this length the change of main steel force is:

$$\Delta N_{s1} = \rho_w f_{yw} b \frac{x^2}{2z} \qquad (12)$$

The above derivation of cot θ is subject to two limits, one corresponding to failure of the web concrete and the other an overall upper limit related to compatibility of the truss model. These are given in Fig 1.

The length with stirrups at 100 mm centres beyond 'x' is (605-x) mm and induces a change of the steel force

$$\Delta N_{s2} = (605-x) \sum f_b u \qquad (13)$$

Beyond this there is a further bar length of 1050 mm contributing

$$\Delta N_{s3} = 1050 \sum f_b u \qquad (14)$$

with f_b lower than in equation (13) as the stirrups spacing is 200 mm.

For beams F1 and F2, the summations $\sum f_b u$ above are for the corner bars. In F1 they were the only bars, and in F2 a higher bond resistance is obtained by considering the corner bars along with their full f_b, than by considering all three bars at $f_b = 0.1 \sqrt{f_{cu}}$.

The total steel forces at the sections of maximum moment in these beams are:

$$\sum N_s = \Delta N_{s1} + \Delta N_{s2} + \Delta N_{s3} \qquad (15)$$

$$M_{calc} = z \sum N_s \qquad (16)$$

$$V_{calc} = M_{calc} / 0.885 \qquad (17)$$

the 0.885 being in m.

In beam F3, the anchorage of the middle bar depended on the transverse pressure from the loads. The outer bars are predicted to behave as in F2 and to develop a force 1 kN lower than in F2 because of the slightly lower concrete strength. Each load plate was 80 x 80 mm and exerted a transverse pressure p = 0.039V (p in N/mm^2 for V in kN)

From equation (5):

$$f_b = 0.25 \sqrt{f_{cu}} + 0.039V$$

and the total force that can be anchored by the four loads is:

N = 33 + 0784V kN.

Then adding the forces in the three bars, the maximum possible main steel force becomes:

$$\sum N_s = 327 + 0.784V, \text{ and } V = (327 + 0.784) \ \frac{z}{0.885}$$

With   z = 0.242 m, V = 89.5 + 0.214 V, V= 114kN

The calculations for all four beams are summarised in Table 2, which also compares the calculated strengths with the experimental ultimate loads. The ratios V_{cal}/V_u vary from 0.85 to 1.00.

4. SERIES "B" - CANTILEVER BEAMS WITH END LOADS

In the beams of Series B the concrete surfaces were cast flush with the main bars, and the beams were tested as double cantilevers with a central support and the loads near the ends. Beam details are given in Figure 8. Variables were the detailing of the main steel, the diameters of the stirrups and the position of the loading plates relative to the central bars. The crack patterns of the four beams are drawn in Fig.9.

In Beam B1 a crack, which became progressively more inclined, formed at the section where the central bar was curtailed. Inclined extensions of flexural cracks nearer the support formed later. Failure occurred in the bond of the central bar, over the whole of its length, and in the bond of the outer bars, along the length from the section of curtailment to the end of the beam. The force in the central bar at the section of maximum moment was monitored by a pair of strain gauges and reached its maximum at 77% of the ultimate load after which it decreased 25% by the ultimate load.

The inner bars of Beam B2 were curtailed further from the support than the bar in B1. The first inclined crack occurred from the section of curtailment and was followed by additional shear cracks closer to the support. Failure was in the bond of the outer bars along the length from the curtailment to the beam end. Diagonal cracking was visible on the top surface as a sign of bond distress of the inner bars but their forces at the section of maximum moment reached a peak at the maximum load and declined only as the load decreased with further deflection.

In beam B3 all four bars continued to the beam end and the inner bars were clamped by the loading plate. The stirrup size was also increased from 8 to 10 mm. The first inclined cracking was fairly close to the support, but shear cracking of most of the span followed soon after.

There was diagonal cracking on the top surface running between the inner and outer bars, but with the more favourable detailing of the main steel and the
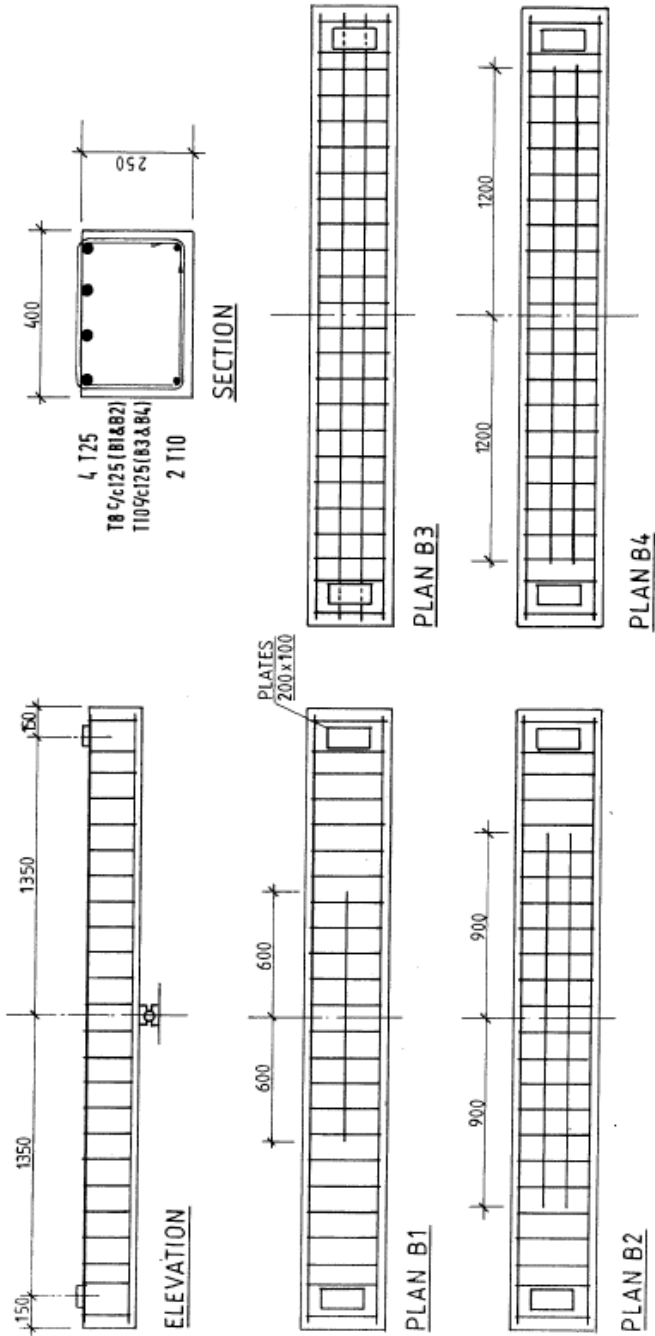
Fig.8 – Tests Series B: Details of the specimen loaded close to the end sections.
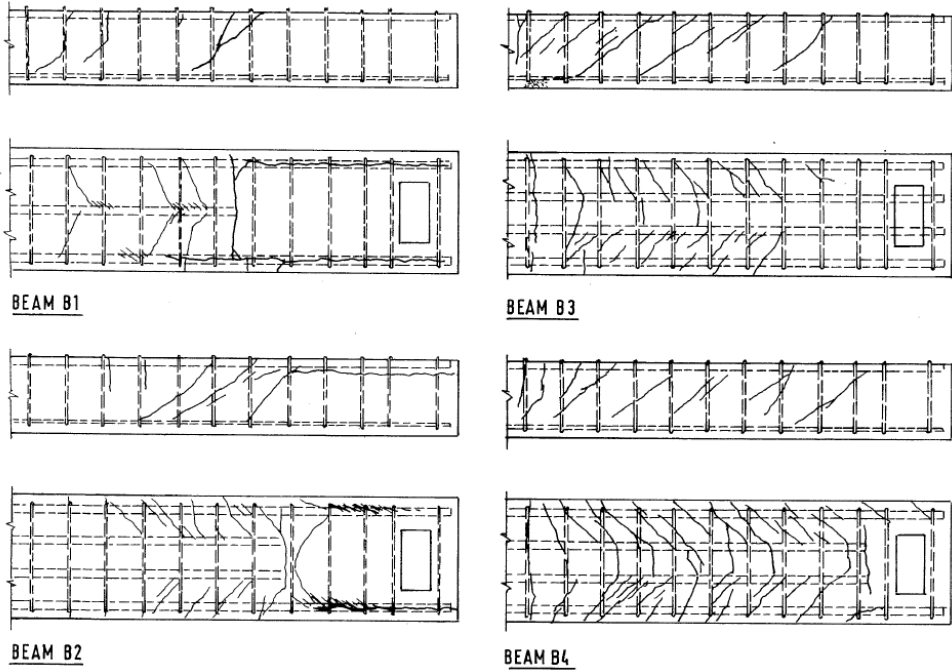
Figure 9 - Tests Series B: Crack patterns of the four beams.B

increased shear reinforcement, the failure was in flexure, with all four bars yielding at midspan. The stresses of the inner bars just before the load plate were only 120 to 140 N/mm^2, showing that considerable bond existing along their lengths.

Beam B4 was similar to B3 except that the inner bars were curtailed just inside the loading plates. Inclined cracking began at the section of curtailment and shear cracks were developed throughout the span. The cracking on the top surface prior to failures was similar to that in B3.

Failure was initiated by distress in the bond of the inner bars. The forces in these bars reached a maximum just before the ultimate load and then decreased. To compensate the forces of the outer bars, the forces in the internal bars increased rapidly and the bars yielded. Their end anchorages had begun to develop longitudinal cracks but did not fail.

Shear cracking loads calculated by means of equation (6) are given in table 3b. They agree well with the experimental values for beams B1 and B2 but are conservative for B3 and B4. The main reason for this is probably that in B4 the curtailed bars were so long that the calculated resistance, dependent on the reduced ρ_1 was not really relevant. In B3 there was no curtailment.

The behaviour of these beams can be represented by the truss models of Fig 10. The truss shown on elevation can be used to determine the inclination of the web

compression and the distribution of the total tension of the top chord. It is supplemented by the plan truss of the middle drawing in order to allow for the effects of the relatively wide spacing of the bars and the fact that the stirrup forces act only at the outer bars. Failure can be predicted to occur either at the section of curtailment or at the section of maximum moment.
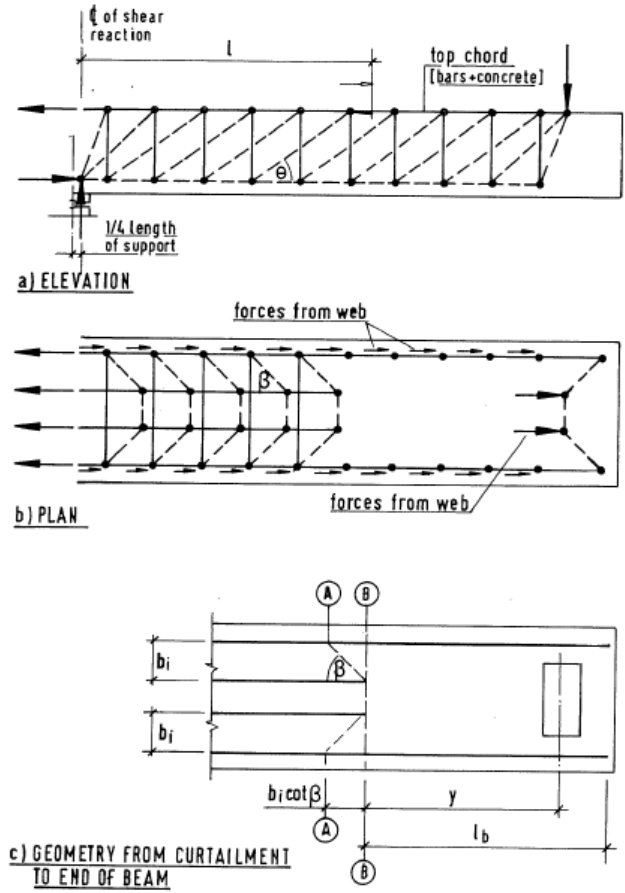

Figure 10 – Truss model for Beams B1-B4.

Near the section of curtailment, anchorage failure of the continuing bars can occur at either of sections AA and BB in Fig l0c:

$$N_{sA} = V\left[\frac{y + b_i \cot\beta}{z} + \frac{\cot\theta}{2}\right]$$ 18)

$$N_{sB} = V \left[\frac{y}{z} + \frac{\cot\theta}{2} \right] \qquad (19)$$

The corresponding resistance, for two bars, in stirrup corners are:

$$N_{RsA} = 2\pi\phi \ (l_b + b_i \cot\theta) \qquad (20)$$

$$N_{RsB} = 2\pi\phi \ f_b \ l_b \qquad (21)$$

The predicted resistance to failure at the curtailment is the lesser than the value given by the following expression:

$$V_l = \frac{2\pi\varphi f_b (l_b + b_1 \cot\beta)}{(y + b_1 \cot\beta)/z + 0.5\cot\theta} \qquad (22)$$

and
$$V_l = \frac{2\pi\varphi f_b l_b}{(y/z + 0.5\cot\beta)} \qquad (23)$$

where z can be obtained iteratively as a function of the load or taken conservatively as the flexural value at the ULS. In either case it is the lever arm at the section of maximum moment, as the truss is drawn with parallel chords. For the present analysis, z has been taken as 200 mm, which is just above the flexural value. $\cot\beta$ is taken at 1.0.

Cotθ can be determined by simultaneous solution of equation (22) or (23) with $V = \rho_w f_{yw} bz \cot\theta$ to give a predicted resistance V_1 to bond failure from the section of curtailment (not applicable to beam B3). The differences between the results obtained using equation (22) or (23) are small.

A bond failure will occur from the section of curtailment only if the load corresponding to bond failure from the section of maximum moment is higher.

In considering the latter type of failure, the forces in the short bars are maximised by maximising the rates of change close to the support. The lengths x' from where the forces in the inner bar begin to change to where the rate of change reaches its maximum corresponding to f_b is as follows:

$$x' = n \pi \phi \ f_b \ (z/\rho_w f_{yw} b) \qquad (24)$$

where n is the number of inner bars

With uniform bond along the remainder of the length, the maximum force developed by the inner bar is

$$N_i = n\pi\phi \ f_b \ [1 - b_i \cot\beta - 0.5x'] \le A_{si}f_y \qquad (25)$$

where l is the length from the section of maximum moment to the bar end.

The force that can be developed by the outer bars is equal to their force at the section of curtailment. $N_{sc} = 2\pi\phi\ f_b l_b$ plus the total change of main steel force from the section of maximum moment to that of curtailment $\Delta N_s = Vl/z - 0.5V \cot\theta$, minus the force N_i going to the inner bars

$$N_{so,max} = N_{sc} + Vl/z - 0.5V \cot\theta - N_i \le A_{sc}f_y \qquad (26)$$

In evaluating ΔN_s, V can be taken as V_l. The total steel force at the section of maximum moment is then

$$\Sigma N_s = N_{so,max} + N_i \qquad (27)$$

$$M_{calc} = z\ \Sigma N_s \qquad (28)$$

and $V_2 = M_{calc}\ /1.325m \qquad (29)$

The predicted failure load is the lesser of V_1, and V_2.

Such calculations for beams B 1, B2 and B4 are summarised in Table 3 and give calculated loads which are from 85% to 98% of the experimental values.

For beam B3, with no curtailment and with the inner bars clamped by the loading plates, the calculations are simpler.

Ignoring the extension of the inner bars beyond the load plates, their bonded length is 1.375m and n $\pi\phi\ f_b l$ = 399 kN. The pressure at the loading plates is $0.05V$ in N/mm^2 if V is in kN, and the additional bond resistance from equation (3) is $0\ 3\sqrt{f_{cu}} + 0.1\ V\ N/mm^2$. It acts on a surface area 2π x 25 x 100 mm^2 and gives an additional resistance of $29 + 1.571\ V_{kw}$.

For the outer bars $n\pi\phi\ f_b$ = 655 kN, but the truss action does not allow a uniform bond and $0.5V \cot\theta$ must be subtracted (see Fig 1). The ultimate load can be calculated directly if $\cot\theta$ is expressed in terms of V, but a trial and error approach can be simpler. The calculated flexural capacity is V_{flex}= 163 kN and for this $\cot\theta = V/\rho_w f_{yw} bz$ = 1.24.

The maximum main steel force that can be developed at the section of maximum moment is then N = 428 + 1.571V + 901 = 0.62V. If V = 163 kN, N = 1484 kN as compared with the yield force of 1080 kN. Thus no bond failure is to be expected and flexural failure is predicted at a load of 163 kN which is 94% of the experimental ultimate load of 173 kN.

5. SERIES "C" - RESTRAINED BEAMS

The details of the beams of Series C are shown in Fig 11. In the critical region between the interior load and the interior support, the positive moment at the load and the negative moment at the support were equal and the detailing of the top and bottom bars was similar but anti-symmetrical. In each set of tension steel, the two

inner bars were curtailed before the central section of contraflexure and the two outer bars extended beyond it. Both the top and bottom bars were exposed to mid-barrel throughout the lengths from the sections of maximum moment to the further away sections of curtailment.

The variables in the series were the beam depth, and thence the maximum M/Vd which was 2.43 for C1 and 3.33 for the other beams, the detailing of the shear reinforcement and the orientation of the bar ribs relative to the concrete surface. These details are shown in Fig 11. The concrete strength also varied considerably.
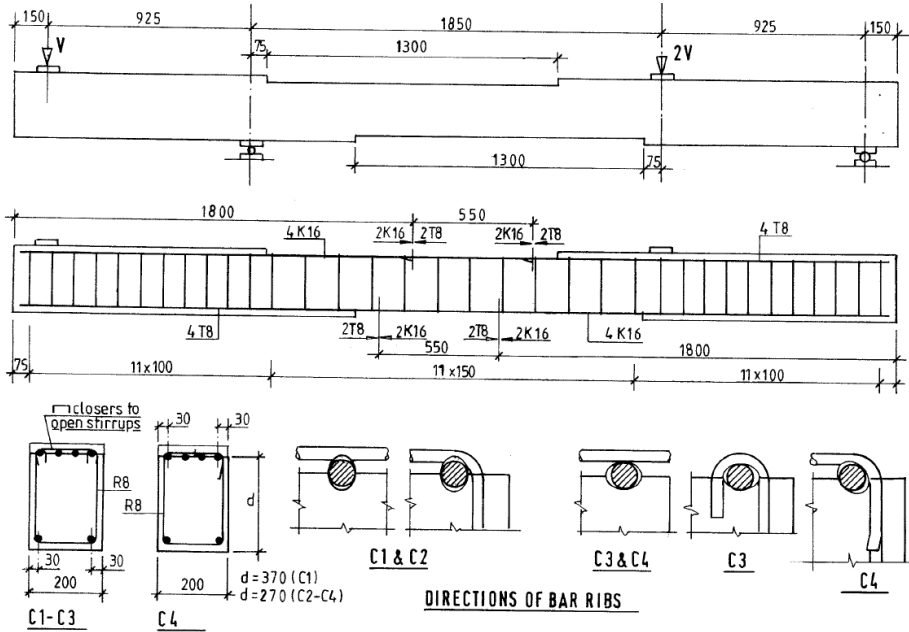

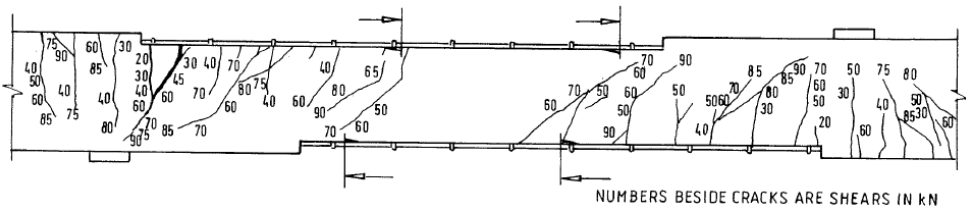Figure 11 – Tests Series C: details of the specimens.

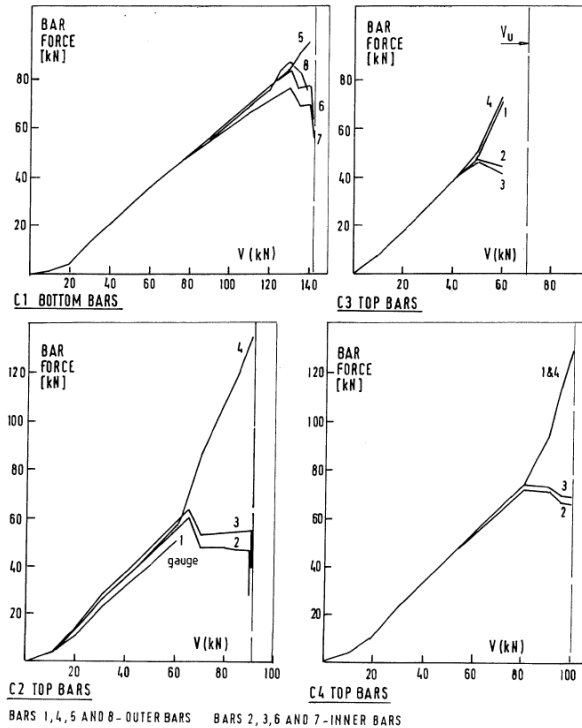Figure 12 - Tests Series C: crack pattern of Beam C2.

117

Figure 13 - Tests Series C: plots of the forces in the top (a) and bottom bars (b-d).

All beams developed patterns of flexural and shear cracks similar to that of beam C2, which is drawn in Fig 12. In no case was there any cracking in the region of contraflexure.

At both sections of maximum moment the strains of each of the four main bars was measured using a pair of horizontal gauges at opposite ends of a horizontal diameter. Bar forces calculated from these strains are plotted in Fig 13 for the steel (top or bottom) involved in the failure. AH eight bars were strained similarly at stages up to and beyond shear cracking. Close to failure, the strains of the inner (shorter) top bars of beams C2 to C4 peaked and then decreased gradually with increasing load. The last strains measured in these bars, other than during the process of failure, were from 82% to 93% of their maximum values. In C2 and C4, failure occurred when the outer bars yielded and allowed rotation at steeply inclined cracks near the support. In C3, where the concrete strength was much lower than in the outer beams, the longer bars did not yield but their anchorages failed.

In beams C2 and C4 the strains of all the bottom bars continued to increase up to failure. In beam C1 there were decreases of strain in all four inner bars and also in one outer bottom bar. The failure of C1 was by the anchorage of the bottom bars.

The details of the stirrups and the directions of the main bars' ribs do not seem to have had any great influence on the beams' behaviour, which was clearly more affected by concrete strength.
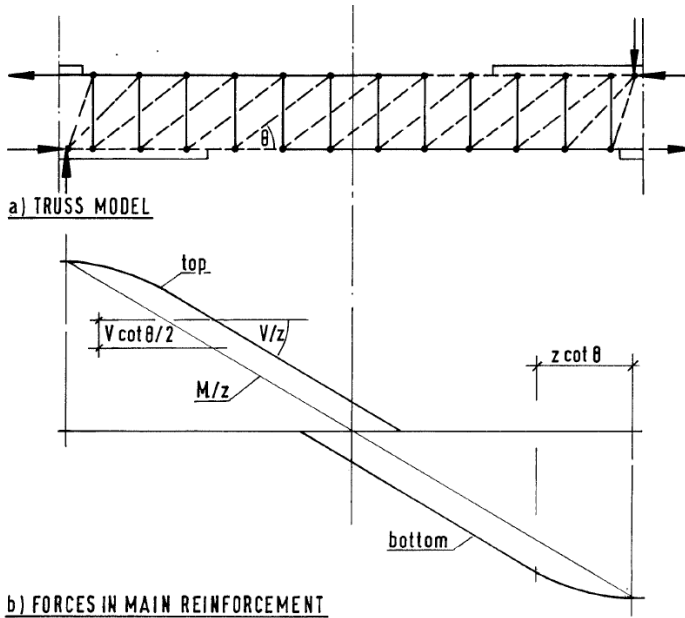

Figure 14 – Truss model for the beams of Series C.

A truss model is shown in Fig 14. As the tension in both the top and bottom bars extend beyond the sections where the inner bars are curtailed, the capacity as limited by bond is defined very simply by equating $\Sigma f_b \pi \phi$ for the longer (outer bars) to V/z. According to the recommendations made, the inner bars' bond must be discounted if the full value of f_b is to be used for the outer bars. The solution for V is limited by the yield of the outer bars. The results obtained are given in table 4, and the calculated strengths are low in relation to the experimental ones, with V_{calc} from 75 to 80% of V_u.

This result is probably acceptable, and it would be difficult to improve upon it without considerable complications. To effect an improvement would require two things. First the structural model would have to be modified to take account of the lack of shear cracking near the section of contraflexure. Secondly account would have to be taken of some residual post-peak bond of the inner bars, which clearly did make a contribution here but might not do so in somewhat wider members, in which the inner bars really would be without restraint from stirrups.

6. SERIES "T" - SIMPLY SUPPORTED T-BEAMS

Two T-beams were tested with the main reinforcement partially exposed in one shear span. As shown in Fig 15 the main steel was two vertical pairs of bars. In Beam T1 the lower bars, which continued to the support were exposed to mid-barrel, while the upper (curtailed) bars were fully embedded. In Beam T2 the "delamination" was continued upward to the curtailed bars.

In the initial tests of both beams, loads were applied at 1/3 points of the span. Following failures in the shear spans in which bars were exposed, the beams were retested with the support at the exposed end moved in to a position below what had been a loading point, and with a single load applied at the centre of the reduced span of 1.866m.
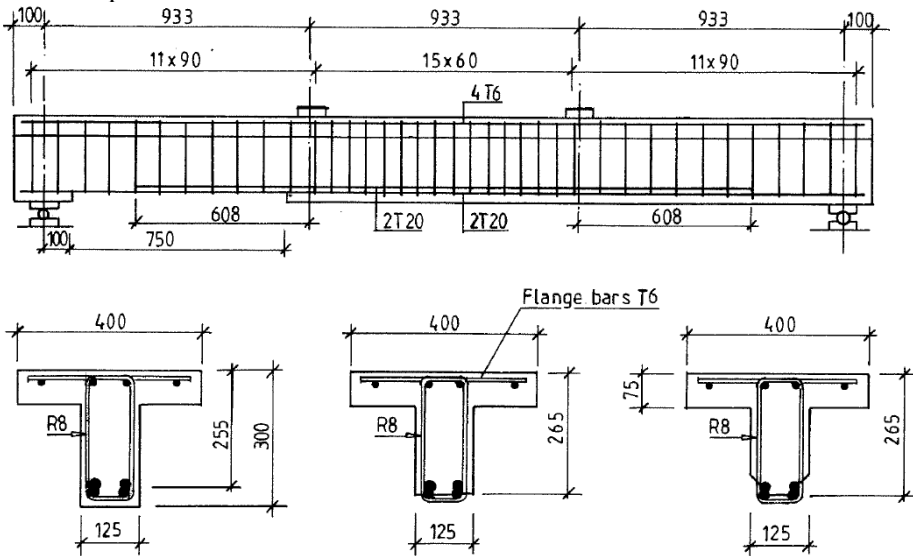

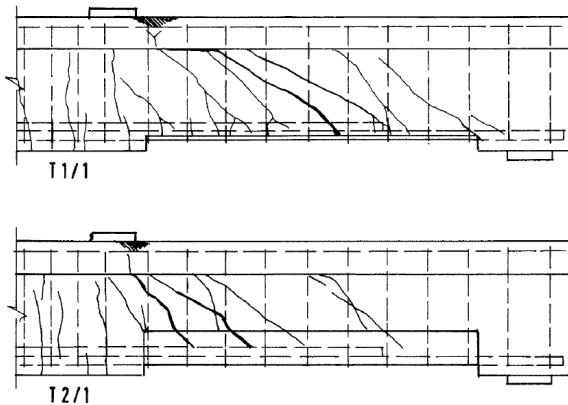Figure 15 – Test Series T: details of the reinforcement.

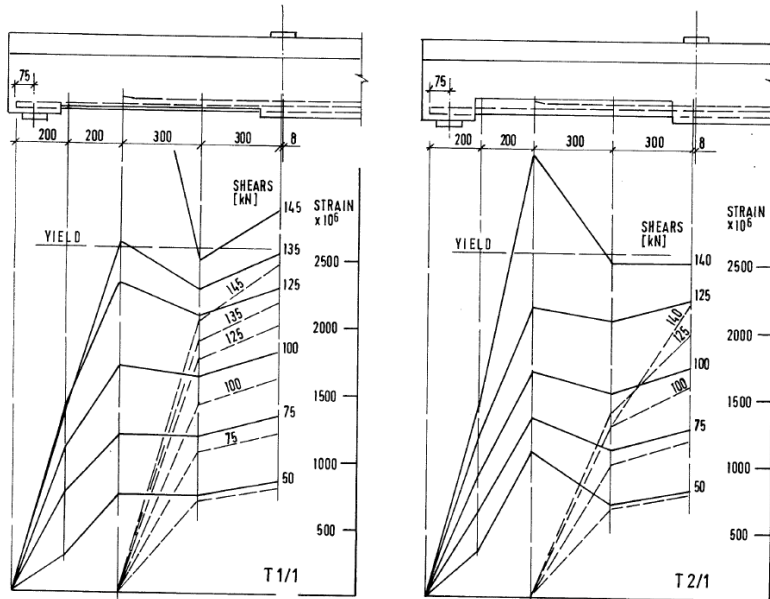Figure 16 – Crack patterns in tests T1/1 and T1/2.

Figure 17 – Plots of the main steel strains in beams T1/1 and T1/2.

The results of the four tests are summarised in Table 5 and it can be seen that the reductions of strength due to exposure were very small.

In test T1/1 the failure was by rotation at a shear crack which reached more or less to the ends of the curtailed bars. The non-curtailed bars yielded at the section of curtailment. In T2/1, with the greater exposure, the anchorages of the curtailed bars began to slip and large rotations occurred in shear cracks closer to the load. The final crack patterns from these two tests are shown in Fig 16.

In the second tests, the shear spans with no bar exposure underwent ordinary shear failures, which were probably affected by the curtailments.

Most of the stirrups had yielded by failure in all the tests, the only major exception being for those near the support of the exposed span of Beam 2, where there was no cracking - see Fig 16.

Distributions of main steel strains at stages close to failure are plotted in Fig 17, where it can be seen that the bond stresses of the curtailed bars increased throughout test T 1/1 but reduced a little just before failure in T2/1. There is no indication of bond failures of the lower (more exposed) bars, which were anchored at the beam ends where they had cover and transverse pressure from the supports.

The behaviour of these beams can be modelled as in Fig 18. If bond were not a problem, failure would be yielding of the longer main bars at the section of curtailment and consequent rotation at an inclined crack at which the stirrups would yield.

325

z cot θ

M/z

$\dfrac{V \cot \theta}{2}$

TRUSS MODEL AND MAIN STEEL FORCE

l = 608

dN /dx for
upper bars
eqn (35)

As fy for
long bars

Max dNs/dx for
curtailed bars

y

DIVISION OF MAIN STEEL FORCE BETWEEN
LONG AND CURTAILED BARS

Figure 18 – Truss model for the beams of series T.
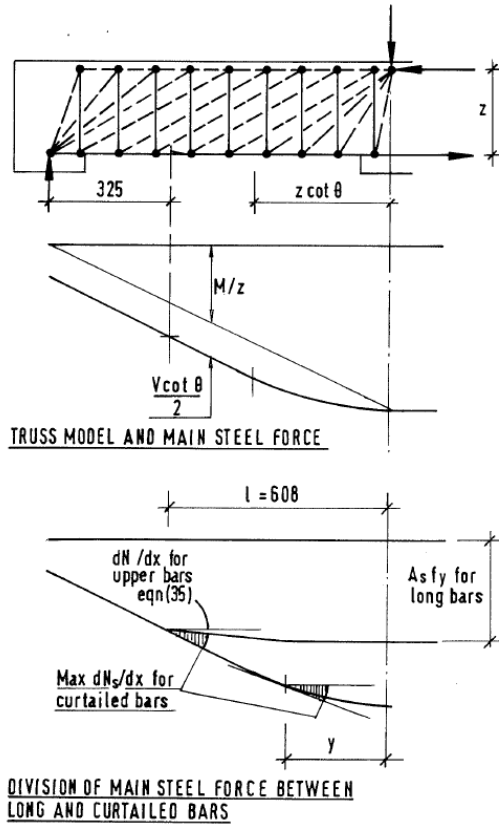
At the curtailment:

$$N_s = \frac{M}{z} + \frac{V \cot \theta}{2} = \frac{0.325V}{z} + \frac{V \cot \theta}{2} \tag{30}$$

while

$$V = \rho_w f_{yw} b_w z \, \cot \theta \tag{31}$$

Combining these equations gives:

$$V_1^2 + 0.65 \, \rho_w f_{yw} b_w \, V_1 - 2 \, \rho_w f_{yw} b_w z \, N_{sy} = 0 \tag{32}$$

where N_{sy} is the capacity of the longer bars at yield.

In the present case the bond capacity of the lower bars is marginally below V_l/z, which in principle affects the truss action between the curtailment and the support. However the deficit is small and the bars are well anchored at their ends so that very minor arching by the main thrust should remove any problem.

What is more of an issue is the bond in the length to the load side of the curtailment, where the rate of change of force in the main steel is required to be V/z. If the bond resistance Of the upper bars is $f_{b,sup}$, they can provide $\delta N_S/\delta_x = 2\pi\phi f_{b,sup}$. This is sufficient for the total applied effect at a distance x from the load where:

$$\rho_w f_{yw} b_w (x/z) = 2\pi\phi f_{b.sup} => (x/z) = \frac{2\pi\phi f_{b,sup}}{\rho_w f_{yw} b} \qquad (33)$$

Between this section and the curtailment the lower bars can make a contribution to $\delta N_s/\delta x$ but this is limited by the maximum for $A_{s,inf}{\cdot}f_y$ and the force N_{sc} at the section of curtailment which is as follows:

$$\frac{0.325V}{z} + \frac{V^2}{2\rho_w f_{yw} bz} = \frac{V}{z} \qquad (34)$$

The contribution to $\delta N_S/\delta x$ is restricted to $(A_{s,inf}{\cdot}f_y - N_{sc})/(l-x)$, making the total rate of force as follows:

$$2\pi\phi f_{b.sup} + \frac{A_{s,inf}f_y - N_{sc}}{(1-x)} + = \frac{V}{z} \qquad (35)$$

which allows the ultimate shear V_2 to be calculated. $V_{u,calc}$ is then the lesser of V_1 and V_2.

The calculations and test results are summarised in Table 5, which shows all the ratios of calculated to experimental strength to be between 0.90 and 0.92.

CONCLUSIONS

The beams of four test series, involving mid-barrel and flush exposure of main reinforcement, have been analysed using the bond resistances, given by equations (1) to (5), in basic truss models. The calculated beam strengths range from 0.75 to 1.00 times the experimental values, with all but one of the ratios below 0.88 being for Series C, for which the conservatism is explicable if not easily addressed.

On the basis that a characteristic strength should have a 5% probability of not being achieved, the calculations have provided correct predictions of characteristic resistance, as indicated by the following values:

mean $V_{calc}/V_u = 0.88$
standard deviation of $V_{calc}/V_u = 0.076$
mean + 1.64 standard deviations = 1.00.

This is clearly a naive interpretation of what has been found, but it is true that for a range of situations involving delamination of cover to main steel, the proposed expressions for bond strength, used together with straightforward truss models, can provide reasonable assessments of the strengths of members with simulated deterioration by delamination.

It should be noted that - although the truss modelling used is fundamentally straightforward - its use in cases such as those considered here does require some thought and care.

Predicted shear cracking loads ranged from about 0.73 to 1.17 times the actual values. The accuracy is probably satisfactory given that "actual" values are inevitably somewhat subjective for beams with shear reinforcement.

The assessment of real deteriorating structures is of course more complex than that of the beams considered here. The effects of loss of bar area and loss of concrete in the compression zone must be considered, but the greatest difficulty is estimating the severity and extent of any damage.

ACKNOWLEDGEMENTS

REFERENCES

Regan P. E. and Kennedy Reid I.L. (2010). "Assessment of Concrete Structures Affected by Cover Delamination - Part 1: Effect of Bond Loss", *Studies and Researches – Annual Review of Structural Concrete - V. 29.* Ed. by Politecnico di Milano and Italcementi, pub. by Starrylink (Brescia, Italy), pp. 245-275.

NOTATION

Most of the symbols used are specific to one type of beam or model and are defined where they occur. The following symbols are used more generally:

N_s force in main tension steel
V_{calc} calculated (characteristic) shear force at failure of beam
V_{cr} experimental shear force at shear cracking
$V_{k,red}$ calculated shear force at shear cracking, allowing for influence of delamination
V_u experimental shear force at failure

f_b bond stress for calculation of beam strength (f_{b1}.. f_{b5})
f_{cu} cube crushing strength of concrete
f_y yield stress
f_{yw} yield stress of web reinforcement
u   bar perimeter
z   internal lever arm

θ angle between web compression and axis of beam
ρ_l ratio of main tension reinforcement ($A_s/b_w d$)
ρ_w ratio of web reinforcement

Suffices relating to main tension reinforcement
i - inner bars,   o   - outer bar
inf - lower bars, sup - upper bar

Table 1 – Beams Series "F" - Analysis for Shear Cracking

Beam No	f_{cu} (N/mm^2)	ρ_1 %	Vk,red[(1)] (kN)	values of f_b (N/mm^2)		$z\Sigma f_b$[(2)] (kN)	Predicted V (kN) at shear Cracking
				for outer bars	for inner bars		
F1	52.5	1.84	55.7	1.95	-	74.1	55.7
F2	44.6	1.75	52.0	2.08	- [(3)]	63.3	52.0
F3	44.1	1.75	51.7	2.07	- [(4)]	63.0	51.7
F4	50.9	58.2	58.2	0.71	0.71[(5)]	38.5	no shear cracking

1) $V_{k,red}$ calculated for full value of ρ_1
2) z calculated for flexural failure with all bars at yield
3) The inner bar of F2 is neglected as the maximum Σuf_b, correspomds to full use of the outer   bars and no reliance on the inner one.
4) The inner bar of F3 is neglected as the clamping at loads does not affect the critical region
5) All bars of F4 are taken into account using the lower bond stress of the
   dominant inner bars to maximiseΣuf_b

Table 2 – Beams Series "F" - Ultimate Load Analysis

General data

Main bars T12 f_y = 500 N/mm^2 T20 f_y = 480 N/mm^2, T25 f_y = 475 N/mm^2
Stirrups R6 f_{yw} = 330 N/mm^2

Beam No	f_{cu} (N/mm^2)	Corner bars						cot θ	l (mm)
		detail	f_{b1} (N/mm^2)		$\Sigma\, f_{b1}\, u$ (kN)				
			end	support	end	support			
F1	52.5	2T25	1.34	1.95	211	307	1.645	398
F2	44.6	2T20	1.38	2.08	173	261	1.399	339
F3	44.1	2T20	1.37	2.07	172	260	1.393	337
F4	50.9	2T12	0.71	0.71	54	54	-	-

Beam No	Corner bars				Inner bars		Total N_s (kN)	V_{calc} (kN)	V_u (kN)	$\dfrac{V_{calc}}{V_u}$
	ΔN_{s1} (kN)	ΔN_{s2} (kN)	ΔN_{s3} (kN)	ΣN_s (kN)	detail	N_s (kN)				
F1	61	64	222	347	-	-	347	95	112	0.85
F2	44	69	182	295	1T20	-	295	98	94	0.88
F3	43	70	181	294	1T20	122	416	114	114	1.00
F4	-	-	-	89	2T25	185	274	75	80	0.94

<u>Table 3 – Beams Series "B" -. Data and Analysis</u>

<u>General data</u>
b = 400 mm, d = 237 mm, z taken as 200 mm
Stirrups f_{yw} = 531 N/mm^2 in B1 and B2, f_{yw} = 480 N/mm^2 in B3 and B4
Main bars f_y = 520 N/mm^2 in B1 and B2, f_y = 550 N/mm^2 in B3 and B4
Comp bars f_y = 521 N/mm^2 in B1 and B2, f_y = 480 N/mm^2 in B3 and B4

a) <u>Beam details</u>

Beam No	f_{cu} (MPa)	$\rho_w f_{yw} bz$ (kN)	Corner bars		Middle Bars			y	$b_i \cot\beta$	1_b
			detail	f_b (MPa)	detail	1	f_b (MPa)			
B1	29.7	85.6	2T25	2.95	1T25	575	1.64	750	162	875
B2	29.7	85.6	2T25	2.95	2T25	875	1.64	450	108	575
B3	38.0	131.2	2T25	4.17	2T25	1375	1.85	-	108	-
B4	38.0	131.2	2T25	4.17	2T25	1175	1.85	150	108	275

Notes: f_b calculated from equation (2), for dimensions 1, y, $b_i \cot\beta$, and 1_b – see Fig. 10 – in millimetres; stirrups: T8@125.

b) <u>Calculation of $V_{k,red}$ and V_1</u>

Beam No	ρ	$V_{k,red}$ (kN)	V_{cr} (kN)	$\cot\theta$	V_1 (kN)
B1	1.04	70	72-80	1.10	94
B2	1.04	70	60-70	1.10	94
B3	2.07	95	130	-	-
B4	1.04	76	101	1.05	138

Note: $V_{k,red}$ from equation (6)

c) <u>Calculation of V_2</u>

Beam No	x' (mm)	N_i (kN)	ΔN_s (kN)	ΔN_s-N_i (kN)	N_{sc} (kN)	$N_{so,max}$ (kN)	$N_{s,max}$ (kN)	$V_2/V_{calc}/V_u$	$\dfrac{V_{calc}}{V_u}$
B1	60	49	219	170	404	511*	560	85/85/91	0.93
B2	120	182	360	178	322	500	682	103/94/96	0.98
B3	88	297	738	441	176	540*	837	126/126/149	0.85

*Limited by $A_{so} \cdot f_y$

<u>Table 4 – Beams Series "C" -. Data and Analysis</u>

General
Main steel $\qquad f_y = 670 \text{ N/mm}^2$
$\qquad\qquad\qquad f_{yw} = 350 \text{ N/mm}^2$

Beam No	d (mm)	f_{cu} (MPa)	$z^{(1)}$ (mm)	$V_{k,red}$ (kN)	V_{cr} (kN)	$V_{calc,2}^{(2)}$ (kN)	$V_{calc,2}^{(3)}$ (kN)	V_u (V_{calc}/V_u)
C1	370	49	219	170	404	511*	560	85 (0.93)
C2	270	182	360	178	322	500	682	103 (0.98)
C3	270	297	738	441	176	540*	837	126 (0.85)
C4	270							

Notes:
1) z calculated for uls flexural with two main bars at yield
2) strength calculated for two main bars at yield $V = N_{sy\,z}/0,9(m)$
3) strength calculated as $V = 2_{fb}\,\pi\,\phi\,z$

<u>Table 5 – Beams Series "T" -. Ultimate Load Analysis</u>

<u>General data</u>
b_w = 125 mm, d = 255 mm, z = 227 mm for T1, z = 232 mm for T2,1 = 608 mm
Stirrups f_{yw} = 300 N/mm^2, $\rho_w f_{yw}$ = 2.68 N/mm^2 $\rho_w f_{yw} b_w$ = 335kN/m
Main steel f_y = 510 N/mm^2 $A_{s,inf} f_y = A_{s,sup} f_y$ = 320.5 kN

f_b for exposed bars = (0.3 + 15 $_{Ass}$ / $s_v \phi$) $\sqrt{f_{cu}}$ = 0.519 $\sqrt{f_{cu}}$.

Beam No	d (mm)	f_{cu} (MPa)	$z^{(1)}$ (mm)	$V_{k,red}$ (kN)	V_{cr} (kN)	$V_{calc,2}^{(2)}$ (kN)	$V_{calc,2}^{(3)}$ (kN)	V_u (V_{calc}/V_u)
T1/1	41.7	137	4.52	568	485	135	135	147 (0.92)
T1/2	41.7	137	4.52	568	485	135	135	150 (0.90)
T2/1	51.2	139	3.71	466	323	131	131	144 (0.91)
T2/2	51.2	139	5.05	635	440	141	139	155 (0.90)

Notes:
1) $N_{s, cut}$ = 1.43 V + V^2/152
2) in calculating $f_{b,sup}$ (the limit bond stress for the upper bars) A_{ss} / s ϕ , A_{ss} as
been taken as   the area of one stirrup leg.

FE ANALYSIS OF SHRINKAGE AND THERMAL CRACKING IN CONCRETE WALLS

Cristina Zanotti[1], Alberto Meda[2]

Giovanni Plizzari[3], Stefano Cangiano[4]

ABSTRACT

Shrinkage and thermal gradients often concur in early-age concrete cracking. It is nowadays recognized that a proper design of durable constructions should account for the effect of hygro-thermal strains. Massive constructions such as concrete walls can be significantly affected by shrinkage and thermal cracking because of their large size and particular geometry.

A numerical study on shrinkage and thermal cracking in concrete walls is presented in this paper. Both the risk of early-age thermal cracking and the development of long-term crack patterns are discussed with regard to a specific case study. Aim of the paper is to provide some useful suggestions for structural design and build-up procedures, as well as some indications on the procedures to be adopted in the analysis.

[1] PhD Candidate, Department DICATA, Università di Brescia, Brescia, Italy.
[2] Associate Professor, Civil Engineering Department, Università di Roma "Tor Vergata", Rome, Italy.
[3] Professor, Department DICATA, Università di Brescia, Brescia, Italy.
[4] MS Eng. Research Manager, CTG - Italcementi Group, Bergamo, Italy.

1. INTRODUCTION

Shrinkage and thermal strains are nowadays recognized as among the major causes of cracking in many concrete structures. Since such a cracking can compromise durability, a proper design of structure, materials, and construction procedures is required to prevent those effects.

Durability is nowadays gaining attention by designers since several standards underline the necessity of guaranteeing an adequate service life to the structure. Besides being enhanced by concrete compactness (i.e. reduced porosity) which can be attained by reducing the water/cement ratio, durability can be improved by controlling crack width, since cracks represent an easy way for aggressive agents to reach and corrode the reinforcement.

Shrinkage is mainly associated with the transport of water inside the concrete (ACI 209.1R, 2005; Lura, 2003). Among the many different shrinkage forms that are recognized at present, autogenous and long-term drying shrinkage play a major role in cracking of massive structures made with ordinary concrete. The temperature rise in hardening concrete is a consequence of the heat produced during cement hydration.

Past negative experiences show that concrete walls can be significantly affected by shrinkage and thermal cracking, mainly due to their relatively small thickness and large size (ACI 224.1R, 1993; Kjellman and Olofsson, 2001; Cusson and Repette, 2000).

Results from a numerical study on shrinkage and thermal cracking in concrete walls are presented in the following.

Aim of this paper is to provide some useful suggestions to properly design durable concrete walls. Nonlinear analyses were performed for both the structural behavior and heat transfer, by means of Diana FE Code (Release 9.1 and 9.3; Manie and Kikstra, 2008).

The major factors concurring to early-age thermal cracking can be summarized as follows: (1) constraints provided by adjacent elements that contrast thermal dilation; (2) thermal gradients due to heat transfer between contiguous members; and (3) sudden cooling due to the early removal of the formworks (Springenschmid, 1995; Plizzari et al., 2009).

Shrinkage-induced stresses in concrete walls are mainly due to the differential volume changes with respect to the foundation slab, because of the different casting times and different geometries (the latter affects the rate of drying).

The case study analyzed in the following is a concrete wall exhibiting time-dependent strain profiles induced by either early-age thermal gradients or shrinkage (Fig. 1).

The wall has a cross section of 5 x 0.5 m and a length of 30 m, while the slab foundation has a width equal to 1.5 m and a thickness of 0.5 m. Some geometrical features are varied for a parametric study presented in the second part of this paper.

The paper is divided into two main sections: (1) risk of early-age thermal cracking, and (2) crack-pattern development due to shrinkage or thermal volume changes. A short presentation of the case study and of the modeling come before each section.
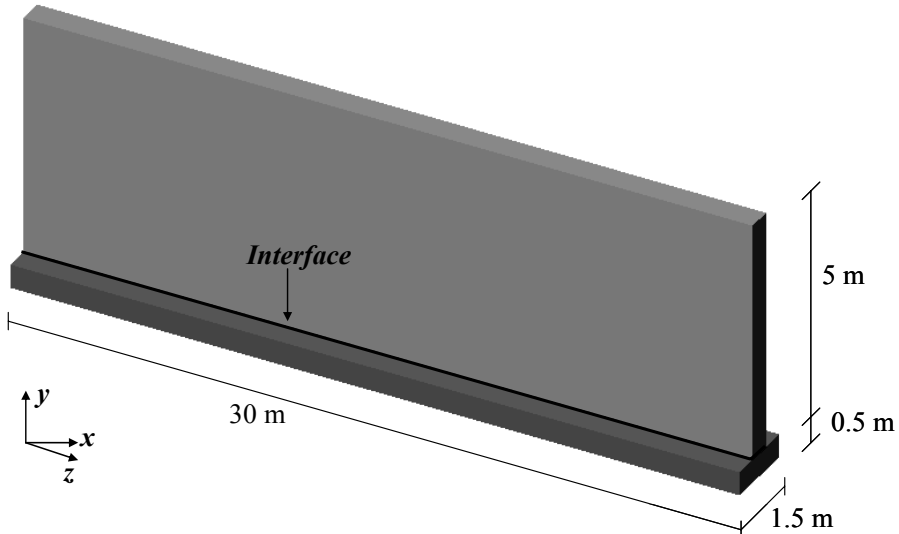

Figure 1 - Reference geometry (Zanotti et al., 2010a).

2. RISK OF EARLY-AGE THERMAL CRACKING

Multi-phase nonlinear coupled flow-stress analyses were performed to study the risk of thermal cracking during concrete hardening. Either simultaneous or differential casting of the foundation slab and the wall were assumed. In the former case, the construction process is subdivided into 2 phases: concrete casting, and removal of formworks (2, 4 or 6 days after casting). In the latter case, the construction process is subdivided into 4 phases: slab casting, removal of slab formworks (2, 4 or 6 days after slab casting), wall casting (7, 14 or 28 days after slab casting), and removal of wall formworks (2, 4 or 6 days after wall casting).

Thermal gradients across the thickness are recognized as the major cause of early-age thermal cracking in 2-D thin members (Kjellman and Olofsson, 2001). A plain-strain 2D-model was therefore adopted in this first part of the work (Fig. 2a). Concrete parts and forms are modeled by means of 40x40 mm or 40x10 mm quadrilateral isoparametric elements, while triangular isoparametric elements are used for the soil. The integration scheme is linear for heat-transfer analysis and quadratic for structural analysis so that compatibility is guaranteed.

Two-node boundary elements are placed along the perimeter of the construction to model convection during the thermal analysis. Therefore, boundary elements lay on the outer edges of the formworks, the wall, the slab and the soil.

At each phase, only the boundary elements that lay on the lines actually involved in convection were activated. Adiabatic conditions were imposed along the vertical line of symmetry (line AB, Fig. 2a). Moreover, adiabatic conditions were assumed along both the lower and the lateral edges of the soil (lines BC and CD, Fig. 2a), in order to model the effect of the surrounding soil that was not included in the mesh. The size of the soil included in the mesh was properly designed in order to ensure that the edges BC and CD (Fig. 2a) are far enough from the concrete slab and thus are not affected by the exchange of heat between the concrete slab and the soil.

Concerning the structural analysis, horizontal translational constraints were applied along the axis of symmetry (line AB, Fig. 2a) and the lateral edges of soil (lines BC and CD, Fig. 2a), while vertical translational constraints are placed only along the lower horizontal edge of soil. The crack risk, χ, is defined by Eq. 1.

$$\chi(t) = \max \left[\frac{\sigma_I(t, x, y)}{f_{ct}(r(t, x, y))} \right]_{x,y} \tag{1}$$

where t = time; x, y, z = global coordinates; σ_I = maximum principal stress; and f_{ct} = concrete tensile strength. Cracks should appear when $\chi = 1$ but they form earlier because of the random nature of the tensile strength; hence, a value lower than 1 has been adopted to stay on the safe side ($\chi = 0.7$).

2.1 Heat transfer analysis , hydration process and material behavior

Aim of the heat transfer analysis is to determine the development of both temperature gradients and concrete properties during and after hydration.

Temperature is the unknown degree of freedom of the equation for global heat transfer (Eq. 2):

$$\rho c \frac{\partial T}{\partial t} = \nabla(k \nabla T) + q \tag{2}$$

where T is temperature, t is time, ρ is the material density, c is specific heat, k is thermal conductivity, ∇ is the spatial gradient and q is the rate of heat generation.

Reference is made to the nonlinear formulation suggested by Reinhardt et al. (1982) for modeling concrete hardening and temperature development. The degree of reaction, r, as defined by Eq. 3, is the parameter accounting for the hardening stage of the concrete:

$$r(t, x, y, z) = \frac{Q(t, x, y, z)}{Q_{max}} \tag{3}$$

where t is time, x, y, z are the global coordinates, Q is the actual amount of heat that has been generated in each specific point of the concrete construction at time t, and Q_{max} is the total amount of heat produced by the hydration reactions. Q_{max} is a function of just the chemical composition and the total volume of the concrete. Cement hydration is completed when r = 1.

The rate of heat generation, q, is affected by both the temperature and the degree of reaction. In order to make the numerical procedure easier, the function $q(r,T)$ can be split into two different parts, one depending on r and one depending on T only (Eq. 4). The well-known Arrhenius relation, here named $g(T)$, is commonly used for temperature:

$$\frac{\partial Q}{\partial t} = q(t, x, y, z) = g(T) f(r) = a \exp\left(-\frac{b}{T(t, x, y, z)}\right) f(r(t, x, y, z)) \qquad (4)$$

where a and b are material constants. Arrhenius constant, b, is given a value of 6000. Term $af(r)$ is the rate of heat generation in adiabatic conditions and can be derived from experimental adiabatic temperature-time curves (Fig. 2b). Provided that the amount of heat produced by hydration reactions depends on concrete chemical and physical properties, two different mix-designs for a C30/37 concrete are considered in the present work: the first mix is made with standard constituents, whereas blast furnace slag is added to the second mix. Cubic specimens were insulated by means of polystyrene layers and the temperatures developed during the first week after casting were monitored. The results are shown in Fig. 2b, where the beneficial role of blast-furnace slag for limiting hydration heat is evident.

The adiabatic function $af(r)$ is derived from the adiabatic temperature-time curves by means of Eq. 5:

$$af(r) = \overline{q} \exp\left(\frac{b}{T}\right) = \frac{c\Delta T}{\Delta t} \exp\left(\frac{b}{T}\right) \qquad (5)$$

where Δt is a given time increment, c is the specific heat, and $\overline{q}$ is the average rate of heat evolution within Δt. Function $f(r)$ is scaled to 1, so that the constant a takes the meaning of the maximum rate of heat evolution, equal to the maximum value of term $af(r)$.

Thermal and mechanical properties assumed for hardened concrete at ambient temperature, formworks and soil, are listed in Table 1. A thickness of 20 mm or 5 mm is assumed for timber and steel forms, respectively. The laws assumed to model the influence of the degree of hydration on concrete thermal and mechanical properties are shown in Fig. 2c (Reinhardt et al., 1982; Onken and Rostasy, 1995).

Table 1. Thermal and mechanical properties at 20°C: thermal conductivity k, specific heat c, convection coefficient h and density ρ; Young Modulus E, Poisson coefficient ν and tensile strength f_{ct}.

Material	k [W/mK]	c [J/kgK]	h [W/m²K]	ρ [kg/m³]	E [MPa]	ν	f_{ct} [MPa]
Concrete	1.19	900	25	2300	33000	0.2	2.9
Soil	1.1	880	-	1600	100	0.35	-
Wood	0.12	3780	4	300	-	-	-
Steel	40	473	15.46	7900	-	-	-
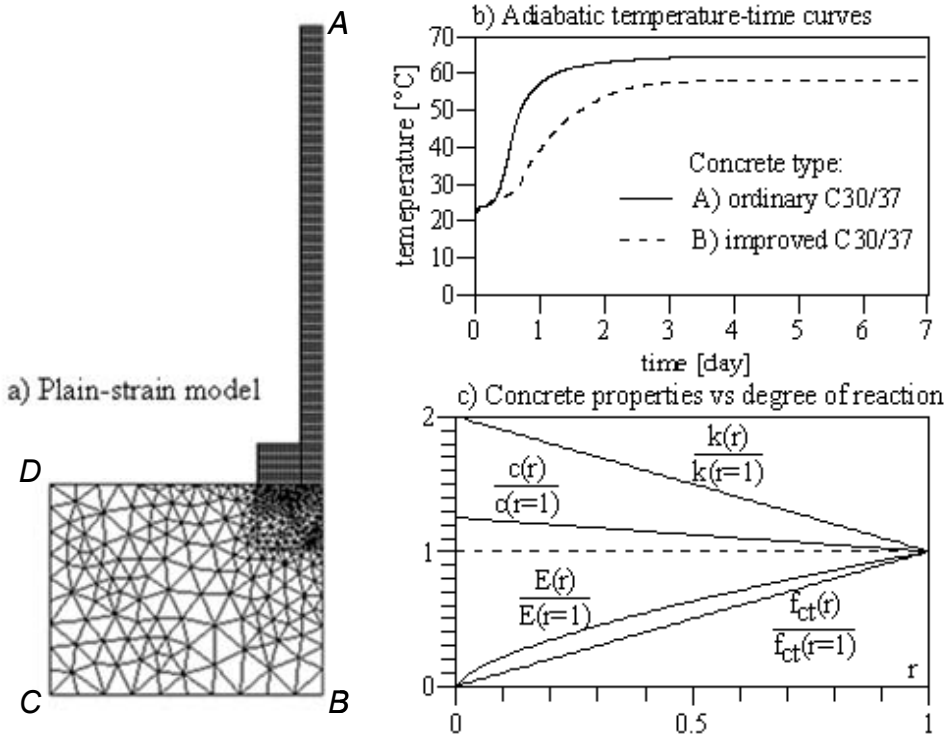
Figure 2 – (a) Plain-strain model; (b) experimental adiabatic temperature-time curves; and (c) plots of thermal conductivity k, specific heat c, Young Modulus E and tensile strength f_{ct} versus the degree of reaction r (Zanotti et al., 2010a).

2.2 Temperature development

Figs. 3 and 4 show the development of both the temperature and the degree of reaction during the first days, when the foundation and the wall are not cast simultaneously (the timber formwork have a thickness of 20 mm). A steady ambient temperature of 21.7°C is assumed. It should be noted that the temperature

rise in the slab is lower than that in the wall due to the different geometry. The slab temperature equals the ambient temperature a week after casting (Fig. 3a), while the hydration reactions are almost entirely exhausted at that time ($0.9 < r < 1$, Fig. 3b). Obviously, lower temperatures are registered close to the edges of the construction, due to the heat transfer to the environment (Figs. 3a, 4a). Accordingly, the inner concrete parts harden faster than the external ones (Figs. 3b, 4b).
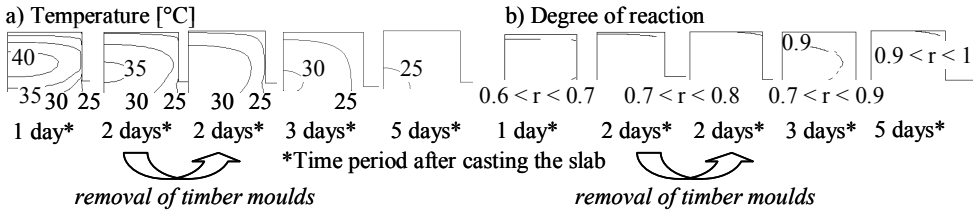

Fig. 3 – Plots of the temperature (a) and of the degree of reaction (b) in the concrete slab throughout the first days, before casting the wall (in the case of non-simultaneous casting of wall and slab); timber is assuned for the formworks.
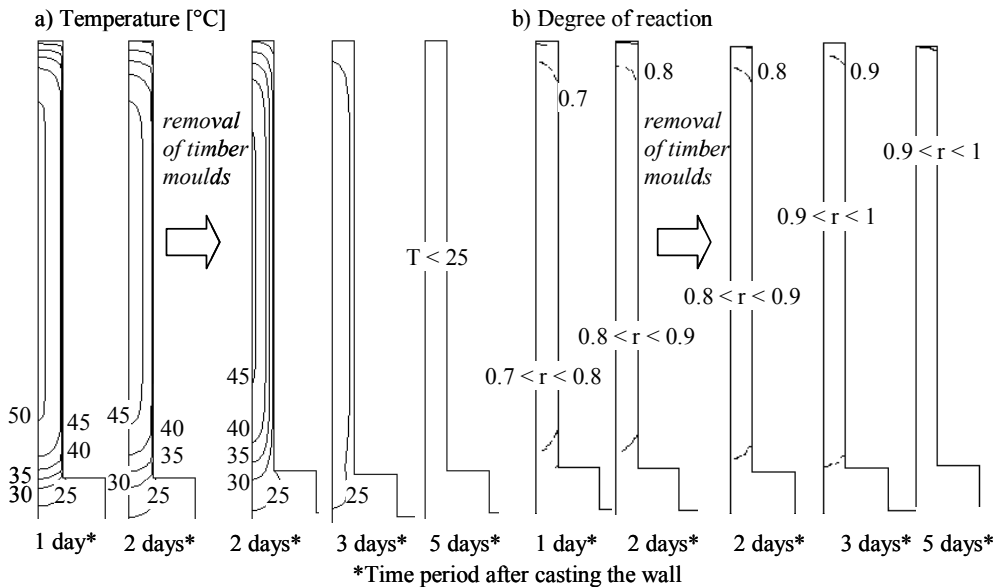
Fig. 4 – Plots of the temperature (a) and of the degree of reaction (b) in the concrete wall throughout the first days, in the case of non simultaneous casting with timber formworks (Zanotti et al., 2010b).

Therefore, a lower insulation (provided by the forms) from the environment provokes higher thermal gradients within the cross section and a slower hardening process. Note that removing the highly-insulating timber formworks causes a sudden cooling of concrete, starting from the lateral edges.

2.3 Risk of cracking

Figure 5 shows the evolution of the crack risk in the wall as a function of time, by assuming that the wall is cast at least one week after the foundation. Timber formworks (Fig.5a) and steel formworks (Fig.5b) are adopted and the laying time of formworks varies from 2 to 6 days. According to the numerical results, timber formworks are able to prevent wall cracking since the maximum crack risk (which is reached about one day after casting) is lower than 0.7 (point A, Fig. 5a). However, if formworks are removed too early (two days after casting, when concrete temperature is still high), the sudden cooling shown in Fig. 4a causes surface cracking (point B, Fig. 5a). The crack risk can be significantly reduced by postponing the removal of formworks from 2 to 4 days (points C and D, Fig. 5a).

The crack risk turns out to be higher than 1 a few hours after casting in the case of steel moulds, due to the their lower insulation properties (point A, Fig. 5b). A lower amount of heat is accumulated during the laying of steel moulds; thus, the removal of steel moulds cause only a slight increase of the crack risk (points B, C, D, Fig. 5b).

Note that two very different types of cracks may appear (Fig. 6a). The early removal of well-insulating formworks may produce surface cracks, whereas more severe through cracking may develop in the core of the section because of inadequate insulation soon after casting (Kjellman and Olofsson, 2001). Therefore, the first crack type appears after the removal of formworks, while the second crack type appears at an earlier stage (a few hours after casting).

In Fig. 6b, the maximum values of the crack risk obtained straight after casting as well as after the removal of formworks, are compared for various values of the following parameters: mould type, mould laying time, time span between foundation casting and wall casting, and concrete mix (i.e. the adiabatic temperature-time curves of Fig. 2b). When casting simultaneously the wall and the foundation, a higher amount of material is hydrated at the same time and the crack risk increases.

The addition of blast-furnace slag in the concrete mix allows to reduce and to retard the heat development, as shown by the experimental temperature-time curves (Fig. 2b), with the beneficial effect of a markedly reduced crack risk.

When using timber formworks with simultaneous casting, the crack risk is reduced from 1.1 to 0.65 (Fig. 6b); the risk further decreases up to 0.35 when the wall is cast after the foundation. On the other hand, the improvement of the mix composition does not fully prevent surface cracking, even though the risk is slightly reduced.
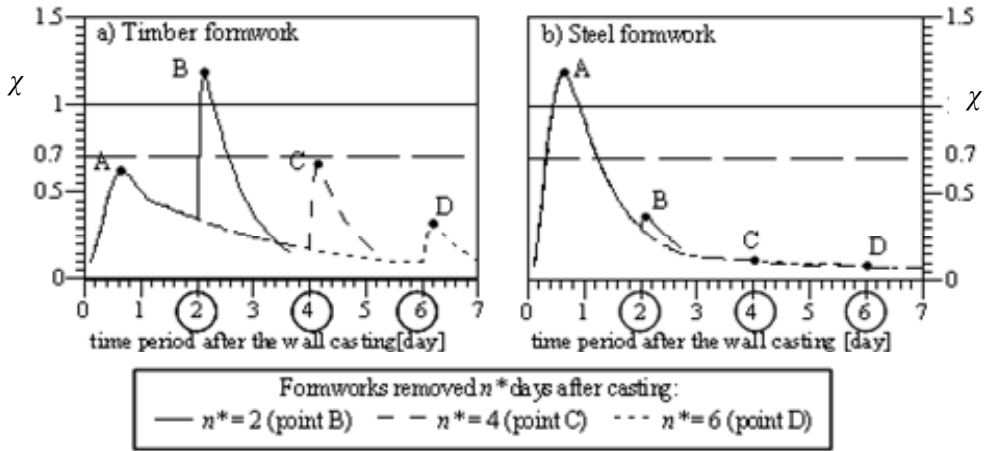
Figure 5 - Ordinary concrete C30/37 (type A, see Fig. 2b); wall and foundation slab cast in succession: risk of cracking (χ) in the wall through the first week after casting, with (a) timber formworks; and (b) steel formworks (Zanotti et al., 2010b).
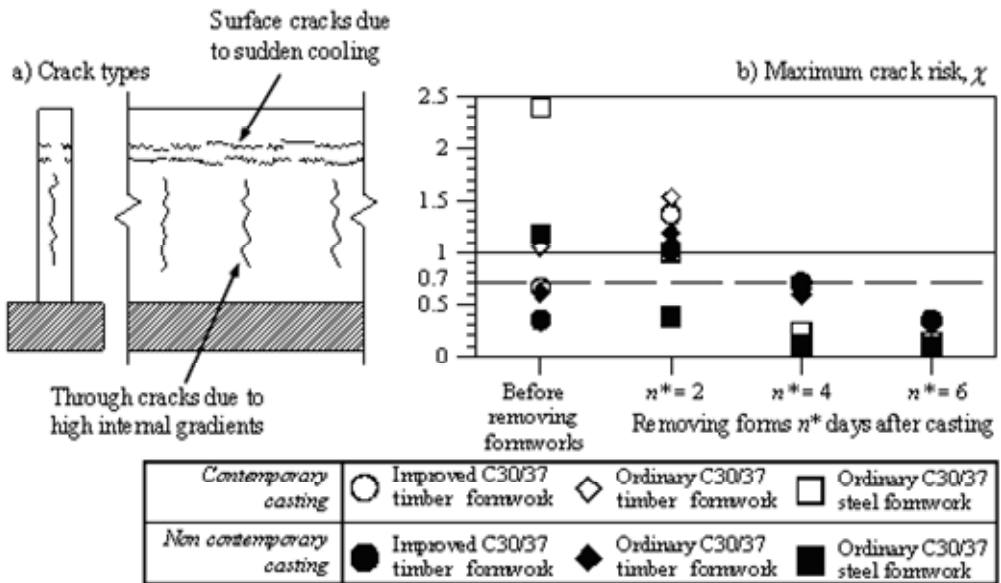

Figure 6 – (a) Different types of cracks that may appear in the wall; and (b) maximum crack risk before and after the removal of the formworks, for contemporary and non-contemporary casting of the foundation slab and of the wall (Zanotti et al., 2010b).

The removal of the timber formworks two days after casting brings in a crack risk equal to 1.3 or to 1, depending on whether the casting of the foundation slab and that of the wall are simultaneous or are performed in successive times (of course, first the slab and later the wall). Timber formworks should be kept in place at least for 3 or 4 days.

3. CRACK PATTERNS DUE TO SHRINKAGE OR THERMAL VOLUME CHANGES

A 3-D model was adopted in order to describe concrete shrinkage as a time-increasing volume contraction. The risk of shrinkage cracking varies depending on the different constraints that, acting on the structure, restrict the concrete volume changes.

Different degrees of restraint act on the wall due to the adjacent concrete slab, the steel rebars, and the soil foundation. A preliminary study indicated that the main cause of shrinkage cracking is the differential shrinkage between the wall and the foundation slab (Plizzari et al., 2009), while the degree of restraint provided by soil friction resulted negligible in comparison with the constraint provided by the slab. Therefore, soil friction was neglected and the soil was modeled by means of no-tension vertical springs acting along the intrados of the foundation slab (Winkler-type soil with elastic stiffness in compression $k_w = 90 \times 10^6$ N/m^3).

Linear-strain isoparametric cubic elements (with a side of 125 mm) are used for concrete modeling.
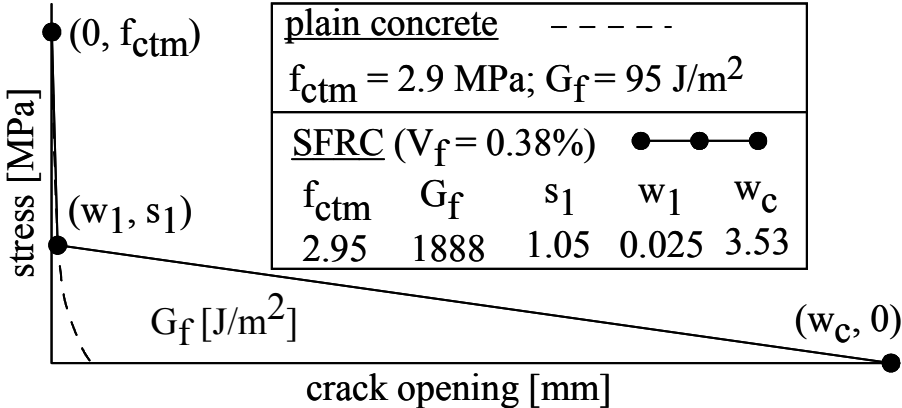

Figure 7 – Concrete in tension, without/with steel fibers: tension softening laws (Cornelissen et al., 1986; CEB-FIP Model Code 1990; Cominoli et al., 2005; Zanotti et al., 2010a).

3.1 Crack modeling

The development of crack patterns caused by time-dependent volume changes is studied by smearing the cracks and combining the smeared-crack approach with the multi-directional fixed crack model (Rots, 1988). Nonlinear tension softening for plain concrete was introduced as suggested by Cornelissen et al. (1986), see Fig. 7; fracture energy G_f was evaluated according to MC1990 (1993). Steel Fiber-Reinforced Concrete (SFRC) was modeled as a homogeneous material, whose mechanical properties were experimentally determined by means of fracture tests (Cominoli et al., 2005); a bi-linear law was adopted to describe tension softening of SFRC (Fig. 7). Linear elasticity was assumed for compression, as limited stresses were expected.

The wall-to-slab foundation joint is modeled by means of zero-thickness interface elements. The elastic normal stiffness D_{11} is given by Equation 6:

$$D_{11} = \frac{t_n}{\Delta u_n} = \frac{E}{l_n} = \frac{E}{10^{-4} l_t} = \frac{E}{10^{-5} m} = 3.3 \cdot 10^{15} \frac{N}{m^3} \tag{6}$$

where t_n is the average normal stress, Δu_n is the relative displacement in the normal direction; and E is the concrete elastic modulus (= 3.3 GPa; EC2, 2005).

The elastic tangential stiffness D_{22} is determined by assuming small displacements and small strains in the elastic field (Eqs. 7,8):

$$G = \frac{t_t}{\gamma} = t_t \frac{l_n}{\Delta u_t} \tag{7}$$

$$D_{22} = \frac{t_t}{\Delta u_t} = \frac{G}{l_n} = \frac{D_{11}}{2(1+\nu)} = 1.375 \cdot 10^{15} \frac{N}{m^3} \tag{8}$$

where t_t is average tangential stress; Δu_t is the relative displacement in the tangential direction; γ is the shear rate; G is the shear modulus; and ν is the Poisson coefficient (equal to 0.2).

In order to verify the compatibility between the stiffness of concrete bricks and the interface elements, a number of numerical tests in both normal and tangential directions was performed (Plizzari et al., 2009).

The nonlinear interface behavior between the wall and the foundation is modeled according to Mohr-Coulomb. Two different surface types are considered: smooth and rough interface. The former represents any situation with a very low degree of restraint between the wall and the foundation; conversely, a rough interface represents those situations characterized by high degree of restraint.

Finally, the maximum restraint condition is represented by perfect bond between the two structural elements (no mutual slip or detachments).

The interface properties are reported in Table 2 and are based on the parameters suggested by the Eurocode 2 (EC2, 2005) for cast joints. Tension softening is neglected at the interface and associated plasticity is assumed.

Table 2. Parameters assumed for the nonlinear interface behavior (EC2, 2005).

Surface type	Cohesion coefficient μ [MPa]	Friction angle ϕ	Tensile strength $f_{t,int}$ [MPa]
smooth	1.305	26.5°	1.45
rough	1.725	35°	1.86

3.2 Steel reinforcement

A symmetrical elasto-plastic behavior with hardening was assumed for the steel under tensile and compressive stresses (Fig. 8).

The longitudinal reinforcement acts as an internal constraint if the shrinkage mainly develops along the longitudinal axis of the wall. In order to account for this internal constraint, the rebars placed in the wall are modeled by means of truss elements, whereas embedded reinforcement is adopted for the foundation slab. While truss elements - as discrete elements – can act as internal constraints for the wall, embedded reinforcement is only able to simulate an improvement of the concrete mechanical properties that comes as a consequence of the presence of rebars. On the other hand, as a major advantage, embedded reinforcement is very easy to handle.

Stirrups laying in vertical direction weaken the resistant concrete section. Modeling of stirrup geometrical volumes, however, would require a very fine mesh, which is incompatible with the wall size. Therefore, such an effect is considered by properly decreasing the tensile strength of the elements containing the stirrups (Plizzari et al., 2009).
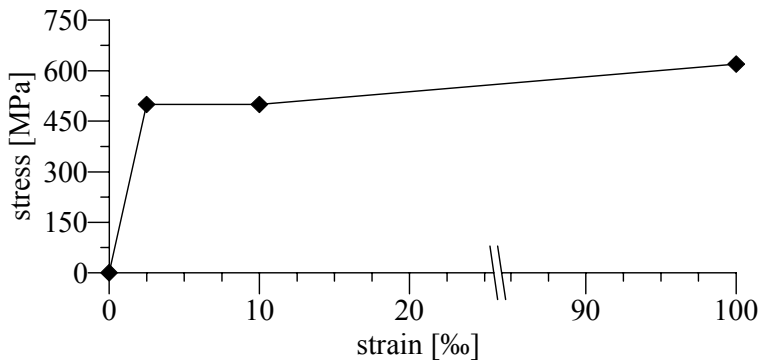

Figure 8 – Steel law in tension and compression (Zanotti et al., 2010a).

3.3 Crack patterns and influence of longitudinal reinforcement

Regardless of the properties of the wall-foundation interface or of the amount of the reinforcement, first cracking of R/C walls always occurs for shrinkage strains approaching 50 $\mu\varepsilon$. In the diagram of Fig. 9, the maximum crack openings reached in the structure for increasing shrinkage strains (that is, volume changes) are compared, for three different reinforcement ratios ρ_s. The beneficial contribution of longitudinal reinforcement is clearly visible: the higher the amount of reinforcement, the smaller the maximum crack opening corresponding to a given value of shrinkage strains (e.g., a crack opening of 0.5 mm is reached when strains are equal to 135×10^{-6} with the lowest reinforcement ratio, and equal to $145 \ 10^{-6}$ in the other cases). The influence of steel rebars on crack opening increases for increasing shrinkage strains; as a matter of fact, a crack opening of 0.8 mm is associated with volume changes equal to $135 \ 10^{-6}$, $150 \ 10^{-6}$, or $210 \ 10^{-6}$, depending on the reinforcement ratio.
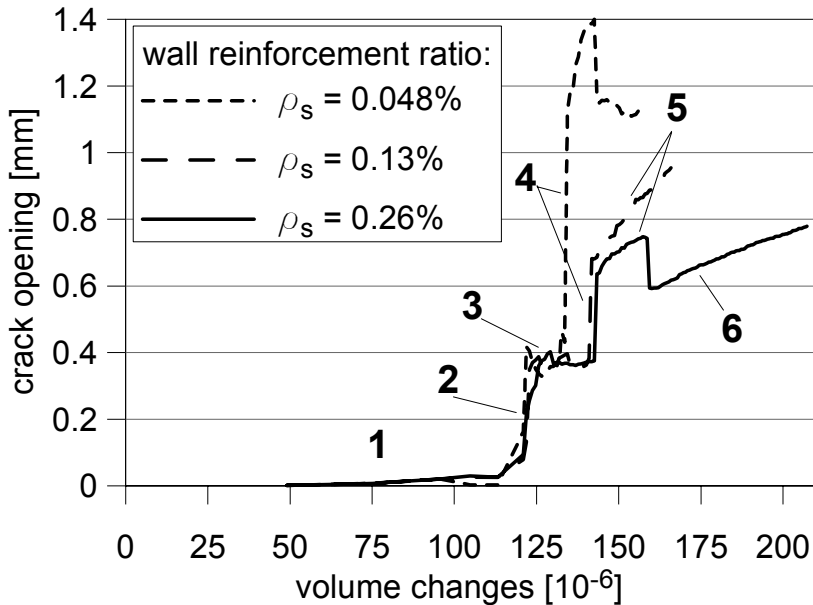

Figure 9 - Maximum crack opening as a function of shrinkage strains (or volume changes), in case of rough wall-foundation interface (Meda et al., 2010).

Should the longitudinal rebars not affect first cracking and enhance globally the crack pattern, the internal restraint effect would be apparently negligible, compared with the restraint provided by the foundation slab.

Three different crack levels may be identified (Fig. 10):

- 1st level: cracks spread along the wall base (strongly affected by the properties of both stirrups and wall-foundation interface);

- 2nd level: localized vertical cracks that do not reach the top of the wall;

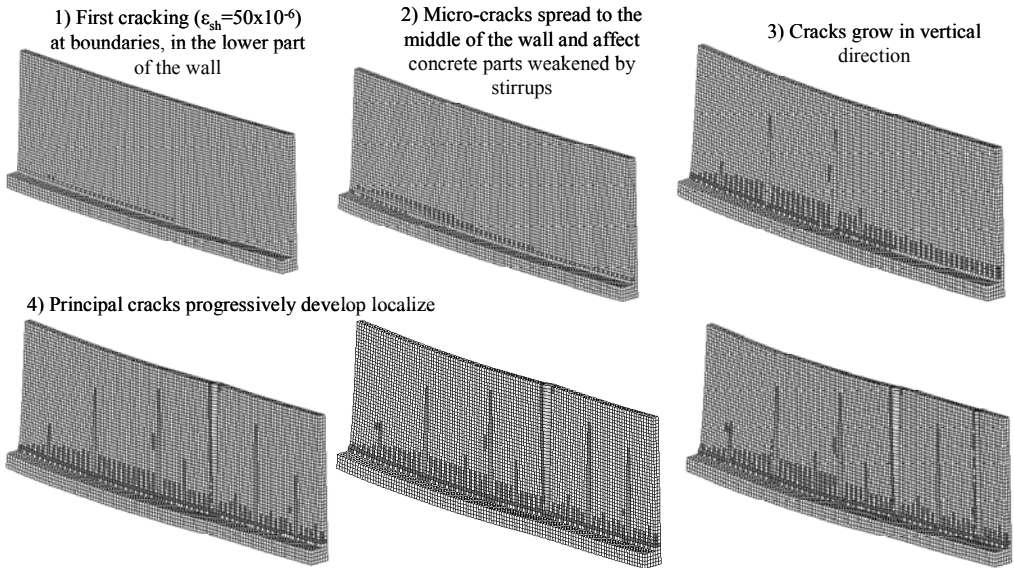- 3rd level: vertical cracks covering the whole height.

Figure 10 – Crack-pattern development for increasing shrinkage strains (reinforcement ratio of the wall $\rho_s = 0.13\%$; rough wall-foundation interface).

The different branches of the curves of the maximum crack-opening versus shrinkage volume changes (or strains, Fig. 9), correspond to different stages of the wall cracking, as shown in Fig. 10. Cracking stages can be summarized as follows:

(1) Micro-cracks spread along the wall base (1st level).
(2) First vertical macro-cracks form (2nd level) and strains localize, followed by a sudden increment of the maximum crack opening.
(3) Other vertical macro-cracks develop (2nd level); in this stage, the increase of shrinkage strains is followed by multiple-cracking, without any increases of the maximum crack opening, this being a plus provided by the reinforcement.
(4) Two vertical cracks - equally far from the boundaries and from each other - reach the top of the wall (3rd level), with the wall resulting subdivided in three equal parts.
(5) Primary macro-cracks develop (3rd level); with the largest reinforcement ratio, a further vertical crack develops at this stage; consequently, primary cracks open less than in the other cases.

(6) In the wall having the largest reinforcement ratio, the strains localize around the <u>new vertical crack</u> (point 5); accordingly, the primary cracks are partially closed and the maximum crack opening suddenly decreases to 0.6 mm; later on, the crack opening starts increasing again up to 0.8-1 mm for shrinkage strains that are significantly higher than in the other cases.

3.4 Influence of the properties of the wall-foundation interface

In the diagrams of Figs. 11 and 12, the responses of different walls having the same amount of longitudinal reinforcement, but different degrees of restraint with the foundation slab (different wall-foundation interface properties), are compared. A better structural performance is achieved in the case of a smooth wall-foundation interface than in the case of a rough interface (i.e. with more friction).

The influence of the wall-foundation interface on crack patterns is particularly significant for $\rho_s = 0.048\%$ (lowest reinforcement ratio, Fig. 11). Conversely, interface roughness plays a minor role for higher values of ρ_s, since in these cases the reinforcement is able to effectively limit crack opening (Fig. 12).
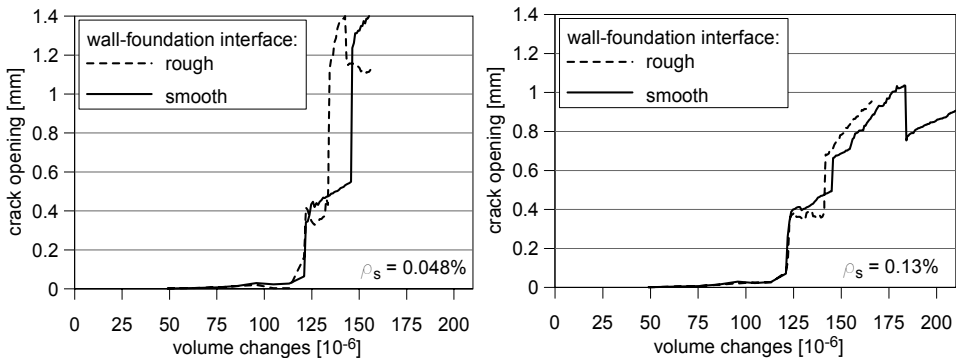

Figure 11 – Plots of the maximum crack opening versus shrinkage volume changes (or strains) in the wall: reinforcement ratio $\rho_s = 0.048\%$ (left) and $= 0.13\%$ (right); see Meda et al. 2010.

3.5 Influence of geometry

In Figure 12 the plots of the maximum crack opening versus shrinkage strains are shown for various wall geometries. Beside the reference geometry, having height $H = 5$ m and length $L = 6H = 30$ m, two further cases are considered: the first with a height reduced by 50% ($H = 2.5$ m and $L = 12H = 30$ m) and the second with a length increased by 50% ($H = 5$ m and $L = 4H = 20$ m). It can be observed that, by reducing the ratio L/H, the structure performance is improved. L/H can be reduced
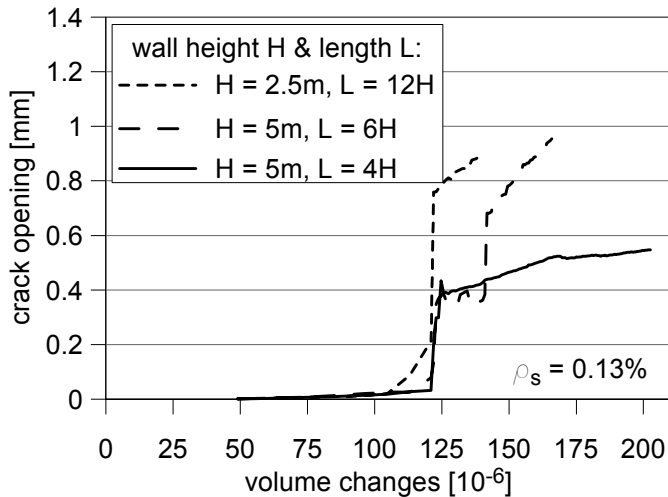
Figure 12 – Plots of the maximum crack opening versus shrinkage strains in the wall having a reinforcement ratio $\rho_s = 0.13\%$, a rough wall-foundation interface and three different height-length ratios (Meda et al, 2010).

by reducing L (for instance, by placing proper vertical joints) or by increasing H, that provides a further small benefit, i.e. the reduction of the constraint provided by the foundation slab, due to the increment of the ratio between the cross area of the wall and that of the foundation (Cusson and Repette, 2000).

In the wall with L/H = 12 (Fig. 13), a larger number of primary vertical cracks (3rd level) can develop in comparison with the other two cases; the spacing is almost equal to the wall height. One can observe that lower vertical stresses are involved and, in the central part of the structure, no compressive longitudinal stresses develop. Conversely, boundary effects are unchanged. In the case with the reference height of 5 m and a reduced length (L = 4H = 20 m), the influence of the vertical compressive stresses is greater and no primary crack appears (Fig. 14). The longitudinal stresses are markedly nonlinear and the boundary effects influence the whole length.
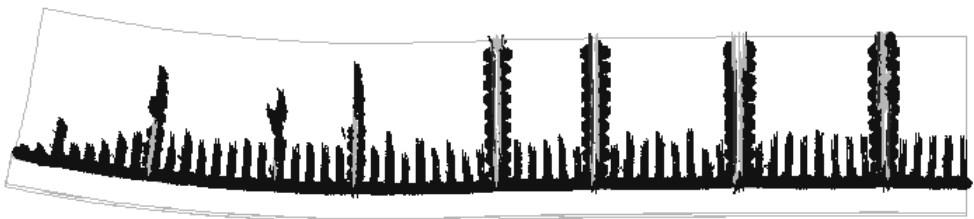

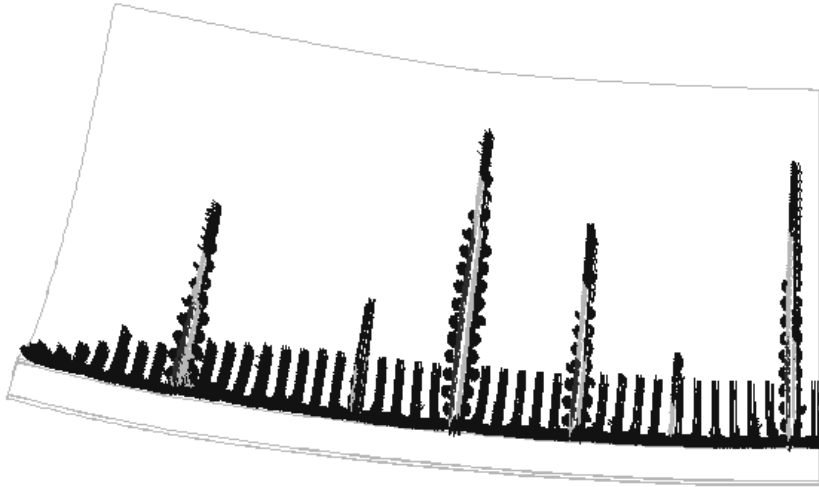Figure 13 - Crack pattern of the wall having height H = 2.5 m and length L = 12H = 30m (Meda et al., 2010).

Figure 14 - Crack pattern of the wall having height H = 5 m and length L = 4H = 20m (Meda et al., 2010).

3.6 Fiber-Reinforced Concrete

Previous diagrams show that the structural performance can be improved by increasing the amount of longitudinal reinforcement or by placing vertical joints (in order to reduce L/H).

These solutions, however, these solutions turn out to be effective only in the case of large deformations, to limit crack opening above 0.3 mm.

Smeared reinforcement - such as fibers – may be added to the concrete mix in order to increase concrete toughness (Fig. 2) and, therefore, to better control micro-cracking. In Fig. 15 the responses of a wall reinforced by means of ordinary rebars (ρ_s = 0.13%, Curve 1) and a wall reinforced with hooked steel fibers (v_f = 0.38%, Curve 2) are compared. Fibers are shown to effectively control micro-crack opening, contrary to conventional rebars that are effective only for larger deformations. Finally, an optimized solution for designing the reinforcement with respect to shrinkage effects may be achieved by properly combining fibers and rebars.

Therefore, the behavior of a FRC wall reinforced with steel rebars placed at the top is analyzed, assuming that that the maximum opening of the primary cracks occurs at the top of the wall. The results show that the performance of the FRC wall under large deformations can be improved by placing longitudinal rebars at the top, since crack opening is further reduced (Curve 3, Fig. 15).
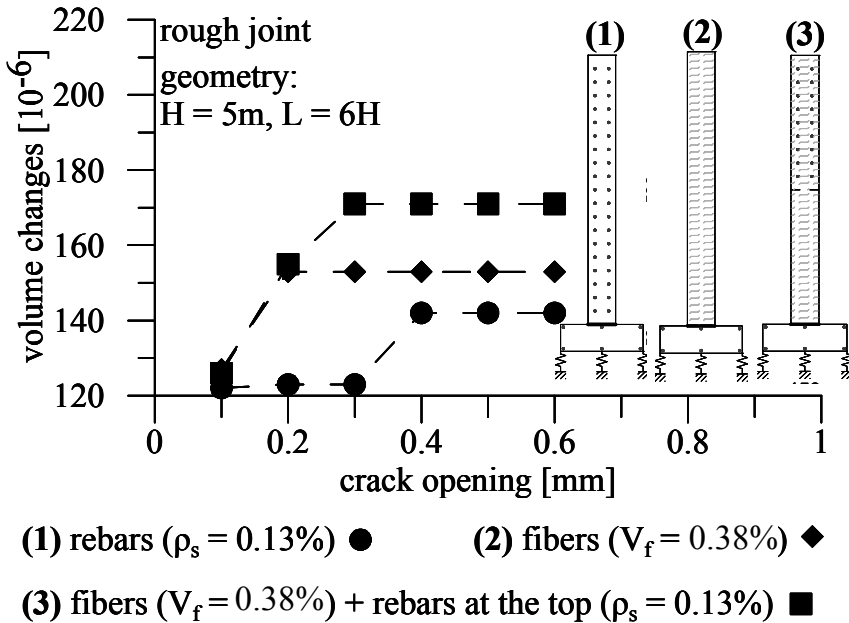
Figure 15 - Response of the walls reinforced with rebars (Curve 1), with fibers (Curve 2) and with an optimized combination of rebars and fibers (Curve 3, Zanotti et al. 2010a).

4. CONCLUDING REMARKS

A parametric study on the risk of thermal and shrinkage cracking was presented and discussed in this paper with the aim of providing some useful information for a proper design of concrete walls with regard to hygro-thermal phenomena.

The main results can be summarized as follows.

- Thin walls made of ordinary concrete are actually exposed to the risk of early-age thermal cracking mainly due to the low thickness and the large size; compared with shrinkage, hydration heat can produce more significant and damaging effects.

- Early-age thermal cracking can be prevented – or limited – by optimizing the construction process with some simple expedients, such as adopting moulds that are able to provide enough insulation or postponing mould removal.

- Particular constituents, such as blast-furnace slag, added to the concrete mix moderate and limit the hydration-heat development.

- Differential volume changes between the wall and the slab foundation may foster the formation of micro-cracks along the wall base, as well as the propagation of more damaging vertical cracks throughout the whole height.

- Major factors affecting shrinkage cracking are the geometry of the wall and of the slab foundation, the roughness of the cast joint, the longitudinal and transverse reinforcement, and the steel-fiber content.

- An effective control of both micro- and macro-cracks can be achieved by optimizing the reinforcement, through a proper combination of steel fibers and conventional bars.

The results obtained in the present study clearly demonstrate that performance requirements for concrete structures should include, beside the usual strength class, workability class and exposure class, a maximum shrinkage deformation; this requirement will better guarantee the crack control which is of paramount importance for durability and consequently, for guaranteeing a proper the service life of the structure.

ACKNOWLEDGEMENTS

NOTATION

The following symbols are used in this paper:

c	=	specific heat
E	=	Young modulus
D_{11} , D_{22}	=	interface normal , tangential stiffness
f_{ct}	=	concrete tensile strength
$f_{t,int}$	=	interface tensile strength
G	=	shear modulus
G_f	=	fracture energy
H	=	wall height
k	=	thermal conductivity
L	=	wall length
Q	=	hydration heat
r	=	degree of reaction in hydration processes

t	=	time
t_n, t_t	=	average normal , tangential interface stress
T	=	temperature
v_f	=	fiber volume fraction
x, y, z	=	global coordinates
χ	=	crack risk
Δu_n, Δu_t	=	relative interface normal , tangential
ϕ	=	friction angle
γ	=	shear rate
μ	=	cohesion coefficient
ν	=	Poisson ratio
ρ_s	=	steel reinforcement ratio

REFERENCES

American Concrete Institute (1993). *Causes, Evaluation and Repair of Cracks in Concrete Structures*. ACI 224.1R-93.

American Concrete Institute (2005). *Report on Factors Affecting Shrinkage and Creep of Hardened Concrete*. ACI 209.1R-05.

Cominoli L., Meda A. and Plizzari G. (2005). "Hybrid Fibers to Enhance Fracture Properties of Concrete Pavements". *Proc. Third Int. Conf. on Construction Materials*, Vancouver, 2005.

Comité Euro-International du Béton (1990). *CEB-FIP Model Code.*

Cornelissen H.A.W., Hordijk D.A. and Reinhardt H.W. (1986). "Experimental Determination of Crack Softening Characteristics of Normal-Weight and Lightweight Concrete". *Heron*, 31 (2).

Cusson D. and Repette W. (2000). "Early-Age Cracking in Reconstructed Bridge Barrier Walls". *ACI Materials Journal*, 97(4), pp. 438-446.

EC2 (2005). *Design of Concrete Structures. Part 1-1: General Rules and Rules for Buildings*. EN1992-1-1.

Kjellman O. and Olofsson J. (2001). "3D Structural Analysis of Crack Risk in Hardening Concrete (Verification of an Engineering Method)". *Report No. 2001:53-2*, Department of Civil & Mining Engineering, Luleå University of Technology, Luleå (Sweden).

Lura P. (2003). *Autogenous Deformation and Internal Curing of Concrete*. Doctoral Thesis, DUP Science.

Manie J. and Kikstra W.P. (2008). *Analysis Procedures - DIANA – Finite Element Analysis. User's Manual Release 9.3.* Delft: TNO DIANA BV.

Meda A., Plizzari G., Zanotti C. and Cangiano S. (2010). "Crack Risk Analysis in Structural Elements Exposed to Hygro-Thermal Phenomena". *Proc. Seventh Int. Conf. on Fracture Mechanics of Concrete & Concrete Structures*, Jeju (Korea).

Onken P. and Rostàsy F. (1995). "Wirksame betonzugfestigkeit im bauwerk bei früh einsetzendem temperaturzawang" (Effective Concrete Strength in Tension in the Constructions Subjected to a Previous Temperature Increase). *DAfStb Heft 449*, Berlin (Germany), Beuth-Verlag.

Plizzari G., Meda A. and Zanotti C. (2009). *Numerical Investigation on the Risk of Early Cracking in Concrete Structures (in Italian).* Technical Report, No.7/ 2009, University of Brescia, DICATA Department, in press.

Reinhardt H.W., Blaawendraad J. and Jongendijk J. (1982). "Temperature Development in Concrete Structures Taking Account of State-Dependent Properties". *Proc. Int. Conf. of Concrete at Early Ages,* RILEM, Paris (France).

Rots J.C. (1988). *Computational Modeling of Concrete Fracture.* Doctoral Thesis, Delft University of Technology, Delft (The Netherlands).

Springenschmid R. (1995). "Thermal Cracking in Concrete at Early Ages". *Proc. Int. RILEM Symposium*, Munich (Germany), October 1994, pub. by E & FN Spon.

Zanotti C., Meda A., Plizzari G. and Cangiano S. (2010a). "Crack-Risk Minimization in Concrete Structures undergoing Hygrothermal Phenomena". *Proc. Third fib Int. Conf. and Exhibition*, Washington D.C. (USA).

Zanotti C., Meda A., Plizzari G. and Cangiano S. (2010b). "Evaluation of the Risk of Cracking in Thin Concrete Walls due to Hydration Heat". *Proc. Sixth Int. Conf. on Concrete Under Severe Conditions – Environment and Loading (CONSEC10)*, Merida (Yucatan, Mexico).

TRIAXIAL BEHAVIOR OF CONCRETE: EFFECT OF CONCRETE MIX DESIGN

Laurent Daudeville[1], Xuan Hong Vu[2] and Yann Malecot[1]

ABSTRACT

The identification of concrete behavior under dynamical loading (near-field detonation or ballistic impact) is the objective of this paper. In order to reproduce high stress levels according to well-controlled loading paths, static tests were carried out on concrete specimens, by means of a very high-capacity triaxial press (stress levels close to 1 GPa).

The effect that concrete mix design (water-cement ratio, cement-paste volume, aggregate size) has on concrete behavior under high triaxial loading is specifically addressed, with reference to static conditions. The experimental results confirm that highly-confined concrete behaves like a granular assembly, with the cement matrix playing no role at all.

The mechanical behavior of highly-confined concrete is hardly affected by water/cement ratio. Furthermore, increasing the cement-paste volume and the aggregate size has different effects with respect to little-confined concrete, where both the strength and the stiffness increase significantly in the former case and slightly in the latter case.

Finally, increasing the confinement level tends to homogenize the ultimate strengths of different concretes, as shown by the experimental results of this project concerning three concretes covering the range 20-60 MPa.

KEYWORDS : concrete, mix design, high confinement, triaxial tests

---

[1] Professor, Université Joseph Fourier, Laboratoire 3S-R, Grenoble, France.
[2] Associate Prof., Université Claude Bernard, Laboratoire GCIE, Lyon, France.

1. INTRODUCTION

Concrete undergoes very severe triaxial loads in case of violent explosions or ballistic impacts (Warren et al., 2004). In such exceptional cases, and especially under impact, the target may be completely perforated. Hence the validation of concrete constitutive models, taking into account simultaneously the phenomena of brittle damage and irreversible strain in compaction, requires specific tests capable of reproducing complex loading paths.

The static characterization of a material in order to predict its dynamic behavior is nothing new in the study of geomaterials. Thereby the strain rate effects need to be studied as well. The rheological behavior of concrete under confined compression hardly depends on the strain rate in both dried and wet specimens (Forquin et al., 2010). Thus, the strain rate effect in compression can be neglected in numerical simulations (Hentz et al., 2004). The strong loading rate dependency in tension can mainly be explained by the influence of the propagation velocity of defects (Hild et al., 2003) and must be taken into account in simulations.

The static characterization has three advantages: the instrumentation of the specimen may be more complete than in a dynamical test; the loading path can be better controlled; and running the test is less expensive.

A high-capacity press, called GIGA, has been specifically designed and installed in the 3S-R Laboratory in collaboration with the technical center "Centre d'Etudes de Gramat" of DGA (Délégation Générale pour l'Armement, French Ministry of Defense). This joint effort is part of a larger research project on the vulnerability of concrete infrastructures under impact. This press allows to study ordinary concrete behavior for stress levels of the order of Giga Pascal (Vu et al., 2009a; Vu et al., 2009b; Gabet et al., 2008; Poinard et al., 2010; Dupray et al., 2009). Within this context, the influence of the mix design (aggregate volume, aggregate size, water-cement ratio) on concrete behavior under high triaxial compression loading is investigated.

Most of the available experimental results refers to triaxial loading with moderate confining pressure (Li et al. 1970). More specifically, experimental studies on the triaxial behavior of cementitious materials have been carried out on small mortar samples (Bazant et al. 1986; Burlion et al. 2001). The novelty of the present study is that the analysis of the triaxial response refers to "real" concrete, with aggregate dimensions close to one centimeter, at very high confinement levels.

The experimental set-up used to perform the current study is described in Section 2, while Section 3 presents the main results concerning the effects of the water/cement ratio, and Sections 4 and 5 introduce the influence of coarse-aggregate size and cement-paste volume, respectively.

The presentation of the main conclusions and the outlook of the future work end the paper.

2. EXPERIMENTAL SET-UP

The GIGA press is a large-capacity triaxial press, which has been specifically designed and developed for this study. Cylindrical concrete specimens ($\varnothing = 70$ mm; h = 140 mm) can be tested by applying confining pressures as large as 0.85 GPa and axial stresses up to 2.35 GPa. A picture of the press, as well as a section of the specimen and of the loading apparatus are shown in Figure 1 (Vu et al., 2009c).

The concrete specimen, surrounded by a membrane impermeable to the confinement fluid, is placed between tungsten-carbide caps. The instrumentation of the specimens consists of one Linear Variable Differential Transformer (LVDT) for measuring the axial displacement, one axial gauge and two circumferential gauges (Figure 2).
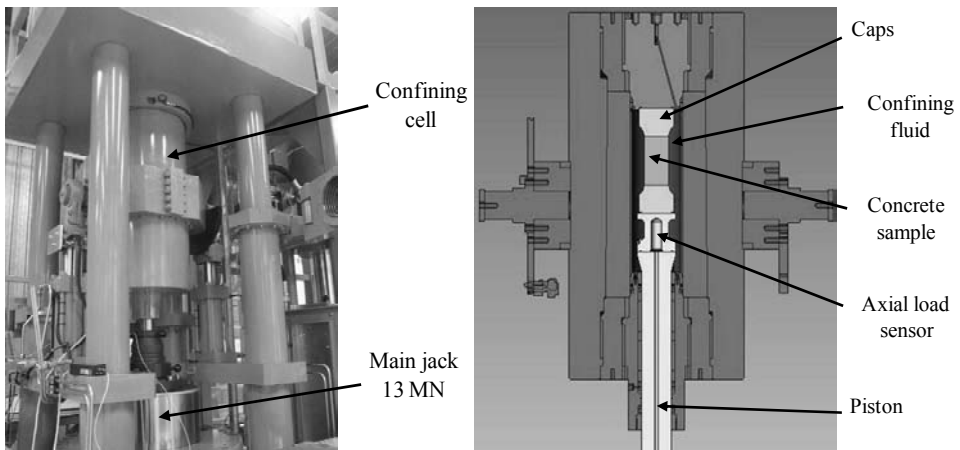
Figure 1 – GIGA press (left); and cross-section of the confining cell (right).

The LVDT sensor used in this study is Type 500XS-3013 by Schaevitz Sensors Company. The gauges (EP-08-10CBE-12 type from Vishay Micro-measurements Company) are 28 mm long. These gauges allow strain measurements up to 15%. The axial stress applied to the specimen and the pressure inside the cell are monitored by means of force- and pressure-sensors. The porous nature of the concrete requires the development of a protective multilayer membrane surrounding the specimen, in order to prevent the confining fluid from infiltrating the specimen (Vu et al., 2009c), see Figure 2.

Compressive stresses and contraction strains are assumed to be positive; the following symbols are used : σ_x = principal axial stress; p = pressure inside the confining cell; σ_m = mean stress; q = principal-stress difference (deviatoric stress); ε_v = volumetric strain; ε_x = axial strain; and ε_θ = circumferential strain:

$$\sigma_m = \frac{\sigma_x + 2p}{3} \qquad\qquad q = \sigma_x - p \qquad\qquad \varepsilon_v = \varepsilon_x + 2\varepsilon_\theta$$
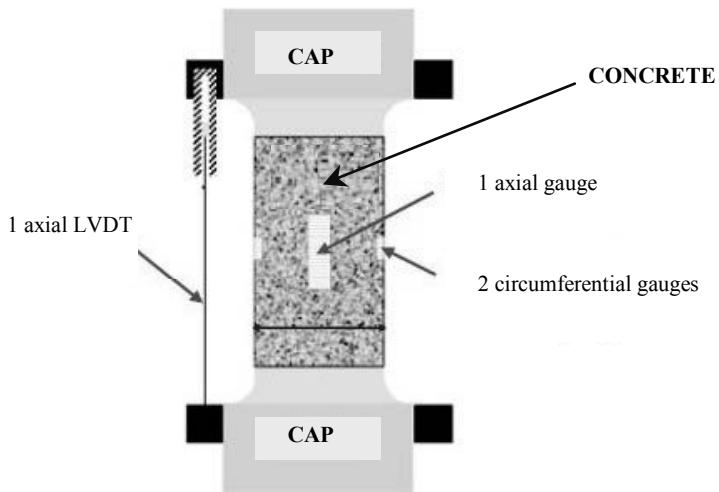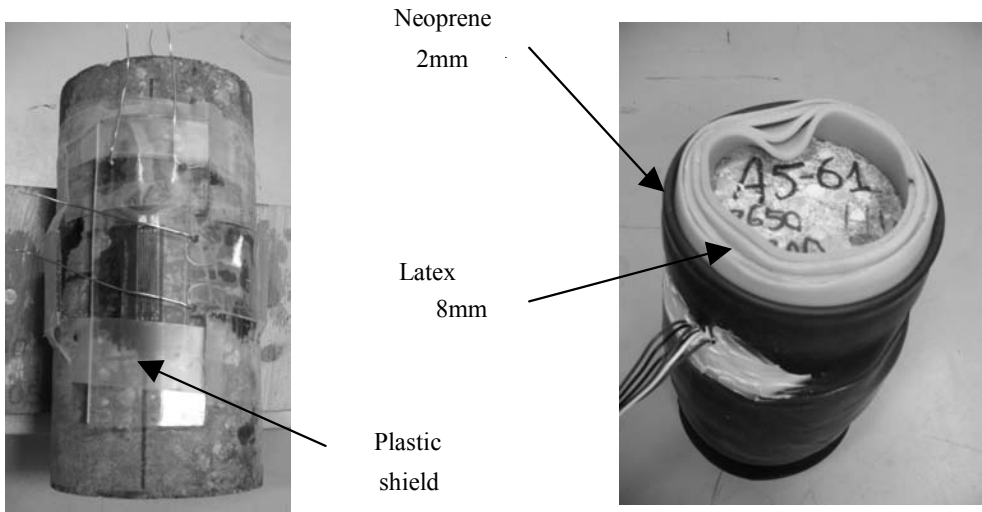

Figure 2 – Instrumentation and protective membrane.

All tests were carried out according to the same loading procedure. Each test in triaxial compression starts with hydrostatic loading. This stage is called "hydrostatic phase". Once the desired confinement is reached, the specimen is axially loaded, while the confining pressure is kept constant (Figure 3). This stage is called "deviatoric phase". Note that in all tests the value of the maximum deviatoric stress is not imposed, but it is measured during the test.

The tests were carried by controlling the confining pressure p and the piston displacement (Figure 1, displacement-controlled tests)).
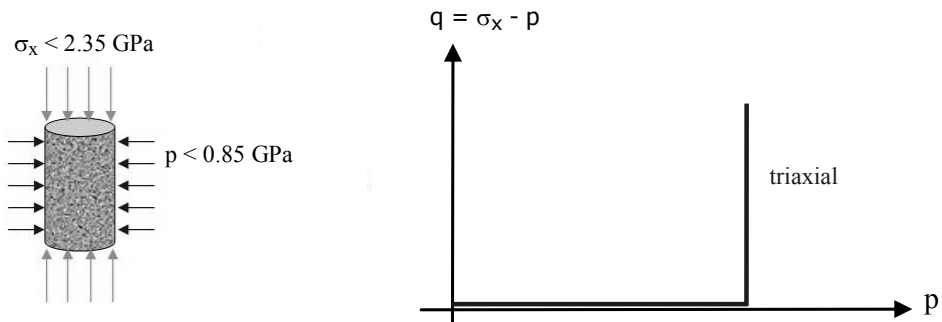
Figure 3 – Loading path.

3. INFLUENCE OF THE WATER/CEMENT RATIO

In order to study the effect of water/cement (w/c) ratio, the first step was to define the mix design of a "reference" concrete called R30A7. Because of the value 0.60 adopted for the water/cement ratio, the reference concrete is called EC06 in this section. (However, R30A7 and EC06 are synonims). By altering the water/cement ratio, two "modified" concretes (EC04 with w/c = 0.4 and EC08 with w/c = 0.8) were prepared (Vu et al., 2009b).

Except for the water/cement ratio, the three mixes are very close, and their aggregate skeletons are almost identical (Table 1).

A suitable procedure for manufacturing the specimens was defined in order to minimize the variability of concrete mechanical properties (Vu et al., 2009b). After cutting the extremities of the specimens to the desired length and smoothing the end sections, all specimens were stored in water for three months, in accordance with an identical curing procedure. The specimens were then dried for 3-6 months in a drying oven at 50°C and 8% RH. Mass stabilization, however, was reached after one month, when the daily variation - after the spell inside the oven - did not exceed 0.1%.

The triaxial tests were carried out with the confining pressure ranging from 0 to 650 MPa (Vu et al., 2009b). Figure 4 shows the results of the unconfined tests. As expected, the decrease of the water/cement (w/c) ratio produces an increase of both the peak stress σ_{max} and the Young's modulus E_c. Figure 5 shows the deviatoric part of the triaxial state of stress in the tests carried out at a confining pressure of 650 MPa.

The results indicate that the deviatoric behaviors of concretes EC08, EC06 and EC04 practically coincide. This result confirms that in highly-confined concrete, the cementitious matrix loses its cohesion, and that concrete behavior is mostly controlled by a sort of "granular stacking".

Since the granular skeletons of the concretes in question are identical, similar deviatoric behaviors were expected, which implies that in highly-confined conditions, concrete behavior is hardly sensitive to water/cement ratio.

Concrete mix design	EC04	EC06	EC08
Gravel from 0.5 to 8 mm (kg/m^3)	1000	1008	991
Sand ≤ 1800 μm (kg/m^3)	832	838	824
Cement CEM I 52.5 N PM ES CP2 (kg/m^3)	349	263	226
Water (kg/m^3)	136	169	181
Sikafluid Superplasticizer (kg/m^3)	4.5	0	0
Volume of entrapped air in fresh concrete (dm^3/m^3)	41	34	50.5
Mass per unit volume (kg/m^3)	2322	2278	2252
Water/cement (w/c) ratio	0.39	0.64	0.80
Cement paste volume V_p (m^3/m^3)	0.250	0.252	0.248
Concrete properties			
Unconfined compressive strength at 28 days (MPa)	57.0[*]	28.6	21.0[*]
Average slump (Abrams' cone, cm)	7.0	6.9	14.0
Porosity accessible to water	7 %	12 %	14 %

Table 1 – Mix design and mechanical properties of concretes EC04, EC06, EC08.

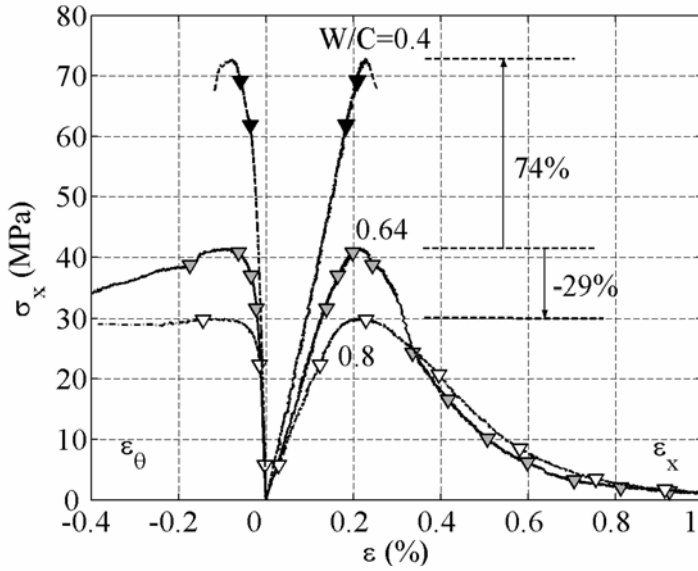Figure 4 – Unconfined compression - Experimental results for concretes EC08 (w/c = 0.8); EC06 (w/c = 0.64); and EC04 (w/c =0.4): plots of the axial stress σ_x vs. the strains ε_x and ε_θ.
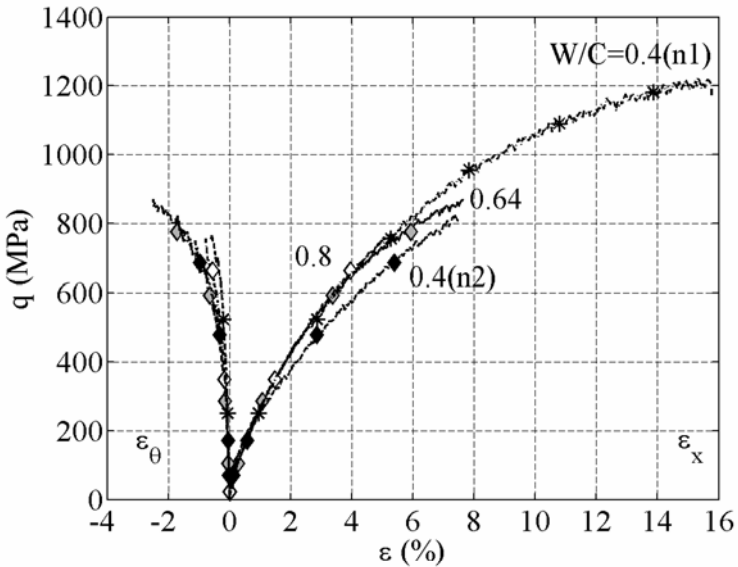

Figure 5 – Confined compression (650 MPa) - Experimental results for concretes EC08 (w/c = 0.8); EC06 (w/c = 0.64) and EC04 (w/c =0.4): plots of the stress deviator q vs. the strains ε_x and ε_θ. The tests on concrete EC04 are indicated separately for the first test (n1) and for the second test (n2).

4. INFLUENCE OF COARSE-AGGREGATE SIZE

In order to study the effect of coarse-aggregate size, from the mix design of the reference concrete (R30A7) two other concretes (Dmin) and (Dmax) were prepared with different maximum aggregate-size (d_a). Compared to Concrete R30A7 (d_a = 8 mm), Concrete Dmin has smaller aggregates (d_a = 3.15 mm), while Concrete Dmax has larger aggregates (d_a = 20 mm).

4.1 Modified mix designs

The modified mix designs are shown in Table 2, where the mix design of the reference concrete is indicated as well. The modified mixes (Dmin and Dmax) have the same cement-paste volume (total volume of water and cement) and the same aggregate volume as the reference mix (R30A7). Gravel with size 0.5-8 mm is replaced with gravel with size 2-3.15 mm in the mix Dmin and with gravel 0.5-20 in the mix Dmax. The granulometric curves are given in Figure 6. The specimens with the mixes Dmin and Dmax were cast, cured and dried exactly in the same manner as in the case of mix of R30A7. The porosity (Table 2) was measured by means of a high-pressure mercury-intrusion porosimeter. The values are similar because the three concretes have the same cement-paste volume and the same aggregate volume.
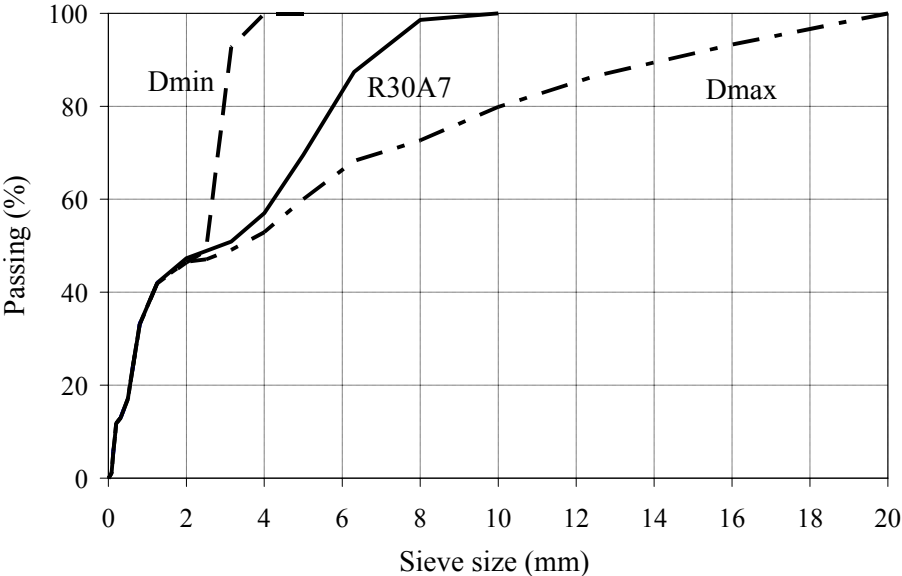

Figure 6 – Granulometric curves of concretes R30A7 (ref..), Dmin and Dmax

The granulometry of concrete R30A7 was established by means of the rather empirical Dreux's method (Dreux, 1985), in order to optimize the compactness of the granular skeleton. Hence, any change of coarse-aggregate size with respect to the reference concrete leads to a non-optimal compactness of the granular skeleton. In more detail, any reduction of the coarse-aggregate size contributes to the reduction of the compactness of the mix and to the increase of the friction between the cement paste and the aggregate particles. Conversely, any increase of coarse-aggregate size implies a larger granular range and leads to a better compactness. On the other hand, the "entanglement" of the coarse aggregate contributes to concrete compressive strength (Kaplan, 1959) and to concrete fracture energy, making crack propagation more difficult (i.e. more energy is required to force the crack to propagate, see Neville, 2002).

Concrete mix design (kg/m^3) and porosity (%)	Dmin	Dmax	R30A7
Gravel from 2 to 3.15 mm (d_a = 3.15 mm)	1006	-	
Gravel from 0.5 to 20 mm (d_a = 20 mm)	-	995	
Gravel from 0.5 to 8 mm (d_a = 8 mm)	-	-	1008
Sand ≤ 1800 μm	838	838	838
Cement CEM I 52.5 N PM ES CP2 (Vicat)	263	263	263
Water	169	169	169
Porosity accessible to mercury (%)	11.5	10.7	12.6

Table 2 – Mix design and porosity of concretes Dmin, Dmax and R30A7 characterized by different values of the maximum aggregate size (d_a).

4.2 Results of the triaxial tests

The behaviors of the three concretes Dmin, Dmax and R30A7 during the triaxial tests carried out at no confinement (0 MPa, unconfined compression), at 100 MPa and 650 MPa are presented and discussed in the following.

4.2.1 Unconfined-compression tests

In Figures 7 and 8, the responses of the three concretes R30A7, Dmin and Dmax tested in unconfined compression are shown, in terms of mean stress vs. volumetric strain, and axial stress vs. circumferential and axial strains. The slight differences of the volumetric behaviors (Figure 7) are related to the small differences in terms of porosity (Table 2). Under unconfined compression, both the strength and the Young's modulus increase with the size of the coarse aggregate (Figure 8), as observed in the literature (Kaplan, 1959).
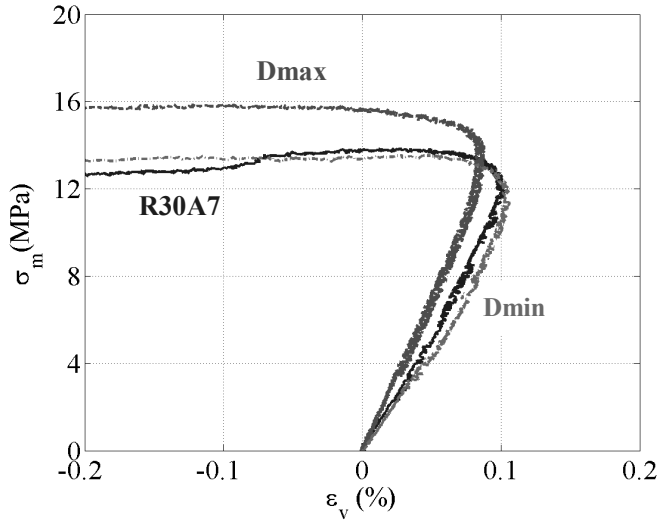
Figure 7 – Unconfined compression: plots of the mean stress σ_m vs. the volumetric strain ε_v for concretes R30A7 (solid line), Dmin (dash-dotted line) and Dmax (dashed line).
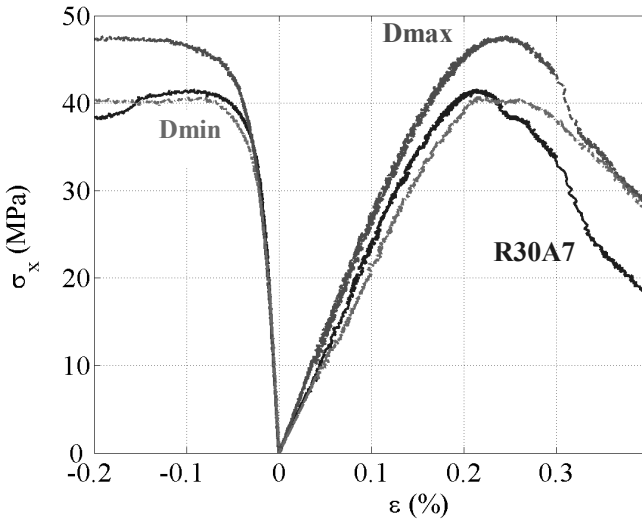

Figure 8 – Unconfined compression: plots of the axial stress σ_x vs. the strains ε_x and ε_θ for concretes R30A7 (solid line), Dmin (dash-dotted line) and Dmax (dashed line).

4.2.2 Tests carried out at 100 MPa confinement level

In Figures 9 and 10, the results of the triaxial tests carried out on the three concretes (Dmax, R30A7, Dmin) at 100 MPa confinement are shown.

Figure 9 shows that during the initial hydrostatic loading process, the volumetric responses of the three concretes are similar because of their similar porosities. Figure 10 indicates that the conclusions obtained in the case of unconfined compression are still valid.

At 100 MPa confinement level, concrete deviatoric behavior exhibits a stress threshold (peak deviatoric stress or extended plateau). This behavior can be explained by observing that at 100 MPa confinement level the cement matrix is still rather undamaged after the hydrostatic phase.

At higher confinement levels, when the cement matrix is seriously damaged after the hydrostatic phase, concrete displays a strain-hardening deviatoric behavior (as in the case shown in the next section).

4.2.3 Tests carried out at 650 MPa confinement level

Figures 11, 12 (that is an enlargement of figure 11) and 13 show the results of the triaxial tests carried out on the three concretes (Dmax, R3A7, Dmin) at 650 MPa confinement level.

Two tests were carried out on concrete Dmin (Dmin-a and Dmin-b), but in the former test both the LVDT and the gauges were used, while in the latter test only the LVDT was active. These figures confirm previous findings.

The compaction processes of the three concretes in the hydrostatic phase of the loading are similar because of the similar porosities of the materials (Figure 11). In the deviatoric phase, the largest volumetric strain is observed in concrete Dmin.

Furthermore, there is a transition from contraction to dilatancy in concretes Dmax and R30A7. This transition can be easily identified in Figure 12 (square symbol for concrete R30A7 and elliptic symbol for concrete Dmax), and corresponds to the maximum volumetric-strain state, in terms of contraction in the material. this transition can be defined as the strain limit-state of the material.

The mean stress level corresponding to this transition is slightly higher in concrete R30A7, whereas no contraction-dilatancy transition was observed in concrete Dmin, something that may be explained by observing that in this concrete the maximum mean stress level (about 950 MPa) does not create the conditions for the contraction-dilatancy transition.

Summing up, the higher the size of coarse aggregate, the lower the mean stress level corresponding to the concrete strain limit-state.
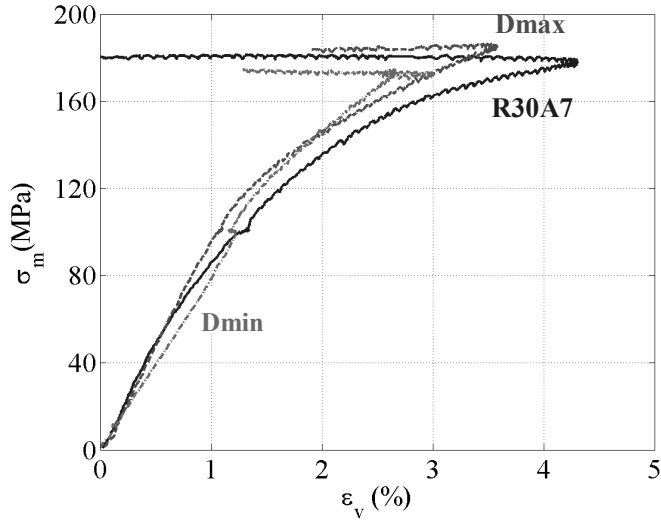
Figure 9 – Triaxial compression at 100 MPa confinement level: plots of the mean stress σ_m vs. the volumetric strain ε_v for concretes R30A7 (solid line), Dmin (dash-dotted line) and Dmax (dashed line).
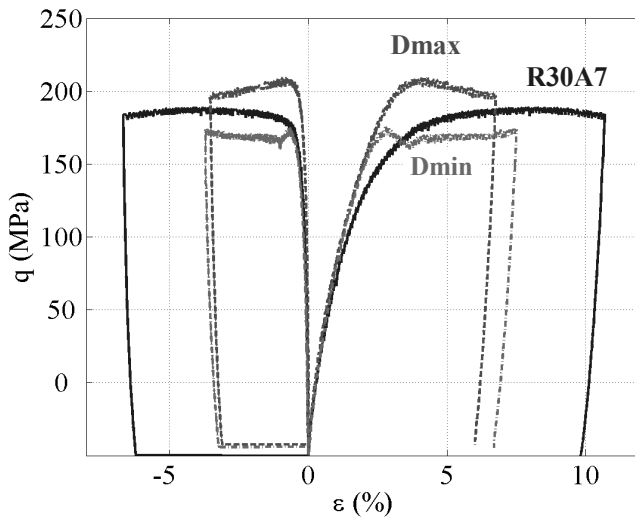

Figure 10 – Triaxial compression at 100 MPa confinement level: plots of the stress deviator q vs. the strains ε_x and ε_θ for concretes R30A7 (solid line), Dmin (dash-dotted line) and Dmax (dashed line).
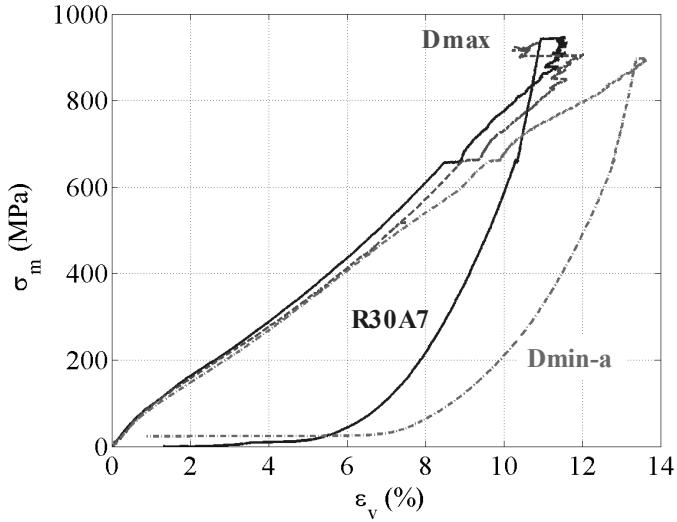
Figure 11 – Triaxial compression at 650 MPa confinement level: plots of the mean stress σ_m vs. the volumetric strain ε_v for concretes R30A7, Dmax and Dmin (Dmin-a: first test carried out on concrete Dmin).
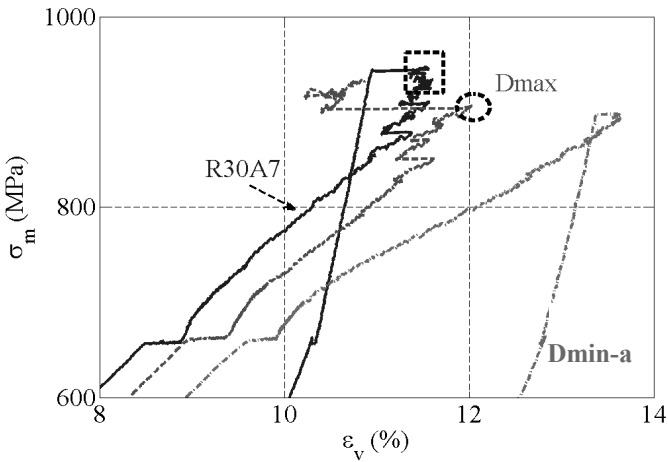

Figure 12 – Enlargement of figure 11 - Triaxial compression at 650 MPa confinement level: plots of the mean stress σ_m vs. the volumetric strain ε_v for concretes R30A7 (solid line), Dmax (dashed line) and Dmin (dash-dotted line) (Dmin-a: first test carried out on concrete Dmin). Contraction-dilatancy transition: square symbol for concrete R30A7 and elliptic symbol for concrete Dmax.
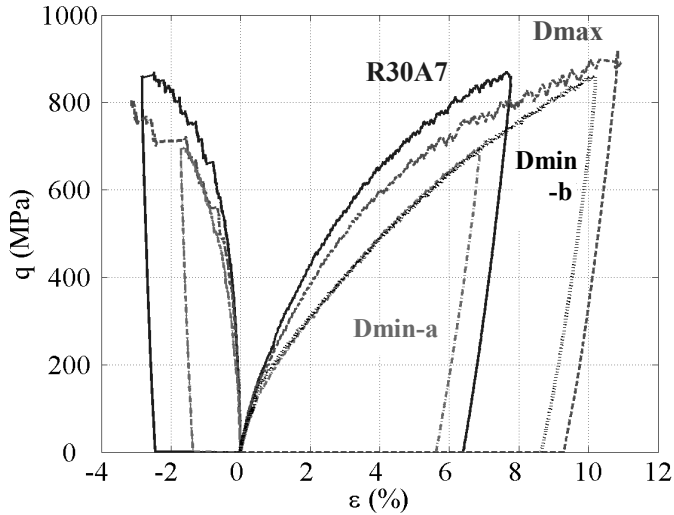
Figure 13 – Triaxial compression at 650 MPa confinement level: plots of the stress deviator q vs. the strains ε_x and ε_θ for concrete samples R30A7 (solid line), Dmin-a (dash-dotted line), Dmin-b (dashed line) and Dmax (dashed line).

Note: Dmin-a and Dmin-b indicate the two tests carried out on two different samples of concrete Dmin.

The three concretes have a hardening behavior (Figure 13), as the confining pressure corresponding to the transition between brittle and hardening behaviors has been exceeded. (The value of this confining pressure is close to 100MPa for concrete R30A7, Figure10).

Below this confining level, the cement matrix is still cohesive and it is mainly the cement matrix that contributes to concrete response. Above this confinement level, the cement matrix has lost its cohesion, and concrete response is governed by the stacking of the aggregate particles (concrete behaves like a granular material).

The capability of the aggregate particles to rotate under shear loading seems to be related to aggregate size. Thus, the higher the aggregate size, the lower the deformation capability of the concrete.

Contrary to what has been observed in unconfined compression, at 650MPa confinement level, the differences among the plots of the deviatoric stress are rather limited (the maximum difference is about 160 MPa for values of the deviatoric strain close to 6%). A more thorough examination of the curves in Figure 13 shows that at high deviatoric strain levels (above 6%) the axial tangent stiffness of concrete D_{min} is higher than that of concrete D_{max}.

5. INFLUENCE OF THE CEMENT-PASTE VOLUME

The influence of the cement-paste volume (or of the aggregate volume) with constant water/cement ratio and gravel/sand ratio is now presented.

5.1 Mix design

Two modified mix designs were adopted (Table 3). The first (Vpi) has a cement-paste volume reduced by 40 liters (per 1000 liters of concrete) and the second (Vps) increased by 40 liters. A volume reduction of the cement paste at constant water/cement ratio requires the amount of water to be reduced; hence, it is necessary to add a water-reducing additive (Sikafluid) to guarantee a slump of at least 70 mm (concrete Vpi). Conversely, the concrete Vps is more liquid and should not be vibrated, in order to avoid aggregate segregation. Casting, curing, drying and manufacturing of the specimens made of concretes Vpi and Vps were the same as for concrete R30A7.

The values of the porosity accessible to mercury intrusion are presented in Table 3, where it is shown that the smaller the cement-paste volume (or the larger the aggregate volume), the larger the porosity.

Concrete mix design (kg/m^3) and porosity (%)	Vpi	Vps	R30A7
Gravel from 0.5 to 8 mm	1064	950	1008
Sand ≤ 1800 μm	885	791	838
Cement CEM I 52.5 N PM ES CP2 (Vicat)	221	304	263
Water (water reducing admixture Sikafluid)	138 (5.31)	196	169
Porosity accessible to mercury (%)	15.2	11.7	12.6

Table 3 – Mix design and porosity of the three concretes tested to study the effect of cement-paste volume.

5.2 Results of the triaxial tests

The behavior of the three concretes Vpi, Vps and R30A7 during the triaxial tests carried out at no confinement (0 MPa, unconfined compression) and at 100 MPa and 650 MPa confinement is presented in the following.

5.2.1 Unconfined-compression tests

In unconfined compression (Figures 14 and 15), the volumetric strain decreases slightly, while the strength and the Young's modulus increase significantly following the increase of cement-paste volume. The strength of concrete Vps is
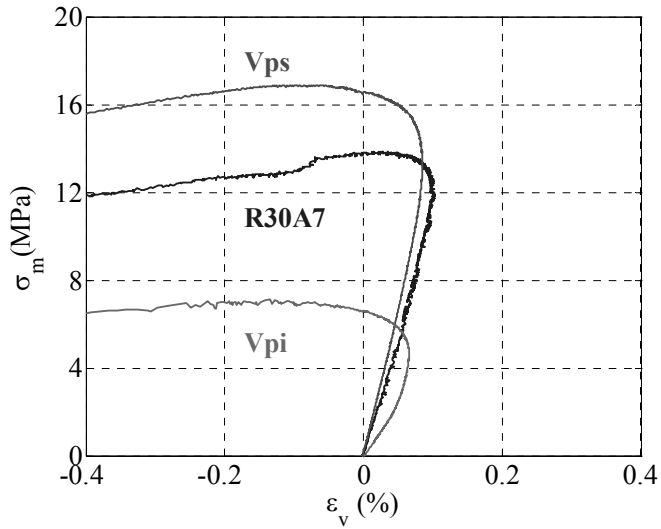
Figure 14 – Unconfined compression: plots of the mean stress σ_m vs. the volumetric strain ε_v for concretes R30A7 (solid line), Vpi (dash-dotted line) and Vps (dashed line).
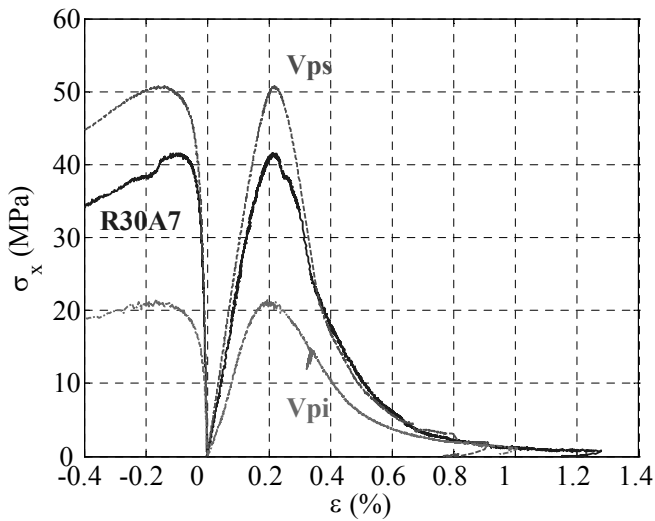

Figure 15 – Unconfined compression: plots of the axial stress σ_x vs. the strains ε_x and ε_θ for concretes R30A7 (solid line), Vpi (dash-dotted line) and Vps (dashed line).

2.5 times higher than that of concrete Vpi (Figure 14), in agreement with the information available in the literature (Singh 1958).

5.2.2 Tests carried out at 100 MPa confinement level

Figure 16 shows the volumetric responses of the three concretes. During the initial hydrostatic phase, the volumetric strain of concrete Vpi is the highest and that of concrete Vps is the lowest. This result is coherent with the different porosity of the concretes (Table 3).

Figure 17 presents the deviatoric responses of the three concretes. Compared to simple compression, a decrease can be observed in terms of difference among the strengths of the three concretes. Furthermore, concrete Vps has a stress peak, followed by strain softening. Concrete R30A7 shows a ductile behavior with a horizontal plateau. Concrete Vpi exhibits a strain-hardening behavior.

5.2.3 Tests carried out at 650 MPa confinement lvel

Figures 18 and 19 show the results of the triaxial tests carried out on the three concretes (Vps, R3A7, Vpi) at 650 MPa confinement level. At very high confinement levels, a decrease of the cement-paste volume brings in an increase of the deformation capacity (Figure 18), because the phenomena observed at low confinement levels are reversed (the cementitious matrix is no longer cohesive).

At 650MPa confinement level, the differences between the deviatoric stress of the three concretes are rather limited (the maximum difference is about 200 MPa for values of the deviatoric strain close to 4%).

A more thorough observation of the curves in Figure 19 indicates that for high deviatoric strain levels (above 6%), the larger the cement-paste volume, the smaller the axial tangent stiffness of the concrete. Thus, at high confinement levels, any reduction of the cement-paste volume increases the deformation capacity of the material; as a result, the deviatoric stress slightly depends on the cement-paste volume. At high deviatoric strain levels, the larger the cement-paste volume, the smaller the axial tangent stiffness.

6. CONCLUSION AND FUTURE WORK

In this experimental investigation about the effects that mix design has on concrete behavior at very high confinement levels, a reference concrete (mix R30A7) was modified by varying only very few parameters, in order to identify the factors that play the leading role,. Thus, the effects of water/cement ratio, coarse-aggregate size and cement-paste volume were studied separately, keeping all other quantities constant.

The test results confirm that at high confinement-levels, concrete behaves like a granular material with hardly any influence of cement-matrix strength and water/cement ratio.
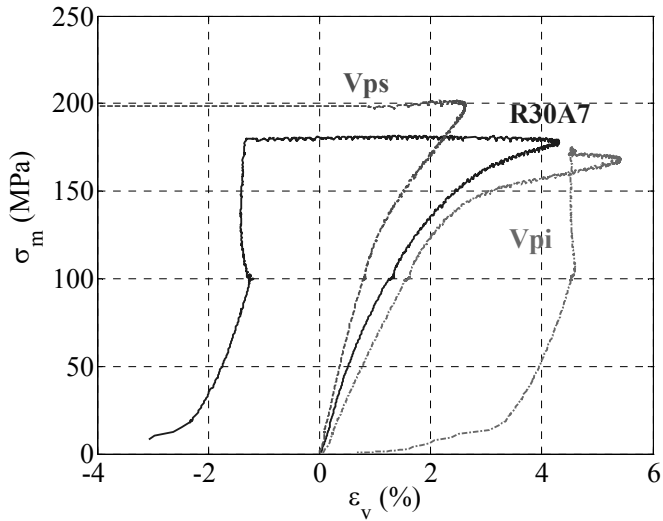
Figure 16 – Triaxial compression at 100 MPa confinement level: plots of the mean stress σ_m vs. the volumetric strain ε_v for concretes R30A7 (solid line), Vpi (dash-dotted line) and Vps (dashed line).

Figure 17 – Triaxial compression at 100 MPa confinement level: plots of the stress deviator q vs. the strains ε_x and ε_θ for concretes R30A7 (solid line), Vpi (dash-dotted line) and Vps (dashed line).

Figure 18 – Triaxial compression at 650 MPa confinement level: plots of the mean stress σ_m vs. the volumetric strain ε_v for concretes R30A7 (solid line), Vpi (dash-dotted line) and Vps (dashed line).
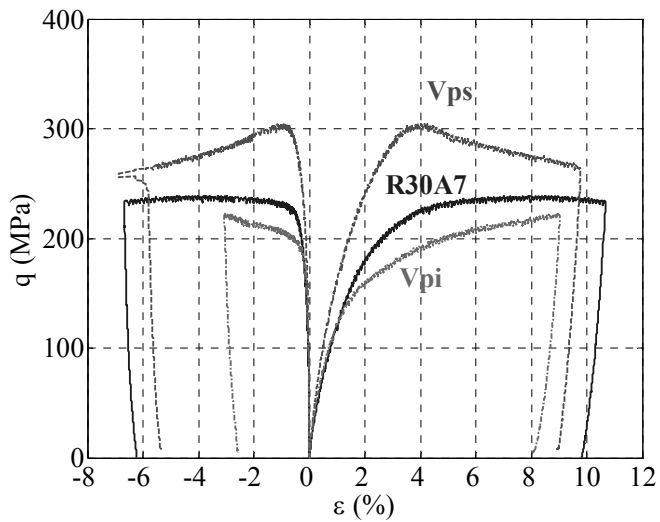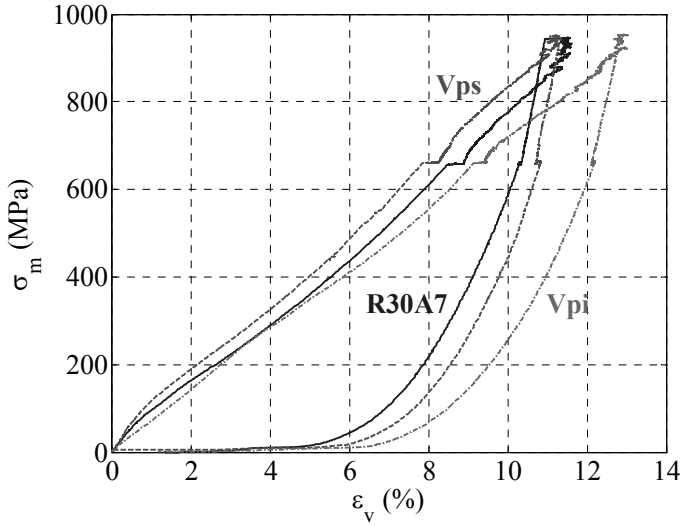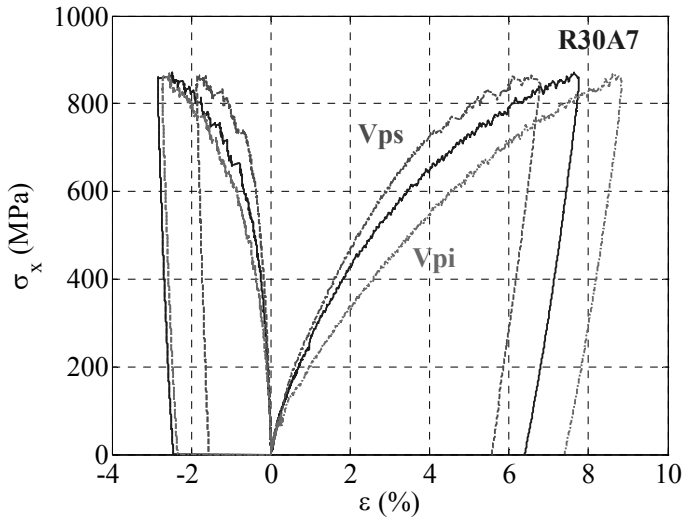

Figure 19 – Triaxial compression at 650 MPa confinement level: plots of the stress deviator q vs. the strains ε_x and ε_θ for concretes R30A7 (solid line), Vpi (dash-dotted line) and Vps (dashed line).

Coarse-aggregate size has a significant influence on the strain limit-state of concrete at high confinement-levels, since the higher the coarse-aggregate size, the lower the mean stress level corresponding to concrete strain limit-state. Furthermore, contrary to what has been observed in unconfined compression, at high confinement-levels the coarse-aggregate size has only a slight influence on the deviatoric-stress level; and the axial tangent stiffness increases (at high deviatoric strain levels), if the coarse-aggregate size is reduced.

The results of this study confirm earlier findings about the effects of cement-paste volume (or of aggregate volume). The cement-paste volume has a great influence at low confinement levels.

At high confinement levels, however, the cement matrix is no longer cohesive and concrete triaxial behavior is mostly governed by the stacking of the aggregate particles (concrete tends to behave as a granular material). Contrary to what has been observed in unconfined compression, at high confinement levels decreasing cement-paste volume increases concrete deformation capacity, with little effects on the deviatoric stresses.

At high confinement levels and at high deviatoric-strain levels, decreasing cement-paste volume increases concrete axial tangent stiffness.

For mean stress levels below 950 MPa and deviatoric stress levels below 900 MPa, coarse-aggregate size and cement paste volume have a limited influence on concrete strength. Furthermore, the tests show that at high mean stress levels and high strain levels, decreasing coarse-aggregate size and cement- paste volume may increase concrete axial tangent stiffness under extreme loads.

From an application standpoint, the results of this project show that concrete strength under extreme loads (such as impact or explosion) is governed by neither cement content nor water/cement ratio, contrary to what occurs under unconfined compression.

This rather unexpected result shows that the simplified formulae aimed at the design of concrete structures subjected to accidental or terrorist events must be considered with caution. Among these formulae, those by Li et al. (2003) concerning the penetration depth of a missile into a thick concrete slab, and by Berriaud et al. (1978) and Fullard et al. (1991) concerning the perforation ballistic limit of a reinforced concrete slab should be recalled, because the strength f_c in unconfined conditions is the only mechanical parameter introduced for the concrete.

As for the test set-up used in this study, axial stresses as large as 1.6 GPa can be applied to concrete specimens (diameter 70 mm; length 140 mm).

Some modifications and improvements, however, are in progress on the set-up in order to accommodate smaller specimens (diameter 50 mm; length 105 mm) and to induce higher deviatoric stresses.

In this way, the roles played by coarse-aggregate size and cement-paste volume will be more thoroughly investigated with reference to concrete deviatoric behavior.

REFERENCES

Bazant Z., Bishop F. and Chang, T. (1986). "Confined Compression Tests of Cement Paste and Concrete up to 300 ksi". *ACI Journal*, 33, pp.553–560.

Berriaud C., Sokolovsky A., Gueraud R., Dulac J. and Labrot R. (1978). "Local Behaviour of Reinforced-Concrete Walls under the Impact of a Non-Deformable Projectile" (in French). *Nuclear Engineering and Design*, 45 (2), pp. 457-469.

Burlion N., Pijaudier-Cabot G. and Dahan N. (2001). "Experimental Analysis of Compaction of Concrete and Mortar". *International Journal for Numerical and Analytical Methods in Geomechanics*, 25, pp.1467–1486.

Dreux G. (1985). *Nouveau guide du béton (New Guidelines for Concrete,* in French*)*, Eyrolles Ed.

Dupray F. Malecot Y., Daudeville L. and Buzaud E. (2009). "A Mesoscopic Model for the Behavior of Concrete under High Confinement". *International Journal for Numerical and Analytical Methods in Geomechanics*, 33, pp.1407-1423.

Forquin P., Safa K. and Gary G. (2010). "Influence of Free Water on the Quasi-Static and Dynamic Strength of Concrete in Confined Compression Tests". *Cement and Concrete Research*, 40(2), pp. 321-333.

Fullard K., Baum M.R. and Barr P. (1991). "The Assessment of Impact of Nuclear Power Plant Structures in the United Kingdom". *Nuclear Engineering and Design*, 130, pp.113-120.

Gabet T., Malécot Y. and Daudeville L. (2008). "Triaxial Behavior of Concrete under High Stresses - Influence of the Loading Path on Compaction and Limit States". *Cement and Concrete Research*,. 38 (3), pp.403-412.

Hentz S., Donze F. and Daudeville L. (2004). "Discrete Element Modelling of Concrete Submitted to Dynamic Loading at High Strain Rates". *Computers and Structures*, 82 (29-30), pp. 2509-2524

Hild F., Denoual C., Forquin P. and Brajer X. (2003). "On the Probabilistic-Deterministic Transition Strains Involved in a Fragmentation Process of Brittle Materials". *Computers and Structures*, 81(12), pp.1241–1254.

Kaplan M.F. (1959). "Flexural and Compressive Strength of Concrete as Affected by Properties of Coarse Aggregates". *ACI Journal Proc.*, 55 (11), pp.1193-1208.

Li H. and Pugh D. (1970). *Mechanical Behaviour of Materials under Pressure*. Elsevier, 1970.

Li Q.M. and Chen X.W. (2003). "Dimensionless Formulae for Penetration Depth of Concrete Target Impacted by a Non-Deformable Projectile". *International Journal of Impact Engineering*. 28(1), pp.93-116.

Neville A. M. (2002). *Properties of concrete*. Fourth Edition. Pearson Prentice Hall. 2002.

Poinard C., Malecot Y. and Daudeville L. (2010). "Damage of Concrete in a very High-Stress State - Experimental Investigation". *Materials and Structures*, 43(1-2), pp.15-29.

Singh B.G. (1958). "Specific Surface of Aggregates Related to Compressive and Flexural Strength of Concrete". *ACI Journal Proceedings*, 54 (4), pp.897-907.

Vu X. H., Malecot Y., Daudeville L. and Buzaud E. (2009a). "Experimental Analysis of Concrete Behavior under High Confinement - Effect of the Saturation Ratio". *International Journal of Solids and Structures*, 46, pp.1105-1120.

Vu X.H., Malecot Y., Daudeville L. and Buzaud E. (2009b). "Effect of the Water/Cement Ratio on Concrete Behavior under Extreme Loading". *International Journal for Numerical and Analytical Methods in Geomechanics*, 33(17), pp.1867–1888.

Vu X.H., Malecot Y. and Daudeville L. (2009c). "Strain Measurements on Porous Concrete Samples for Triaxial Compression and Extension Tests under very High Confinement". *Journal of Strain Analysis for Engineering Design*, 44(8), pp.633-657.

Warren T., Fossum A. and Frew D. (2004). "Experimental Investigation of Size Effect in Concrete Fracture under Multiaxial Compression into Low-Strength Concrete (23 MPa): Target Characterization and Simulations". *International Journal of Impact Engineering*. 30, pp.477-503.

OPPORTUNITIES FOR INNOVATION AND PERSPECTIVES FOR SUSTAINABLE TECHNOLOGIES IN CONCRETE INDUSTRY

Giacomo Moriconi[1]

ABSTRACT

The concrete construction industry has the responsibility before the Society to take actions in order to reduce its environmental impact. The concrete industry, however, should not consider this obligation in negative terms, because it will bring in the opportunity to develop innovative technologies, to make concrete production more sustainable and to foster the design of higher-value buildings.

To move toward ecological sustainability, however, radical improvements in the production of goods should be achieved, by reducing drastically the consumption of raw materials. In the case of modern building materials, the long-term solution to the challenge of sustainability lies in markedly improving their durability.

Last but not least, one should remember that our resources are limited, and this is the case also of the minerals required by cement and concrete production, that have already been depleted - or even exhausted - in some locations. Yet, in spite of the growing awareness that resources are becoming scanty, there is a strong resistance against developing new sources.

---

[1] Professor, Department of Materials and Environmental Engineering and Physics, Università Politecnica delle Marche, Ancona, Italy.

1. INTRODUCTION

The rapid industrialization and population growth in last decades since the 1960s have resulted in the consumption of enormous amounts of earth's resources to produce goods and energy, causing unprecedented environmental changes on a global scale, according to many scholars.

Fortunately, mankind has recognized the nature of the problem, by accepting the challenge and developing the concept of "sustainable development".

Over 2.5 billion tons a year of cement, and enormous amounts of water and aggregates, are consumed worlwide in the production of concrete. These amounts will likely increase. Hence, the concrete construction industry has a responsibility to the society to take immediate action to reduce its environmental impact, by limiting the emission of carbon dioxide and of other greenhouse gases (GHGs). The concrete industry, however, should not consider this obligation in negative terms, as it offers the opportunity to develop innovative technologies. Their aim should not be to introduce new types of concrete, manufactured with expensive materials and special methods, but to formulate low-cost and highly durable concrete mixes containing the largest possible amounts of industrial and urban by-products, as a partial replacement of portland cement, virgin aggregate and water (Naik 2002; Mehta 2004). Selection of materials minimizing environmental impact should be encouraged, by providing means for the life-cycle assessment of the cradle-to-grave implications of building materials, in terms of carbon-dioxide emission, required primary energy, air and water pollution, and depletion of the environmental resources. Life-cycle assessment should be used to check whether the environmental performance of a structure exceeds defined performance values.

According to this new vision, notwithstanding the energy consumption of cement production and the related GHG emissions, concrete can take care of these negative effects and become an environmentally-sustainable material. This outstanding concrete property is mainly attributable to the possibility of easily incorporating mineral additions in the mix. Another positive property of concrete is carbon-dioxide uptake. Although the amount of uptake is low during the service life, the specific surface is multiplied - and the carbonation rate accelerates significantly - when a concrete structure is demolished and the concrete is crushed for future use. Some studies indicate that carbon-dioxide uptake can have a large effect on life cycle assessment.

The above-described approach will undoubtedly improve the technological sustainability of concrete as a construction material. To move toward ecological sustainability, however, it is necessary to achieve radical improvements in the production of our goods, by reducing drastically the wasteful consumption of raw materials. With reference to modern construction materials, the long-term solution to the problem of sustainability lies in markedly improving their durability, by applying the "making do with less" approach (Mehta, 2004). Otherwise, if the construction industry – and the Society as a whole - will continue with the

business-as-usual approach, the no-return point will be reached, with the natural support systems irreversibly damaged.

Much of the discussion of the sustainability of concrete industry has dealt so far with issues related to the materials (how to replace portland cement and to recycle the concrete removed from existing structures). However, any treatment of the sustainability of concrete industry should consider industry's concerns, that go well beyond the "greenness" of any given technology. For example, if the public opinion or the designers perceive concrete as a non-durable material, or as a material that is more difficult than others to design with, the sustainability of the industry is affected. A related view is that public funding is becoming a very limited resource, that has to meet many demands. As a result, publicly-funded infrastructures simply must last longer, since their replacement before a reasonable life span cannot be accepted (Holland 2002).

Last but not least, resources are limited, and this is the case also for the resources required by cement and concrete production, that have been depleted – oe even exhausted - in many locations. Yet, in spite of the growing awareness that resources are scanty, there is a strong resistance against developing new sources.

2. SUSTAINABILITY AND CONSTRUCTION DEVELOPMENT

Among the challenges of the future, "sustainability" is – according to many scholars - fundamental for all future developments of mankind.

The term sustainability entered into the public arena with the publication of the report *Our Common Future* (1987) by the World Commission on Environment and Development (also known as the Brundtland Commission Report). The Commission defined *sustainable development* as the ability to meet our current needs without compromising the ability of future generations to meet theirs. With an unprecedented rise in human population from 1.5 to 6 billion, during the short span of about 100 years, a sharp growth of both the agricultural and industrial sectors of the economy has occurred. Furthermore, with the rapid urbanization at the close of the 20th Century, it became clear that the World is running out of cheap sources of energy, water, and minerals. At the same time, the economic development model and the technological choices pursued by the industrialized nations have proved to be highly wasteful in terms of energy and resources (Mehta, 2004).

Sustainability has become an important transnational force, as global warming is believed to be one of the most serious environmental threat (see for instance the data available for the growth trend of carbon dioxide, Naik, 2007), which has to do primarily with the carbon dioxide released from the burning of the fossil fuels used to meet our hunger for energy, transportation and manufactured products. At the same time, the models at the base of our economic development and technological choices pursued by the industrialized nations have proved to be highly wasteful in

terms of energy and resources. Thus, what common sense should have taught time ago and direct experience is teaching now is that "*in a finite planet, the model of unlimited growth, unrestricted use of natural resources, and uncontrolled pollution of the environment is a recipe for self-destruction*" (Mehta 2004).

In the context of sustainability and global warming – which are the two most powerful forces shaping our world today - it is timely to review the current trends in the construction industry. Worldwide, buildings and other structures are a large consumer of energy and natural resources. They consume nearly 40% of the crushed stone together with sand and gravel, 25% of virgin wood, 16% of water, and 40% of the total energy (Mehta 2004). The most significant environmental impact of buildings is associated with their use, because of heating, cooling, lighting, ventilation, and waste disposal. In the industrialized countries, green-building design is a growing movement, that places environmental considerations at the forefront of the design process, in order to encourage any approach aimed at minimizing the use of energy and materials, and at reducing pollution (Mehta 2004).

Concrete is the most widely used building material in the world. To meet the estimated demand for concrete in the world, people are consuming very large amounts of cement, sand, gravel, crushed rock and fresh water for concrete mixing and curing. Furthermore, clinker production requires large amounts of fossil fuels. Definitely, among the manufacturing industries the concrete industry is the largest consumer of natural resources. Just to have an idea of this scenario, consider a bridge, which is – by its very nature – a friendly construction that connects communities otherwise separated by physical discontinuities, favours cultural exchanges, and widens knowledge and social horizons. Can a concrete bridge be considered sustainable, if each kilometre requires 30,000 tons of limestone rock (equivalent to the volume of concrete resulting from the demolition of a tall building), 2.5 million liters of water (equal to the water required by a person for 50 years), and will emit five million kilograms of carbon dioxide in the atmosphere, increasing the greenhouse effect and reducing the air quality without any respect for national borders? (Moriconi 2007).

Portland cement, the principal hydraulic cement being used worldwide in modern concrete structures, is not only a product of an energy-intensive industry but is also responsible for emitting GHGs, in so favoring global warming. The emissions of greenhouse gas associated with cement's production are estimated to amount to approximately 7% of the total carbon-dioxide emission. Moreover, modern portland-cement concrete is prone to cracking and not very durable. Thus, the efficiency of the concrete industry is rather poor in terms of materials performance.

According to several publications (see – for instance – Mehta, 2004 and Mehta 2009), the concrete industry may become sustainable by sparing concrete-making materials, by improving concrete durability and by adopting a holistic approach in both research activities concerning concrete technology and field practice.

Each step aimed at sustainability requires innovative thinking. Short-term strategies are necessary to foster a sustainable development, based (a) on the use of blended cements instead of pure portland cement, and (b) on the reduction of the clinker factor in blended cements through an increasing use of either industrial by-products or natural mineral additions. Moreover, the largest possible amount of waste materials coming from demolitions should be recycled as a partial replacement of virgin aggregates in concrete and mortar mixes.

The above-described methods will no doubt improve the technological sustainability of concrete as a construction material. However, to move toward ecological sustainability, we should radically improve resource conservation and productivity, by reducing drastically the wasteful consumption of materials. This means that the long-term solution to the challenge of sustainability of modern construction materials lies in dramatically improving their durability.

Nearly one-third of the total concrete produced today goes into repair and replacement of existing structures. However, should engineers start building their structures with a new type of concrete with a service life of 500 years instead of 50, then fresh concrete would be required only for new structures. According to this scenario, by the year 2050 the consumption of concrete should start to decline, even if the number of new structures would still increase because of the expected growrh of the population.

3. SUSTAINABILITY AND INNOVATION

As stated earlier, short-term and long-term strategies should not be mistrusted by concrete-construction industry, because of the ensuing opportunities to develop innovative technologies. Some innovation opportunities are described in the following.

3.1 Construction and Demolition Waste (C&DW)

Consider recycling of construction and demolition waste, which are at the extremities of concrete life-cycle loop (Corinaldesi et al., 2008). Construction and demolition waste (C&DW) can be suitably processed in recycling plants in order to produce recycled aggregates for new concrete (see the European Norm EN 12620, issued in 2006). The reuse of construction and demolition waste is essential from the viewpoint of concrete life-cycle assessment, because in this way aggregate production will be less demanding and safer, and concrete quality guaranteed, the environmental impact will decrease and the cost-effectiveness of the construction will be higher.

The previously-examined impact of cement on the environment can hardly be reduced. However, if the whole life-cycle of cement-based products is considered, the emission of carbon dioxide during the production of cement (because of

calcination of limestone) will be – at least partially – balanced by concrete carbonation during the building life-cycle. In this way, the environmental impact of cement is attenuated.

As for the environmental impact of aggregates, taking into account that the availability of natural aggregates is confined to mined, crushed and graded stone, it is useful to underline that mining of one ton of natural aggregates requires 20 MJ from oil and 9 MJ from electricity, while one ton of crushed stone requires 120 MJ from oil and 50 MJ from electricity, without including the energy for transporting the aggregates to the building site (Worrell et al., 1994). On the other hand, the energy required by the production of recycled aggregates from construction and demolition waste is close to 40 MJ from oil and to 15 MJ from electricity (Nicosia et al., 2000), that is less than one third of the energy required for crushed stone. In addition, by using demolished concrete for the aggregates, waste material can be recovered for useful applications instead of being disposed of in a landfill.

In Table 1 a conventional scenario is compared with a recycling scenario for ordinary concrete, by replacing fine crushed stone with recycled concrete (same volume fraction and same granulometry). The only differences in the mix design are due to the different mass per unit volume of the natural and recycled aggregates, and to the slightly higher cement content in the "recycled" concrete to offset the somewhat lower strength of the recycled aggregates. In spite of this, however, there is evidence concerning the closeness of the mechanical performance of the two materials.

Table 1 - Conventional vs. recycling scenario for ordinary concrete.

Mix Design	Conventional	Recycling
W/C	0.55	0.53
Water, kg	185	185
Cement Type CEM II/B-L, kg	335	350
Fine sand (0-4 mm), kg (% by volume)	346 (20)	343 (20)
Coarse sand (0-5 mm), kg (% by volume)	348 (20)	345 (20)
Fine crushed gravel (6-12 mm), kg (% by volume)	526 (30)	-
Recycled concrete (6-12 mm), kg (% by volume)	-	499 (30)
Crushed gravel (11-22 mm), kg (% by volume)	527 (30)	524 (30)
Superplasticizer, kg (% by weight of cement)	3.35 (1.0)	3.50 (1.0)
Air-entraining admixture, kg (% by weight of cement)	0.2 (0.06)	0.2 (0.06)
28-day compressive strength (MPa)	30	30
28-day tensile strength (MPa)	1.9	2.0
28-day secant elastic modulus (GPa)	31.2	31.1
180-day drying shrinkage (μm/m)	700	650

On the basis of these results, and of other well-documented findings, the most recent technical norms for the constructions issued by the Italian Council of the Public Works (January 2008) allow the use of recycled aggregates in structural concrete, ready-mix concrete and concrete for precast members included, as shown in Table 2.

Table 2 – Italian Technical Norms for Constructions (January 2008).

Origin of the recycled material	Concrete R_{ck} (*) (N/mm^2)	Percentage of use
building demolition (rubble)	= C 8/10	up to 100%
demolition of only concrete and r.c.	≤ C 30/37	≤ 30%
	≤ C 20/25	up to 60%
reuse of concrete inside qualified prefabrication plants – all strength classes	≤C45/55	up to 15%
concrete > C 45/55	same original strength class	up to 5%

(*) R_{ck} = concrete compressive characteristic strength measured on cubes.

It must be underlined that in Table 2 only coarse aggregates made of recycled concrete coming from demolition of concrete and reinforced-concrete structures can be used in new structural concrete (maximum percentage of recycled aggregates 30%, maximum concrete grade R_{ck} = 37 MPa). The percentage may be raised to 60% if concrete grade does not exceed 25 MPa. Recycled material coming "un-clean" from building demolitions (concrete rubble containing brick shards and low amounts of glass, as well as asphalt rubble) can be used only for non structural concrete (concrete grade not exceeding 10 MPa), as in sub-foundations and roadbeds. (In some codes, however, these "un-clean" concretes are allowed for structural use by adopting correcting factors related to the amounts of brick shards and glass rubble).

In any case, according to Italian technical norms for constructions, recycled aggregates are required to be chemically and physically certified prior to be used in concrete production; also the concrete should be tested and certified. In general, concrete containing recycled aggregates exhibits a slightly lower density (however higher than 2300 kg/m³) and a slightly higher water absorption (up to 7-8%), whilst all the other chemical and physical properties comply with the standard limits, including alkali reactivity (which is absent) and freezing resistance. On the other hand, their high water absorption seems to be responsible for the lower

drying shrinkage of recycled-aggregate concrete (Corinaldesi and Moriconi, 2010), thanks to the internal curing, as in lightweight concrete.

Regarding the economic impact and cost effectiveness, traditional costs have to be compared with eco-balanced costs, which take into account environmental costs. In this case, the eco-costs are the expenses for eliminating the environmental impact caused by the extraction of virgin aggregates and also the expenses to eliminate the environmental load if C&DW are not used in concrete (= cost of waste disposal in landfills). Table 3 shows a higher eco-balanced cost for the traditional scenario due to environmental remediation after quarrying, while a much lower eco-balanced cost is observed for the proposed recycling scenario, due to the saving of waste-disposal costs.

Table 3 - Traditional and eco-balanced costs (€) per cubic meter of concrete.

Type of concrete	Traditional cost	Eco-balanced cost
Conventional scenario	64	> 89
Recycling scenario	63	38

The results of this study show that recycled-aggregate concrete may have a satisfactory quality as a structural material through materials selection. In addition, the use of recycled aggregates can reduce both the environmental impact and the cost (in particular the eco-balanced cost) of concrete. It has been also suggested (Dosho, 2007) that – should concrete containing recycled coarse aggregate have a 30-50% replacement ratio – the costs would be reduced by about 40% in the case of new buildings and carbon-dioxide emissions would decrease by about 25%, with the same quality and safety levels of conventional concrete.

3.2 Cyclic behaviour of the joints made of recycled-aggregate concrete

Tests have been carried out on real-scale R/C beam-column joints made with recycled-aggregate concrete (Figure 1), in order to simulate joint behaviour in seismic conditions (Corinaldesi and Moriconi, 2006).

The joints have been designed according to Eurocodes 2 and 8. The load-displacement hysteretic cycles have been recorded for increasing displacements of the beam end up to 150 mm (Figure 2). Joint collapse occurred because of beam rupture according to the strong column - weak beam concept, at a maximum moment equal to 1.5 times the design moment (which is much larger than the maximum moment suggested by Eurocode = 1.2 times the design moment). Moreover, the dissipated energy was always very high at each displacement level and cycle.

Recycled-aggregate concrete exhibits a behaviour close to that of traditional concrete under seismic action, but its energy-dissipation capability is greater thanks to its larger deformability, which makes recycled-aggregate concrete suitable for structural use in seismic areas with replacement ratios up to 30%. Hence, new design criteria for recycled-aggregate concrete may be introduced on the basis of shear and not of the tensile strength.

Figure 1 – Typical test on a scaled beam-column joint made of recycled-aggregate concrete, under cyclic loading.
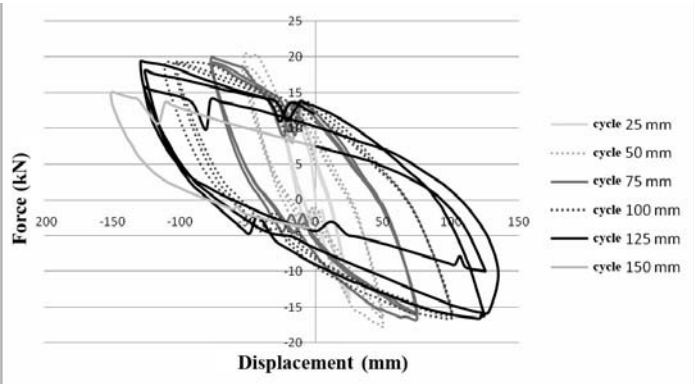
Figure 2 – Typica load-displacement hysteretic cycles.

3.3 Environmentally-friendly mortars

In the perspective of full C&DW recycling, the fine fraction produced by the recycling plants (which is detrimental to recycled-aggregate concrete strength) may be used as fine aggregate in mortars (recycled-aggregate mortars). In the same way, the brick fraction of C&DW may be ground in order to obtain a brick powder to be used as a binder in mortars.
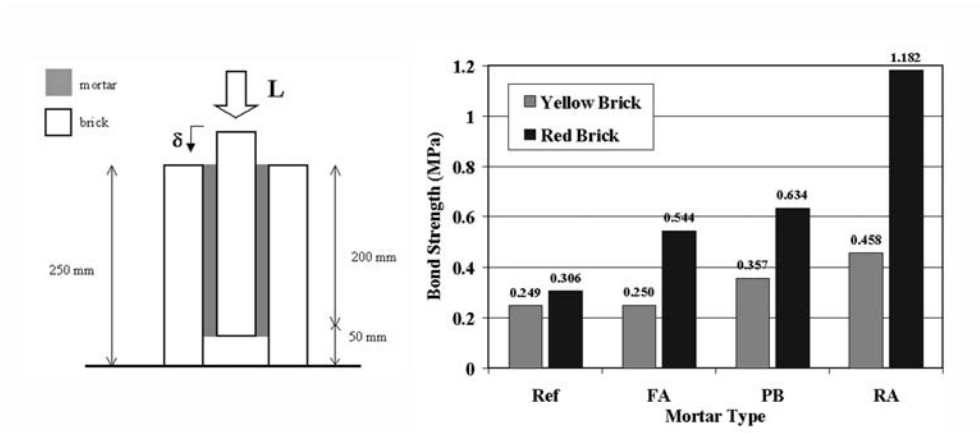

Figure 3 - Bond strength of mortar layers placed bricks.

Comparing recycled-aggregate mortars (RA), mortars with the cement partially replaced by brick powder (PB), cement mortars (Ref) and mortars containing fly ash (FA), allows to observe that environmentally-friendly mortars exhibit a lower compressive strength. However, in terms of mortar-brick bond (Figure 3), environmentally friendly mortars exhibit a much better bond strength, something welcome, as the interfaces are generally recognized as the weak chain link in masonry assemblies (Corinaldesi et al., 2002; Moriconi et al., 2003; Corinaldesi and Moriconi, 2009). These results are good news, since the interface shear strength is often more critical than the compressive strength in the collapse mechanisms typical of masonry buildings subjected to the horizontal loads induced by seismic action.

3.4 Rubble powder as a mineral addition in self-compacting concrete

Hundred percent recycling becomes viable on condition that the very fine fraction (0-90 µm) remaining from the recycling plant be used as mineral addition for reducing bleeding and segregation in concrete.

Rubble powder has been used to prepare self-compacting concrete, as a filler replacing limestone powder (Corinaldesi and Moriconi, 2003). Using rubble powder allowed to pass all self-compactability tests, and the compressive strength was hardly affected. As a matter of fact, the rubble powder (that is the finest fraction produced during the C&DW recycling process) proved to be an excellent filler for self-compacting concrete; this means that even the *rejection of a rejection* can be profitably used (Moriconi 2005).

3.5 Affordable Reactive Powder Concrete

As a final example, the use of silica fume can be considered from a different point of view in relation to sustainability, as silica fume is in itself a waste material, which increases both the mechanical and physical properties of a concrete, if added to the mix in proper amounts.

Special mixes with silica fume and very fine aggregates can push concrete properties to the extreme, like in Reactive Powder Concrete (RPC).

Reactive Powder Concrete (Richard and Cheyrezy, 1994), with compressive strength higher than 200 and up to 800 MPa, as well as flexural strength higher than 60 and up to 150 MPa, is a new material for structural use, even though its application fields are still rather undefined. Reactive Powder Concrete can be considered as the ultimate step in the development of high-performance concrete, even though its classification as a concrete is questionable, because its microstructure and mechanical behaviour are markedly different from those of ordinary and high-performance concretes. Furthermore, RPC's production technology – based on pressure moulding, thermal curing and extrusion – is totally different from that of ordinary concrete. The exceptional mechanical and physical properties of RPC makes it suitable for new shapes and structural types specifically designed for the use of this material.

Reactive Powder Concrete was listed by Roy (1987, 1992) among the "Densified materials with Small Particles" belonging to the general class of Chemically-Bonded Ceramics. Their mechanical performance is exceptional, due to the extremely closed microstructure resulting from the introduction of very fine well-graded aggregates and reinforcing constituents (microfibers), used in an integrated way, particularly when prepared in an intensive mixer able to exert high shear stresses and formed by compressive moulding. However, due to their complexity, high cost and apparent failure to comply with sustainability issues (energy-hungry manufacturing process), RPC's development is having little or no impact on the concrete industry as a whole.

Nevertheless, should lower mechanical properties be accepted (i.e. no pressure moulding and thermal curing, but soft casting), RPC would become more appealing from the sustainability point of view by using more common and easily available constituents, like limestone cement instead of pure portland cement, ordinary grey silica fume instead of white high class silica fume and very fine

limestone aggregate instead of quartz sand and microsilica (Moriconi and Corinaldesi, 2009). Mechanical performance (Table 3), which is slightly improved by thermal curing (that, however, is not fundamental) will be a bit lower, still much higher than in ordinary concrete, without decreasing RPC's high durability.

Table 3 – Mix design, processing treatment and related mechanical performance of laboratory-prepared RPCs.

Constituents [kg/m3]	RPC 200-a	RPC 200-b
CEM II/A-L 42.5 R Cement	960	960
Silica Fume (18 m^2/g)	250	250
Limestone Aggregate (0.15-1 mm)	960	960
Superplasticizer	96	96
Brassed Steel Fibres (L/d = 72)	192	192
Water	240	240
Treatment	RPC 200-a	RPC 200-b
Curing Temperature, °C	20	160
Mechanical Performance	RPC 200-a	RPC 200-b
Compressive Strength [MPa]	150	170
Flexural Strength [MPa]	33	34
Tensile Strength [MPa]	14	15
Fracture Energy [J/m^2]	44000	45000
Secant Elastic Modulus [GPa]	36	40
Tangent Elastic Modulus [GPa]	63	77
Poisson Modulus	0.19	0.17
Bond Strength with Steel Fibers [MPa]	32	34

Table 4 - Characteristics and performance of someconstruction materials.

Property / Material	RC	Glulam	Steel	RPC 200
Elastic Modulus [GPa]	25	12	210	60
Compressive Strength [MPa]	30	32	360	200
Tensile Strength [MPa]	3	15	360	45
Flexural Strength [MPa]	5	32	360	60
Unit Weight [kN/m^3]	25	5	78.5	25
Specific Elasticity [10^6 m]	1.0	2.4	2.7	2.6
Specific Strength [10^3 m]	1.2	6.4	4.6	8.7
Elastic Strain [%]	0.15	0.25	0.18	0.33
Ultimate Strain [%]	0.30	0.25	14	2
Ductility [%]	2.0	1.0	77	6.1
Fracture Energy [J/m^2]	300-400	-	-	20000-40000

By comparing RPC's performance with that of other available construction materials (Table 4), like reinforced concrete (RC), glued-laminate timber (glulam) and steel, RPC comes out with the highest values of specific elasticity (elastic modulus per unit weight), specific strength (strength per unit weight) and fracture energy. Hence, provided that RPC is reinforced with large amounts of steel microfibers (more than 4% by volume), its toughness – or ductility - is outstanding indeed (*toughness* = ability to keep a *sizable strength* even at large strains; *ductility* = ability to keep *integrity* even at large strains; often *toughness* is used for materials and *ductility* for structures). .
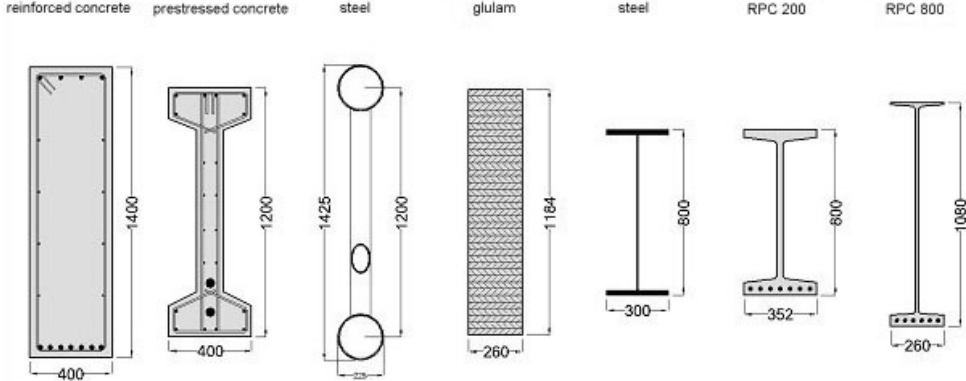
Figure 4 - Comparison of equivalent-strength beam sections obtained from calculations with seven different structural materials (all dimension are in mm).
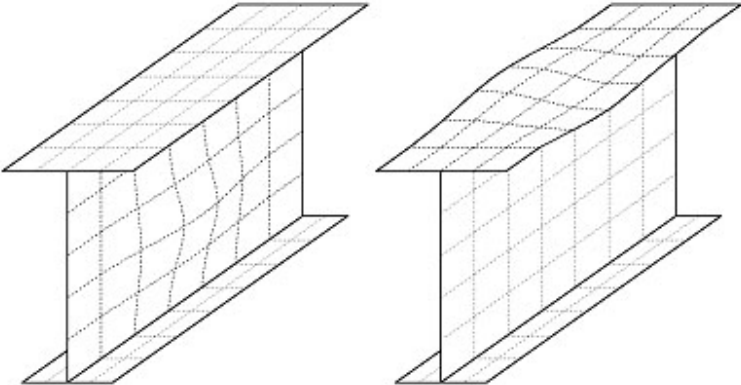
Figure 5 - Local instability in the thin parts of a structural member (beam): web (left) and flanges (right).

Equivalent-strength beam sections obtained from calculations for seven different structural materials show that RPC elements can be shaped and sized just like steel (Figure 4). However, local instabilities cannot be ruled out, as in the web and in the flanges of a steel beam (Figures 5 and 6).
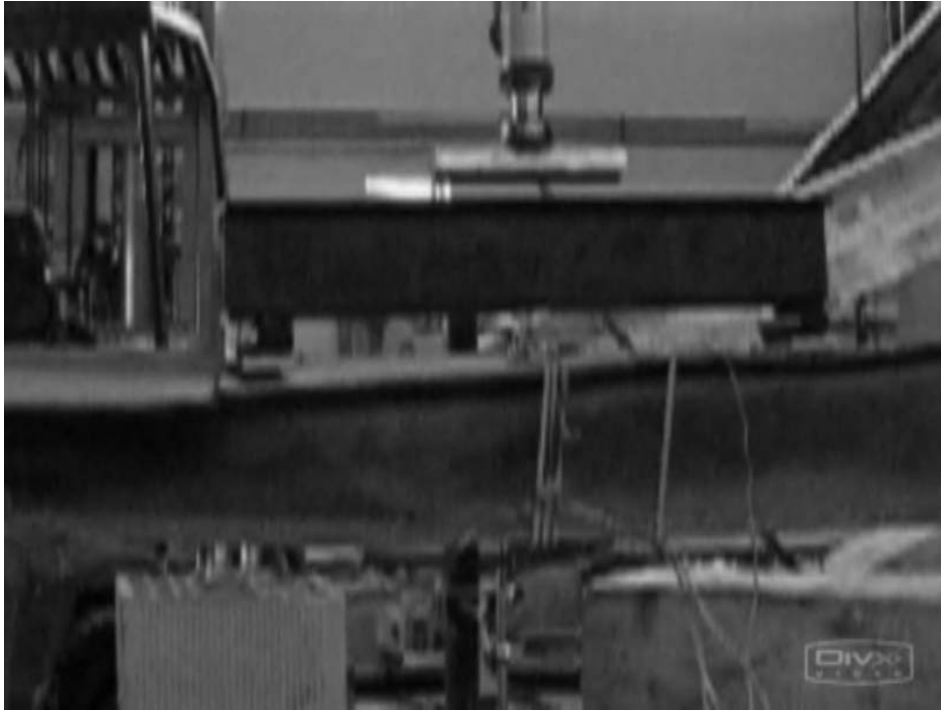

Figure 6 - Twisted I-shaped RPC beam under flexural stress.

RPC's opens new scenarios for highly-innovative – and even revolutionary - structures, since the traditional limits of cementitious materials are overrun, and steel efficiency and strength are challenged.

CONCLUSIONS

Against the indiscriminate use of natural non-renewable resources, today's technologies make by-products and secondary raw materials available to increase the sustainability of concrete structures.

As an example, concrete manufactured by using recycled aggregates is not less strong and durable than ordinary concrete when used in R/C structures. Using other by-products like fly ash and silica fume increases markedly concrete strength and durability.

In spite of the recent progresses in developing and using by-products and waste materials in structural concrete, designers and scholars should not give up challenging structures in the perspective of "sustainable development", and should adopt the *making do with less* approach, as far as possible.

ACKNOWLEDGEMENTS

REFERENCES

Corinaldesi V., Giuggiolini M. and Moriconi, G. (2002). *Waste Management*, 22(8), pp.893-899.

Corinaldesi V. and Moriconi G. (2003). "The Use of Recycled Aggregates from Building Demolition in Self-Compacting Concrete". *Proc. 3rd Int. RILEM Symposium on Self-Compacting Concrete*, RILEM Publication s.a.r.l., Bagneux, France, pp. 251-260.

Corinaldesi V. and Moriconi G. (2006). "Behavior of Beam-Column Joints Made of Sustainable Concrete under Cyclic Loading". *ASCE - Journal of Materials in Civil Engineering*, 18(5), pp. 650-658.

Corinaldesi V., Dezi L. and Moriconi G. (2008). "Recycling C&DW: A Way for Closing The Concrete Loop". *Proc.First Int. Symposium on Life-Cycle Civil Engineering*. Taylor & Francis Group, London (U.K.), pp. 799-804.

Corinaldesi V. and Moriconi G. (2009). "Behaviour of Cementitious Mortars Containing Different Kinds of Recycled Aggregate". *Construction and Building Materials*, 23(1), pp. 289–294.

Corinaldesi V. and Moriconi G. (2010). "Recycling of Rubble from Building Demolition for Low-Shrinkage Concretes". *Waste Management*, 30(4), pp. 655–659.

Dosho Y. (2007). "Development of a Sustainable Concrete Waste Recycling System". *Journal of Advanced Concrete Technology*, 5(1), pp. 27-42.

Holland T. C. (2002). "Sustainability of the Concrete Industry – What Should be ACI's Role?". *ACI-Concrete International*, 24(7), pp. 35-40.

Mehta P. K. (2004). "The Next Revolution in Materials of Construction". *VII AIMAT*, Ancona (Italy), Key-Note Lecture, 19 pp.

Mehta P. K. (2009). "Global Concrete Industry Sustainability". *ACI-Concrete International*, 31(2), pp. 45-48.

Moriconi G., Corinaldesi V. and Antonucci, R. (2003). "Environmentally-Friendly Mortars: a Way to Improve Bond between Mortar and Brick". *Materials & Structures*, 36(264), pp. 702-708.

Moriconi G. (2005). "Aggregate from Recycled Concrete and Demolition Wastes". *Proc. 2nd Int. Symposium on Concrete Technology for Sustainable Development with Emphasis on Infrastructure.* N. Bhanumathidas and N. Kalidas eds., Hyderabad (India), pp. 543-555.

Moriconi G. (2007). "Recyclable Materials in Concrete Technology: Sustainability and Durability". *Proc.1st Int. Conf. on Sustainable Construction Materials and Technologies.* R.N. Kraus, T.R. Naik, P. Claisse and H. Sadeghi-Pouya eds., Coventry (U.K.), pp. 1-12.

Moriconi G. and Corinaldesi V. (2009). "Cement-Based Composites for Structural Use: Design of Reactive Powder Concrete Elements". *Excellence in Concrete Construction through Innovation.* Taylor & Francis Group, London (U.K.), pp. 239-244.

Naik T. R. (2002). "Greener Concrete Using Recycled Materials". *ACI-Concrete International*, 24(7), pp. 45-49.

Naik T. R. (2007). "Sustainability of the Cement and Concrete Industries". *Proc.1st Int. Conf. on Sustainable Construction Materials and Technologies.* R.N. Kraus, T.R. Naik, P. Claisse and H. Sadeghi-Pouya eds., Coventry (U.K.).

Nicosia S., Lucchese A., Rizzo G. and Ercoli L. (2000). "A Contribution to the Ecobalance of the Recycling of Wastes from Construction and Demolition" (in Italian). *Innovation in Waste Management*, C.I.P.A., Milan (Italy), pp. 399-414.

Richard P. and Cheyrezy M.H. (1994). "Reactive Powder Concrete with High Ductility and 200-800 MPa Compressive Strength". *Proc. Int. Congress on Concrete Technology: Past, Present and Future*, P.K. Mehta ed., San Francisco (USA), pp. 507-518.

Roy D.M. (1987). "New Stronger Cement Materials: Chemically-Bonded Ceramics". *Science*, 235(4789), pp. 651-658.

Roy D.M. (1992). "Advanced Cement Systems Including CBC, DSP, MDF". *Proc. 9th Int. Congress on the Chemistry of Cement*; New Delhi (India), Vol. I, pp. 357-380.

Worrell E., van Heijningen R.J.J., de Castro J.F.M., Hazewinkel J.H.O., de Beer G., Faau A.P.C. and Vringer K. (1994). "New Gross-Energy Requirement Figures for Material Production". *Energy*, 19(6), pp. 627-640.

FLEXURAL FATIGUE OF FLY-ASH FIBRE-REINFORCED CONCRETE

Atef Badr[1]

ABSTRACT

In well-designed concrete mixes, the modification of the microstructure of concrete by using fly ash (FA) can produce concrete with desirable performance with regard to durability. However, this modification can also impair the ability of concrete to resist dynamic loads such as high cyclic loading. The potential reduction in the ability to resist dynamic loads can be restored by the ductility imparted by the addition of short steel fibres. This paper reports the results from a programme of laboratory research, which has been conducted to investigate the effect of fly ash on the fatigue strength of fibre-reinforced concrete (FRC).

Six different mixes were investigated. Three mixes without fibres, comprising a control mix without fly ash and two mixes containing fly ash at cement replacement levels of 25 % and 50 % on mass-to-mass basis. Three counterpart FRC mixes were produced by the addition of 1% (by volume) steel fibres.

The results show that fly ash has no effect on the absolute values of flexural fatigue strength. However, the normalised flexural fatigue strength of each fly-ash mix is slightly better than that of the counterpart Portland cement (CEM1) mix. As a conservative approach, it can be stated that fatigue strength of mixes containing fly ash is at least comparable to that of the counterpart CEM1 mixes. However, the effect of increasing fly-ash replacement level from 25 to 50% is negligible and, therefore, it is suggested to open a debate on amending the current BS EN 197 standards, which limit the use of fly ash to a replacement level of 35%.

KEYWORDS: Fly ash, fibres, replacement level, flexural fatigue

[1] PhD, MSc, BSc (Hons), CEng, MICE, FHEA
  School of Built Environment & Engineering, University of Bolton, UK

1. INTRODUCTION

In a bid to improve the sustainability of concrete and reduce its environmental impact, researchers and concrete technologists opted to use industrial by-products to replace part of the Portland cement (CEM1). Fly ash (FA), ground granulated blast furnace slag (GGBS) and silica fume (SF) are the most popular examples.

The utilisation of these materials in the production of concrete not only reduces its environmental impact but also enhances certain properties of concrete. Indeed, FA has become one of the most extensively used ingredient in the production of high-performance concrete (HPC) with desirable performance characteristics such as low porosity and permeability, as well as resistance to chemical attacks (Cabrera and Atis, 1999; Neville and Brooks, 1997; Sear, 2001). However, one of the main disadvantages of FA composites and HPC could be a reduction in the fracture energy and their tendency to exhibit increased brittleness (Bharatkumar et al., 2005; Brincker et al., 1997; Mendis, 2003). This mode of brittleness manifests itself in the reduction of desirable properties such as fatigue behaviour and resistance to fatigue crack growth. Taylor and Tait (2000) reported that mortar mixes containing fly ash were slightly less resistant to fatigue crack growth, particularly at later ages. The use of fibre reinforcement, however, provides an energy-absorption capability as well as a load-bearing capacity after cracking, which leads to enhanced static, impact and fatigue resistance (Badr et al., 2000; Uygunoğlu, 2008; Xu and Shi, 2009; Yazıcı et al., 2007). Thus it is rational to expect that the brittleness of concrete composites containing FA could be moderated by the improved ductility provided by the addition of fibres.

The most common applications for FRC include pavements such as in airports, highways and bridge decks (Gopalaratnam and Cherian, 2002; Krstulovic-Opara et al., 1995). In the design of these structures, fatigue strength is an important performance criterion, as they are required to withstand high cyclic loading.

2. OBJECTIVES AND SCOPE

This research was primarily conducted to investigate the effect of FA on the flexural fatigue strength of FRC, as adding FA increases concrete brittleness and - in principle - may diminish its fatigue strength.

In addition, the effectiveness of steel fibres in the presence of FA was also investigated.

3. EXPERIMENTAL PROGRAMME

The objectives of this investigation were achieved by studying six different mixes. A control mix was produced with neither FA nor fibres. A counterpart mix was produced with 1% (by volume) steel-fibre reinforcement but without FA. The effect of FA was investigated at two replacement levels (25 % and 50 %) on a

mass-to-mass basis. Four mixes containing FA were produced, two mixes without fibres and two mixes with 1% steel-fibre reinforcement.

3.1. Materials

Portland cement (CEM1), conforming to BS EN 197-1:2000, was used in this study as the main binder. Fly ash (FA), conforming to BS EN 4501-1:2005, was used as a cement replacement material. Table 1 gives the chemical composition of CEM1 and FA. The coarse aggregate was natural gravel of 10-mm nominal maximum size. The fine aggregate was quartzite sand (medium grading in accordance with zone MP of BS EN 12620:2008). A polymeric superplasticiser based on naphthalene sulphonates was added to the concrete mix to enhance its workability. Corrugated steel fibres were used (Figure 1) with nominal length of 50 mm and nominal diameter of 1 mm.

Table 1 - Chemical composition of the cementitious materials

Oxide	Oxide Content %	
	Portland Cement	Fly Ash
SiO2	20.39	53.17
Al2O3	4.58	24.30
Fe2O3	2.42	9.96
CaO	63.17	2.98
MgO	2.26	1.49
SO3	3.51	1.58
Na2O	0.21	0.94
K2O	0.76	2.43
Loss on ignition	1.69	2.58

3.2. Mix Proportions

Trial mixes were optimised, experimentally, to accommodate the fibre reinforcement. The optimised mix proportions were 1/1.9/2.1/0.42 (cement/sand/ coarse aggregate/ water) with a nominal cementitious content of 440 kg/m^3. These ratios were kept constant for all mixes. However, the addition of fibre and/or cement replacement materials changed the consistence of the fresh concrete as measured by the slump test according to BS EN 12350-2:2009. A slump of class S2 (40 to 100 mm) was maintained for all mixes by varying the dosage of the superplasticiser. The proportions of the various mixes are presented in Table 2.

The term "CEM-000" was used to identify the control Portland cement mix without FA or fibre reinforcement. The FA mixes were identified based on the level of replacement; i.e. FA25-000 and FA50-000. The Three counterpart FRC mixes were identified by the suffix FRC. For example, FA25-FRC denotes a FRC mix with 25% of the cement replaced with FA.
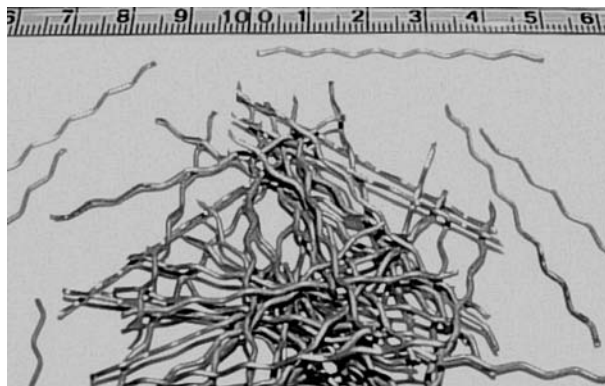

Figure 1 - Steel fibres used in this investigation.

Table 2 - Details of mix proportions / m^3

Mix	CEM1 kg	FA kg	Sand kg	Gravel kg	W/C Ratio	Fibre %	SP kg	Slump mm
CEM-000	440	-	836	924	0.42	0	0.00	40
FA25-000	310	110	836	924	0.42	0	0.00	50
FA50-000	220	220	836	924	0.42	0	0.00	110
CEM-FRC	440	-	836	924	0.42	1	3.52	40
FA25-FRC	310	110	836	924	0.42	1	2.20	70
FA50-FRC	220	220	836	924	0.42	1	0.00	100

3.3. Mixing and Production of Specimens

All concrete mixtures were produced using a rotary-drum concrete mixer. The aggregates and the cementitious material were initially mixed dry for 1 minute, before adding about half of the mixing water. After two minutes of mixing, the remaining mixing water and superplasticiser (if any) were added. Mixing was continued for a further three minutes, before adding the steel fibres, where applicable. The fibres were sprinkled into the drum by hand. Mixing was continued for a further three minutes to achieve uniform distribution of fibres.

Concrete specimens were produced for the different tests, including cubes (side = 100 mm) for compressive strength tests, and prisms (500×100×100 mm) for both static and fatigue tests in bending. The specimens were cast in 50 mm layers. Each layer was fully compacted, using a vibrating table. The specimens were covered with wet hessian and polyethylene sheets overnight. They were then de-moulded after 24 hours and cured in a curing water basin for 7 days. The water temperature was monitored continuously and the average was 20 ± 3 ^{o}C. After the initial 7-day wet curing, all specimens were transferred to an environmental chamber maintained at 20 ± 2 ^{o}C and 40 ± 5 % relative humidity, until the desired testing age was reached.

4. TEST PROCEDURES

4.1. Compressive Strength

The compressive strength was determined at the age of 28 days as a means of quality control. Another set of specimens were tested at the age of 91 days. The compressive strength of the hardened concrete cubes was determined according to BS EN 12390-3:2009. The tests were carried out using a digital automatic testing machine of a 3000 kN capacity, in accordance with BS EN12390-4:2000.

4.2. Static Flexural Strength

The static flexural test for each mix was carried out to establish the maximum stress level for the fatigue test. The static flexural strength was determined in accordance with BS EN 12390-5:2009. Five prisms from each mix were tested using third-points loading on a 300 mm span. The average of these five tests was taken as the static flexural strength "f_{sf}" of the mix.

4.3. Flexural Fatigue Strength

All fatigue tests were carried out using a closed-lop Electrohydraulic Universal Testing Machine. The third-points loading configuration used for determining the static flexural strength was also used in the flexural-fatigue strength tests. The

fatigue tests were conducted at various stress level "S", which relates the maximum fatigue stress "f_{max}" to the corresponding static flexural strength "f_{sf}" (thus $S = f_{max} / f_{sf}$). The stress level "S" ranged from 0.65 to 0.90. The fatigue tests were carried out by applying constant-amplitude sinusoidal non-reversal loads at a constant frequency of 20 cycles per second (20 Hz). Galloway and Raithby (1979) showed that the frequency of loading had no effect on fatigue performance over the range 4 to 20 Hz, and suggested the 20 Hz to be adopted as a standard-test frequency for fatigue testing of cement-bound materials. In all cases, the minimum load was kept at 0.5 kN to hold the specimen in place and avoid disruption in the loading system.

The fatigue strength is recorded as the number of cycles to failure of the specimen at a given stress level.

5.   RESULTS AND DISCUSSION

5.1. Compressive Strength

The compressive strength results at the ages of 28 and 91 days are given in Table 3, where each value represents the average of three specimens with a maximum variation of 5%.

Table 3 - Compressive and static flexural strength results

Mix	Compressive Strength MPa		Static Flexural Strength MPa
	28 days	91 days	91 days
CEM-000	60.5	71.7 (+19%)	5.42
FA25-000	56.2	68.8 (+22%)	5.37
FA50-000	54.9	67.9 (+24%)	5.26
CEM-FRC	68.7	80.3 (+17%)	6.59
FA25-FRC	64.8	78.7 (+21%)	6.93
FA50-FRC	63.3	77.5 (+22%)	6.73

The effect of FA on the compressive strength can be seen from Table 3. As it would be expected, mixes containing FA showed the lowest values compared to the counterpart CEM1 mixes. The difference was clearer at 28 days with an

average reduction of 8%. However, the strength of the FA mixes at the age of 91 days was very close to that of the CEM1 mixes (for all mixes, the mean increase compared to the 28-days strength is close to 20%). FA contributes more to the strength development at later ages (Lam et al., 1998; Oner et al., 2005; Sear, 2001). It was interesting to notice that the damage done due to increasing the FA replacement level from 25 to 50% was negligible. The average compressive strength of FA50-000 and FA50-FRC mixes was only 2% less than that of the FA25-000 and FA25-FRC mixes. This finding needs to be investigated further because it could have important implications on the concrete industry, as well as on the current standards. The possibility of increasing the level of cement replacement without adverse effect on the strength will certainly improve the reputation of concrete in terms of sustainability and environmental impact. Let alone the cost saving from the difference in prices between FA and CEM1. In addition this could open the door for debates on changing the current BS EN 197 standards, which limit the use of FA to a replacement level of 35%.

The effect of steel fibre can be detected by comparing the compressive strength of the plain mixes without fibres (CEM-000, FA25-000 and FA50-000) to the fibre-reinforced mixes (CEM-FRC, FA25- FRC and FA50- FRC). It can be seen that the addition of 1% (by volume) steel fibres resulted in higher strength regardless of the binder type or the age at testing. The average compressive strength of the FRC mixes was higher than that of plain mixes without fibres by 15%. The increase in compressive strength as a result of using steel fibres is in agreement with reported literature. Yazıcı et al. (2007) reported that usage of steel fibres in concrete increases the compressive strength by about 4–19%.

5.2. Static Flexural Strength

At the age of at 91 days, the static flexural strength "f_{sf}" of each mix was determined as the ultimate static flexural stress (modulus of rupture). The results are given in Table 3, where each value represents the average of five specimens.

The effect of steel fibre and FA on the static flexural strength was similar to the effect on compressive strength. However, the increase in the flexural strength due to the use of steel fibres was more noticeable. Steel fibres increased the static flexural strength by about 26 %. The corresponding increase in the compressive strength was 15 %. Lee and Barr (2004) indicated that the use of fibres is more effective under flexural loading than in compression. Under flexural loading, the fibres would be able to bridge cracks and arrest their propagation. Conversely, the mode of failure under compression loads does not induce a significant contribution from the fibres.

FA slightly reduced the flexural strength of the FA mixes without fibres (FA25-000 and FA50-000), compared to the control mix CEM-000. The average flexural strength for the FA mixes without fibres was only 2% less than that of the CEM-000 mix. However, FA slightly increased the flexural strength of FA mixes with

fibres (FA25-FRC and FA50-FRC). The average flexural strength for FA mixes with fibres was increased by 4% compared to the CEM-FRC mix. These values, whether it is the increase or the decrease, are small and could be attributed to variations within experimental results. However, the results followed a trend and in most cases the change was exaggerated as a result of raising the replacement level. For example, the flexural strength of mix FA25-000 was 5.37 MPa compared to 5.42 MPa for mix CEM-000. Raising the level of replacement to 50% resulted in a further reduction in the flexural strength so that the flexural strength of mix FA50-000 was only 5.26 MPa.

While it is easy to understand and explain the slight reduction of flexural strength of FA mixes without fibres (FA25-000 and FA50-000), the increase in the case of fibre-reinforced FA mixes (FA25-FRC and FA50-FRC) deserves an explanation. One could suggest that there was a synergy action between steel fibres and FA so that the fibres were more effective in the presence of FA. This can be attributed to enhancement in the properties of the transition zone at the fibre-paste interfaces.

5.3. Flexural Fatigue Strength

The results of the fatigue tests show that there is a non-linear relationship between the flexural fatigue strength and the number of loading cycles. However, presenting the flexural stress versus the logarithm of the number of cycles to failure transforms the relationship into a linear relationship, as can be seen in Figure 2.
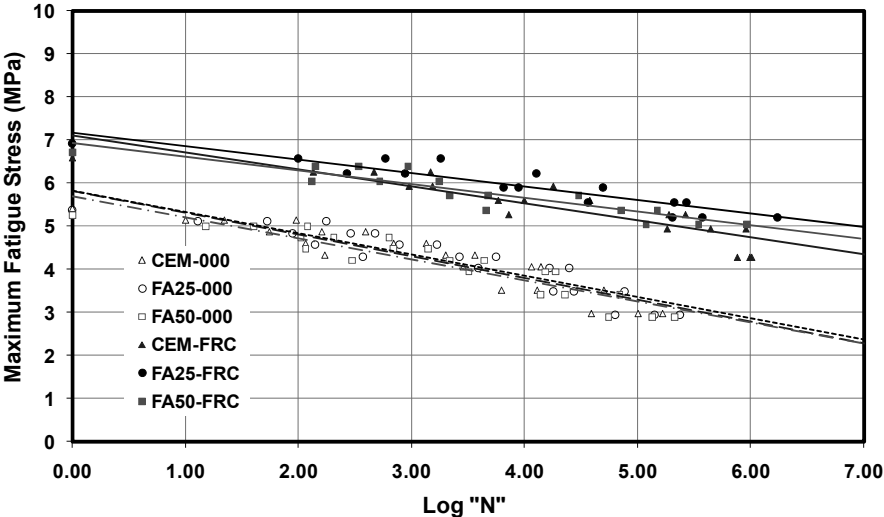
Figure 2 - Fatigue strength versus logarithm of number of cycles.

For every individual mix, the relationship is best described by a linear trend obtained by the least squares best fit. These linear relationships between fatigue stress and the logarithm of the number of cycles are commonly reported in the literature (Jun and Stang, 1998; Katoh et al., 2007; Ramakrishnan et al, 1992; Singh et al., 2005).

It can be seen from Figure 2 that steel fibres enhance the flexural fatigue behaviour significantly, particularly at high number of cycles. Based on the relationships in Figure 2, it seems that there is no difference in the behaviour of the three mixes without fibres (CEM-000, FA25-000 and FA50-000) indicating that FA has no effect on the flexural fatigue strength of concrete mixes without fibres. However, it is difficult to detect the effect of FA on the flexural fatigue strength in the presence of steel fibres, as the effect seems to vary with the number of cycles.

It is often acknowledged that the static flexural strength could have a crucial effect on the flexural fatigue behaviour (Jun and Stang, 1998; Singh et al., 2005). In order to eliminate the effect of the static flexural strength, the results of the flexural fatigue tests are normalised with respect to the static flexural strength of each mix. The normalised values are plotted against the logarithm of the number of cycles, as shown in Figure 3. Presenting the data in this way makes the effect of FA and steel fibres very clear. For example, Figure 3 reveals a slight increase in the normalised flexural fatigue for FA mixes compared to the counterpart CEM mixes.
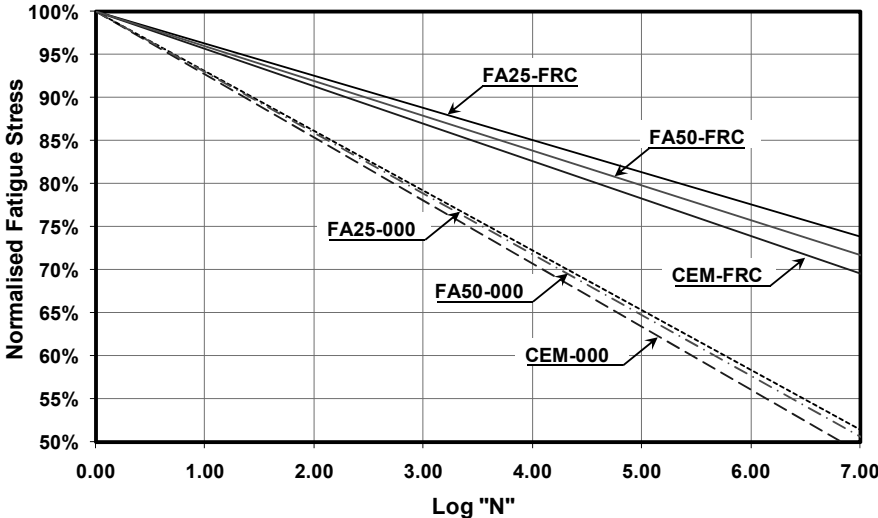

Figure 3 - Normalised fatigue strength versus logarithm of number of cycles.

Figure 3 also made a distinction between the effects of the two replacement levels. The improvement due to the use of 25% FA was slightly better than the improvement obtained using 50% FA. Again, it could be argued that the increase due to the use of FA was small and should be ignored. Nevertheless, the increase was noticed in all mixes containing FA and, therefore, this observation should be considered as a trend. However, as a conservative approach, the results obtained in this study suggest that the fatigue strength of mixes containing FA is at least comparable to that of the Portland cement mixes.

In addition, Figure 3 showed that the increase due to the use of steel fibre was more significant in mixes containing FA. Among all mixes, the optimum fatigue performance was obtained from the FA25-FRC mix. This underlines a positive synergy action between steel fibres and FA, which manifests itself as an improved effectiveness of the fibres in the presence of FA.

The linear equations for the trends obtained by the least-square best fit for every individual mix were used to isolate the effect of each parameter (FA and/or steel fibres) at 10^5 and 10^6 cycles. The results are presented in the bar chart given in Figure 4.
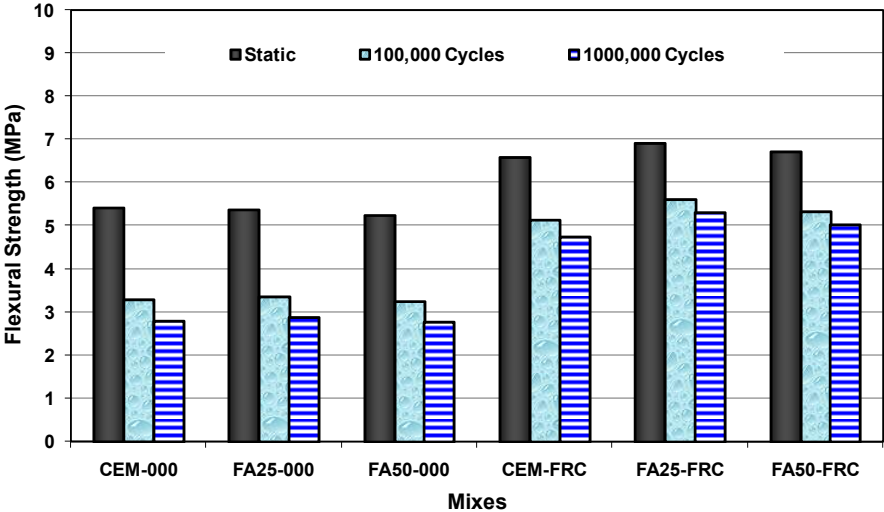
Figure 4 - Effect of fibres and fly ash at different number of cycles.

It can be seen that the effect of each parameter on the flexural fatigue strength was more or less similar to the effect on static flexural strength. In addition, Figure 4 revealed an interesting point. For all mixes, the reduction in flexural strength due to increasing the number of cycles from 10^5 to 10^6 is negligible compared to the damage that have already been done by the first 10^5 cycles. An attempt to

understand this point can be made in the light of the mechanism of fatigue failure in concrete as suggested by Gopalaratnam and Cherian (2002). They suggested that in the first stage of fatigue failure, fatigue damage is accumulated in the concrete matrix resulting in rapid cracking and deflection with increasing the number of fatigue cycles. The second stage is characterised by little or no growth in cracks and deflections due to stable and steady damage process. Therefore the results obtained in this study suggests that the first 10^5 cycles can be considered as the end limit of the first stage of the failure mechanism, whereas the second stage can be correlated to the number of cycles between 10^5 and 10^6. This outcome, if confirmed, could have important technical and economical implications. For example, it might be sufficient to perform fatigue tests up to 10^5 cycles to rank or compare several concrete mixes. However, further research is needed to confirm this finding.

6. CONCLUSIONS

For the concrete mixes, materials and testing methods used in this research, the following conclusions may be drawn:

- Replacing 25% of Portland cement with fly ash results in a reduction in concrete compressive strength by 8%. However the reduction due to increasing fly-ash replacement level from 25 to 50% is negligible. This finding could open the door for debates on amending the current BS EN 197 standards which limit the use of fly ash to a replacement level of 35%. (However, further tests on cements rather than on concretes, specifically aimed at FA replacement of klinker should be planned and carried out).

- Fly ash slightly reduces the flexural strength of mixes without fibres. However, it slightly increases the flexural strength of the FRC mixes suggesting a positive interaction between the fibres and fly ash, so that the fibres are more effective in the presence of fly ash.

- The relationship between flexural-fatigue strength and the logarithm of the number of cycles showed that fly ash has no effect on the flexural fatigue strength of concrete mixes without fibres. However, the normalised flexural-fatigue strength of each fly-ash mix (with or without fibres) enhances slightly compared to that of the counterpart CEM mix.

- Steel fibres enhance the flexural-fatigue behaviour significantly, particularly in mixes containing fly ash. The optimum fatigue performance is obtained from a fibre-reinforced mix with 25% fly ash.

- As a conservative approach, the results obtained in this study suggest that fatigue strength of fly-ash concrete is at least comparable to that of counterpart CEM1 mixes.

- The reduction in flexural strength, due to increasing the number of loading cycles from 10^5 to 10^6 , is negligible compared to the damage produced by the first 10^5 cycles. Thus, it might be sufficient to perform fatigue tests up to 10^5 cycles to rank several concrete mixes.

REFERENCES

Badr A., Brooks J., Abdel Reheem A. and El-Saeid A. (2000). "Impact Resistance and Compressive Strength of Steel and Organic Natural Fibre Reinforced Concretes". *Proc. 10th Concrete Communication Conf.*, June 29-30, Birmingham, UK, pp. 347-354.

Bharatkumar B., Raghuprasad B., Ramachandramurthy D., Narayanan R. and Gopalakrishnan S. (2005). "Effect of Fly Ash and Slag on the Fracture Characteristics of High Performance Concrete". *Materials and Structures*, Vol.38, No.1, pp. 63-72.

Brincker R., Simonsen J. and Hansen W. (1997). "Some Aspects of Formation of Cracks in FRC with Main Reinforcement". *Nordic Concrete Research*, No.20, 1-2/97, Oslo, pp. 1-15.

Cabrera J. and Atis C. (1999). "Design and Properties of High-Volume Fly Ash High-Performance Concrete". *ACI Special Publication*, Vol.186, pp. 21-38.

Galloway J. and Raithby K. (1979). "Effect of Rate of Loading on Flexural Strength and Fatigue Performance of Concrete". *TRRL Laboratory Report LR547*, Transport and Road Research Laboratory, Crowthorne, UK, 18 pp.

Gopalaratnam V. and Cherian T. (2002). "Fatigue Characteristics of Fiber Reinforced Concrete for Pavement Applications". *ACI Special Publication*, Vol.206, pp. 91-108.

Jun Z. and Stang H. (1998). "Fatigue Performance in Flexure of Fiber Reinforced Concrete". *ACI Materials Journal*, Vol.95, No.6, pp 58-67.

Katoh Y., Hamada S., Ichioka T. and Kobayshi R. (2007). "Flexural Fatigue Strength and Design by the P-S-N Curve for HVFA Pavement Concrete". *Journal of the Society of Materials Science*, Japan, Vol.56, No.4, pp.377-382.

Krstulovic-Opara N., Haghayeghi A., Haida M. and Krauss P. (1995). "Use of Conventional and High-Performance Steel-Fiber Reinforced Concrete for Bridge Deck Overlays." *ACI Materials Journal*, Vol.92, No.6, pp 669-677.

Lam L., Wong Y. and Poon C. (1998). "Effect of Fly Ash and Silica Fume on Compressive and Fracture Behaviours of Concrete." *Cement and Concrete Research*, Vol.28, No.2, pp. 271-283.

Lee M. and Barr B. (2004). "An Overview of the Fatigue Behaviour of Plain and Fibre Reinforced Concrete". *Cement and Concrete Composites*, Vol.26, pp. 299-305.

Mendis P. (2003). "Design of High-Strength Concrete Members: State-of-the-Art". *Progress in Structural Engineering and Materials*, Vol.5, No.1, pp. 1-15.

Neville A. and Brooks J. (1997). "Concrete Technology," *Longman Scientific & Technical*, London, England, 5th edition.

Oner A., Akyuz S. and Yildiz R. (2005). "An Experimental Study on Strength Development of Concrete Containing Fly Ash and Optimum Usage of Fly Ash in Concrete". *Cement and Concrete Research*, Vol.35, No.6, pp. 1165-1171.

Ramakrishnan V., Wu G. and Hosalli G. (1992). "Flexural Fatigue Strength, Endurance Limit and Impact Strength of Fiber Reinforced Concretes". *Transportation Research Record*, No.1226, pp 17-24.

Sear L. (2001). "Properties and Use of Coal Fly Ash: A Valuable Industrial By-Product". *Thomas Telford*, London, England, 1st edition.

Singh S., Singh B. and Kaushik S. (2005). "Probability of Fatigue Failure of Steel Fibrous Concrete". *Magazine of Concrete Research*, Vol.57, No.2, pp. 65-72.

Taylor P. and Tait R. (2000). "Investigation of Fatigue Crack Growth Mechanisms in Mortars Containing Fly Ash". *ACI Special Publication*, Vol.189, pp. 203-222.

Uygunoğlu T. (2008). "Investigation of Microstructure and Flexural Behavior of Steel-Fiber Reinforced Concrete". *Materials and Structures*, Vol.41, No.8, pp. 1441-1449.

Xu B. and Shi H. (2009). "Correlations Among Mechanical Properties of Steel Fiber Reinforced Concrete". *Construction and Building Materials*, Vol.23, No.12, pp. 3468-3474.

Yazıcı S., İnan G. and Tabak V. (2007). "Effect of Aspect Ratio and Volume Fraction of Steel Fiber on the Mechanical Properties of SFRC". *Construction and Building Materials*, Vol.21, No.6, pp. 1250-1254.

Technical Notes

A FOLDED-PLATE PAVILLION IN CAGLIARI-SARDINIA: A RE-EXAMINATION ACCORDING TO THE ITALIAN CODE OF 2008

Sergio Tattoni[1], Antonello Mastinu[2], Riccardo Porcu[1], Flavio Stochino[1]

ABSTRACT

The paper deals with the structural behaviour of the CasMez Pavilion, which is a R/C folded-plate structure built during the 50's as a symbol of Cagliari Exhibition Center (Fiera di Cagliari). The many changes occurred during its lifetime have markedly modified CasMez aspect with respect to the original project of 1953, that was characterized by features and proportions inspired by lightness and freedom. During the years, these changes brought to light some flaws of the structure, making it necessary to assess its safety level on the basis of the Limit-States Method, according to the recently-introduced Italian Design Code (2008). To this end, a thorough study of the structural behaviour was carried out. This study gave the opportunity to compare the original and the modern design methods and concepts. Within this context, the objective of this paper is two-fold: (1) to ascertain whether the assumptions used in the original structural analysis were adequate; and (2) to determine whether the structure can be considered "safe" according to the current Italian Design Code. The results are somewhat contradictory: whereas the original design is - on the whole - very conservative, a certain underestimation of the internal forces in some members is evident as a result of the use of FE analysis.

KEYWORDS: Existing R/C structures**, f**olded plates, FE analysis

---

[1] Department of Structural Engineering, University of Cagliari, Cagliari - Italy
[2] Civil Engineer, Bosa (Oristano) - Italy

1. INTRODUCTION

The CasMez pavilion was designed in 1953 by Arch. Adalberto Libera to the order of Cassa del Mezzogiorno (*Agency for the Development of Southern Italy*), in order to be a landmark of the New Trade Fair Center (*Fiera Campionaria*) of Cagliari, the capital city of Sardinia in the southern part of the island.

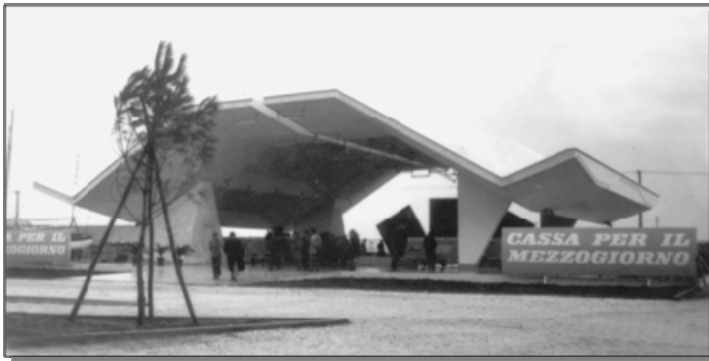The structural analysis was performed by MS Eng. Giorgio Girardet. There are no doubts that this structure is an outstanding example of the 20th Century architectural heritage.

Figure 1 - The CasMez pavilion during the opening ceremony.

The architectural idea was to build an open space for exhibitions appropriate for the typical warm weather and mild wind of Cagliari. It is interesting to quote Libera's original thinking: *"Dato il clima tipicamente mediterraneo di Cagliari si è pensato ad un organismo adeguato a quelle condizioni climatiche, e cioè ad uno spazio adombrato e ventilato"* (*"Because of the typical Mediterranean weather of Cagliari, our objective was to create a structure suitable to these environmental conditions, i.e. a shady and airy space"*).

The building was aligned with the avenue leading to the trade fair center and welcomed the visitor with its symmetrical shape.

The feeling of lightness and freedom is expressed by the wing shape of the roof, by the triangular shape of the columns, and - above all - by the absence of lateral walls. In this way, the visitor can see the whole city even from inside the pavilion.

Unfortunately, the main feature of the building proved to be its worse limit, since it could be used only during the summer. For this reason, in 1973 Architects Ubaldo and Roberto Badas were asked to design a system of walls to close laterally the building. The destination of the building was modified, and so the

functional and aesthetical intent of the original designer. (However, closing the building – already fallen into disuse – prevented its demolition).

Figure 2 - The building after the addition of the cladding walls.

1.1 Geometry of the Structure

The structure consists of two portals (see Figure 3). The portals are characterized by two T-shaped beam-columns, connected by a central hinge; the resulting structural model is a three-hinged statically determined arch. (Just before the grand opening, the two foundation footings of the south-east side underwent a large settlement – up to 50 cm – followed by the rotation of the whole structure about its longitudinal axis, see Fassio, 2004, and Loddo, 2001; because of its being statically determined, the structure did not exhibit any evident damage).

The triangular columns are tapered; each portal has only two parts with constant height connected asymmetrically with the others.

The 15 m-apart portals are connected by means of 10 longitudinal beams (each 26 m long and placed 2.50-3.40 m apart), and have a cantilever of 5.5 m at both ends (see Figure 4). The dimensions of the portal are the following: length = 12.90 m, width = 7.75 m, and thickness = 450 mm.

The R/C 100 mm-thick roof slab has a peculiar shape, because it joins the beams partly along their bottom and partly along their top, following the compression zones of the beams, that are subjected to bending actions (see Figure 5). This slab has both an architectural and a structural function. (Note that this conclusion comes from authors' analysis, as the designer never mentioned "structural functions" and probably was not aware of any of them).

As for the dimensions of the beams, in the central part (length = 18 m) the section is rectangular (1000 × 200 mm). The two cantilever at the ends have a variable section, with a maximum thickness of 300 mm. The foundations consist of four 2.2 × 2.2 × 1 m footings, each supported by four bored piles with a diameter of 400 mm.
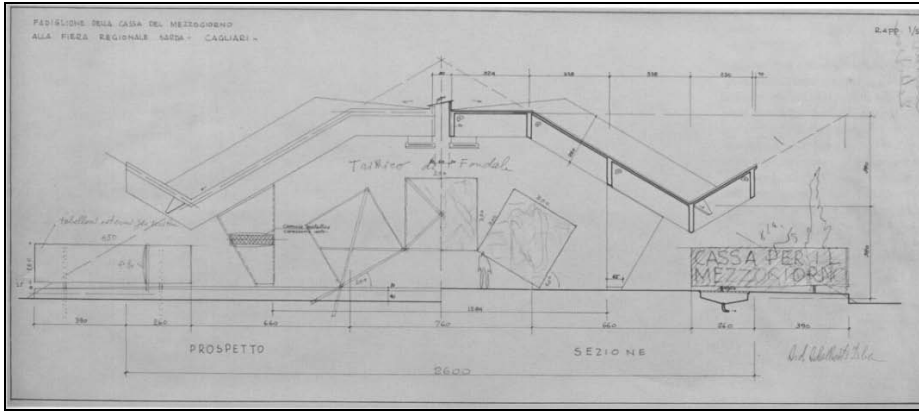
Figure 3 - Front view (left) and section (right) of the structure (original drawings).
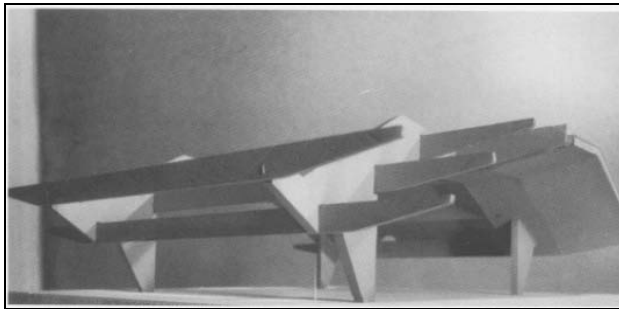

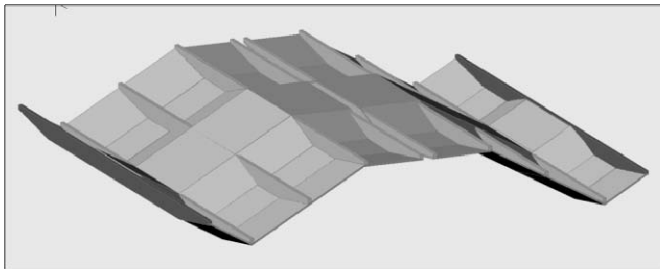Figure 4 - View of the structural members from the original timber model.

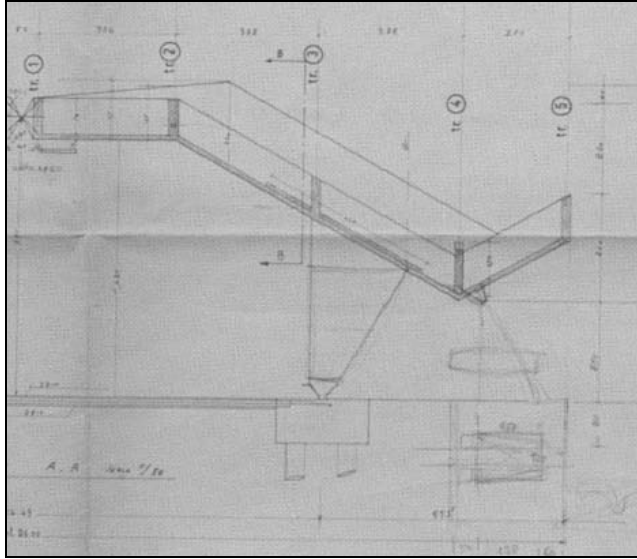Figure 5 - Beams and slab of the roof.

Figure 6 - Footings on piles (from the original drawings).

1.2 Materials

The original calculations and drawings hardly give any useful indications concerning the materials. The only available indication for the concrete is: "*Cemento per strutture in elevazione tipo 680*" (it means *"Cement to be used in the concrete for any structure except foundations, with a cubic compressive strength = 680 kg/cm^2 at 28 days"*; it is apparently a high-quality cement).

Obviously this information is not sufficient to clearly determine the mechanical properties of the concrete. For this reason, it was necessary to take into consideration several non destructive tests carried out on some beams (Vacca, 2004), by using the ultralsonic technique and the Schmidt-Hammer method. The compressive strength of the concrete was evaluated by means of well-established correlations, taking into account the scattering due to carbonation, surface inhomogeneity and human errors:

$$R_{ck} = R_{cm} = 25 \, [MPa] \tag{1}$$

Since concrete was cast decades ago, significant in-time variations of the compressive strength (because of the effects of shrinkage and creep) are not expected. (Hence, these phenomena can be neglected). As concrete strength has been evaluated from in–situ tests, the characteristic value is assumed to coincide with the mean value.
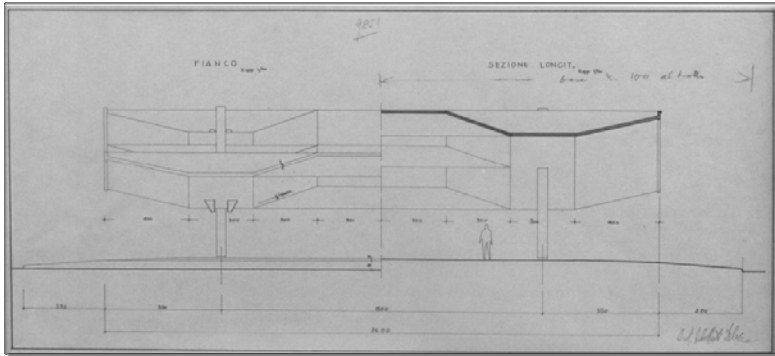
Fig. 7 - Lateral view of the structure (from the original drawings).

From the original calculations, the allowable stress for steel was determined as:

$$\sigma_{s,adm} = 1400 \; Kg/cm^2 = 140 \quad MPa \tag{2}$$

According to the technical documents of the 40s-50s (Santarella,1940), the above-mentioned value corresponds to "mild steel", with a nominal yield stress equal to:

$$f_y = 230 \; MPa \tag{3}$$

According to the design provisions of the time (Santarella, 1947), the calculation procedure used by the structural designer was based on the traditional method of the *working* (or *allowable*) stresses, through the tables of the coefficients "*r, s, t*" . The allowable stress of the concrete (containing high-strength aluminous cement, see the decree of the Italian Ministry for Public Works, dated November 16, 1939) is:

$$\sigma_{c,adm} = 50 \; Kg/cm^2 = 5 \, MPa \tag{4}$$

The ratio between the elastic moduli m = E_s/E_c was assumed equal to 10.

2.   ORIGINAL DESIGN AND CALCULATIONS

2.1   Loads and load combinations

The original documents concerning the design of the structure were found in the library of the School of Architecture of the Cagliari University. Consequently, the calculations and the diagrams of the internal forces were available.

Two load types were considered:

- the dead load;

- service load of 120 kg/m^2 (1.2 kN/m^2) on the horizontal part of the roof, and of 100 kg/m^2 (1.0 kN/m^2) in the inclined part of the roof.

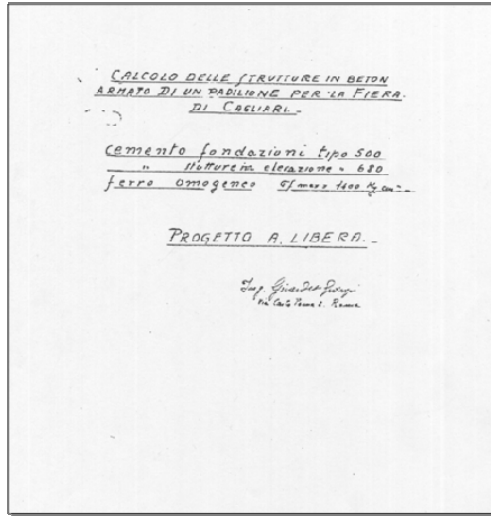There are no references to standard prescriptions.

Figure 8 - Original front page of the calculation report.

2.2 Structural analysis

The internal forces were determined by considering the structural members as if they were isolated. The slab was calculated as a 1 m-wide strip simply supported by two beams. The structural continuity was not taken into account; the slab, however, was divided into four parts, with different spans for each semi-portals. The maximum sagging and hogging moments were given the values $\pm qL_i^2/10$ and $\pm qL_i^2/12$ respectively, depending (surprisingly!) on the slope of the roof. This simplistic method, that inevitably leads to an overestimation of the internal forces, is very conservative. The beams too were considered as statically-determined (continuous beams over two supports, the portals, with two symmetrical cantilevers), and their internal forces were calculated by using simple equilibrium equations. The most significant cross-sections were designed by the tabular method. With reference to the allowable-stress method, the r coefficient is calculated from the bending moment (Santarella, 1940 and 1947):

$$r = \frac{h}{\sqrt{\dfrac{M}{b}}}$$

(5)

where: h = effective depth of the cross-section (from now on indicated with "d")

b = width of the cross-section

M = bending moment.

From the value of the r coefficient, and by imposing the allowable stress in the steel and the value of the ratio of the elastic moduli m, it is possible to determine the value of the maximum compressive stress in the concrete, as well as a second coefficient t, that can be used to calculate the amount of reinforcing steel A from the following relation:

$$A = t \cdot \sqrt{M \cdot b}$$
(6)

As for the portals, the attention of the designer was focused only on bending. To calculate the bending moment, each portal was subdivided into five parts, starting from the central hinge (Figure 9), and the bending moment at each node was determined.

The axial force in the members of the portal was calculated in a different way. For each semi-portal (see Figure 10), the resulting compressive force applied to the center of mass was first calculated, and then it was verified that the moment of these forces around the hinge located at the bottom of the column (Node A, Figure 9) has positive sign counterclockwise for the semi-portal sketched in Figure 9). By following this procedure, it is possible to make sure that the central hinge is always compressed.

To this purpose, three load combinations were considered:

      (1) full load on the whole semi-portal;

      (2) live load only on the central span, between the hinge and the column;

      (3) live load only on the cantilever.

The three combinations taken into account are instrumental (a) the first for maximizing the reaction at the bottom of the column; (b) the second for maximizing the compressive axial force at the central hinge; and (c) the third to ensure that there is no tension at the central hinge (Figure 11).
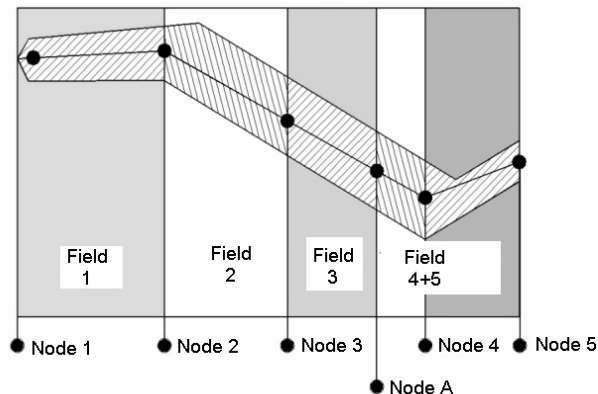

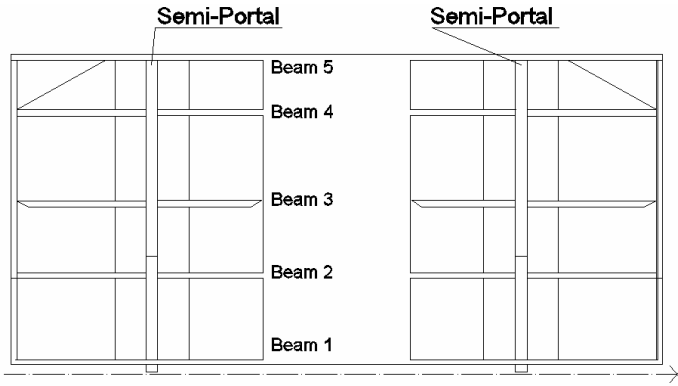Figure 9 - Scheme of the different portions of the portal.

Figure 10 - Roof plan: numbered starting from the central hinge.

2.3 Report on the Calculations

From the examination of the original calculations, characterized by the simplified models typical of that time, some inaccuracies are evident. The hypothesis that the available calculation report is only a draft could explain, but not justify the inconsistencies. For instance, the calculation neglects the dead load of some parts of the structure.

Going into more details, there are apparently errors in the calculation of the dead load of some parts of the portal, because of inaccuracies in the geometry adopted in the calculations: the width of the beams is 300 mm, whereas the actual value is 400 mm . (This last value, however, was correctly introduced into the first part of the report). There is a mistake also in the computed length of the beams supported by the columns: the actual value is 2.65 m, and not 2.10 m, as in the calculations.

	M	A=A'	R_q	R_g
Field 1	455	3.9	750	570
Field 2	445	3.82	860	685
Field 3	445	3.82	860	685
Field 4+5	280	2.42	610	495
M= maximum bending moment [kgm]; A'= compression reinforcement [cm^2/m]; A= tension reinforcement [cm^2/m]; R_q= reaction at the extremities under the full load [kg/m]; R_g= reaction at the extremities under the self-weight [kg/m].				

Table 1 - Results concerning the slab (from the original calculations).

It is fair to say that these mistakes did not affect markedly the results: the differences are not significant, with respect to the total load acting on the structure. Regardless of these small mistakes, the most stressed members are Beams n°3, Node 4 of the portal, and the hinge at the bottom of the column. These results were in some way expected, because they are consistent with the calculation model, even if the structural role of the slab was not taken into account. Probably, the main differences are to be expected for the beams. (This issue will be discussed later, taking advantage of finite-element analysis).

In Table 1 and subsequent tables a synthesis of the results coming from the original calculations is presented. (Same units as in the original documents).

	M	Y_q	Y_g	A	A'
Beam 1	22400	17120	12300		
Beam 2	35300	27300	20050	23.8	27.5
Beam 3	36700	28600	21400	24.8	28.5
Beam 4	31000	25000	19000	22	24.8
Beam 5		15400	10800		
M = maximum bending moment [kgm]; A'= compression reinforcement [cm^2]; A = tension reinforcement [cm^2]; Y_q= reaction at the extremities under the full load [kg]; Y_g= reaction at the extremities under the self-weight [kg].					

Table 2 - Results for beams from the original calculations.

	H
Loading condition 1	6050
Loading condition 2	13300
Loading condition 3	-560
H= horizontal reaction in kg. **Loading condition 1** = load on arch and cantilever **Loading condition 2** = loaded arch, unloaded cantilever. **Loading condition 3** = unloaded arch, loaded cantilever.	

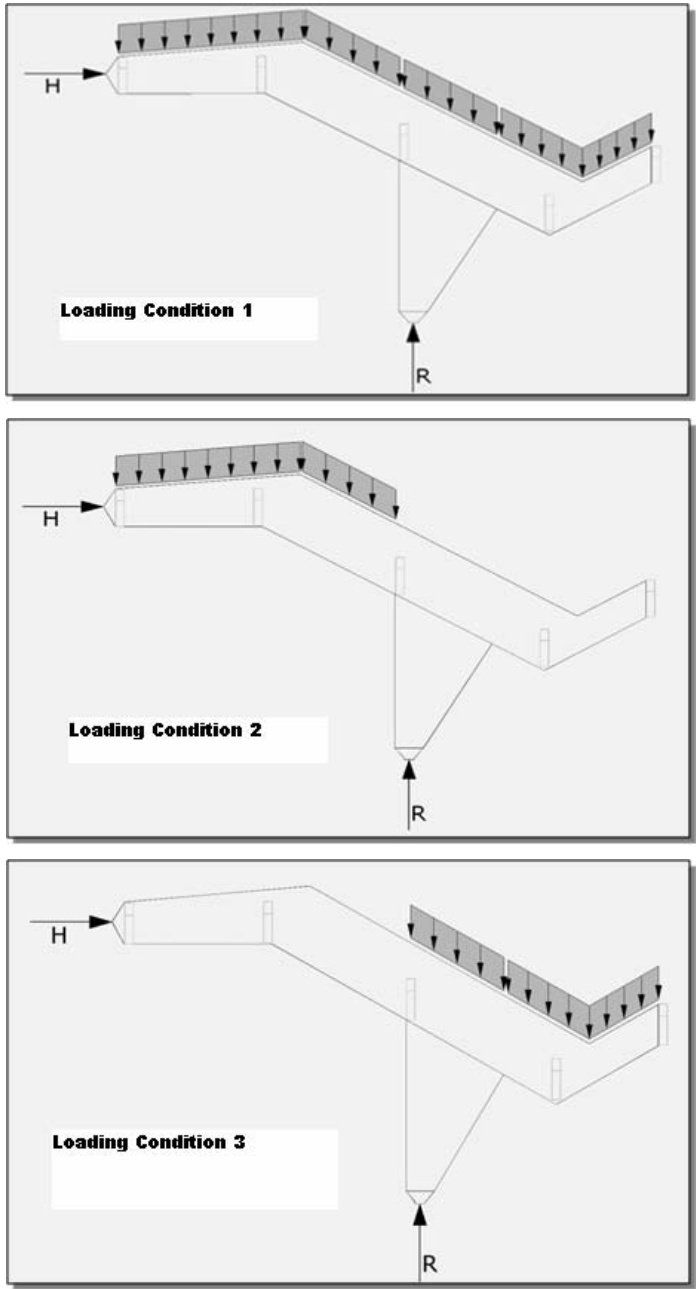Table 3 - Forces at the central hinge (from original calculations).

Fig. 11 - Load combinations.

3. STRUCTURAL ANALYSIS WITH FINITE ELEMENTS

3.1 Structural models

Even if the structure is rather simple, and it would be possible to analyze it by means of simplified methods, a FE model of the whole building was developed.

This was done by using MIDAS/Civil, a software from the MIDAS package. The first choice was about the type of finite element. The particular shape of the building, especially the slab, suggests to use solid elements. Actually it would not be possible to correctly enforce the constraint between the plate and beam elements because the slab is alternatively inserted in the upper or in the lower part of the beams (Figure 5). The Authors' choice allows the model to be more realistic, but on the other hand implies a computational effort to transform the nodal forces into generalized internal forces in the most significant sections.

The value of the bending moment, for example, was calculated by means of the following procedure: the single nodal forces were multiplied by the distance between their application point, and the centroid of the cross-section in question. The total value was obtained by summing up the contributions of all nodal forces. As for axial and shear forces, the same procedure was adopted, but in a simpler way: each nodal force, in the normal and in the transverse direction, was added.

Two models were set up: one including the structural role of the slab (Figure 13), i.e. the slab stiffness contributes to the stiffness of the beams, and the second with the continuous slab simply supported by the beams (Figure 14).

In this way it is possible to compare and to evaluate the degree of approximation of the original calculations.

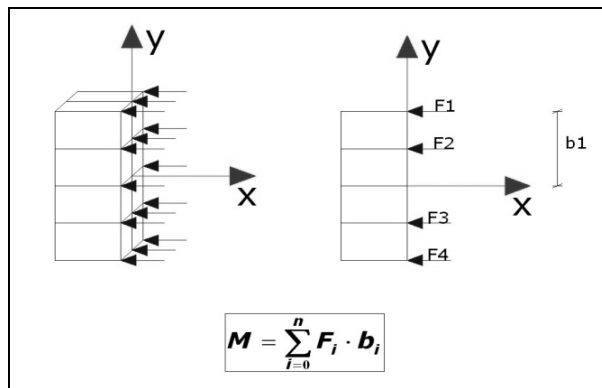$$M = \sum_{i=0}^{n} F_i \cdot b_i$$

Figure 12 - Calculation of the bending moment from the nodal forces in the 3D FE analysis.

The second model (Figure 14) was built in more steps: at first the reactions on the continuous simply-supported slab were calculated. Then, these actions were directly applied to a FE model of the beams and columns without the slab.
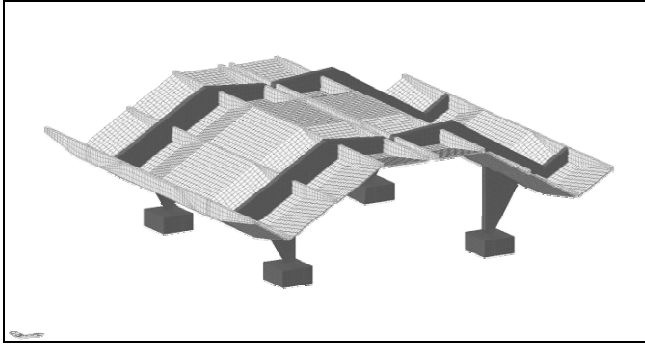
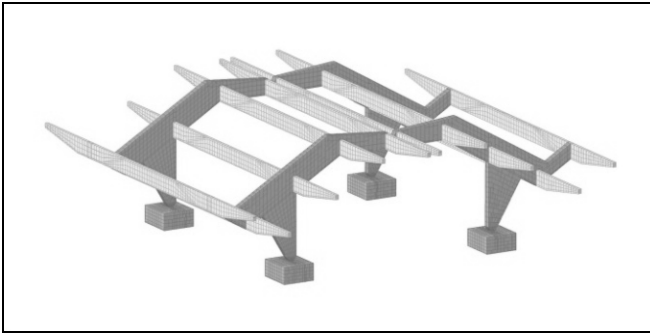Figure 13 - F.E. model including the structural role of the slab.

Figure 14 - F.E. model neglecting the structural role of the slab.

The structure was fully restrained at the base of the footings. Soil-structure interaction was not considered, as justified by the structure being statically determined. There is no interruption, even between the bottom of each column, and its footing: the hinge behavior is enforced through the small size of the contact surface.
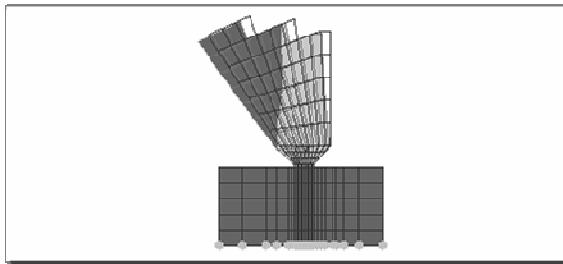

Figure 15 - Connection between column and footing.

With a little extension of the section at the bottom of the columns, the rotations are compatible with those of an hinge (see the demonstration in the following, Fig.15).

The structural analysis was based on linear elasticity, because the main objective was to study the structural behaviour at the serviceability limit state. The non-linear properties of the materials were considered only at the ultimate limit state.

3.2 Loads

The loads acting on the structure were defined according to the Italian Code (2008), with particular attention to the wind, as required by the rather peculiar shape of the slab (Figures 16 and 17). As for the snow load, the possibility of a non uniform distribution was taken into account (Figure 18).
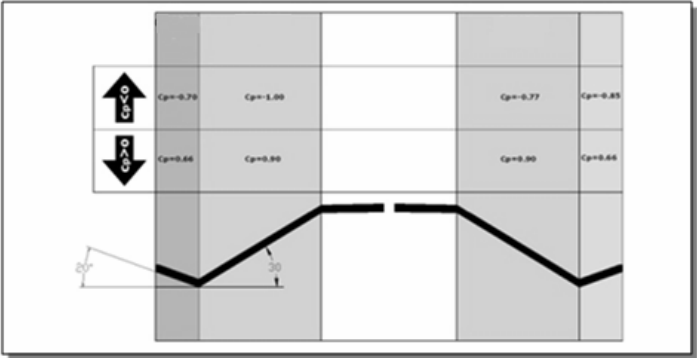
Figure 16 - Values of the shape coefficient Cp for the wind in the transverse direction.

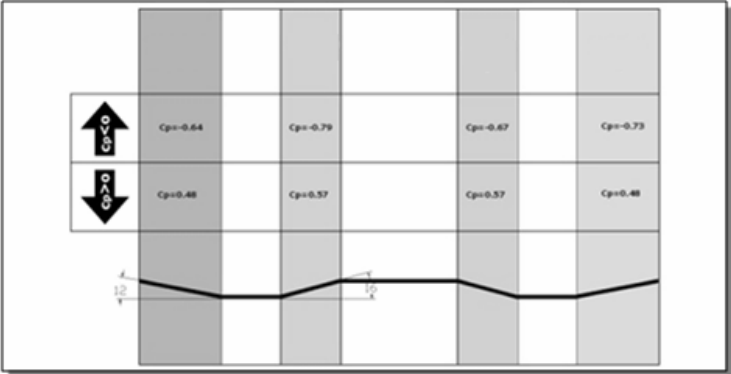

Figure 17 - Values of the shape coefficient Cp for the wind in the longitudinal direction.
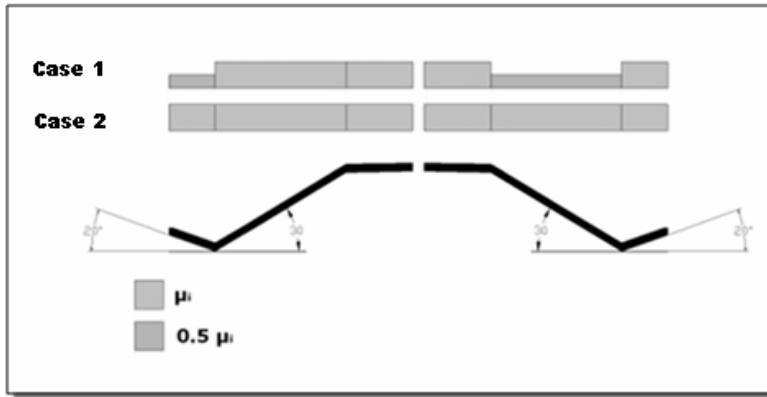
Figure 18 - Scheme of the snow distribution on the roof.

Thirty-eight load conditions were examined at the ultimate limit state, and seven load conditions for the serviceability state limit. In this way it was possible to consider the worst loading condition for each structural element.

3.3 Safety assessment

The safety checks based on the original report were developed according to the allowable stress method. They were compared with calculations based on the limit state method for the first FE model (i.e. including the cooperation between slab and beams). For each calculation, three different conditions, indicated with A,B,C, are presented in the following:

A- Calculation based on the original report;
B- Calculation based on the first FE model (i.e. cooperation of the slab included)
C- Calculation based on the second FE model (i.e. neglecting the cooperation of the slab)

In the calculations at the ultimate limit state for Cases A and B, only bending was considered; on the contrary, in Case C both the bending moment and the normal force were introduced. Some tables containing the most significant results included in Appendix I.

3.4 Comparison of the results

3.4.1 Slab

The results concerning the slab, for the Cases A,B and C, are similar and comparable, as should be expected, because the slab is continuous, and the continuity was taken into account in the three models. Obviously, Model A is the most conservative for the above-mentioned reasons. Furthermore, all checks were satisfied in both the serviceability and the ultimate limit states.
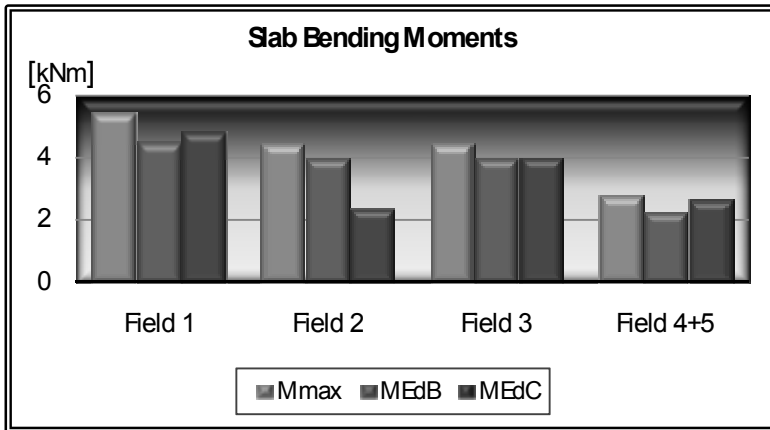
Figure 19 - Values of the bending moment M at midspan in the different slab fields. M_{max}= maximum M according to Model A; M_{EdB}, M_{EdC} = design values of the applied bending moment according to Models B and C.
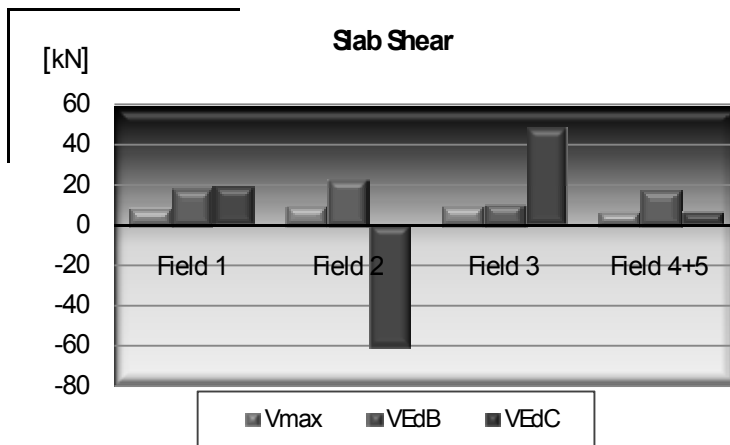

Figure 20 - Values of the shearing force V in the most significant sections of the slab. V_{max}= maximum V according to Model A; V_{EdB}, V_{EdC} = design values of the applied shearing forces according to Models B and C.

The most peculiar situation is that of Field n°2: in comparison to Model A, the bending action of Model C is reduced by 50%. Moreover, shear exhibits an opposite sign compared to Models A and B (Figures 19 and 20). Such an occurrence may be due to the structural role of the slab, that transfers the stresses from the beam to the portal, as stressed in the next section.

3.4.2 Beams

The beams are the most interesting elements: from bending moment calculation (Figure 21), the differences between Models A, B and C are evident. It should be pointed out that in Model A loads were calculated in deterministic way following the code of the time, without combinations coefficients ψ. In Models B and C loads were calculated following current Italian code.

Taking into account that in Model C there the slab is also subjected to compressive forces, the authors produce a comparison between the amount of reinforcing steel calculated according to the current standard, and the reinforcing steel determined on the basis of the original design. This comparison is rather interesting, and it is shown in Figure 22: the amount of reinforcing steel at the midspan of each beam is represented.
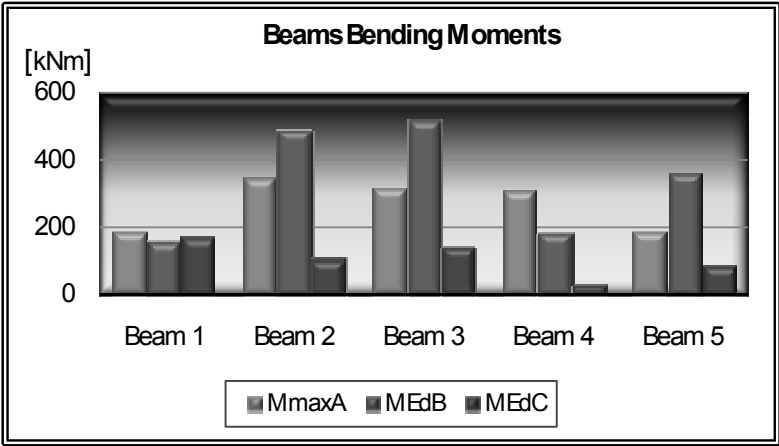

Figure 21 - Negative bending moments in the beams.

The values obtained by means of the three models are very different, but considering the total amount of the reinforcement (i.e. the sum of the reinforcement areas of the beams in one half-portal) Models B and C are equivalent. The reinforcement calculated originally is larger (at any given section) than those calculated by means of the other two models. Going into more details, the total reinforcement is about twice as much as that evaluated with Models B and C. This means that these elements were designed in a very conservative way. Furthermore, Models B and C are based on a sort of "super beam-slab element". Model C, that takes into account the structural role of the slab, is a better approximation of the real situation; hence, the results yielded by Model C are more accurate, especially in terms of required reinforcement.

Figure 23 shows that Models B and C yield very different shear values. As an example, in Beam 2 (Field 2 of the slab) the values have opposite sign.

Considering the limits of the original calculations, focusing on Models B and C (that are - on the whole - more homogeneous) seems reasonable.

Note that the shearing force in Beam n°4 according to Model C is more than twice as large as that obtained with Model B. Furthermore, Beams n° 2 and 4 (Fig.25) are placed near the folds of the slab, outside the fold and inside the fold, respectively.

The structural role of the slab influences both the longitudinal beams and the portal: therefore, because of the diffusion of the nodal forces from the central hinge, the slab is compressed.

Because of the structural continuity between the slab and the beams near the corners, the internal actions are summed up and yield a downward force on Beam n°4. This increase of the load brings in an increase of the shearing force as well.
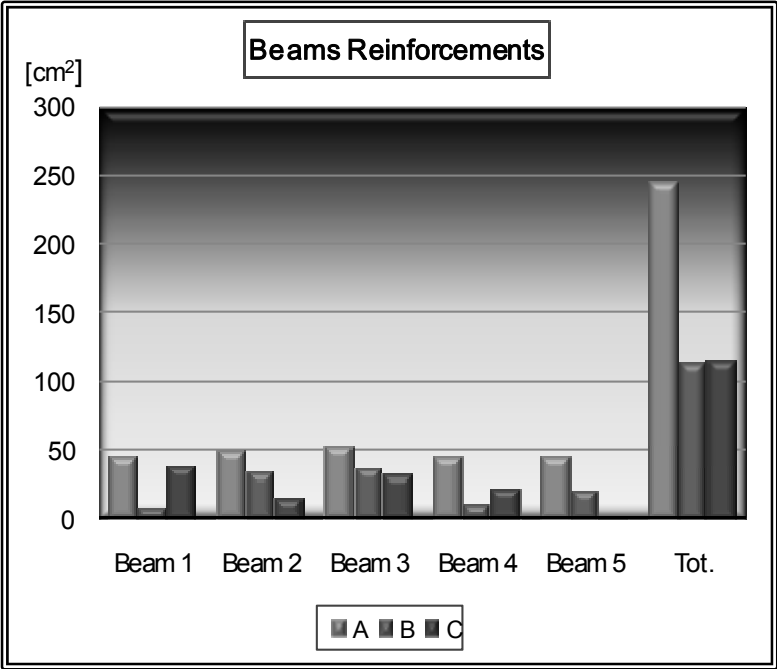

Figure 22 - Summary of the reinforcement of the beams.

An opposite situation develops in Beam n°2, where the absolute value of the internal actions is larger than the applied loads, and therefore an inversion of the sign of the shearing force is observed (Figures 23 and 26). As for Beams n° 3 and

5, according to Model B, the internal forces are larger than those obtained with Model C (Figure 21 for the positive moment; Figure 23 for the shearing forces at the extremities.
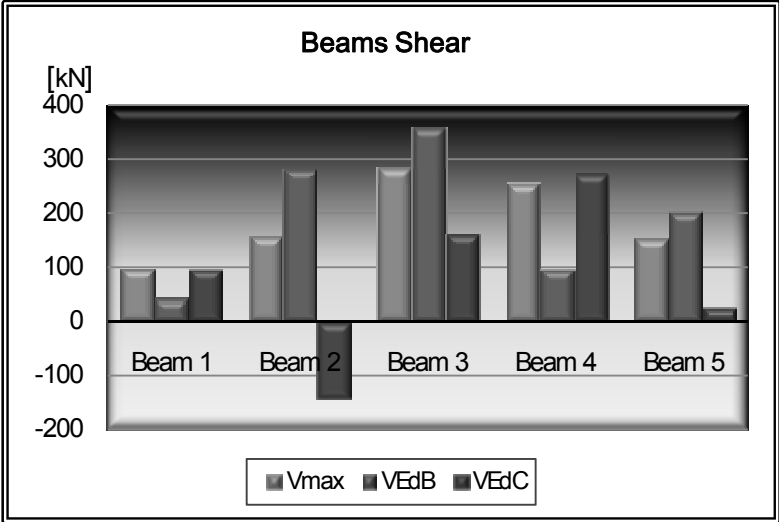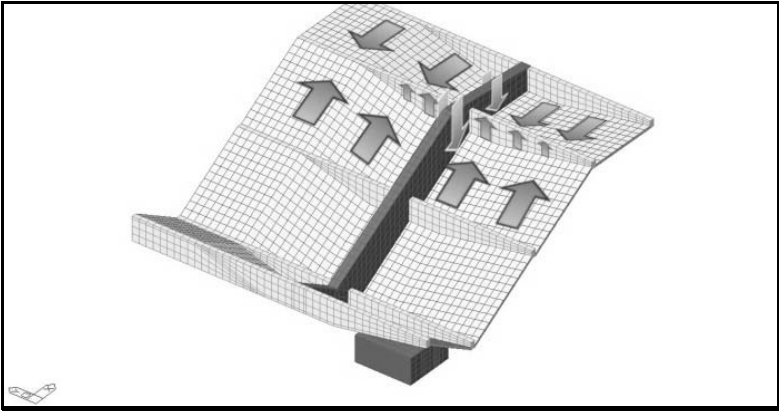

Figure 23 - Shearing forces in the beams.

Figure 24 - Sketch of the interaction between the slab and the beams.

This effect can be understood considering that the pavilion roof is a folded structure. From a rough estimation, the inertia of the slab turns out to be

approximately 120% larger than that of the beams (Fig.27). Therefore, the composite action of the slab and of the beams is remarkable indeed!
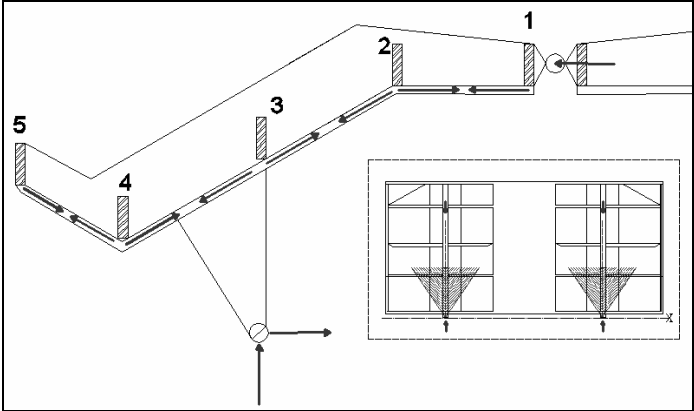

Figure 25 - Diffusion of the forces from the central hinge to the slab. Lateral and plan view.
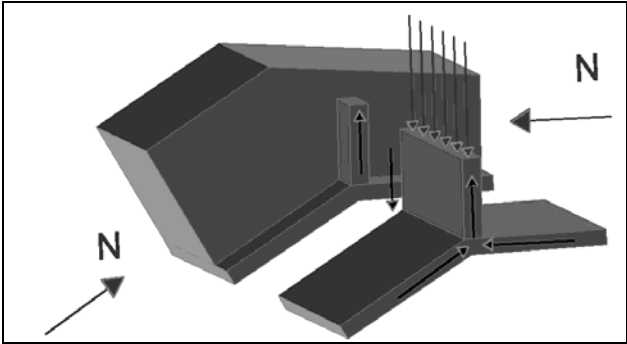

Figure 26 - Transversal view of the slab and of the beam at the corner, showing the internal axial force.

Along any given transverse section of the roof, the equations of equilibrium are never satisfied, if reference is made to the beams or to the slab, disregarding their mutual interaction. On the contrary, the equations are satisfied, if reference is made to the whole cross section.

Finally, a few words should be devoted to Beam n°1: from the values shown in Figure 23, it is clear that the shear values are larger according to Model C. As for

the flexural behavior of the slab (see Figure 28), in the sections far from the folded part there are local displacements in the slab that indicate that the slab is supported by the end beams.
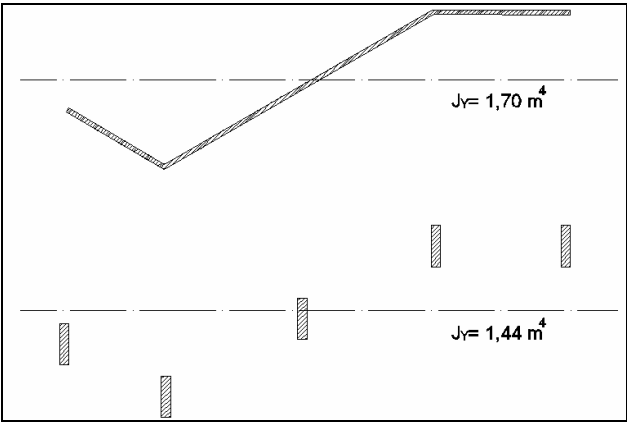
Figure 27 - Moments of the inertia of the beams and of the slab.
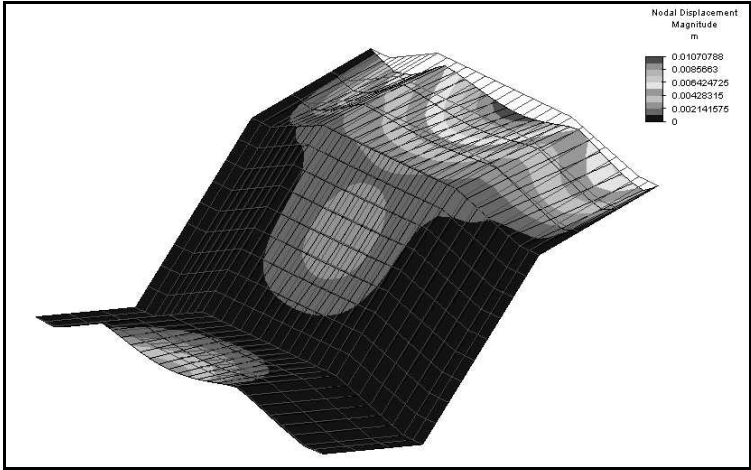
Figure 28 - Displacement contour lines of the slab.

3.4.3 Portal

The calculation shows that - both at the ultimate limit state and in the serviceability limit state - the checks for the slab and the beams are satisfied (as it is the case with the allowable stress method), even taking into account the wind.

On the contrary, for the portal the checks are not satisfied (both at the ULS and in the SLS), if the wind is considered. As shown in Table 4, only for three out of

twelve cases the checks are positive (see Fig. 9 for the exact position of the nodes). This happens only for the less stressed nodes (2 and 4) in the case of the allowable stress method, and for node 4 at the ultimate limit state in Model B. According to Model C, the checks at the different limit states are never satisfied.

Checks	Node 2	Node 3	Node A	Node 4
Bending A	YES	NO	NO	YES
Bending + Axial B	NO	NO	NO	YES
Bending + Axial C	NO	NO	NO	NO

Table 4 - Synthesis of the checks.

It is important to underline that these problems are not caused by the wind. The same problem arises even in ordinary load conditions. In two of the 4 sections, the checks at the limit states are never satisfied. This fact is confirmed by a simple on-site investigation of the structure. There are eight ties placed on the upper side of the beam of the portal (Figure 29): their aim is probably to limit cracking. Unfortunately, no documents about the design of these elements could be found.

Figure 29 - Ties in the upper part of the beams.

3.4.4 Hinge

The checks of the hinges at the bottom of the columns were developed according to Leonhardt et al. (1980); the minimum reinforcement area required - and the minimum rotation capacity - are satisfied. The minimum dimensions, on the contrary, cannot be fulfilled, because of the particular shape of the columns; however, the hinge behavior is guaranteed. Actually, the formulas by Leonhardt et al. (1980) refer to columns of constant cross-section; if the reduction of the cross section towards the hinge is considered, the checks are satisfied (see Appendix II for more details).
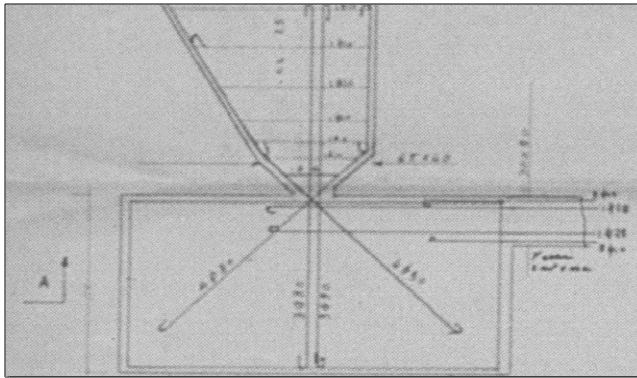

Figure 30 - Drawing of the hinge (from the original documents).

4.   CONCLUSIONS

The use of the FE method allows to analyse the structural behaviour of the rather complex folded cover in question with good accuracy under the service loads, in order to check the correctness of the original project. (Sixty years ago, structural designers had to rely only on tables and slide rules!).

The numerical results allow to conclude that the original reference model was not totally accurate in describing the real structural behavior; however, it was sufficient for most of the structural members, thanks to a very conservative approach. This is true, but for the portal: probably in this case there were some errors in working out a behavioral model and in the calculations.

In the original design, the three-hinged arch behavior was not fully taken into account, and reference was made only to the bending resistance, excluding the normal forces. Actually, the presence of a combined state of bending and axial force revealed by FE analysis justifies the presence of many zones subjected to tensile stresses, contrary to what normally happens in three-hinged arches. This anomaly can be caused by two factors:

- the cantilever produces negative bending;

- the very low slope (almost horizontal) of the upper part of the portal, and the position of the central hinge, that is just a little higher than the top of the columns.

This result is demonstrated by the ties placed at the extrados of the portals, in order to limit cracking.

The important structural role of the slab becomes evident from FE analysis. From the comparison of the results obtained by Models B and C, i.e. with and without the composite action of the slab and of the portal beams, it was found that the structural behavior is quite different, and some internal actions even exhibit opposite signs (e.g. shear of Beam no. 2).

Otherwise, considering the structure on the whole, there were no strong differences in terms of required reinforcement. A more accurate knowledge of the structural behavior (by taking into account the structural role of the slab as in Model B) would allow a more accurate design of the structural members, avoiding marked differences among the various sections.

Consider, for example, the reinforcement of Beam no.1: with Model B an area of reinforcement of 8.9 cm^2 is sufficient, whereas according to Model C 39.5 cm^2 are required.

The other objective of this paper is to verify if the structure can be considered safe according to the current Italian standard. Apart from the afore-mentioned calculation errors, it can be said that the original reference code was sufficient to guarantee an adequate safety level.

Actually, the FE model set-up for this analysis and new performance-based standards make it possible to have a more accurate load definition, a better knowledge of the structural behavior and, consequently, a refined judgment in evaluating the actual safety levels.

The last consideration regards the importance of the link between shape and structure. Despite the denial of its importance by some scholars, it is indeed true! The structural analysis carried out with the aim of a better modeling, shows how the shape concepts introduced by Architect Libera directly correspond to an appropriate structural behavior.

These concepts are, for instance, the change in position of the slab with the sign of the bending moment, the folded plate behavior of the cover, and the shape of the portals similar to a three-hinged arch. In cases similar to that investigated here, namely buildings with a strong architectural value, the structural engineer should try to rationalize the architect's point of view by means of a synergic action.

Structural conception must be in agreement with the level and the characteristics of the building. If the building is complex, too simplistic approaches (looking "smart") should be avoided. Perhaps simple approaches could be used in the design of ordinary buildings, but in the case of rather complex structures like the CasMez pavilion the risk of errors is too high .

5.   ACKNOWLEDGMENTS

REFERENCES

[1] AICAP (2008). *Guida All'uso dell'Eurocodice 2 con riferimento alle norme tecniche D.M. 14.1.2008 (Guidelines for the use of EC2 with reference to the Decree 14 January 2008 of the Italian Ministry for Public Works)*, pub. by Edizioni Pubblicemento.

[2] Concu G., De Nicolo B., Meloni D. and Mistretta F. (2006). "NDT Methods for Structural Investigation of a Damaged Concrete Pavilion". *Proc. Int. Conf. on Structural Faults and Repair,* Edinburgh, Scotland (UK).

[3] De Nicolo B., Concu G. and Meloni D. (2004). "Il padiglione ex Casmez-Adalberto Libera"(The Exhibition Hall Casmez by Adalberto Libera). 3rd Regional Conf. on the Restoration of Modern Civil and Industrial Structures, *oral communication,* Cagliari.

[4] Fassio A. (2004). *Nel Dopoguerra - Il linguaggio della struttura - La tipologia dell'abitare - L'esperienza di Cagliari (Past the 2nd World War – What a structure tells us – Buildings typology – The experience of Cagliari).* Pub. by C. Delfino Editore, Cagliari - Italy.

[5] Leonhardt F. and Monning E. (1980). *Reinforced- and Prestressed Concrete : Design and Building Technologies – 2nd Volume on Special Cases (in Italian).* Pub. by Edizioni Di Scienza e Tecnica, Milano - Italy.

[6] Loddo G. (2001). *Il Padiglione Casmez di Adalberto Libera alla Fiera di Cagliari (The Exhibition Hall by Adalberto Libera in the Exhibition Fair of Cagliari).* Pub. by CUEC Editrice, Cagliari - Italy.

[7] Mastinu A. (2009). **"**Padiglione CASMEZ – Analisi statica strutturale alla luce delle nuove normative*" (Exhibition Hall Casmez – Structural Analysis according to the New Italian Building Code).* MS Thesis, University of Cagliari, Cagliari – Italy.

[8] Santarella L. (1940). *Il Cemento Armato - Volume Primo : la tecnica e la statica (Reinforced Concrete – 1st Volume: Building Technology and Design).*7th edition, pub. by Hoepli, Milan – Italy.

[9] Santarella L. (1947). *Handbook of Reinforced Concrete (in Italian).*17th edition, pub. by Hoepli, Milan – Italy.

[10] Vacca S. (2004) .*"*Prove non distruttive sulle strutture del Padiglione Libera*"* (Non-Destructive Tests on the Structural Members of the Exhibition Hall by Libera)*. MS Thesis,* University of Cagliari, Cagliari – Italy.

ITALIAN DOCUMENTS

[A] DM 14 01 2008 - Norme tecniche per le costruzioni.

[B] CNR-DT 207/2008 – Istruzioni per la valutazione delle azioni e degli effetti del vento sulle costruzioni.

[C] UNI EN 1992-1-1 EUROCODICE 2 - Progettazione delle strutture di calcestruzzo.

[D] Ordinanza n° 3519 28/04/2006 - Criteri per l'individuazione delle zone sismiche.

[E] Delibera G.R. 30 marzo 2004, n. 15/31.

[F] R.DL 16.11.1939- Norme per l'esecuzione delle opere in conglomerato cementizio semplice ed armato.

APPENDIX I- Synthesis of the results

	Field 1	Field 2	Field 3	Field 4+5
M_{maxA} kNm	5.46	4.45	4.45	2.80
M_{EdB} kNm	4.50	4.00	4.00	2.30
M_{EdC} kNm	4.80	2.40	4.00	2.67

Table 5 - Maximum internal moments in the slab.

N_{EdC} kN	114.00	65.00	43.00	11.00
V_{EdA} kN	9.00	10.30	10.30	7.30
V_{EdB} kN	18.00	22.80	11.20	17.45
V_{EdC} kN	18.8	-60.10	48.4	6.50

Table 6 - Maximum internal forces in the slab.

	Field 1	Field 2	Field 3	Field 4+5
Bending A (*)	NO	YES	YES	YES
Bending B	YES	YES	YES	YES
Bending + Axial.C	YES	YES	YES	YES
Shear A	YES	YES	YES	YES
Shear B	YES	YES	YES	YES
Shear C	YES	YES	YES	YES

Table 7 - Safety checks in the slab.
(*) The designer did not perform these checks.

	Beam 1	Beam 2	Beam 3	Beam 4	Beam 5
M_{maxA} kNm	191.00	350.00	318.00	310.00	191.00
M_{EdB} kNm	162.00	492.70	524.00	187.00	366.00
M_{EdC} kNm	172.00	108.00	141.50	33.30	91.00
N_{EdC} kN	-455.00	-119.00	-387.00	-418.00	132.00
V_{EdA} kN	99.00	158.00	286.00	255.00	154.00
V_{EdB} kN	44.00	283.00	360.00	98.20	205.00
V_{EdC} kN	98.00	-143.00	162.00	275.00	58.80

Table 8 - Maximum internal forces in the beams.

	Beam 1	Beam 2	Beam 3	Beam 4	Beam 5
Bending A	YES	YES	YES	YES	YES
Bending B	YES	YES	YES	YES	YES
Bending + Axial.C	YES	YES	YES	YES	YES
Shear A	YES	YES	YES	YES	YES
Shear B	YES	YES	YES	YES	YES
Shear C	YES	YES	YES	YES	YES

Table 9 - Safety checks in the beams.

	Beam 1	Beam 2	Beam 3	Beam 4	Beam 5	Tot.
$A_{s.A}\ cm^2$	24.8	27.5	28.5	24.8	24.8	
$A_{s.A}^{I}\ cm^2$	22.0	23.8	24.8	22.0	22.0	245.0
$A_{s.B}\ cm^2$	8.9	28.3	30.0	11.0	21.3	
$A_{s.B}^{I}\ cm^2$	0.0	6.1	7.8	0.0	0.0	113.4
$A_{s.C}\ cm^2$	20.7	8.8	17.3	12.3	1.7	
$A_{s.C}^{I}\ cm^2$	18.8	7.6	15.5	10.9	1.5	115.1

Table 10 - Reinforcement amount of the beams.

	Node 2	Node 3	Node A	Node 4	Bottom pilar.
M_{maxA} kNm	-600.0	-2155.0	-880.00	-288.0	-2901.
N_{maxA} kN	-	-	-	-	-
M_{EdB} kNm	-314.5	-2719.4	-1272.80	-990.1	4693.3
N_{EdB} kN	-14.8	6.9	-422.00	+23.5	3168.0
M_{EdC} kNm	-552.0	-2454.1	-930.00	-464.60	4517.0
N_{EdC} kN	-786	-1354.2	-502.00	-31.3	2864.0

Table 11 - Maximum internal forces in the portal.

	Node 2	Node 3	Node A	Node4	Bottom pilar
Bending A	YES	NO	NO	YES	YES
Bending + Axial.B	NO	NO	NO	YES	YES
Bending + Axial.C	NO	NO	NO	NO	YES

Table 12 - Safety checks of portal.

APPENDIX II- Checks of the hinge at the bottom of the columns

Geometric data:

$a = 24cm$ $\qquad$ $N_D = 993kN$

$b = 40cm$ $\qquad$ $\beta_{wN} = 25N/mm^2$

$d = 38cm$ $\qquad$ $\alpha_D = 0.16$

$t = 4.3cm$ $\qquad$ $\alpha_n = 2.05$

$b_r = 21cm$ $\qquad$ $F_G = 960cm^2$

$\beta = 52°$ $\qquad$ $N_{max} = 2578kN$

Minimum area:

$F_{Gmin} = 652cm^2$ $\qquad$ $F_{Gmax} = 2359cm^2$ $\qquad\qquad$ $F_{Gmin} < F_G < F_{Gmax}$.

Checks on the dimensions:

$a \leq 0.3 \cdot d$ $\qquad\qquad$ $a = 24cm \leq 0.3 \cdot d = 11.4cm$

$b_r \geq 0.7 \cdot a \geq 5cm$ $\qquad\qquad$ $b_r = 21cm > 0.7 \cdot a = 16.8cm > 5cm$

$t \leq 0.2 \cdot a \leq 2cm$ $\qquad\qquad$ $t = 4.3cm < 0.2 \cdot a = 4.8cm > 2cm$

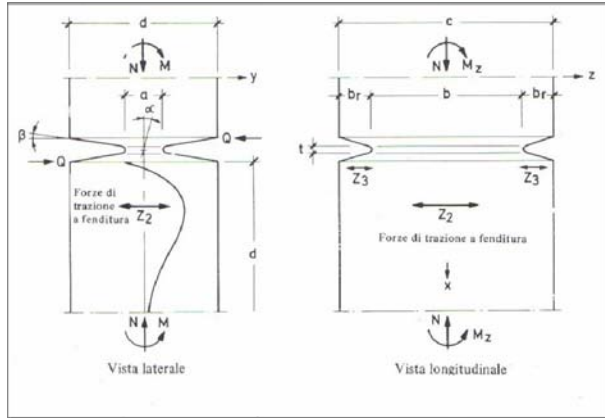$tang\beta \leq 0.1$ $\qquad\qquad$ $tang\beta = 1.28 > 0.1$

Figure 31 - Hinge : definition of the geometry
(from Leonhardt et al., 1980).
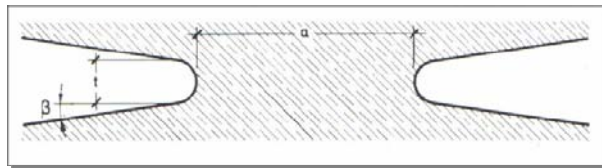
Figure 32 - Hinge : close-up of the critical zone
(from Leonhardt et al., 1980).

Checks on the rotation angle: the allowed rotation angle corresponding to a compressive force N:

$$\alpha_{amm} = \pm 0.8\ N /(F_G\ \beta_w^{1/2}) \leq 15\ ^o/_{oo} \tag{7}$$

Considering that the maximum value in the present case is $N_{max} = 2578$ kN, the design value of the rotation is:

$$\alpha_n = 2.05\ ^o/_{oo} \leq \alpha_{amm} = 13.85\ ^o/_{oo} \tag{8}$$

ON FIRE RESISTANCE OF THIN-WALLED OPEN-SECTION P/C GIRDERS SUPPORTING LARGE INDUSTRIAL ROOFS

Patrick Bamonte[1], Roberto Felicetti[2], Pietro G. Gambarova[3] and Ezio Giuriani[4]

ABSTRACT

Architecturally-valuable thin-walled prestressed girders have been designed and built in Italy for many years since the sixties of the past century. These P/C members are usually found in the large-span covers of office buildings and industrial plants, where *main beams* running from column to column support *secondary beams* placed side-by-side with – or without – interposed concrete or polycarbonate panels.

For both main and secondary beams, different sections have been adopted, from simple double-tee or tee sections to V or inverted-V sections, channel sections and the like. Because of the limited thickness of the webs (something like an obsession in the early phase of P/C mass production) fire resistance is a critical issue, even more since these members frequently exhibit severe symptoms of distress after several decades since their design and construction. (Longitudinal cracking induced by transverse bending and worsened by corrosion often occurs).

In this paper, a main P/C girder with an inverted-V section provided with thin and inclined webs is checked both at the Ultimate Limit State and in fire, with reference to bending and shear. As for shear, both the traditional truss model with variable strut inclination and a dedicated truss model are used, in B-Zones and D-Zones respectively. Reference is made to the provisions of Eurocode 2.

Albeit rather peculiar for its unusual cross-section, the beam in question offers the opportunity to focus the attention on some general aspects concerning the safety verifications on thin-walled concrete members in fire conditions, and on some peculiarities of past design practice.

This paper is an expanded version of a similar paper published in FIB Bulletin No.57 – 2010.

---

[1] Assistant Professor, [2] Associate Professor, [3] Professor,
  DIS - Department of Structural Engineering, Politecnico di Milano, Milan, Italy
[4] Professor, DICATA - Dept. of Civil and Environmental Engineering, University of Brescia, Brescia, Italy

1. INTRODUCTION

The astonishing development of the Italian prefabrication industry in the sixties and seventies of the past century, and the growing interest in the same period for prestressing, favoured the design and construction of many challenging prestressed concrete members. This growth was fostered by the economic boom of the late fifties and sixties, and by the ensuing diffusion of industrial buildings, characterized by large spans and requiring the use of large-span structural members (Barazzetta, 2004).

Beside double-tee girders (I-girders) and tapered beams (deeper at mid-span), that were not very demanding from a structural view point (Taerwe et al., 2006), new types of pioneering P/C members were developed for the roofs of office and light-industry buildings, which were characterized by thin-walled open and complex sections, small-diameter distributed reinforcement and – in general – high static efficiency (see Figure 1, where the main beams have an inverted-V section and the secondary beams a V-section). These prismatic beams (called wing sections in the Italian technical parlance) were a turning point in the conceptual design of roof members. The compression chord and the tension stringer were not aligned on the vertical axis of the cross-section and were not connected by a single web, but by two thin inclined wings.

In the secondary beams, this design philosophy brought in larger widths and simpler connecting members (concrete, glass or plastic panels) placed between the contiguous beams. Different sections (V, U and channel sections) started to be systematically developed in the 80s, when new (and more refined) calculation methods became available to most designers, and full-scale testing allowed to shed some light on such complex phenomena as transverse bending and its interaction with longitudinal bending.

As a matter of fact, the small thickness of the inclined webs enhances the transverse deformability of the section, and makes the ensuing shape loss a very dangerous occurrence, because of the reduction of the internal lever arm, to the detriment of the bending stiffness.

The (often) smooth, small-diameter and distributed bars used for the transverse reinforcement make these beams rather shear-sensitive (especially in the end zones, where prestressing is hardly effective) with reference to both the Ultimate Limit State in shear and the fire.

In this paper a rather stiff pre-tensioned simply-supported beam with an inverted-V section (Figure 2) and length 12 m (= 40 ft) is considered.

To check whether this beam has a sufficient fire resistance, its load-bearing capacity should be assessed not only in bending and shear far from the supports (where the stresses are regularly distributed), but also in the end zones, where the stress field markedly depends on the position of the supports. For instance, in the case in question the beam is in some way suspended at the extremities, where the top chord rests on the columns (Figure 3).

These topics are treated in the paper, where the thermal field in the concrete, in the strands and in the ordinary reinforcement, is investigated in detail, in order to work out the various contributions to fire resistance. Reference is made to the provisions of European Codes (2002, 2004).
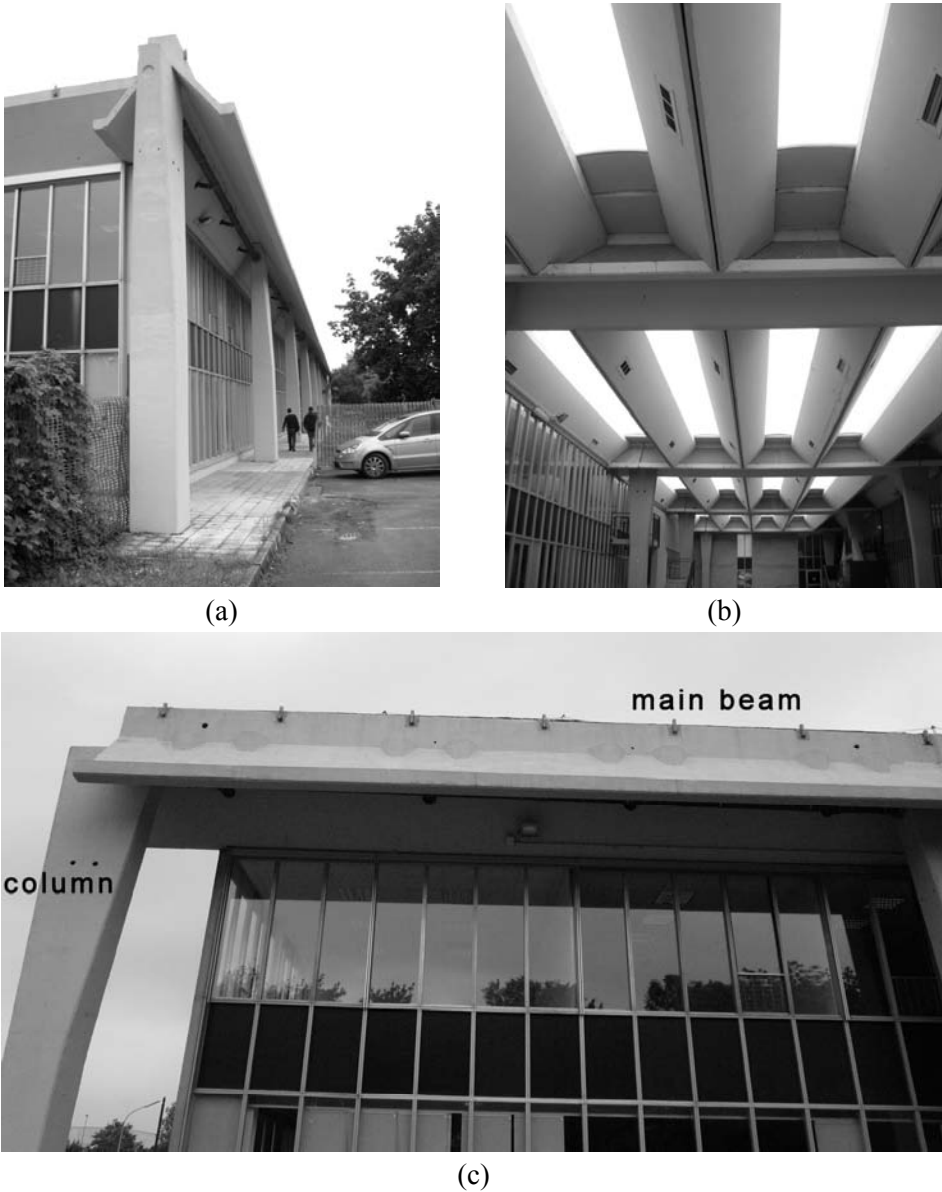

(a)   (b)

(c)

Figure 1 – (a,c) Views of a typical prefabricated roof with external inverted-V main beams resting on tapered columns; and (b) internal V beams.

2. GEOMETRY, PRESTRESSING AND REINFORCEMENT OF THE BEAM

The main roof beams considered in this paper are characterized by an inverted-V section of 1.6 m height, 2.4 m width, and a nominal span of 11.5 m (Figures 2 and 3). The section is constant and there are no end diaphragms. Each main beam supports 4 secondary beams along each side. At each extremity, the secondary beams rest on a couple of teeth protruding laterally from the wings of the main beams. (Hence, the main beams are subjected basically to the rather concentrated loads transmitted by the 4 + 4 secondary beams, Figure 5; each of these loads, however, is applied in the two sections containing the teeth, see Figure 11; note that in the following reference is made to the internal main beams, since the external beams – along the sides of the roof – support only four secondary beams).

The structural layout is that of a simply-supported beam; since this scheme is statically-determinate, all the possible variations of the internal forces ensuing from thermal gradients and prevented thermal dilations in case of fire are ruled out, something that does not occur – for instance – in monolithic slab-type roofs, that exhibit large redistributions of the internal forces in fire conditions (Bamonte et al., 2009; Buchanan, 2002).
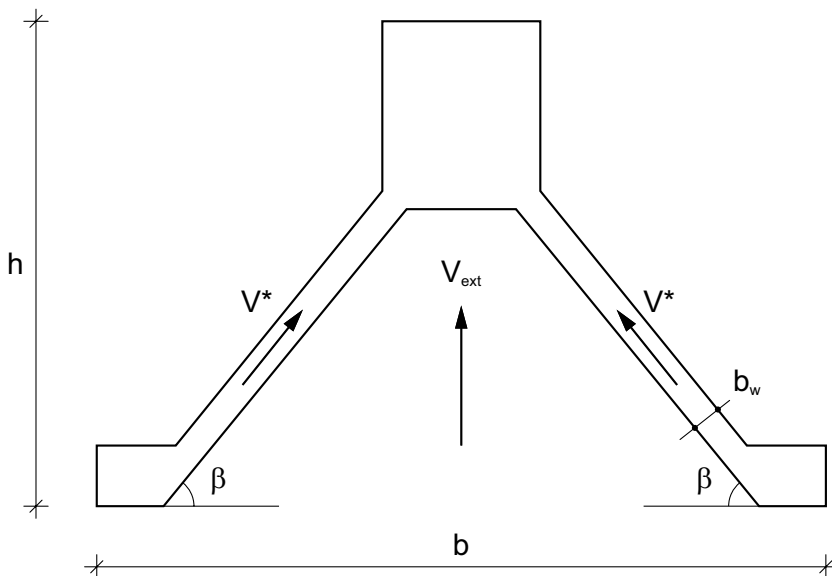

Figure 2 – Example of a wing-type section, with the shear force V_{ext} and its components V^* acting on the wings; and geometry of the section examined in this paper: total depth h = 1600 mm; width b = 2400 mm; thickness of the wings b_w = 90 mm; overall length L = 12 m; and β = 51°.

The support system and the assembly tolerances are such that no significant membrane action in the plane of the roof is to be expected; moreover, the connection devices placed between the main beams and the top of the columns (threaded steel bolts) do not allow the transmission of significant horizontal forces to the columns.

The teeth supporting the secondary beams (Figure 4) are limited to a rather small portion of the beam span and will be ignored in the following, where reference will be made only to the current section.
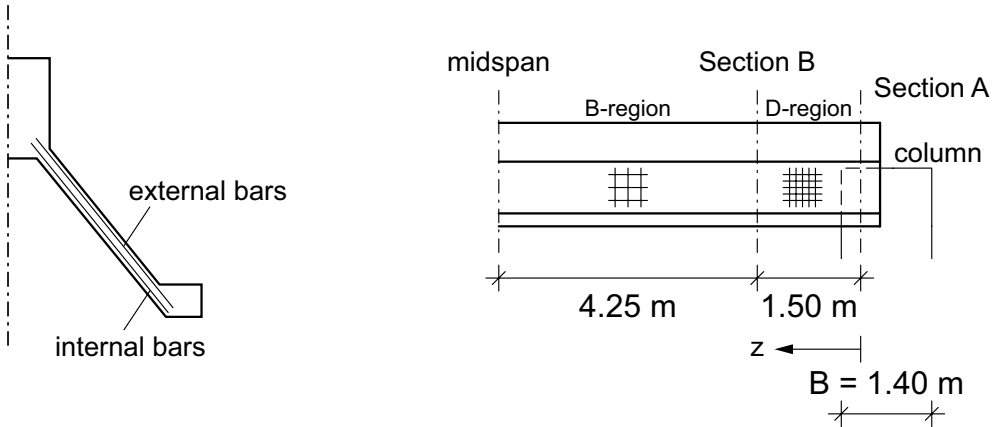

Figure 3 – (a) Half cross-section with the indication of the columns; and (b) lateral view, with the layout of the transverse reinforcement. Section A at z = 0; and Section B at z = 1.50 m.
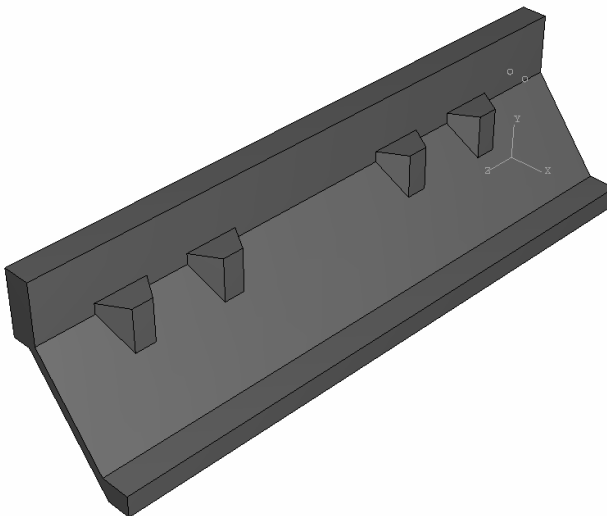

Figure 4 – 3D-view of one quarter of the beam, with the supports for the secondary V beams.

It is worth observing that the two wings connecting the upper compression chord with the bottom tension chord (or stringer) are rather thin (90 mm).

The position of the prestressing reinforcement (26 strands; diameter = 0.5 in; number of wires in each strand = 7; diameter of each wire close to 4.2 mm; cross-sectional area of the strand = 98.7 mm^2) is given in Figure 6, where the boundary conditions adopted in the thermal analysis of the current section are indicated as well. The numbering of the strands was carried out on the basis of the horizontal layers, at increasing values of the coordinates x and y.

From the position of the strands it is possible to determine the effective depth d, that will be used in the following for the calculations. In a structural element that is subjected to a combination of bending and shear, the effective depth is defined as the distance between the top of the compression chord ("extrados") and the tension chord, that coincides with the centroid of the tensile reinforcement. In the case under investigation, it is reasonable to assume that strands 1 to 12 will contribute to the tension force at the ULS, while the strand 13 is located inside the compression chord.

Therefore, the position of the centroid of the tensile reinforcement (y_{av} = 360 mm in Figure 6) is determined as the weighted average of the positions of the single strands, taking into account the fact that the strands are characterized by the same cross-section; the effective depth and the internal lever arm of the section at the ULS are: $d = h - y_{av} = 1600 - 360 = 1240$ mm; $z = 0.9\ d = 1116$ mm; in each web or wing: $d^* = d/\sin(\beta) \approx 1600$ mm; $z^* = z/\sin(\beta) \approx 1400$ mm (Figure 11).

The main geometric properties of the section are:

- Cross-sectional area: $\qquad\qquad\qquad$ A = 6197 cm^2
- Distance of the centroid from the intrados: $\qquad$ y_G = 85 cm
- Second moment with respect to x': $\qquad\qquad$ $I_x' = 16.03 \times 10^6$ cm^4
- Second moment with respect to y: $\qquad\qquad$ $I_y = 20.19 \times 10^6$ cm^4

In Figure 3 the lateral view of one half of the beam shows the layout of the ordinary reinforcement in each inclined web or wing. In each web, the zone closest to the support (D-region) and that close to mid-span (B-region) are differently reinforced. In each web or wing:

- <u>D-region</u>: Vertical reinforcement: two-leg $\varnothing 8$ mm-stirrups (spacing = 70 mm); Horizontal reinforcement: two layers of $\varnothing 8$ mm-bars (spacing 70 mm).

- <u>B-region</u>: Vertical reinforcement: two-leg $\varnothing 6$ mm-stirrups (spacing = 200 mm); Horizontal reinforcement: two layers of $\varnothing 8$ mm-bars (spacing = 210 mm).

In this paper, reference will be made to both D- and B-regions, as the former is characterized by diffusive stresses and the latter by regularly-distributed stresses.

3. LOADS AND INTERNAL FORCES

The dead load consists of the self-weight of the main beam and of the four rather concentrated loads transmitted by the secondary beams (Figure 5). These loads are applied at 1.25 and 4.25 m from each support. The self-weight of the beam is determined on the basis of the previously calculated cross-sectional area (current section). As for the loads transmitted by the secondary beams, reference should be made separately to their self weight, and to their permanent and variable loads. Assuming for each secondary beam the following values:

- Length = 18 m
- Spacing (mean plane-to-mean plane) = 3.0 m
- Sectional area = 2705 cm^2
- Area pertaining to each secondary beam = $3.0 \times 18.0 = 540$ m^2
- Self weight of the concrete panels covering or connecting the secondary beams = 1.0 kN/m^2
- Snow load (the only variable or live load) = 1.50 kN/m^2

    The following loads should be resisted by each main beam:

- Self-weight of the main beam: $g_{k1} = 15.50$ kN/m
- Self-weight of the secondary beams: $P_{gk1} = 121.50$ kN
- Permanent loads applied to the secondary beams (including the overlapping of the panels): $P_{gk2} = 73.80$ kN
- Snow load transmitted by each couple of secondary beams: $P_{qk1} = 81.00$ kN

    The applied loads and the diagrams of the internal forces (bending moment and shearing force) are indicated in Figure 5. Note that the diagrams refer to the Ultimate Limit State and to fire, respectively. Hence, two situations are considered:

- in ordinary conditions, following the provisions of the Italian Code (that is very similar to Eurocode 2), the Ultimate Limit State (ULS) is checked with the self-weight of the element increased by 30%, and the superimposed permanent and variable loads increased by 50%;

- in fire conditions the beam is subjected to the permanent loads at their characteristic values (i.e. the values are not increased), plus a suitable share of the variable load (for the snow on roof elements = 20%).

On the basis of the aforementioned provisions, the maximum bending moment at mid-span has the following values:

- Bending moment in fire conditions: $M_{fire} = 1419$ kNm
- Bending moment at the Ultimate Limit State: $M_{ULS} = 2479$ kNm
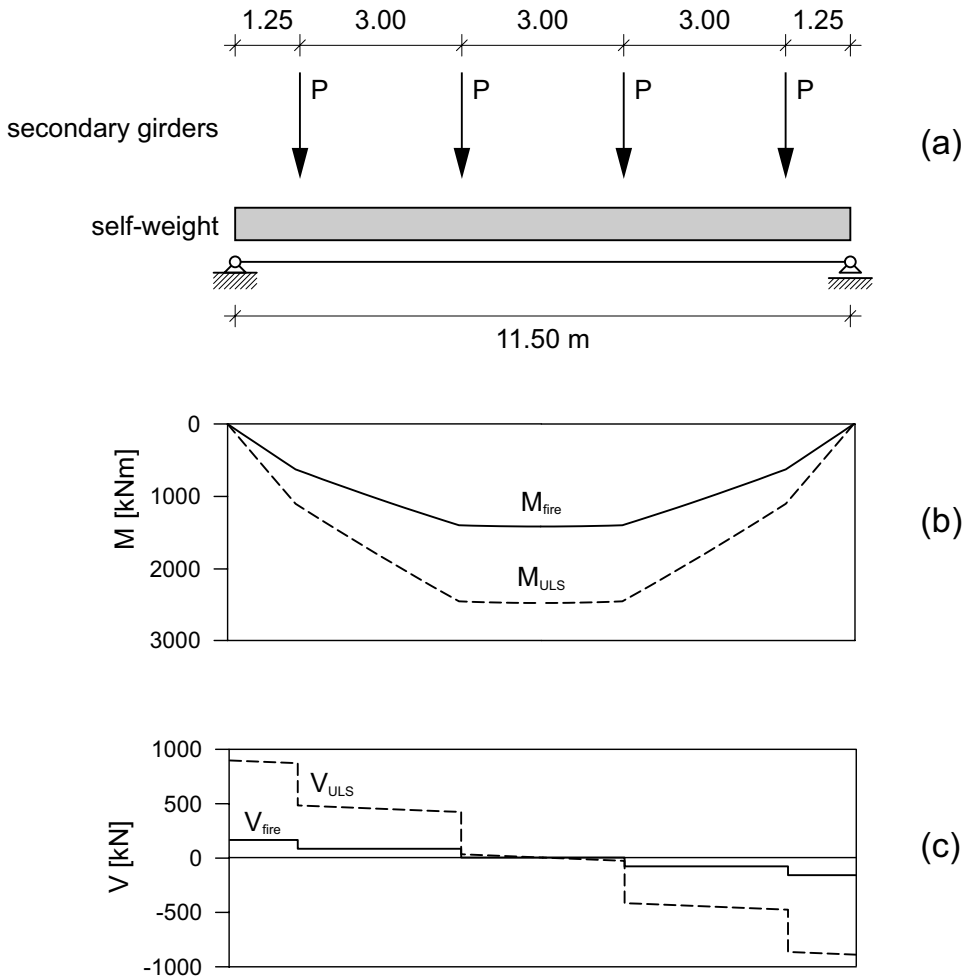
Figure 5 – (a) Loads acting on the beam; and (b,c) diagrams of the internal forces, at the Ultimate Limit State (dashed curves) and in fire (continuous curves). $P_{fire} = 212$ kN; $P_{ULS} = 390$ kN.

The same provisions are used for the maximum shear force, that occurs near the supports (D-region, Section A, $z = 0$, Figure 3):

- Shear force in Section A in fire conditions: $V_{A,fire} = 512$ kN
- Shear force in Section A at the Ultimate Limit State: $V_{A,ULS} = 896$ kN

Since the arrangement of the transverse reinforcement is not span-wise uniform, the shear-bearing capacity should be checked also in the B-region (Section B, $z = 1.50$, Figure 3):

- Shear force in Section B in fire conditions: $V_{B,fire} = 277$ kN

- Shear force in Section B at the Ultimate Limit State: $V_{B,ULS} = 476$ kN

Note that for simplicity the suffix "Sd" has not been introduced (for instance, $M_{Sd,fire}$ and $M_{Sd,ULS}$, instead of M_{fire} and M_{ULS}).

Finally, being simply supported with no axial restraints, the beam is subjected to no redistributions of the internal forces, which can be assumed to be constant during the fire.

4. MATERIALS PROPERTIES

The following materials properties were assumed according to the provisions of EC2:

- Characteristic cubic/cylindrical strength of the concrete:
$$R_{ck}/f_{ck} = 45/35 \text{ MPa}$$

- Design strength at the ULS under sustained loads (uniaxial/biaxial stresses)
$$f_{cd}/f_{cd}' = 19.8/9.9 \text{ MPa}$$

- Design strength in fire (uniaxial/biaxial stresses)
$$f_{cd}/f_{cd}' = 35.0/17.5 \text{ MPa}$$

- Characteristic/design strength at yielding of the transverse reinforcement
$$f_{yk}/f_{yd} = 500/435 \text{ MPa}$$

For the prestressing reinforcement the following values are assumed:

- Elastic modulus of the prestressing reinforcement $E_p = 195000$ MPa

- Characteristic strength of the prestressing steel at failure/at yielding
$$f_{ptk}/f_{p0.1k} = 1668/1422 \text{ MPa}$$

- Initial stress (before concreting) $\sigma_{p0} = 1200$ MPa

- Stress at the serviceability Limit State (strands with low relaxation)
$$\sigma_{p1} = 1000 \text{ MPa}$$

- Initial imposed deformation (before concreting) $\varepsilon_{p0} = 6.15‰$
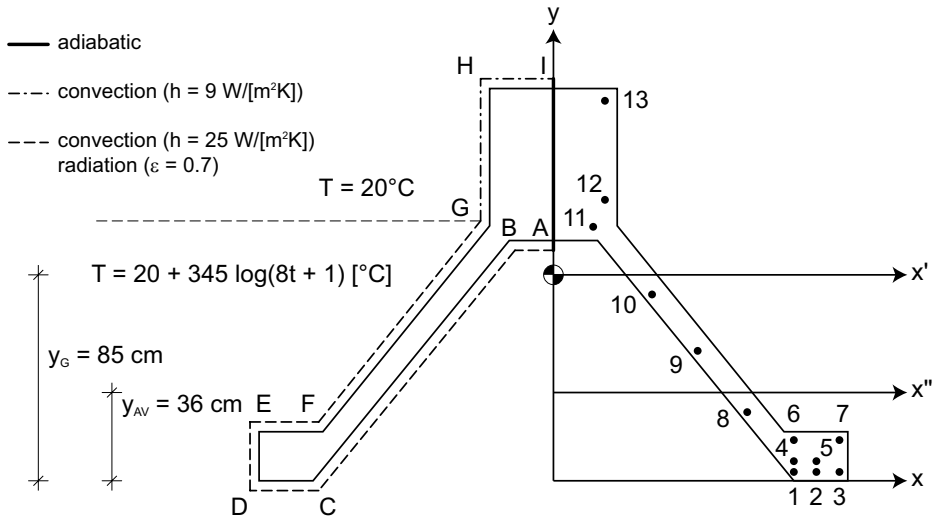
Figure 6 – Prestressing strands, centroid of the section, and centroid of the tension reinforcement at the ULS (Strands 1-12); and boundary conditions of the thermal problem (thick line = adiabatic; dashed line = standard fire; dash-dotted line: 20°C); t = [min].
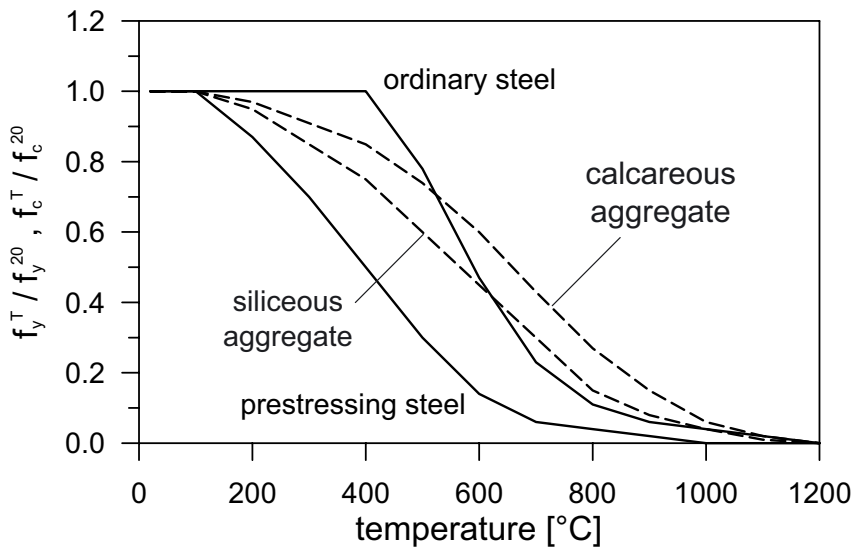

Figure 7 – Decay of the yield strength of the prestressing and ordinary reinforcement (continuous lines), and of concrete compressive strength (dashed lines), as a function of the temperature (EC2).

The deformation imposed to the strands before concreting is a sort of initial "lack of compliance" between the strands and the surrounding concrete, and has to be taken into account in the calculation of the bending capacity at the ULS, after the stress redistributions ensuing from shrinkage, creep and relaxation of the prestressing strands. However, if the prestressing steel has enough ductility (which is usually the case), the bending resistance is little affected by the value of ε_{p0}. Beside the materials properties in ordinary conditions, the properties at high temperature are to be introduced as well. In Figure 7 the normalized decay curves for the prestressing and ordinary steel, and for concrete are plotted as a function of the temperature (Eurocode 2, 2004).

5. FIRE ANALYSIS

5.1 Evaluation of the thermal field

The evaluation of the bearing capacity in fire conditions requires the preliminary thermal analysis of the cross section of the element. The aim of such analysis is to determine the temperature distribution, when the relevant boundaries are exposed to the fire.

In the following, reference is made to the standard ISO-834 temperature-time curve.

In the case under examination, the boundary conditions that are used to represent the fire are the following (Eurocode 1 (2002), Figure 6):

- along the sides defined by Points A-G, where the flames directly attack the surface of the beam, the ambient temperature is assumed to vary following the standard ISO834 temperature-time curve (whose expression is reported in Figure 6, left): the heat transfer to the structural element is governed by convection (convection coefficient = 25 W/[m²·K]) and radiation (concrete emissivity = 0.7);

- along the sides defined by Points G-I, where the surface of the beam is directly exposed to the external environment at 20°C, the heat exchange between the beam and the environment is governed again by convection and radiation; the two phenomena, however, are lumped together, as it is usually done, by introducing convection with a suitably modified coefficient (= 9 W/[m²·K]);

- along the side defined by points I-A there is no heat exchange (adiabatic conditions), because of symmetry.

Heat transfer inside the beam occurs by conduction, that is controlled by concrete thermal properties, namely conductivity and specific heat, and by the density. The values used in the analysis were chosen in accordance with the

provisions of Eurocode 2 (2004). For the thermal conductivity, the Eurocode allows to choose between an upper curve and a lower curve; in the present case, the mean value was assumed in the analysis.

The thermal analysis was carried out by means of the finite element code ABAQUS, by setting up a two-dimensional model of the cross section, that neglects the reinforcement (as usually done in the thermal analysis of R/C and P/C members). Triangular elements with quadratic shape functions (6 nodes for each element) were adopted; the mesh consisted of 1320 elements with 2849 nodes (Figure 8a-d).

Figures 8b-d shows the thermal field for a standard-fire duration of 60, 90 and 120 minutes. The temperature contour lines are plotted only in the area where the temperature is above 500°C. This value is usually considered as a threshold for both concrete and ordinary steel, as both materials suffer a significant strength loss above 500°C, but keep most of their strength unaffected below this temperature.

Therefore, in the so-called simplified approach to fire analysis the 500°C isothermal line separates the area of the section that is fully effective in resisting the fire from the remaining area that is severely damaged and can be neglected (except for the reinforcement comprised in this area). In the following, the simplified approach based on the 500°C-isothermal will be used in bending, but the more refined multi-zone approach will be adopted in shear. (Note that the former approach does not require the knowledge of concrete decay at high temperature, which is required by the latter approach).

Figure 9a shows the temperatures in the prestressing strands as a function of the fire duration; clearly, these values have a significant influence on the overall behaviour of the beam in fire, since (a) the thermal dilations ensuing from the temperature rise bring in a very rapid and sizable prestress loss (Gales et al., 2010); and (b) the above-mentioned thermal damage negatively affects the yield strength, thus reducing the bending capacity in fire.

For instance, at t = 60 minutes, the isothermal line 500°C coincides with the mean line of the section of the wing and the effective or reduced thickness of the wing becomes zero (according to the 500°C-isothermal line approach). This is the reason why a more refined approach should be used in shear (the above-mentioned multi-zone approach), as the shearing force is mainly absorbed by the wings.

The temperatures in Figure 9a are the starting point for evaluating the decay of the mechanical properties of each strand (see in Fig.9b the strength at yielding of each strand as a function of fire duration). To this end, the decay curves provided by the design codes as a function of the temperature should be used (see the curves provided by EC2 in Figure 7).

It is worth noting that beyond 1000°C, the strength of the prestressing steel becomes negligible.
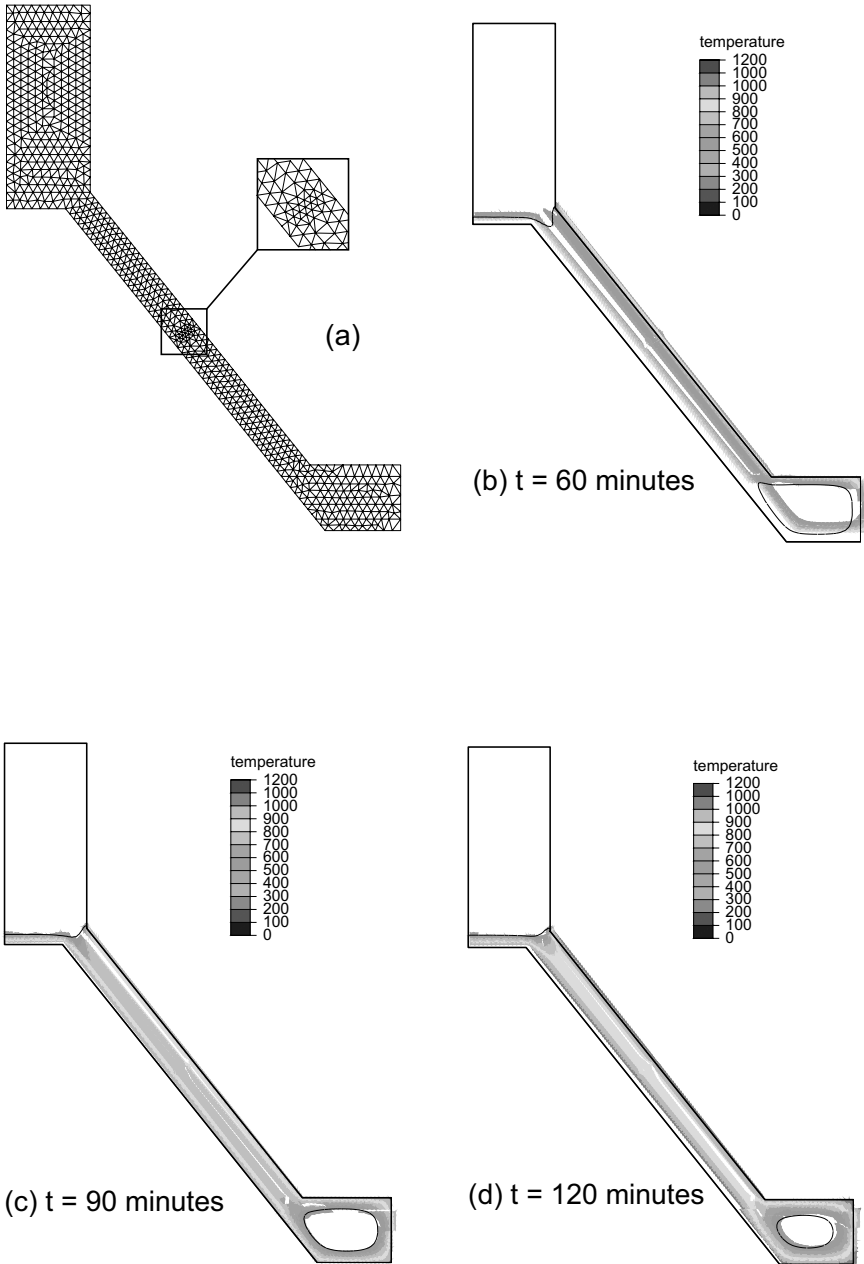
Figure 8 – Thermal analysis: (a) 2D modeling of half section; and (b) position of the 500°C isothermal line inside the section for t = 60 minutes (the wing is totally above 500°C).
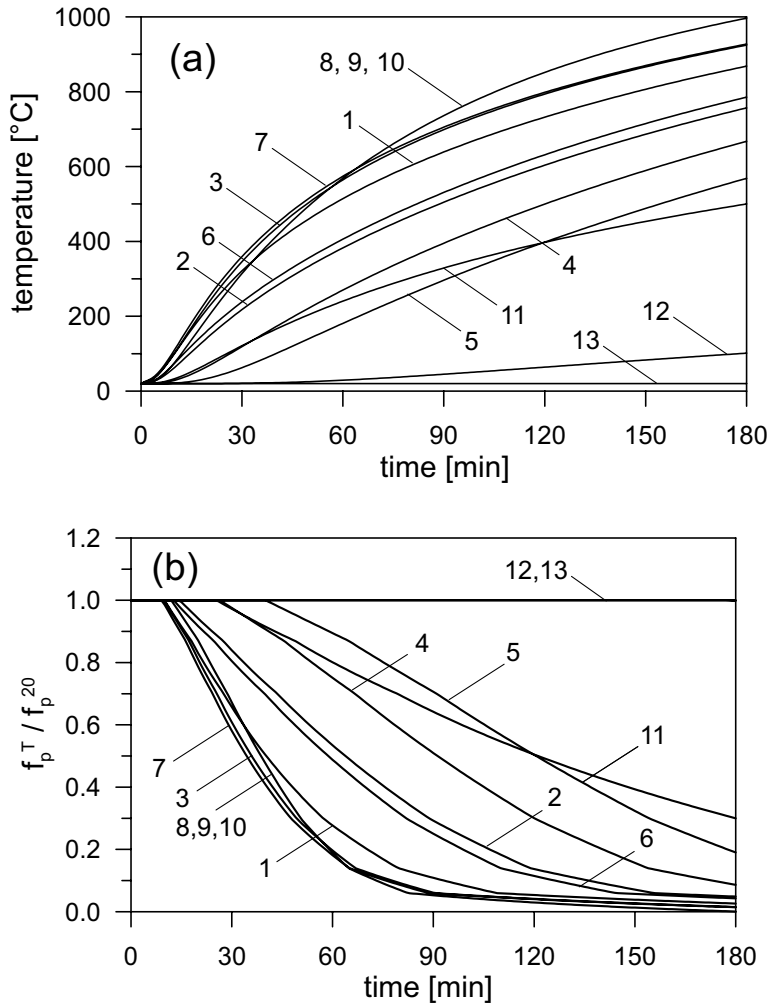
Figure 9 – (a) Temperature and (b) strength at yielding in the prestressing strands, as a function of fire duration (ISO-834 fire).

5.2 Bending capacity at the ULS and in fire

The bending capacity was determined by assuming a non linear distribution of the compression stresses acting on the concrete (approximated by means of a stress block), and an elastic-perfectly plastic behaviour for the prestressing steel, with infinite ductility. The internal lever arm at 20°C turned out to be close to 0.9d.

The resisting moment M_{Rd} is equal to 3173 kNm, that is approximately 30% larger than the design moment at the Ultimate Limit State (3173/2479 = 1.28).

In underreinforced sections, the bending capacity is governed by the yielding of the reinforcing steel, in order to ensure enough ductility at the ULS. The same applies in fire conditions, where the temperature-induced decay of the reinforcing steel determines the decrease of the bending capacity.

Hence, as already mentioned, knowing the decay of the yield strength for each strand is a must; the starting point is the evolution of the temperature in each strand (Figure 9).

The decay of the sectional bearing capacity in bending is evaluated by using the 500°C-isotherm method, which is suggested by the Eurocode 2 for any members subjected to normal stresses. The main assumptions of this simplified method are:

- concrete that has reached temperatures above 500°C is considered totally damaged, and thus not effective from a structural point of view ($f_c^T = 0$);

- concrete that has reached temperatures below 500°C is assumed to have the same mechanical properties as in virgin conditions ($f_c^T = f_c^{20} = f_c$);

- for both the prestressing and ordinary reinforcement, the mechanical decay is evaluated on the basis of the actual temperature (Figures 8 and 9).

It is worth recalling that, in fire conditions, the resistance is evaluated on the basis of the characteristic strengths of the materials, and not of the design strengths, as at the Ultimate Limit State.

The value of the bending moment in fire conditions at mid-span is $M_{Sd,fire} = M_{fire} = 1419$ kNm.

Figure 10 shows the decay of the resisting bending capacity according to two different approaches:

- lower curve (●):   500°C-isotherm method;

- upper curve (◆):   the decay is assumed to be equal to the average decay of the yield strength in the prestressing strands in tension (Strands 1-12); this assumption implies that the internal lever arm is constant during the fire, something that in principle is not correct.

It is worth noting that the two approaches yield results that are practically coincident; the second approach, however, tends to slightly overestimate the contribution of the strands in the web (8, 9 and 10), that are the hottest (Figure 9), and thus are more prone to thermal decay.

The intersection between the curves (representing the decay of the bending capacity) and the horizontal line (representing the bending moment in fire) is close to 80 minutes.
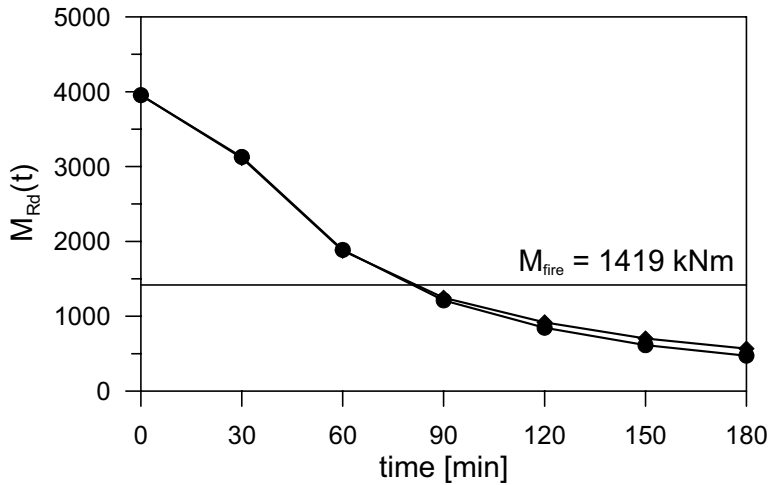
Figure 10 – Evaluation of the fire resistance in bending: (•) 500°C-isotherm method; and (♦) according to the average decay of the yield strength of the prestressing reinforcement.

5.3 Shear capacity at the ULS and in fire

The evaluation of the bearing capacity in shear can be carried out by assuming that the shear force is resisted solely by the two inclined webs, as shown in Figure 2, where the shearing force V_{ext} (due to the external or applied loads) has two components V^* acting on each wing. The angle of the wings with respect to a horizontal axis is $\beta \approx 51°$.

The forces V^* and V_{ext} (the latter evaluated through structural analysis) are related by the following simple expression:

$$V^* = V_{ext}/[2 \cdot \sin(\beta)] \approx 0.64 V_{ext}$$

It is now possible to evaluate the maximum force acting on each single wing, on the basis of the maximum shear values in Section A ($z = 0$) and in Section B ($z = 1.50$ m):

- Shear force in Section A (in fire conditions) $V^*_{A,fire} = 329$ kN
- Shear force in Section A (at the ULS) $V^*_{A,ULS} = 576$ kN
- Shear force in Section B (in fire conditions) $V^*_{B,fire} = 178$ kN
- Shear force in Section B (at the ULS) $V^*_{B,ULS} = 306$ kN

D-region

In this D-region (Schlaich et al., 1987), the reaction exerted by the support spreads into the inclined webs, while the prestressing force – albeit rather distributed – is not totally efficient (and is neglected in the following).

The web behaviour can be modelled through a strut and tie mechanism, with the formation at the onset of collapse of compressive and tensile bands representing the concrete and the reinforcement, respectively.

The position of the struts and ties depends on the geometry, on the size of the bands and on the distribution of the reaction at the supports, see Figure 11, where half a beam is represented ; the loads $P^* = V^*A/4 = 144/82$ kN (at the ULS/in fire, including the self-weight of the beam) act in the mean plane of each wing and are transmitted by the secondary beams in the sections containing the supporting teeth, that are 4 over 50% of the span. (Note that the nominal span in Figure 11 $L_N =$ 11.10 m is slightly smaller than the span $L = 11.50$ m adopted in the evaluation of the internal forces – see Figure 5 – because the reaction has been considered as linearly-distributed at the column-beam contact, that is $B/2 = 70$ cm-long, as the column side is $B = 140$ cm, see Figure 3).

The axial forces in the truss members closest to the support are as follows:

- in fire: $N_{1,fire} = 253$ kN; $N_{2,fire} = -183$ kN; $N_{3,fire} = 35$ kN; $N_{4,fire} = 299$ kN; $N_{5,fire} = -292$ kN
- at the ULS: $N_{1,ULS} = 445$ kN; $N_{2,ULS} = -321$ kN; $N_{3,ULS} = 62$ kN; $N_{4,ULS} = 525$ kN; $N_{5,ULS} = -514$ kN

In order to evaluate the resisting contributions, the resisting sections should be defined. As each member represents a more or less wide "band" related to wing geometry, to the reinforcement and to the loads, among the 5 members belonging to the D-region, only the ties 1 and 4, and the strut 2 will be considered. (As a matter of fact, tie 3 is hardly loaded, and strut 5 takes advantage of the full height of the wing).

For tie 1, all the reinforcement distributed over a length $h^*/2 = 70$ cm in both directions x and y has been considered:

- Vertical reinforcement: two-leg stirrups $\varnothing$8 mm/70 mm
  $\Rightarrow A_y = 1005$ mm^2
- Horizontal reinforcement: two layers of $\varnothing$8 mm/70 mm
  $\Rightarrow A_x = 1005$ mm^2

As the steel ratio in the vertical and horizontal directions are equal, the shear resistance of the reinforcement (after yielding) in any direction – and namely at α' = 56° – is the same as in the x and y directions, it can be assumed that $A_1 = A_y = A_x \approx 1000$ mm^2.
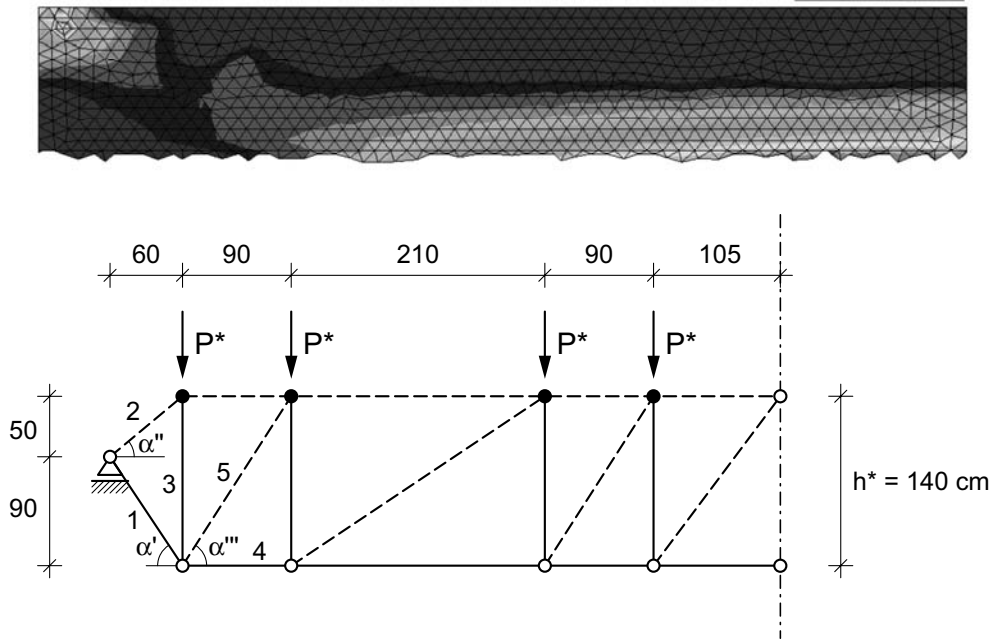
Figure 11 – (a) Map of the principal tensile stresses in each web; and (b) strut-and-tie model adopted in each web for D-regions; the extension to the mid-span section is for the sake of completeness; the traditional variable-inclination model has been used far from the supports (in B-regions); $\alpha' \cong 56°$; $\alpha'' \cong 57°$; $\alpha''' \cong 40°$.

For the tie 4, the strands 1-7 have been grouped together, and therefore the total area is $A_4 = 691$ mm^2

For strut 2, the transverse side of its section is equal to the thickness of the wing ($b_w = 90$ mm), while the other side may be prudentially taken close to 1/5 of the effective depth of of the wing (320 mm). Hence $A_2 = 28800$ mm^2.

Hence, the checks are satisfied both in fire (at t = 0) and at the ULS:

- $N_{1,Rd,fire} = A_1 f_{yk}$ ($N_{1,Rd,ULS} = A_1 f_{yd}$) = 500 kN (435 kN*) $\Rightarrow N_{1,fire}$ ($N_{1,ULS}$) = 253 kN (445 kN*)
- $N_{2,Rd,fire} = A_2 f_{ck}'$ ($N_{2,Rd,ULS} = A_2 f_{cd}'$) = 504 kN (286 kN*) $\Rightarrow N_{2,fire}$ ($N_{2,ULS}$) = 183 kN (321 kN*)
- $N_{4,Rd,fire} = A_4 f_{p0.1k}$ ($N_{4,Rd,ULS} = A_4 f_{pd}$) = 982 kN (855 kN) $\Rightarrow N_{4,fire}$ ($N_{4,ULS}$) = 299 kN (525 kN)

(*) As the focus is on fire resistance, this check may be considered as satisfied.

The resisting contributions $N_{4,Rd,fire}$ and $N_{4,Rd,ULS}$ should be reduced (-25% in the following) to take into account the limited anchored length of the strands,

which prevents them from being fully effective in the section containing the joint among tie 2, tie 3 and strut 5.

It should be remembered that in fire (t ≥ 0) not only the reinforcement, but also the concrete exhibit a mechanical decay. Hence, the resisting contributions of the reinforcement and of the wings will be evaluated separately. (Especially in thin-walled members, the concrete of the webs may be in principle as heat-sensitive as the reinforcement, something that does not occur in solid members, where the mean temperature of the concrete is much lower than that of the reinforcement).

Assuming for the two layers of the transverse reinforcement (stirrups + longitudinal bars) a cover of 20 mm (from the heated surfaces to the axes of the bars, as usual in fire design), the temperature-time curve of the transverse reinforcement is shown in Figure 12, together with the decay of the normalized strength at yielding.

The evaluation of concrete decay under shear-compression (i.e. in the struts) has been performed with the zone method, by subdividing each wing into 8 layers (= 4 zones, Figure 13a), which are symmetric with respect to the mean plane. The evolution of the mean temperature in each layer – as a function of the fire duration – is shown in Figure 13b.
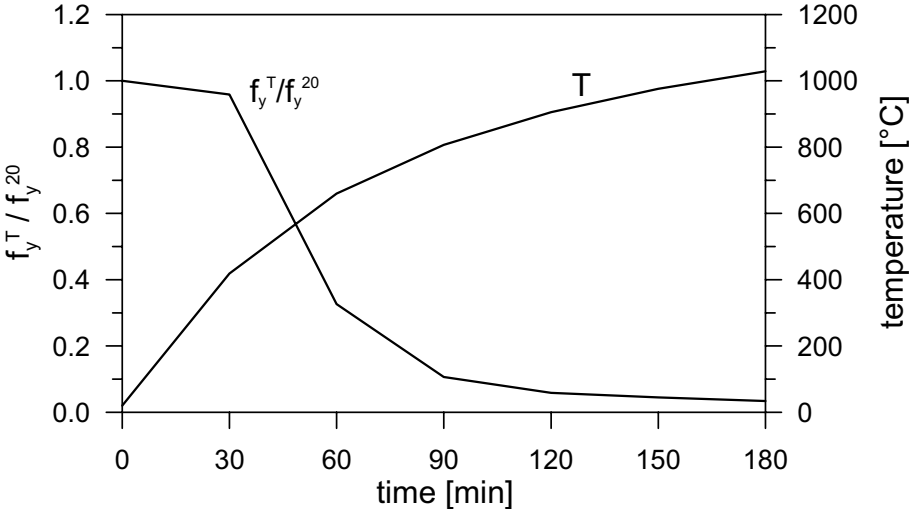
Figure 12 – Plots of the temperature in the transverse reinforcement and of the normalized strength at yielding (according to EC2), as a function of the fire duration.
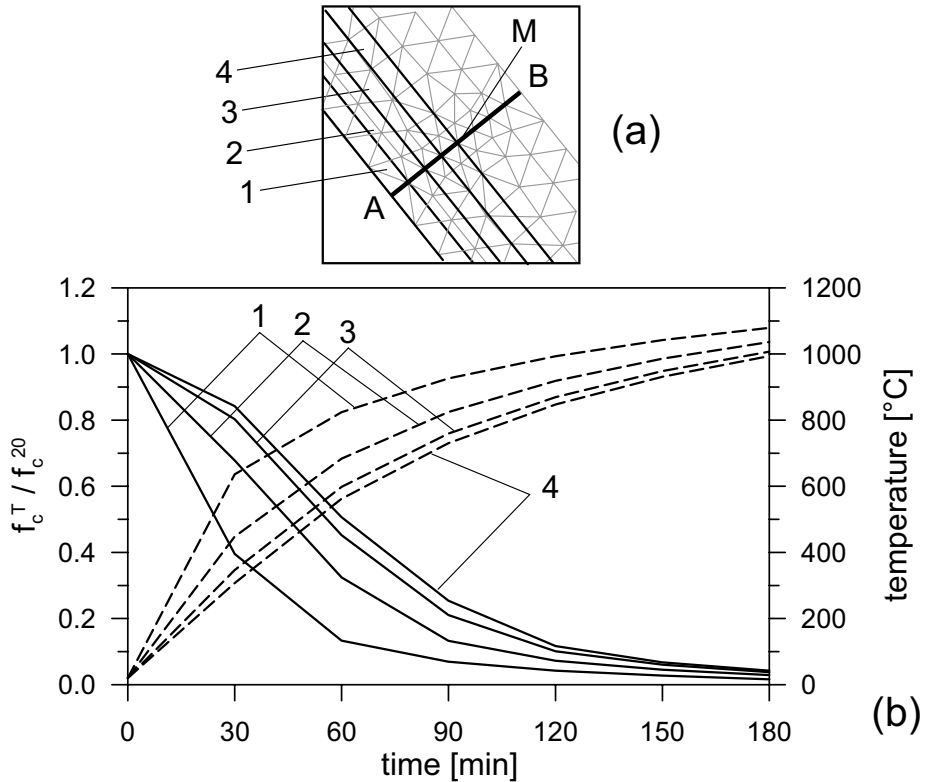
Figure 13 – (a) Subdivision of the wing section into 4 zones; and (b) plots of the mean temperature (dashed curves) and of the normalized concrete strength in each zone (continuous curves), as a function of fire duration.

In Figure 14 the normalized strength decay of the concrete $k_c(M)$ in the mean plane (M along the chord AB, Figure 13a) and the mean normalized strength decay k_{cm} (evaluated among the four zones) are plotted, together with the temperature in the mean plane $T(M)$, as a function of fire duration.

In the following, the expressions of k_{cm}, a_z (= thickness of the totally-damaged layer) and of b_w^R (= effective or reduced thickness) are reported, according to EC2:

$k_{cm} = [(1 - 0.2/n)/n] \cdot \Sigma_i \, k_c(Ti)$ (1)

$a_z = b_w/2 \cdot [1 - k_{cm}/k_c(M)]$ (2)

$b_w^R = b_w - 2a_z = b_w \cdot [k_{cm}/k_c(M)]$ (3)

where: n = number of the zones

                         T_i = mean temperature of the i-th zone

                         b_w = web or wing design thickness

It is worth noting that $k_{cm}/k_c(M)$ brings in the lack of uniformity of the thermal field.

The reduced or effective thickness b_w^R is plotted in Figure 15 as a function of fire duration. Note that (a) at the beginning of the fire ($T = 20°C$), the value of k_{cm} becomes 1 only if $n \rightarrow \infty$ [in our case, with $n = 4$, $k_{cm} = 0.95$, which means: b_w^R (20°C or t = 0) = 85.5 mm, instead of 90 mm]; and (b) the rather odd evolution of b_w^R with the fire duration has to do with the temperature-dependency of k_{cm} and $k_c(M)$.
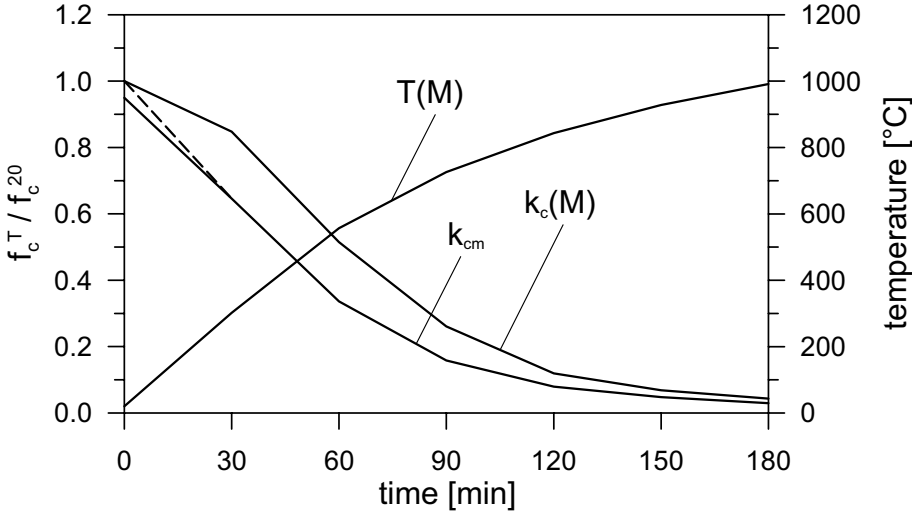
Figure 14 – Plots of the temperature T(M) and of the normalized-strength decay $k_c(M)$ in the mean plane of the wing, and plot of the mean decay of the normalized strength k_{cm}: the dashed curve is in accordance with the actual temperature at the beginning of the fire ($T = 20°C$, ambient temperature), and the continuous curve is in accordance with Eq. (1).

In Figure 16 the axial capacities of the members 1 (tie), 2 (strut) and 4 (tie) are plotted as a function of the fire duration ($N_{1,Rd,fire}$; $N_{2,Rd,fire}$; and $N_{4,Rd,fire}$, respectively), together with the corresponding values of the internal forces in fire conditions ($N_{1,fire}$; $N_{2,fire}$; and $N_{4,fire}$). Note that the axial capacity of each member is obtained by multiplying the reduced section by the strength corresponding to the temperature in the mid-plane T(M).

In the D-region, section $z = 0$ m, the collapse occurs at roughly 50 minutes because of steel yielding in the inclined tie No.1 (Figure 11), while it would occur at roughly 58 minutes in case of concrete crushing in strut No.2 and at 70 minutes in case of steel yielding in tie No.4.

Figure 15 – Plot of the effective or reduced thickness bwR as a function of the fire duration: the dashed curve is in accordance with geometry (bw = 90 mm) and the continuous curve is in accordance with Eq. (1).

Figure 16 – Evaluation of the shear resistance in fire: plots of the different shear-resisting contributions, as a function of the fire duration.
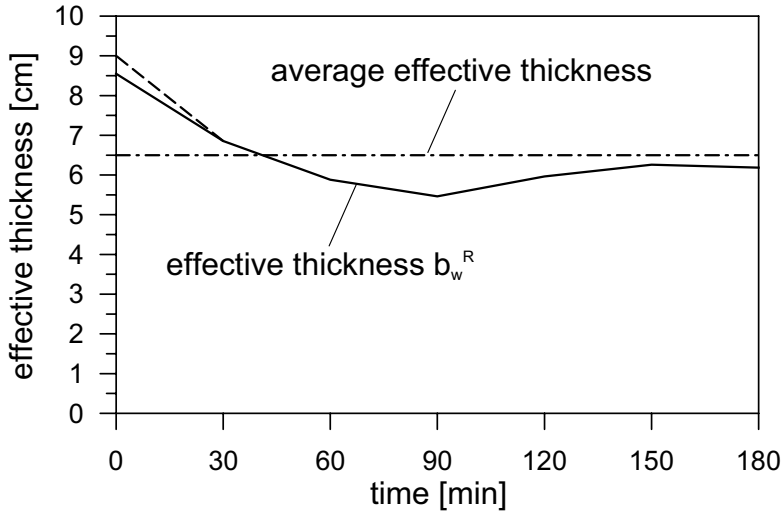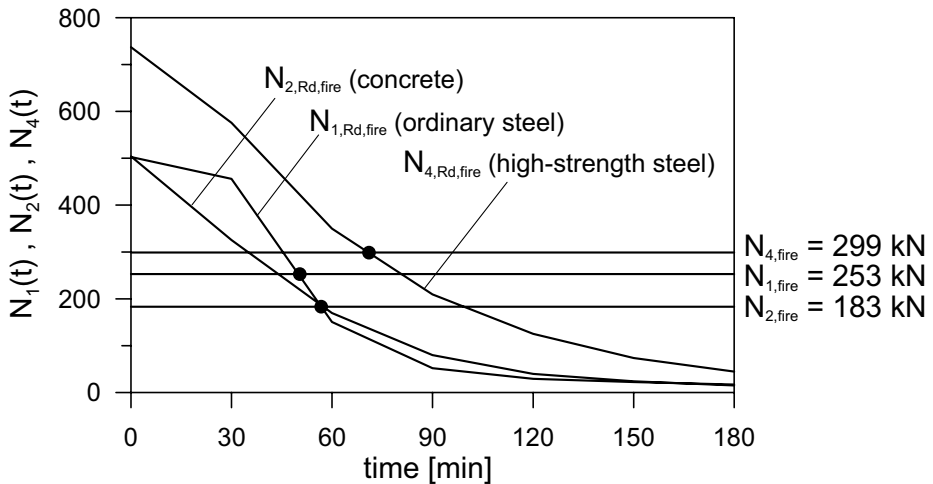
B-region

The bearing capacity is checked by using the traditional truss model, with variable inclination (i.e. to be established by the designer), that is a realistic representation of the mechanical behaviour of thin concrete webs subjected to prevailing shear (Leonhardt et al., 1973; Dei Poli et al., 1987; Adebar et al., 1998; Toniolo and di Prisco, 2010). The resisting mechanism consists of transverse reinforcement, longitudinal reinforcement, concrete compression chord and inclined concrete struts (Figure 17).
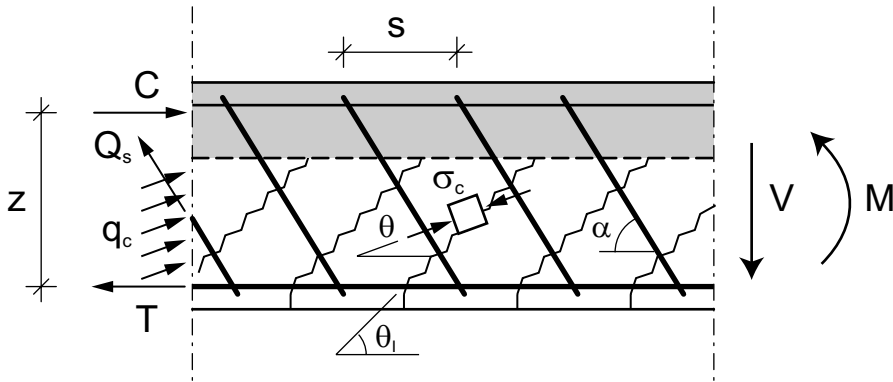
Figure 17 – Shear-resisting truss system ($22° \leq \theta \leq 45°$); $\alpha = 90°$ for stirrups; and $\alpha \neq 0$ for inclined reinforcement (none in the case in question).
The transverse reinforcement consists of stirrups: two-leg $\varnothing$6mm ($A_{sw} = A_{st} = 56.5$ mm^2), with $s_{sw} = 200$ mm.

The contributions to the shear capacity of each wing are as follows (no inclined bars):

- Stirrups $\qquad V^*_{Rsd} = 0.9 \cdot A_{st} \cdot (d^*/s_{st}) \cdot f_{yd} \cdot \cot(\theta)$
- Inclined concrete struts $\qquad V^*_{Rcd} = 0.9 \cdot d^* \cdot b_w \cdot \alpha_c \cdot f_{cd}' \cdot \cot(\theta)/[1 + \cot^2(\theta)]$

where: A_{st} (stirrup area, two legs) = 56.5 mm^2; s_{st} = 200 mm
$\quad\quad$ d^* (effective depth of each single wing) = $d_{AV}/\sin(\beta)$ = 1600 mm
$\quad\quad$ b_w (web or wing thickness) = 90 mm
$\quad\quad$ α_c (coefficient that takes care of the favourable effect of prestressing) = 1.00-1.25 (EC2)

By assuming that (a) the prestressing force is fully distributed on the sections at the ULS ($\alpha_c = 1 + \sigma_{cp}/f_{cd} = 1.21$) and is totally ineffective in fire ($\alpha_c = 1.00$), and (b)

the mean prestressing stress acting in the strands is close to 1000 MPa, the value of θ turns out to be even less than the minimum (22°) specified by EC2. Hence, in the following θ is given the value 22°.

The following values are obtained for the shear resistances:

- $V^*_{B,Rsd}$ = 489 kN at the ULS; and 506 kN in fire (t = 0)
- $V^*_{B,Rcd}$ = 532 kN at the ULS; and 777 kN in fire (t = 0)

The above values of the resisting shear forces are higher than the acting shear forces in both ULS and fire conditions (for t = 0), as $V^*_{B,ULS}$ = 306 kN, and $V^*_{B,fire}$ = 178 kN.

In Figure 18 the decay of the resisting contributions of the stirrups and of the concrete are plotted as a function of the fire duration. The plots of Figure 18 were obtained in the same thermal conditions as those previously discussed for the transverse reinforcement in the D-region (see Figure 12).
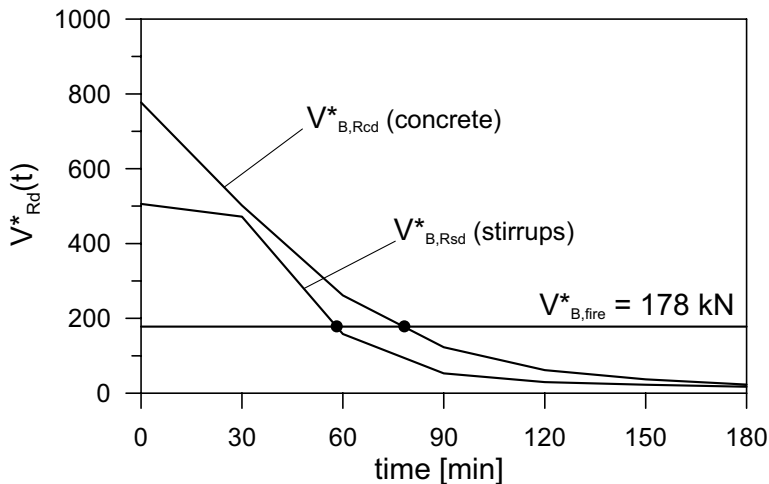
Figure 18 – Evaluation of the fire resistance in shear, Section B with z = 1.5 m.

In the B-region, section z = 1.50 m, the collapse occurs at roughly 60 minutes because of stirrups yielding, while it would occur at roughly 80 minutes in case of concrete crushing.

It is worth noting that in the previous calculations, it was implicitly assumed that in fire conditions the inclination of the concrete struts is the same as in virgin conditions at the Ultimate Limit State (i.e. θ = 22° in the B-region). The strut

inclination, however, is in principle affected by concrete and steel strength decay, as well as by the stress redistribution ensuing from first cracking and from the decreasing effectiveness of prestressing at high temperature. Hence θ dependence on the thermal field should be in some way introduced, but addressing this topic – even concisely – is beyond the scope of this paper.

6. CONCLUDING REMARKS

Thin-walled open-section P/C girders in fire conditions are among the most heat-sensitive structural members, because of their large exposed surfaces, rather small thickness, small-diameter reinforcement and limited cover, not to talk about the distributed prestressing (in pre-tensioned members), that limits the protection offered by the cover to the strands closest to the heated surfaces.

In the heavy-duty inverted-V girder investigated in this paper, the results of the analysis in standard-fire conditions show that bending is not a problem, since the fire resistance is close to 80 minutes. Such a figure (that is appropriate for a single storey, industrial or office building) is predicted by both the 500°C-isotherm method, and the method based on the average decay of the yield strength of the strands, with minimal differences.

In shear (that is definitely dangerous in thin-walled members), the results show that care should be used in modelling the end zones, where strut-and-tie models allow to understand the roles of the concrete struts (whose effective section may markedly decrease because of the heat-induced damage in the concrete) and of the steel ties (either stirrups or prestressing strands). In the case in question, the shear resistance in fire in the end zones (D-regions) turns out to be close to 50 minutes, while in the undisturbed zones (B-regions) is close to 60 minutes (in both cases the reinforcement fails first, but the fire resistance of the concrete in compression is not much larger!).

Two comments may be made with reference to the checks performed in this study: (a) in the end zones, the check at the Ultimate Limit State may be more critical than in fire conditions in spite of the heat-induced materials damage, because in the latter case materials strengths are definitely larger at the onset of fire and loads are definitely smaller; and (b) in the undisturbed zones, decreasing too much the transverse reinforcement – even if justified at the ULS – may lead to a critical situation in fire, because of the little protection offered to the stirrups by the rather small concrete cover.

Furthermore, contrary to solid sections, where concrete tends to keep its integrity in fire and a number of internal redundancies can be mobilized together or after steel yielding, in thin-walled members exposed to fire concrete may become as critical as the reinforcement in terms of resistance, as no sizable contributions coming from the redundancies of the strut-and-tie system should be expected.

ACKNOWLEDGEMENTS

REFERENCES

Adebar P.E., Collins M.P., Mitchell D., Reineck K.H. and Rogowsky D.M.* (1998). "Recent Approaches to Shear Design of Structural Concrete", *ASCE-ACI Committee 445 on Shear and Torsion, ASCE Journal of Structural Engineering*, V.124, No.12, pp.1375-1417 (*Members of Subcommittee 445-1, who prepared this report).

Bamonte P., Felicetti R. and Gambarova P.G. (2009). "Punching Shear in Fire-Damaged Reinforced Concrete Slabs". *ACI Special Publication 265 "Thomas T.C. Hsu Symposium on Shear and Torsion in Concrete Structures"*, pp. 345-366.

Bamonte P., Felicetti R., Gambarova P.G. and Giuriani E. (2010). "Thin-Walled Open-Section P/C Beams in Fire: a Case Study". *fib-Fédération Internationale du Béton, Bulletin No.57*, *Proc. Int. Workshop on "Shear and Punching in RC and FRC Elements", Task Group 4.2, ed. by Giovanni Plizzari and Fausto Minelli*, Salò (Brescia, Italy), October 2010, pp.173-193.

Barazzetta G. (ed., 2004): *Aldo Favini – A Life for Architecture and Engineering (in Italian)*. Pub. by CLUP (Milan, Italy), 126 pp.

Buchanan A. (2002). *Structural Design for Fire Safety*. Wiley & Sons, 436 pp.

CEN, European Committee for Standardization. EN 1991–1–2. *Eurocode 1: Actions on structures – Part 1–2: General actions – Actions on structures exposed to fire*. Brussels, Belgium, 2002.

CEN, European Committee for Standardization. EN 1992–1–2. *Eurocode 2: Design of concrete structures – Part 1–2: General rules – Structural fire design.* Brussels, Belgium, 2004.

Dei Poli S., Gambarova P.G. and Karakoç C. (1987). "Aggregate Interlock Role in R/C Thin-Webbed Beams in Shear". *ASCE Journal of Structural Engineering*, V. 113, No. 1, pp. 1-19.

J. Gales, L. Bisby and C. Macdougall (2010). "Fire-Induced Transient Creep Causing Stress Relaxation and Tendon Rupture in Unbonded Post-Tensioned Structures: Experiments and Modeling". *Proc. Sixth Int. Conf. on "Structures in Fire" – SIF'10*, ed. by Venkatesh Kodur and Jean-Marc Franssen, pub. by DEStech Publications Inc. (Lancaster, PA, USA), East Lansing (Michigan, USA), June 2-4, 2010, pp. 727-734.

Leonhardt F., Koch R. and Rostasy F.S. (1973). "Schubversuche an Spannbetonträgern" (Shear Tests on P/C Girders). *Deutscher Ausschuss für Stahlbeton*, V. 227, Berlin (Germany).

J. Schlaich, K. Schäfer and M. Jennewin (1987). "Toward a Consistent Design of Structural Concrete". *PCI Journal*, Vol. 32, No. 3, pp. 74-149.

Taerwe L., Poppe A.M., Annerel E. and Vandevelde P. (2006). "Structural Assessment of a Pretensioned Concrete Girder after Fire Exposure", *Proc. 2nd Int. fib Congress*, Napoli (Italy), 5-8 June 2006, full paper on CD.

Toniolo G. and di Prisco M. (2010). *Reinforced Concrete – Ultimate Limit State Design (in Italian)*. Pub. by Zanichelli, Bologna (Italy), 569 pp.

ON THE FIRE BEHAVIOR OF A SPECIAL TYPE OF PRESTRESSED COMPOSITE STRUCTURES CALLED PCS

Sergio Tattoni[1], Antonello Gasperi[2]

ABSTRACT

The behavior in fire of a special type of prestressed composite structures is investigated both experimentally and theoretically. This type of prestressed composite structure - called PCS - consists of a *primary structure* and of one or more *prestressing structures* interacting with the primary structure.

A beam provided with *end* and *intermediate contact elements* (all fixed to the beam) makes up the *primary structure*.

A longitudinal strut, a tendon (anchored at the end sections of the longitudinal strut) and a number of deviating elements (all connected to the longitudinal strut and in contact with the tendon) make up the *prestressing structure*.

In the PCS presented in this paper the beam belonging to the primary structure is a traditionally-prestressed concrete box beam, and the prestressing structure is placed inside the internal volume (*hollow core*) of the box beam.

Predicting the thermal field in the prestressing structure (and particularly in the tendon) when the entire structure is subjected to a fire is the primary objective, that is achieved partly experimentally and partly numerically, by investigating the box beam subjected to the Standard Fire (ISO 834). Numerical analysis shows that the temperature of the tendon - inside the box beam - increases slowly and does not exceed 150°C for more then three hours, as confirmed by the experimental results obtained by testing a portion of a reduced-scale concrete box beam, whose thermal behavior is equivalent to that of the full-size box beam.

The conclusion is that the PCS in question, with the prestressing structure placed inside the internal volume of the box beam, is a good structural solution in terms of fire resistance.

---

[1] Professor, Department of Structural Engineering, University of Cagliari, Cagliari, Italy.
2 MS Civil Engineer, Modena, Italy.

1. INTRODUCTION

1.1 Description of the PCS

PCSs are a special type of prestressed composite structures, consisting of a primary structure and of one or more prestressing structures interacting with the primary structure. (For the conceptual design of PCSs, see Antonello Gasperi, 1999 and 2004).

The specific PCS investigated in this research project is illustrated in Fig 1, where the simply-supported PCS (subjected to the loads Q) is indicated with "1". PCS (1) comprises a *primary structure* (3) and a *prestressing structure* (4).

The primary structure (3) consists of a precast concrete beam (3a), two end contact elements (3b) and five intermediate contact elements (3c), all fixed to the beam. The primary structure is in contact with the external supports (2a, 2b) and bears the loads Q. In the primary structure (3), the beam (3a) is a traditionally-prestressed precast concrete beam. (Prestressing is performed by pre-tensioning a number of strands according to the well known technology).

The prestressing structure (4) comprises a longitudinal strut (4a) - primarily subjected to axial compression -, a tendon (4b) anchored at the end sections of the longitudinal strut (4a), and five steel deviating elements (4c) which are connected to the longitudinal strut and are in contact with the tendon. The longitudinal strut (4a) is parallel to the axis of the primary structure and consists of two mutually-connected steel members (5). The tendon (4b) consists of two groups (6) of high-strength steel sheathed strands, that are placed inside as many polymeric ducts filled with a protective material; the strands (and so the tendon) are anchored at the end sections of the longitudinal strut. The relatively-short strut-like deviating elements (4c) give the tendon a curved shape. The prestressing structure is in contact with the primary structure via the contact elements (3c) and (3b).

In PCS (1) the relative longitudinal displacements between the primary structure and the prestressing structure are allowed in correspondence with the intermediate contact elements (3c) and with the end contact element (3b) close to the support (2b); the longitudinal displacements between the primary structure and the prestressing structure are prevented only in correspondence with the end contact element (3b) close to the support (2a). The relative transversal displacements between the primary structure and the prestressing structures are prevented in correspondence with the contact elements (3c) and (3b).

In correspondence with the above-mentioned contact elements, the prestressing structure (4) applies to the primary structure (3) a system of forces that are mainly due to the tensioning of the tendon. (However, a small fraction of these forces is due to the applied loads Q).

The system of forces transmitted by the prestressing structure produces in the primary structure (a) a remarkable bending and shear that partly counterbalance the bending and shear induced by the applied loads, and (b) a negligible axial force due to the friction between the primary and prestressing structures.
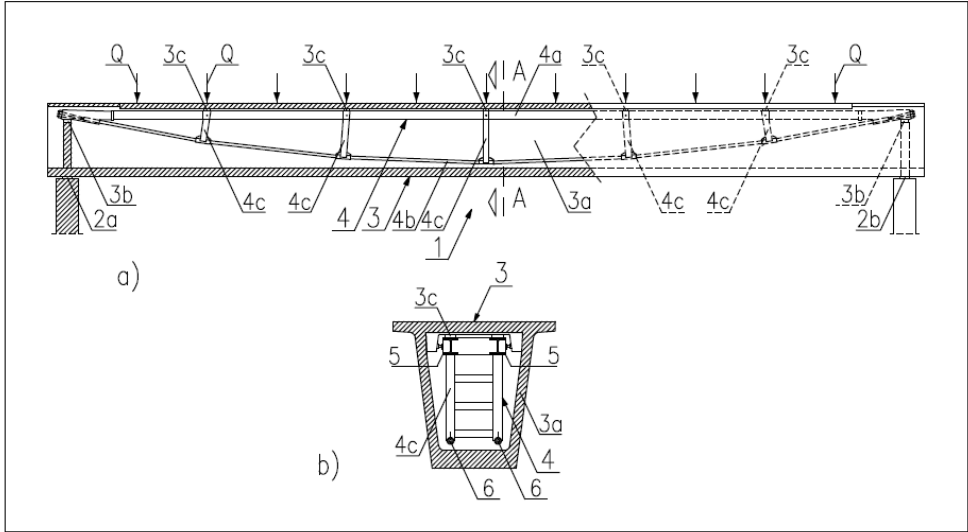
Figure 1 - The PCS indicated with "1": (a) lateral view and longitudinal section; and (b) A-A section.

Disregarding the frictional forces, the prestressing structure applies to the primary structure vertical upward forces in correspondence with the intermediate contact elements (3c), as well as vertical downward forces in correspondence with the end contact elements (3b).

As for the construction procedure of the PCS, the tendon of the prestressing structure is tensioned by means of a hydraulic jack that acts against the longitudinal strut. During the tensioning operations, each of the strands lengthens, freely sliding inside its own sheath, while the longitudinal strut (subjected to compression) shortens and moves longitudinally with respect to the primary structure, except at the end contact element (3b) close to the support (2a). Hence, the longitudinal strut - and not the primary structure - is subjected to compression due to the tensioning of the tendon. Finally, the extremities of the tendon are anchored at the end sections of the strut.

1.2 Objective of the paper

The fire resistance of a reduced-scale PCS similar to PCS (1) is the primary objective of this study, which deals with the numerical and experimental evaluation of the maximum temperature reached by the tendon of the prestressing structure. (For Structural Fire Design see - for instance - Kordina and Meyer-Ottens, 1981; Richter, 1987; Buchanan, 2002; for the study of concrete sections see Tattoni, 1994 and 2005).

Knowing the temperature in the tendon is instrumental in assessing the forces that the prestressing structure transfers to the primary structure in case of fire and in evaluating the fire resistance of the PCS.

The results of this research project give information not only on the fire behavior of the PCS, but also on that of a P/C box beam provided with *external* tendons placed *inside* the hollow core of the box beam (i.e., *not inside* embedded ducts, as in traditional post-tensioned P/C girders, see Tattoni and Gasperi, 2010).
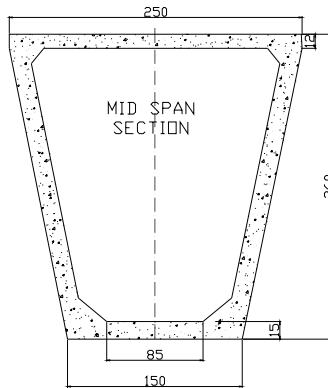
Fig. 2. Typical cross-section of a box beam (Model MG0 in the numerical analysis); the dimensions are in cm; the tendons are not shown.

1.3 Methodological approach

The main dimensions of the concrete cross section of the box beam (primary structure) are illustrated in Fig. 2. The section is characterized by a great free volume inside, whose behavior in fire should be studied by using fluid dynamics, including free-water diffusion and evaporation inside the concrete mass. Considering, however, the complexity of the problem and the uncertainty of the many parameters, performing a specific experimental test was considered the best way to achieve our goal.

In order to simplify the experimental set up and the reduced-scale specimen to be tested, without compromising the results concerning the thermal field, the following simplifications were introduced:

- the reduced-scale box beam representing the primary structure is not prestressed;
- the prestressing structure is limited to a portion of the tendon (no longitudinal strut and deviating elements); the tendon comprises a number of high-strength steel strands.

These simplifications are acceptable, as they do not compromise the results, that are focused on the thermal field. (The longitudinal strut – not present in the scaled-down specimen – is definitely less affected by the temperature than the tendon).

Unfortunately, it was impossible to introduce into the furnace a full-scale portion of the box beam mainly because of its total height (2600 mm) and width (2500 mm). Therefore a reduced-scale specimen was designed and cast.

Instead of simply reducing the size (which could lead to unreliable results), a *thermally-equivalent* specimen was devised (i.e. thermally equivalent to the full-scale primary structure).

In the following Chapter 2 the analytical approach used to define the most appropriate reduced-scale specimen is described, and in Chapter 3 the results concerning the test in the furnace are presented and discussed.

2. NUMERICAL ANALYSIS

2.1 Preliminary remarks

In order to work out an appropriate model, the following considerations were made:
- the temperature inside the hollow core of the section depends on the temperature reached by the internal surfaces;
- the heat inside the core is transferred mainly by convection rather than by radiation or conduction;
- the shape of the isotherms in both the slabs and the walls is nearly parallel to the exposed surfaces, with the exception of the corners;
- the temperature inside the cavity depends mostly on the thickness of the bottom slab and of the walls.
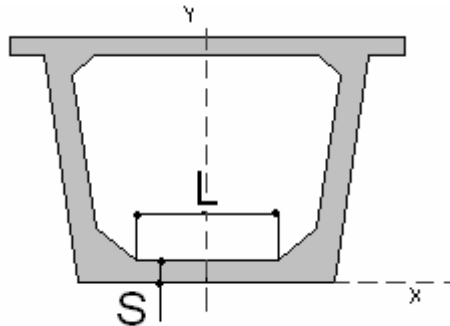

Figure 3 - Significant dimensions in a typical cross-section.

Hence, the physical model of the box was designed to meet the following conditions:
- the material is the same as in the actual box (concrete);
- the thickness S of the walls and of the bottom slab is the same as in the actual box;

- only the length L (length of the bottom slab, corners excluded) is reduced to allow the introduction of the specimen into the furnace, without jeopardizing the closeness between the thermal field of the model and that of the full-scale beam.

Summing up, the problem was reduced to find out the minimum ratio L/S compatible with the thermal response of the actual beam and with the size of the furnace (Fig. 3).

2.2 Models

Four FEM thermal analyses (MG0, MG1, MG2 and MG3) were performed to assess the role that the various geometric parameters play in the thermal field:

- MG0 : actual size of the cross section of the full-scale box beam (ratio between the length L and the thickness S : S/L = 5.6);
- MG1 : L/S = 6;
- MG2 : L/S = 5;
- MG3 : L/S = 4.

The thicknesses of the bottom and top slabs, as well as that of the two lateral walls are the same in all models and equal to those of the given structure. The width of the top slab is also the same in all models, but the distance between the walls varies slightly. The inclination of the walls with respect to the vertical is constant (roughly 22°).

As usual, the reinforcement was neglected in the evaluation of the thermal field.

For the sections considered in the analysis, see Fig.4. For the thermal characteristics of the materials, see Tables I and II.

Table I - Thermal characteristics of concrete (EN 1992-1-2).

Siliceous concrete: constant values			
	Convection coeff. (exposed surfaces.)	25.0 W/m^2°C	
	Convection coeff. (not exposed surf.)	9.0 W/m^2°C	
	Resultant emissivity coefficient.	0.56	
	Radiating coefficient.	31.8×10^{-9}	
Siliceous concrete: values depending on temperature			
	Temperature °C	Mass kg/m^3	Conductivity W/m^2°C	Spec. heat J/Kg°C
	0	2300	2.000	900.0
	275	2250	1.513	1062.0
	550	2250	1.152	1183.0
	825	2250	0.888	1261.0
	1100	2250	0.808	1297.0

Table II - Thermal characteristics of dry air.

Dry air: constant values			
	Convection coeff. (exposed surfaces.)	5.0 W/m^2°C	
	Convection coeff. (not exposed surf.)	5.0 W/m^2°C	
	Resultant emissivity coefficient.	0.56	
	Radiating coefficient.	31.8×10^{-9}	
Dry air: values depending on temperature			
	Temperature °C	Mass kg/m^3	Conductivity W/m^2°C	Spec. heat J/Kg°C
	0	1.3	0.020	1050.0
	275	1.3	0.024	1004.0
	550	0.6	0.042	1040.0
	825	0.6	0.060	1080.0
	1100	0.5	0.075	1120.0
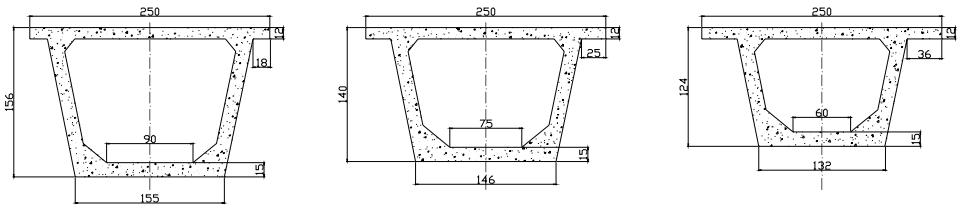
Figure 4 – Geometry of the cross sections (from left to right MG1, MG2, MG3).
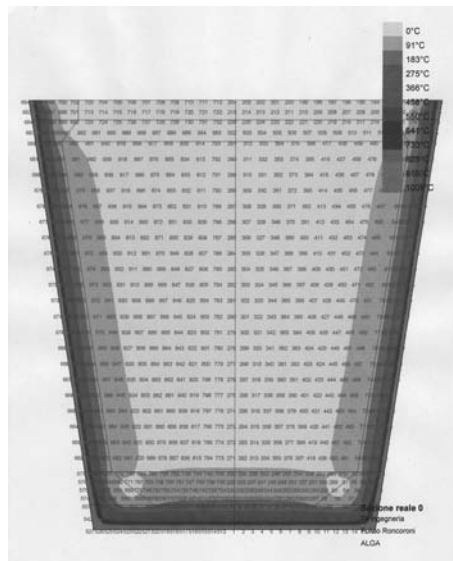
Figure 5 - Thermal map of the original section (MG0) for a fire duration of 120 minutes (ISO 384 Standard Fire).

In the thermal analyses, reference was made to the Standard Fire (temperature-time curve ISO 834). All analyses were carried out by means of the code Fires T3 (Iding et al., 1977).

In Figs. 5 and 6 the thermal maps at a fire duration of 120 minutes are reported for the full-scale section and for the reduced-scale section, respectively.

In all FEM models the thermal fields are very similar. Since the isotherms are mostly parallel to the mean planes of the walls and of the slabs (except in the corner zones), the extension of the bottom slab and of the walls is not a critical parameter in the thermal analyses.

The conclusion is that it is possible to reduce the dimensions of the cross section of the box beam without compromising the thermal field with respect to the full-scale section, as shown by the small (if any) variation of the temperature in the centroid of the top surface of the bottom slab, for various values of the ratio L/S (Fig. 7).

In the following, reference is made to the Model MG3.
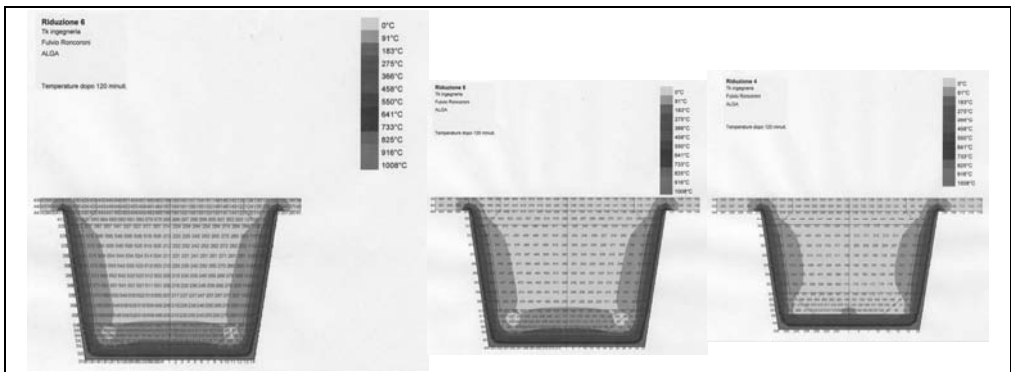
Figure 6 - Thermal maps of the models MG1, MG2 and MG3 (from left to right), after 120 minutes of Standard ISO 834 Fire.
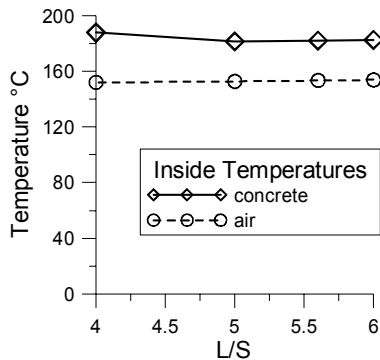
Figure 7 - Temperatures reached after 120 minutes in the middle point of the top surface of the bottom slab.

3. EXPERIMENTAL TEST

3.1 Test specimens

The single reduced-scale specimen was designed and manufactured according to the size introduced in the FE model MG3 (Fig. 8).

The actual mechanical characteristics of the concrete are: $R_{ck.}$= 35 MPa and $R_{cm.}$= 47.5 MPa (siliceous aggregates).

The portion of tendon placed inside the box beam consisted in high-strength steel strands, each of them greased and inserted in a plastic sheath; all strands were inserted inside a high-density polyethylene - HDPE duct (Fig. 8).

Fig. 8 – Reduced-scale specimen and location of the thermocouples (inside the concrete walls and attached to the tendon); specimen length 500 cm.

In order to obtain a complete picture of the thermal behavior of the box beam, 49 thermocouples were used during the test. All thermocouples were positioned with the maximum accuracy. For example some thermocouples were pre-placed inside small concrete prisms (one thermocouple for each prism) and later the prisms were fastened to the reinforcement of the box beam, before casting (see Fig.9 for the location of the thermocouples).

In more detail:

- three thermocouples inside each slab and wall;
- five thermocouples attached to the top surface;
- three thermocouples attached to the internal surface of each slab in the mid section, and 50 and 100 mm from the surface;
- three thermocouples attached to the tendon.

The test was performed in the laboratory of "Istituto Giordano" in Bellaria (Rimini, Italy). The size of the gasoil-fueled furnace was about

250x250x500 cm. The specimen was placed inside the furnace in such a way that its top slab closed the chamber along the top face. Light concrete blocks were used to complete the top closure.

The test was run in accordance with the Italian Norms UNI 7677 and 7678.

CROSS-SECTION

CABLE SECTIONS

UPPER PLAN
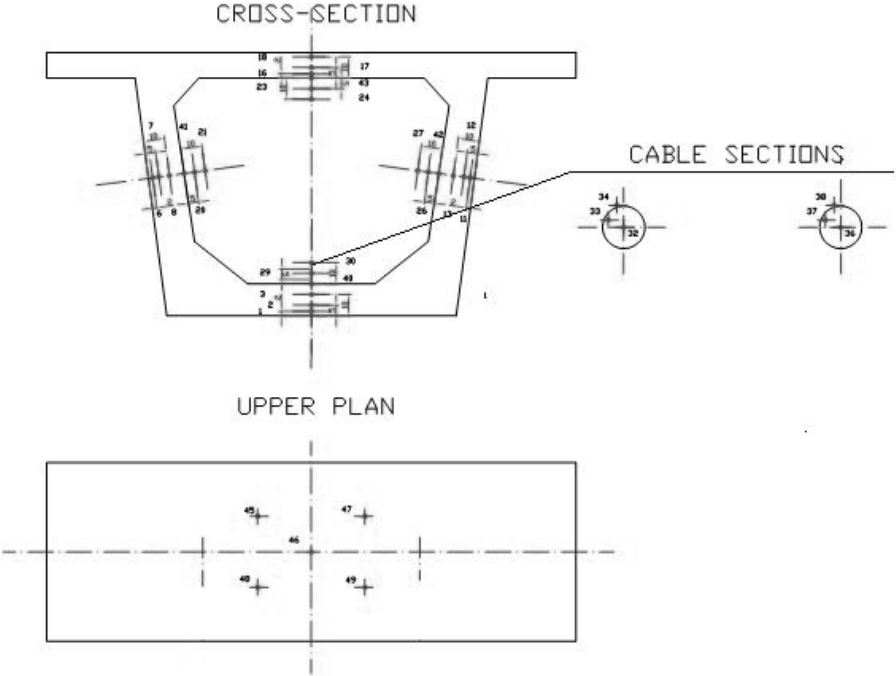
Figure 9 - Location of thermocouples on concrete and tendon.
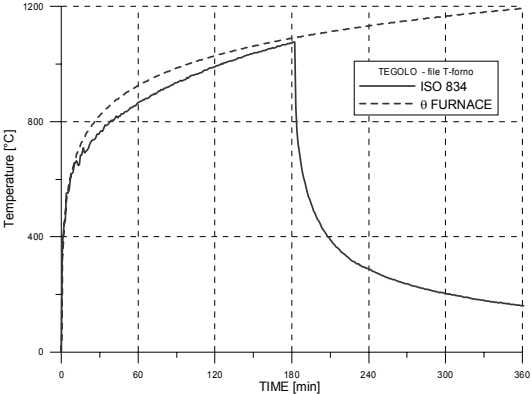
Figure 10 - Temperature-Time curve in the furnace.
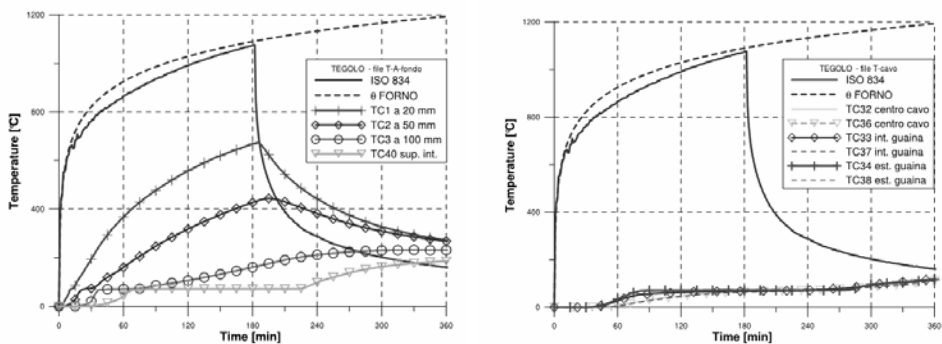
Figure 11 - Temperature profiles in the bottom slab (left) and in the tendon (right).

3.2 Test results

The actual temperature-time curve of the test is plotted in Fig.10. Note that that there is an excellent agreement with the nominal ISO 834 curve. After 180 minutes the burners of the furnace were turned off and the temperatures were recorded up to 360 minutes since the beginning of the heating process. In Fig.11 the most significant temperature profiles are shown.

Some comments:

- the measures of the thermocouples turned out to be rather symmetric;

- the temperature of the air inside the box beam did not vary significantly from point to point;

- the temperature inside the box remained close to 100°C for more than 180 minutes;

- the moisture in the concrete (close to 2 - 3 % at the beginning of the test) migrated toward the internal surface of the box and - by evaporating - contributed to the long period at 100°C of the hollow inside the box ;

- the evaporation of the water was over about 200 minutes after the beginning of the test, which means 20 minutes after the burners were turned off, because of the thermal inertia of the concrete mass;

- concrete spalling reduced the thickness of the bottom slab and of some parts of the walls by about 20 mm in the first 30 - 35 minutes from the beginning of the test (Fig. 12);

- from the point of view the effective geometric properties of the section, as the rate of penetration of the 500°C isotherm is almost constant with the fire duration (Fig.13), both the resisting area A and the moment of inertia J_x exhibit very similar and rather small reductions (not more than -15% after 2 hours of standard fire; the rather small reduction of the moment of inertia ensues from the fact that this parameter depends mainly on the dispersion of the area, that is unaffected by the fire); of course, very similar conclusions apply to concrete box beams prestressed by external tendons.

Figure 12 – Reduced-scale specimen after the test in the furnace: (left) concrete spalling along the intrados of the bottom slab; and (right) strands of the tendon in good conditions.
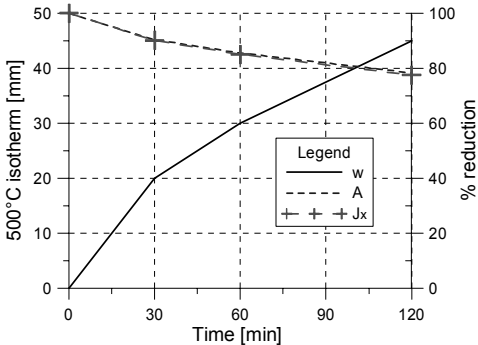
Figure 13 - Position of the 500°C isotherm from the surface exposed to the fire and reduction of the geometrical characteristics of the cross-section (Area A and Moment of Inertia J_x), because of the penetration of the 500°C-isotherm.

4. CONCLUSIONS

The numerical analyses and the experimental test performed in this study in standard-fire conditions give some information about the thermal field inside a traditionally-prestressed concrete box beam, with specific reference to the box beam belonging to the primary structure of the composite girder called PCS.

The numerical analyses allowed to reduce the size of the specimen to be tested in the furnace, without introducing sizable errors in the thermal field with respect to the full-size reference structure.

The experimental test showed that the temperature inside the concrete beam remains low for more than three hours. This phenomenon is partly due to concrete moisture, which moves inward and evaporates. The temperature of the tendon (placed inside the box beam) remained low as well, for more than three hours, which implies that in similar cases the tendons keep their mechanical properties almost unchanged with respect to those at 20°C.

Finally the test results showed that some severe spalling occurred along the intrados of the bottom slab (bottom surface) and - to a minor extent - along the external surfaces of the walls. (The depth of the spalled concrete in the bottom slab was close to 15% of the thickness)

All considered, the theoretical and experimental results clearly show that the proposed PCS – and other similar solutions – are quite efficient in terms of fire resistance, because the primary structure behaves like a protective shield for the internal prestressing structure.

ACKNOWLEDGEMENTS

REFERENCES

Kordina K., Meyer-Ottens C. (1981). *Beton Brandschutz Handbuch (Handbook for Concrete Protection from Fire)*, Beton Verlag, Düsseldorf.

Richter E. (1987). *Zur Berechnung der Biegetragfähigkeit brandbeanspruchter spannbetonbauteile unter Berücksichtigung geeigneter Vereinfachungen für die Materialgesetze (On the evaluation of the bearing capacity of P/C Members in fire by means of appropriate simplified constitutive laws for the materials)*. IBMB, Braunschweig, Heft 80.

Iding R., Bresler B. and Nizamuddin Z. (1977). *Fires-T3. A Computer Program for the Fire Response of Structures*. Fire Research Group, University of California, Report No.UCB FRG 77-15, October.

Italian Code UNI 7677. *Prove al fuoco - Termini e definizioni (Tests in Fire Conditions – Technical Terms and Definitions).*

Italian Code UNI 7678. *Elementi costruttivi - Prove di resistenza al fuoco (Structural Members – Tests for Fire Resistance).*

EN 1992-1-2. *Progetto al fuoco di strutture in c.a.(Concrete Fire Design)..*

Buchanan A. H. (2002). *Structural Design for Fire Safety.* John Wiley & Sons Ldt, Chicester - UK.

Tattoni S. (1994). "Mappe termiche di sezioni in c.a. e normative europee" (Thermal Maps for R/C Sections and European Standards). *Proc. 10th Italian Nat. Conf. of the Society of Building Technology - CTE*, Milan (Italy), November 3-5.

Tattoni S. (2005). "Fire Resistance of Precast Elements: Research Activity within the Italian National Project "ULISSE". *Proc. Int. Workshop on "Fire Design of Concrete Structures: What now? What next*?". FIB Task Group 4.3, ed. by Pietro G. Gambarova, Roberto Felicetti, Alberto Meda and Paolo Riva, pub. by Starrylink (Brescia, Italy), December 2004, pp.307-310.

Gasperi A. (1999). "A Proposal for a New Type of Prestressed Precast Composite Structure". *Proc.16th BIBM Int. Congress*, Venice – Italy.

Gasperi A. (2004). "Le strutture presollecitate composite denominate PCS: una proposta per nuove soluzioni strutturali" (The Prestressed Composite Structures called PCS: a Proposal for Innovative Structural Solutions). *INARCOS No.650*, June.

Tattoni S. and Gasperi A. (2010). "Fire Resistance of a Concrete Box-Beam Prestressed by External Tendons". *Proc. 6th Int. Conf. on "Structures in Fire"- SIF'10, East Lansing (Michigan, USA),* ed. by Venkatesh Kodur and Jean-Marc Franssen, pub. by DEStech Publications Inc. (Lancaster, PA, USA), June 2-4, pp.173-180.

ON THE IDENTIFICATION OF THE REFERENCE ISOTHERM IN THE SIMPLIFIED ANALYSIS OF R/C MEMBERS IN FIRE

Robert Kowalski[1]

ABSTRACT

Calculations concerning unsteady heat flows in commonly-used cross-sections are presented in this paper with reference to R/C beams and slabs. The parameters influencing the heat flow either inside the concrete or through its surfaces are assumed from the codes (EC2, 2004; EC1, 2002).

The numerical results allow to work out a set of diagrams, which simplify the evaluation (a) of the size of the reduced cross-sections, and (b) of the temperature in the reinforcing bars. These diagrams can be useful in the design of R/C beams and slabs using the ''500°C-Isotherm Method'', as time-consuming calculations are no longer necessary for the assessment of the thermal field in the case of unsteady heat flows.

---

[1] Ph.D., D.Sc., Civil Eng., Faculty of Civil Engineering, Warsaw University of Technology, Warsaw, Poland.
  e-mail: r.kowalski@il.pw.edu.pl

1. INTRODUCTION

The load bearing capacity of R/C structural members in fire can be worked out by means of tabulated data, simplified methods or global analyses, as specified also in the codes (EC2, 2004). Global analyses, however, are not only time consuming, but require also a lot of input data (fib, 2007; fib, 2008; Bazant, Kaplan, 1996; Khoury et. al., 2002; Bamonte et. al., 2008), which are not defined in ordinary structural design. On the other hand, fire resistance predicted on the basis of tabulated data is often unreliable. Hence, simplified methods are a handy intermediate solution which combines simplicity and adequate precision, like the "500°C-Isotherm Method" suggested by EC2 (2004). This method is based on two clearly-defined assumptions:

(1) the part of the concrete section that is enveloped by the 500°C-isotherm is fully active (the mechanical properties are assumed to be the same as in virgin conditions); the part of the concrete outside the 500°C-isotherm is neglected (the concrete is assumed to be totally damaged); and

(2) the reinforcing bars have the mechanical properties corresponding to their actual temperature.

In spite of its conceptual simplicity, the "500°C-Isotherm Method" requires a rather time-consuming computational effort. Hence this method is not really "simple" and some designers may go into troubles, when trying to use it.

Additionally, the following points should be stressed:

- the "500°C-Isotherm Method" is recommended only for standard-fire conditions;

- when designing new R/C structures or reassessing existing structures, the parameters influencing the heat flow in concrete are usually not defined; it means that the values of these parameters are in most cases assumed as the mean code values.

For the above-mentioned limits, the analysis based on the "500°C-Isotherm Method" requires repetitive and time consuming calculations, even if the only variable parameters are the dimensions of the "effective" cross-section of the given structural member.

In this paper the calculations of the heat flow in many commonly-used cross-sections for beams and slabs are performed on the basis of the average code values of the parameters influencing the heat flow in concrete cross-sections (EC2, 2004; EC1, 2002). The numerical results allow to draw simplified diagrams (a) for predicting the size of the reduced cross-sections, and (b) for evaluating the temperature in the reinforcing bars. These diagrams make it possible to eliminate time-consuming calculations, when the "500°C-Isotherm Method" is used to evaluate the load-bearing capacity of beams and slabs in fire.

2. PARAMETERS INFLUENCING THE HEAT FLOW IN CONCRETE

For calculating the thermal field in a R/C section one should know: concrete specific heat, thermal conductivity and mass per unit volume as a function of the temperature, and the heat flux through the surface of the member in question.

Figures 1 and 2 show concrete thermal properties recommended in EC2 (2004). In Fig.1, concrete specific heat in the temperature range between 100 and 200°C depends on concrete moisture content. The thick, thin and dashed curves in Fig.1a refer to moisture contents equal to 3%, 1.5% and 0 (completely dry concrete), respectively. The solid curves in Fig.2 refer to the maximum and minimum values of concrete thermal conductivity, while the broken curve gives the average values. (The bottom curve comes from the test results specifically aimed to evaluate concrete thermal conductivity, while the top curve leads to the best fitting of the tests concerning full-size R/C members in fire).
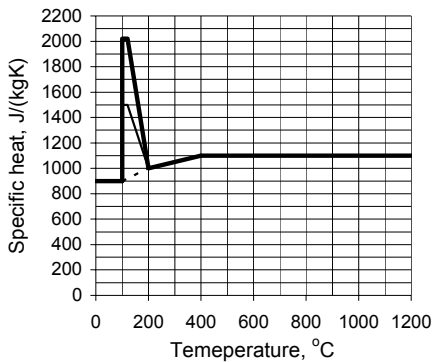
Figure 1 – Concrete specific heat (EC2, 2004)
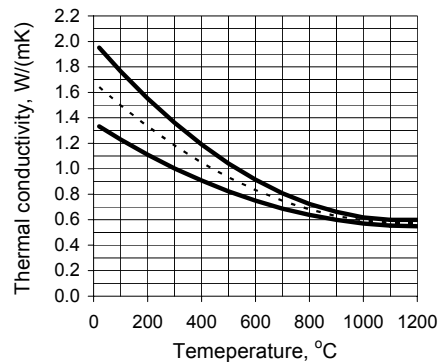
Figure 2 – Concrete thermal conductivity (EC2, 2004).

The heat flux through the surface of the structural member should be determined considering heat transfer by convection and radiation (EC1, 2002).

The convective heat flux component is given by the following formula:

$$h_{net,c} = \alpha_c \cdot (\theta_g - \theta_m) \tag{1}$$

where:
- α_c is the coefficient of heat transfer by convection;
- θ_g is the gas temperature close to the surface of the member [°C];
- θ_m is the temperature of the surface of the member [°C].

In standard-fire conditions, EC1 (2002) recommends for α_c the value 25 W/(m²K).

The heat flux component related to radiation is given by the following formula (EC1, 2002):

$$h_{net,r} = \Phi \cdot \varepsilon_m \cdot \varepsilon_f \cdot \sigma \cdot [(\theta_r + 273)^4 - (\theta_m + 273)^4]$$ (2)

where by default one can assume:
- configuration factor $\Phi = 1.0$;
- surface emissivity of concrete $\varepsilon_m = 0.8$;
- fire emissivity $\varepsilon_f = 1.0$;
- Stephan-Boltzmann constant $\sigma = 5.76 \cdot 10^{-8}$ W/(m^{2}K^4);
- effective temperature of the environment $\theta_r = \theta_g$.

When the above-mentioned values are introduced, Eq. (2) becomes:

$$h_{net,r} = 4{,}61 \cdot 10^{-8} \cdot [(\theta_g + 273)^4 - (\theta_m + 273)^4].$$ (3)

3. ISOTHERM 500°C AND BAR TEMPERATURE IN R/C SLABS

In order to analyse the thermal field inside R/C slab sections in fire, calculations based on finite-element discretization were performed (code LS-DYNA).
Five cases were considered with h (thickness) = 10, 15, 20, 25 and 30 cm. In the one-dimensional modelling, the discretization of the section was based on square elements having a 1 cm-side.
Specific heat of concrete was taken according to Fig.1 for a moisture content equal to 3%. The thermal conductivity of concrete was taken as the average value shown in Fig.2. All slabs were subjected to standard fire (EC1, 2002) acting on the bottom face. The heat flux was calculated as a sum of the values obtained according to Eqs. (1) and (3). The temperature of the gas on the cold surface of the slab was assumed as 20°C, and for this surface the coefficient $\alpha_c = 9$ W/(m^{2}K) was introduced into Eq.(1) according to EC1 (2002).
Figures 3a-f shows the numerical results. The following parts of Fig. 3 (a-f) refer to the standard fire duration of 30, 60, 90, 120, 180 and 240 minutes, respectively.
The right-hand part side of Fig.3 shows the temperature distribution in the cross-section of a slab as a function of the distance from the hot surface. In each figure, five diagrams referring to slab thicknesses h = 10, 15, 20, 25 and 30 cm are shown. The differences among the curves become clear in Figs.3d-f. In Figs.3a-c all curves are very close.
The left-hand side part of Fig.3 shows the values worked out on the basis of the diagrams shown in the right-hand side part of the figure: the position a of the 500°C-isotherm, the temperatures of the bars at the distance 3, 5, and 7 cm from the hot face of the slab and the temperature on the cold face (for $a = h$). These

values are appropriate for all slab thicknesses and for any value of the fire duration comprised between 30 and 120 minutes, as well as for slab thicknesses h ≥ 15 cm and for 180 and 240 minutes of the fire duration.

Considering Fig.3 from the practical point of view one can conclude that for commonly-used values of the slab thickness and for 30-240 minutes of fire duration, the 500°C-isotherm layout and the temperature in the bars do not depend on slab thickness, but only on fire duration. Such fact should be introduced into the codes to simplify the calculations based on the "500°C-Isotherm Method".

Figure 4 shows a proposal by the Author: in the left-hand side of Fig.4 the position of the 500°C-isotherm is given. In the right-hand side of Fig.4 the diagrams for evaluating bar temperature are shown for three values of the distance a: 3, 5 and 7 cm.

a) Fire duration: t = 30 min.

500°C-isotherm at:
a_{500} = 0.9 cm
Temperatures:
a = 3 cm – θ = 220 °C
a = 5 cm – θ = 100 °C
a = 7 cm – θ = 60 °C
a = h   – θ < 200 °C
(for all slab thicknesses)
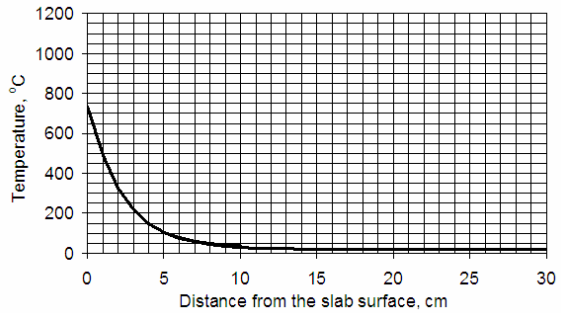
b) Fire duration: t = 60 min.

500°C-isotherm at:
a_{500} = 2.0 cm
Temperatures:
a = 3 cm – θ = 380 °C
a = 5 cm – θ = 220 °C
a = 7 cm – θ = 130 °C
a = h   – θ < 200 °C
(for all slab thicknesses)
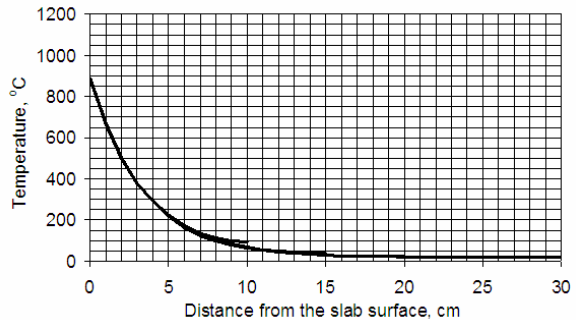
Figures 3a, b – Temperature distribution in the slab cross-sections (heating from the bottom surface according to standard fire).

c) Fire duration: t = 90 min.

500°C-isotherm at:
$a_{500} = 2.7$ cm
Temperatures:
a = 3 cm – θ = 480 $^{\circ}$C
a = 5 cm – θ = 310 $^{\circ}$C
a = 7 cm – θ = 210 $^{\circ}$C
a = h   – θ < 200 $^{\circ}$C
(for all slab thicknesses)
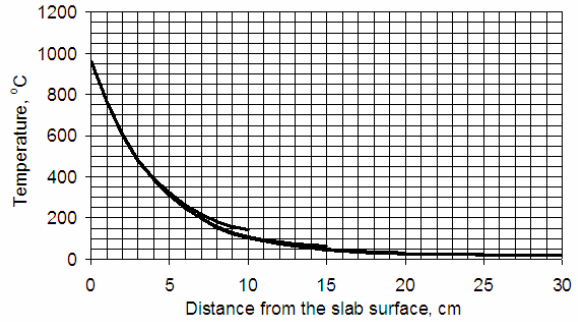
d) Fire duration: t = 120 min.

500°C-isotherm at:
$a_{500} = 3.5$ cm
Temperatures:
a = 3 cm – θ = 560 $^{\circ}$C
a = 5 cm – θ = 380 $^{\circ}$C
a = 7 cm – θ = 260 $^{\circ}$C
a = h   – θ < 200 $^{\circ}$C
(for all slab thicknesses)
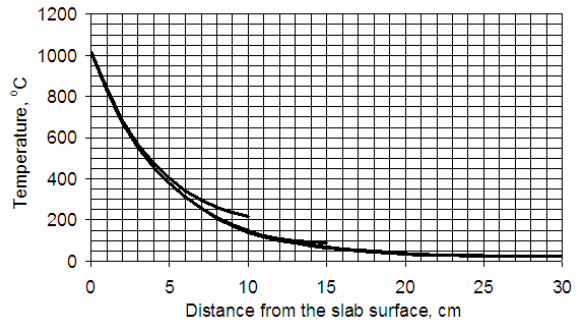
e) Fire duration: t = 180 min.

500°C-isotherm at:
$a_{500} = 4.7$ cm
Temperatures:
a = 3 cm – θ = 670 $^{\circ}$C
a = 5 cm – θ = 480 $^{\circ}$C
a = 7 cm – θ = 350 $^{\circ}$C
a = h   – θ < 200 $^{\circ}$C
(for slabs h $\geq$ 15 cm)
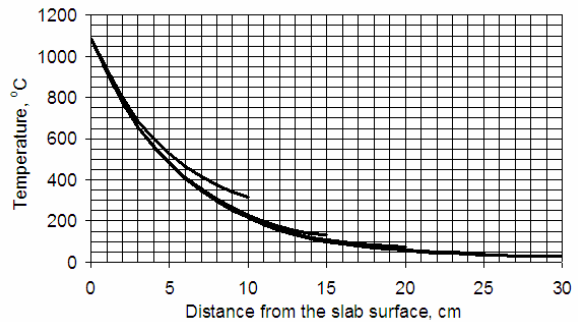
f) Fire duration: t = 240 min.

500°C-isotherm at:
$a_{500} = 5.7$ cm
Temperatures:
a = 3 cm – θ = 730 $^{\circ}$C
a = 5 cm – θ = 540 $^{\circ}$C
a = 7 cm – θ = 430 $^{\circ}$C
a = h   – θ < 200 $^{\circ}$C
(for slabs h $\geq$ 15 cm)
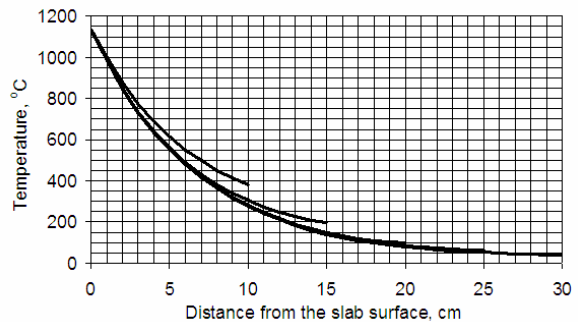
Figures 3c-f – Temperature distribution in the slab cross-sections (heating from the bottom surface according to standard fire).

(a)   (b)

Position of 500°C-isotherm:

Duration of standard fire:
t =   30 min. − a_{500} = 1.0 cm
t =   60 min. − a_{500} = 2.0 cm
t =   90 min. − a_{500} = 3.0 cm
t = 120 min. − a_{500} = 3.5 cm
t = 180 min. − a_{500} = 5.0 cm
t = 240 min. − a_{500} = 6.0 cm
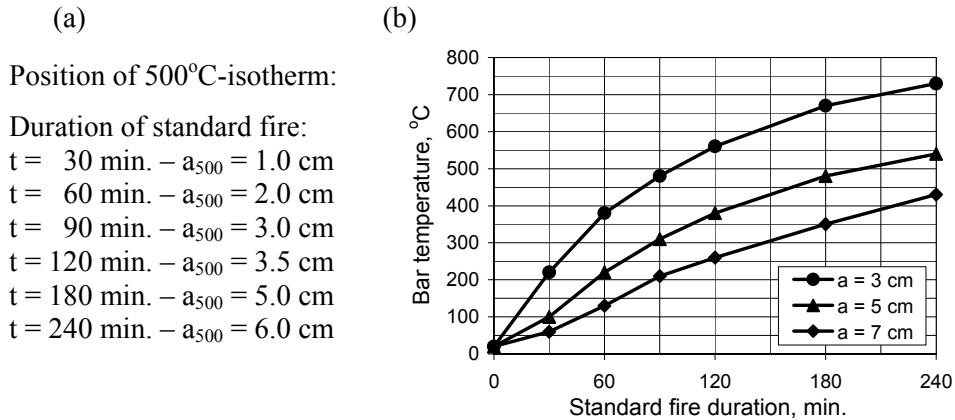
Figure 4 – Recommendation for a simplified evaluation of the temperature in the bars when using the "500°C-Isotherm Method": (a) position of the 500°C-isotherm; and (b) temperature of the reinforcing bars.

4. ISOTHERM 500°C AND TEMPERATURE OF BARS IN R/C BEAMS

4.1. The pattern of the 500°C-isotherm

The analysis of the thermal field inside the cross-section of a R/C beam was performed in two steps. To calculate the thermal field in the part of the section far from the heated bottom face, the behaviour of the web of the beam was assumed to be similar to that of infinite plates (thickness h = 10, 20, 30, 40, 50 and 60 cm) subjected to a one-dimensional unsteady heat flow on both faces (standard fire). Needless to say, the thickness of the plate coincides with the width of the section of the beam (Fig.5). The calculation method, the temperature increase and the properties of concrete were similar to those described in Chapter 3. Figure 6 shows the numerical results.

DISTANCE SHOWN ON HORIZONTAL AXIS IN FIG. 6
1/2 b= 5, 10, 15, 20, 25, 30 cm

b=10, 20, 30, 40, 50, 60 cm
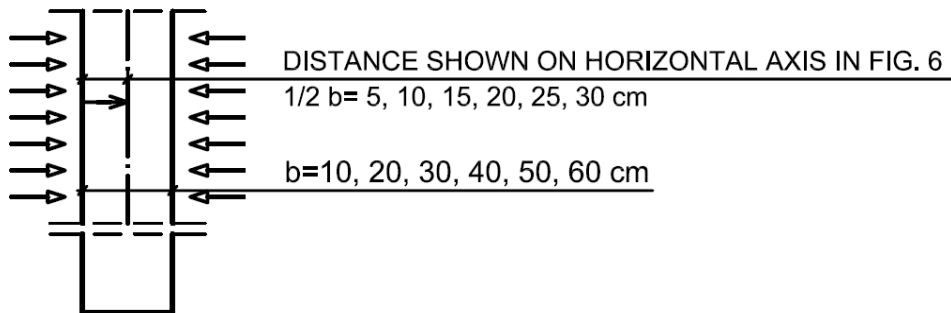
Figure 5 – Infinite plate representing the web of the beam (far from the bottom heated side).

a) Fire duration: t = 30 min.

Position of 500°C-isotherm:
for all slab thicknesses:
a_{500} = 0.9 cm
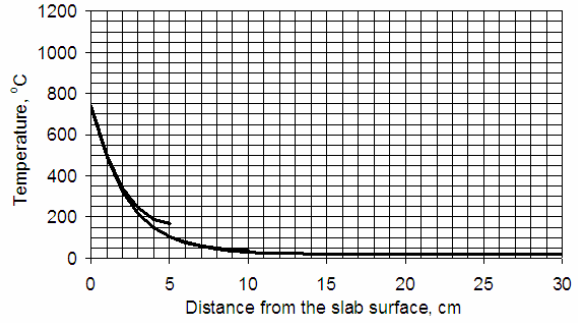
b) Fire duration: t = 60 min.

Position of 500°C-isotherm:
for b=10 cm – a_{500}=3.0 cm,
for b≥20 cm – a_{500} = 2.0 cm.
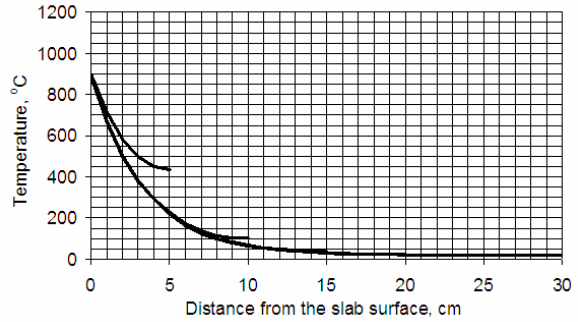
c) Fire duration: t = 90 min.

Position of 500°C-isotherm:
for b=10 cm – a_{500} = 0.5b
(the whole cross-section),
for b≥20 cm – a_{500} = 2.8 cm.
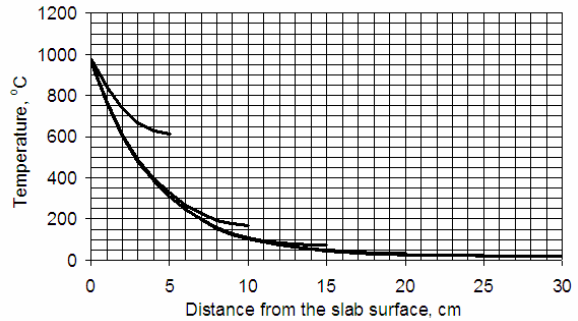
d) Fire duration: t = 120 min.

Position of 500°C-isotherm:
for b=10 cm – a_{500} = 0.5b
(the whole cross-section),
for b=20 cm – a_{500} = 3.7 cm,
for b≥30 cm – a_{500} = 3.5 cm.
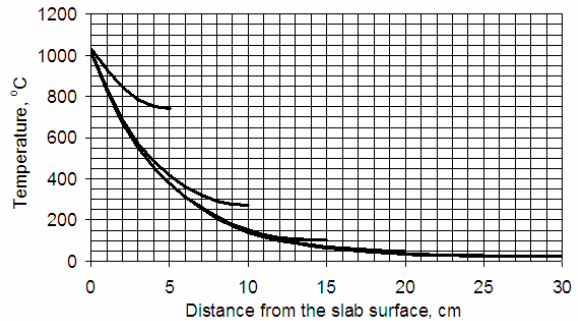
e) Fire duration: t = 180 min.

Position of 500°C-isotherm:
for b=10 cm – a_{500} = 0.5b
(the whole cross-section),
for b=20 cm – a_{500} = 6.3 cm,
for b≥30 cm – a_{500} = 4.7 cm.
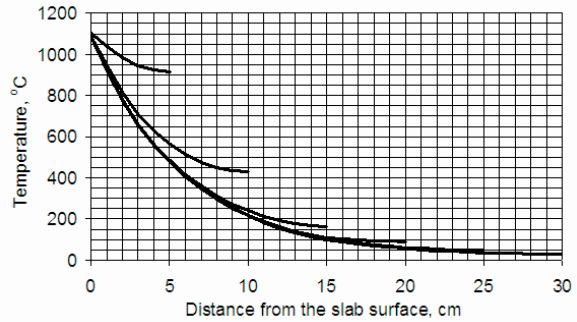
f) Fire duration: t = 240 min.

Position of 500°C-isotherm:
for b≤20 cm – a_{500} = 0.5b
(the whole cross-section),
for b=30 cm – a_{500} = 5.9 cm,
for b≥40 cm – a_{500} = 5.7 cm.
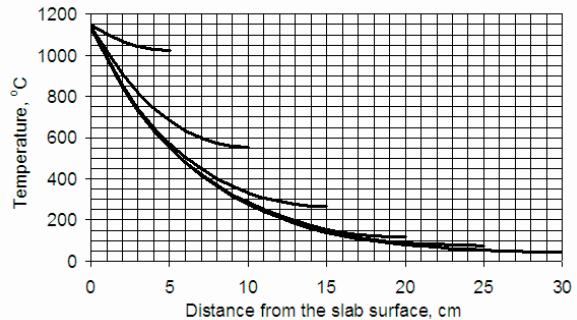
Figures 6a-f – Temperature distribution in the half-part of the infinite concrete vertical plate heated from both sides, representing the web of the beam far from the bottom heated side.

In the right-hand side parts of Figs.6a-f (standard-fire duration of 30, 60, 90, 120, 180 and 240 minutes, respectively), the vertical axis refers to the temperature while the horizontal axis refers to the distance from the heated surface (see Fig.5). Each of Figs. 6a-f shows six diagrams referring to as many values of the thickness. The longer the duration of the fire, the larger the differences among the curves.

In the left-hand side part of each figure, the position of the 500°C-isotherm is evaluated from the diagrams. When the width of the section is large enough, the position of the 500°C-isotherm depends only on fire duration. For instance, for 120 or 180 minutes (Fig.6d-e) the diagrams referring to any width not smaller than 30 cm are very close. When the width is relatively small, even for a rather short fire duration the temperature in the concrete and the position of the 500°C-isotherm increase rapidly (see for instance Fig.6b, for t = 60 min. and b = 10 cm).

In the second step, the two-dimensional unsteady heat flow was calculated in five cases of very elongated rectangular cross-sections (size $^1/_2b \times {}^1/_2h$ = 5×15, 10×30, 15×45, 20×60 and 25×75 cm). They were exposed to high temperature

along the left vertical side and along the bottom side, while there was no heat flow across the mean vertical plane (adiabatic conditions), in order to simulate the corner behaviour in a heated rectangular section (Fig.7). In this way five cross-sections of beams with infinite depth and width b = 10, 20, 30, 40 and 50 cm were analysed (heating along the bottom side and along the two vertical opposite sides).
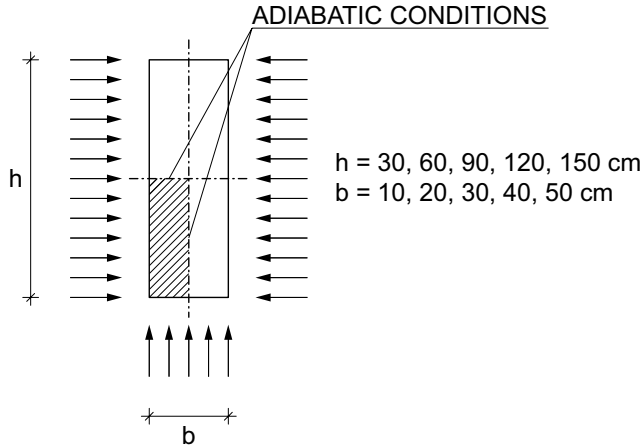
Figure 7 – Layout of the part of the cross-section considered in calculations.
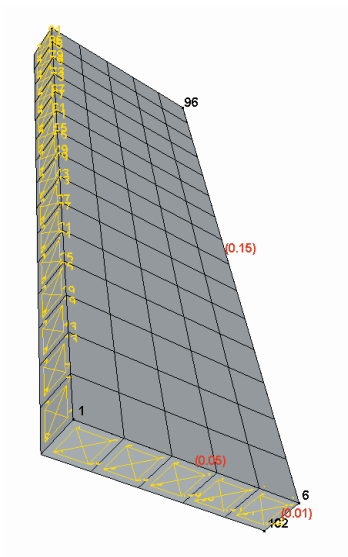
Figure 8 – Three-dimensional model used in the thermal analysis: example with 10 cm section width; heating along the left and bottom faces only.
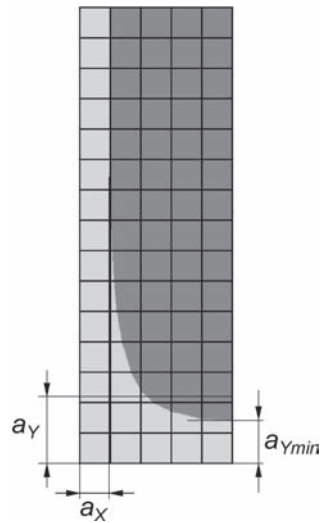
Figure 9 –The coordinates of the 500°C-isotherm given underneath the patterns shown in Fig. 10a-e (example with 10 cm-section width).

290

The calculation was made by means of the code LS-DYNA, using a two-dimensional model. It consisted of three dimensional, eight-node finite elements (side = 1 cm, Fig.8). Concrete moisture content and thermal properties were introduced with the same values adopted in slab analysis.

Figures 10a-e shows the pattern of the 500°C-isotherm for a standard fire duration 30, 60, 90, 120, 180 and 240 min. In all cases, at a certain distance from the bottom face, the 500°C-isotherms become parallel to the vertical sides. (The heating conditions are the same as in the infinite plates shown in Fig.6).

The coordinates of the 500°C-isotherm are indicated underneath the patterns shown in Fig. 10 (see Fig.9):

a_X is the distance between the 500°C-isotherm and the left cross-section side in the part of the cross-section where the 500°C-isotherm is parallel to the vertical side; the values of a_X well correspond to those shown in the left-side part of Fig. 6;

a_{Ymin} is the distance between the 500°C-isotherm and the bottom cross-section side along the symmetry axis of the cross-section;

a_Y is the distance between the 500°C-isotherm and the bottom side, resulting from the calculation of the area $(b - a_X) \times (h - a_Y)$ equal to the area of the part of the cross-section enveloped by the 500°C-isotherm; EC1 (2002) recommends that the real "reduced" cross-section should be replaced by the above-defined rectangle.

30 min.	60 min.	90 min.
$a_X =$ 0.9 cm	$a_X =$ 3.0 cm	
$a_{Ymin} =$ 1.4 cm	$a_{Ymin} =$ 5.8 cm	
$a_Y =$ 2.2 cm	$a_Y =$ 7.2 cm	
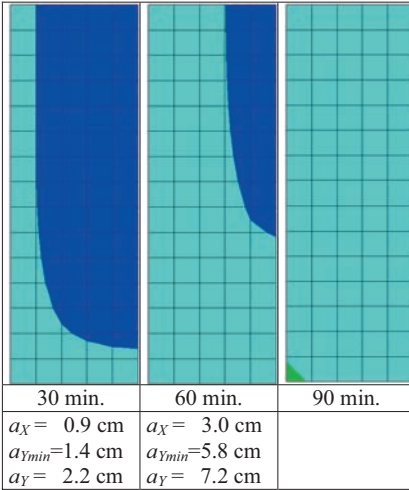
Figure 10a – 500°C-isotherm patterns: cross-section $b \times h = 10 \times 30$ cm ($^1/_2 b \times ^1/_2 h = 5 \times 15$ cm); for any value of the fire duration $t \geq 90$ min. the temperature of the whole cross-section exceeds 500°C.

30 min.	60 min.	90 min.	120 min.	180 min.	240 min.
$a_X = 0.9$ cm	$a_X = 2.0$ cm	$a_X = 2.9$ cm	$a_X = 3.7$ cm	$a_X = 6.3$ cm	
$a_{Ymin}=0.9$ cm	$a_{Ymin}=2.3$ cm	$a_{Ymin}=3.7$ cm	$a_{Ymin}=5.4$ cm	$a_{Ymin}=11.4$ cm	
$a_Y = 1.8$ cm	$a_Y = 3.6$ cm	$a_Y = 5.4$ cm	$a_Y = 7.2$ cm	$a_Y = 13.2$ cm	
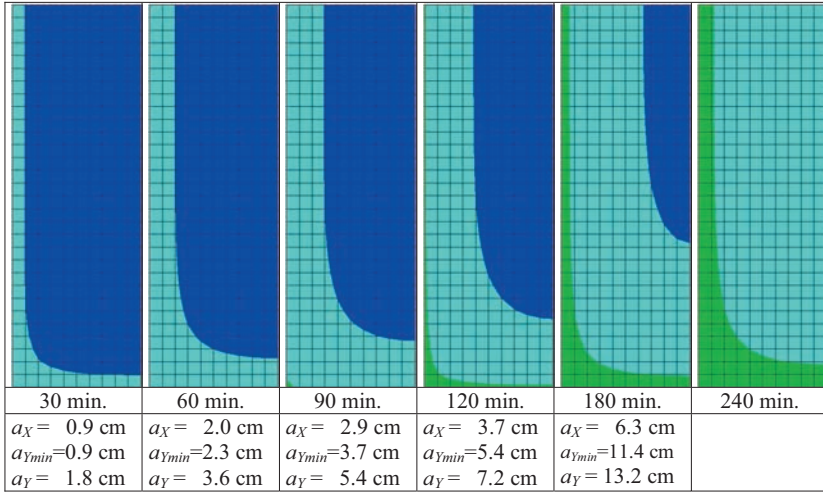
Figure 10b – 500°C-isotherm patterns: cross-section $b \times h = 20 \times 60$ cm ($^1/_2 b \times ^1/_2 h = 10 \times 30$ cm).

30 min.	60 min.	90 min.	120 min.	180 min.	240 min.
$a_X = 0.9$ cm	$a_X = 2.0$ cm	$a_X = 2.9$ cm	$a_X = 3.5$ cm	$a_X = 4.7$ cm	$a_X = 5.9$ cm
$a_{Ymin}=0.9$ cm	$a_{Ymin}=2.0$ cm	$a_{Ymin}=2.9$ cm	$a_{Ymin}=3.9$ cm	$a_{Ymin}= 5.9$ cm	$a_{Ymin}= 8.4$ cm
$a_Y = 1.7$ cm	$a_Y = 3.2$ cm	$a_Y = 4.3$ cm	$a_Y = 5.3$ cm	$a_Y = 7.7$ cm	$a_Y = 11.5$ cm
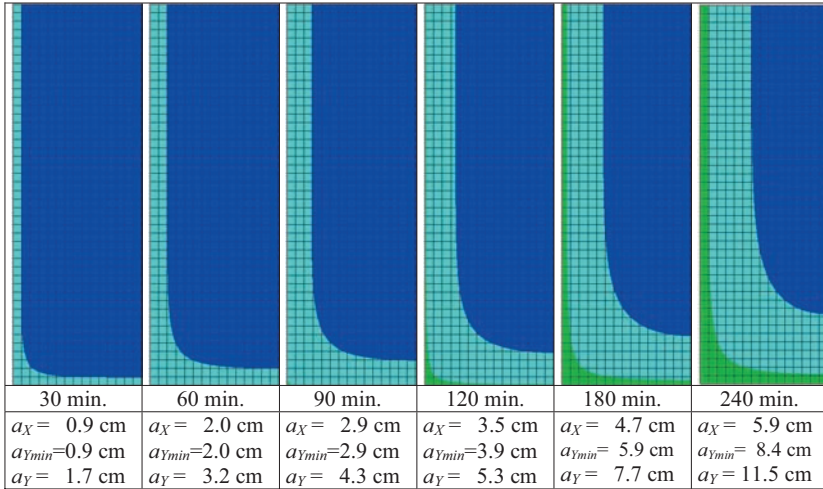
Figure 10c – 500°C-isotherm patterns: cross-section $b \times h = 30 \times 90$ cm ($^1/_2 b \times ^1/_2 h = 15 \times 45$ cm).
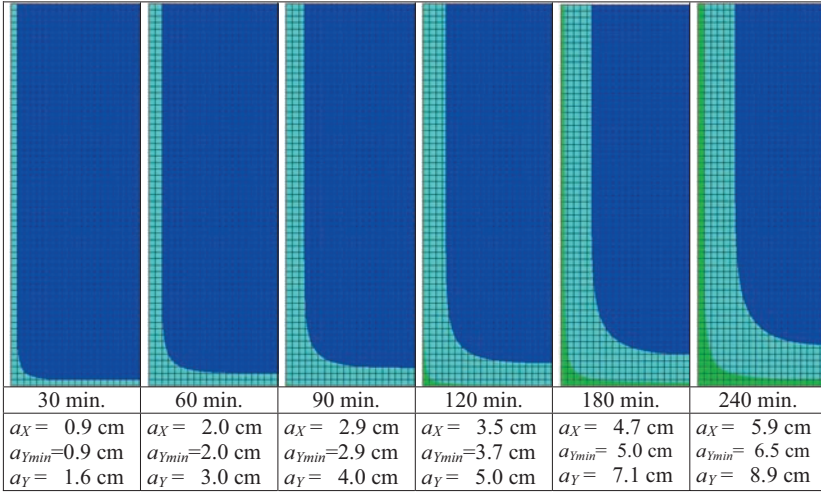
30 min.	60 min.	90 min.	120 min.	180 min.	240 min.
$a_X =$ 0.9 cm	$a_X =$ 2.0 cm	$a_X =$ 2.9 cm	$a_X =$ 3.5 cm	$a_X =$ 4.7 cm	$a_X =$ 5.9 cm
a_{Ymin}=0.9 cm	a_{Ymin}=2.0 cm	a_{Ymin}=2.9 cm	a_{Ymin}=3.7 cm	a_{Ymin}= 5.0 cm	a_{Ymin}= 6.5 cm
$a_Y =$ 1.6 cm	$a_Y =$ 3.0 cm	$a_Y =$ 4.0 cm	$a_Y =$ 5.0 cm	$a_Y =$ 7.1 cm	$a_Y =$ 8.9 cm

Figure 10d – 500ºC-isotherm patterns: cross-section $b \times h = 40 \times 120$ cm ($^1/_2 b \times ^1/_2 h = 20 \times 60$ cm).

30 min.	60 min.	90 min.	120 min.	180 min.	240 min.
$a_X =$ 0.9 cm	$a_X =$ 2.0 cm	$a_X =$ 2.9 cm	$a_X =$ 3.5 cm	$a_X =$ 4.7 cm	$a_X =$ 5.9 cm
a_{Ymin}=0.9 cm	a_{Ymin}=2.0 cm	a_{Ymin}=2.9 cm	a_{Ymin}=3.7 cm	a_{Ymin}= 5.0 cm	a_{Ymin}=6.0 cm
$a_Y =$ 1.5 cm	$a_Y =$ 2.8 cm	$a_Y =$ 3.8 cm	$a_Y =$ 4.7 cm	$a_Y =$ 6.5 cm	$a_Y =$ 8.0 cm
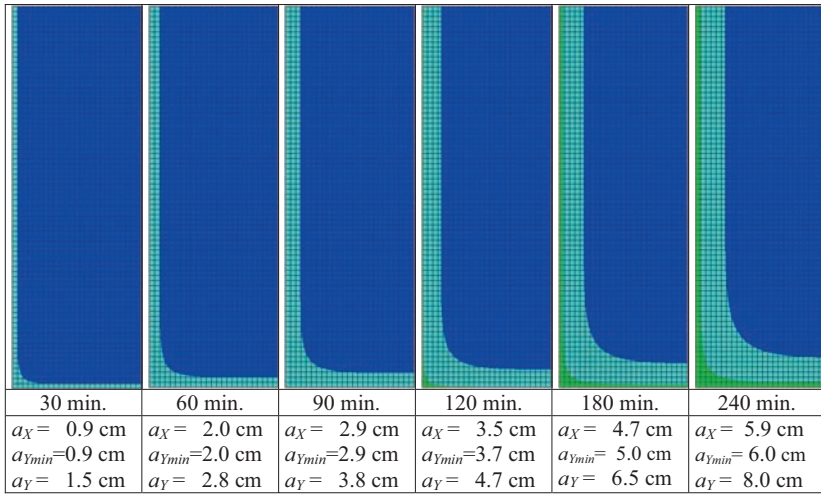
Figure 10e – 500ºC-isotherm patterns: cross-section $b \times h = 50 \times 150$ cm ($^1/_2 b \times ^1/_2 h = 25 \times 75$ cm).

Considering Fig.10 one can conclude that the distance between the 500°C-isotherm and the left vertical side (a_X) does not depend on the cross-section width if this width is 30, 40 or 50 cm. For smaller values of the width (10 and 20 cm), for any short fire duration the influence of the cross-section width plays no major role, but for any long-enough fire duration, the values of a_X increase rapidly.

Figure 11a shows the distance a_X between the 500°C-isotherm and the left vertical side of the section for various values of the cross-section width against the standard fire duration. The diagrams are based of the values shown in Fig. 10.

Figure 11b shows similar diagrams, but the values of a_X are rounded to the multiple of 0.5 cm. The values of a_X for $b \geq 30$ cm are equal to the values of the 500°C-isotherm range proposed for slabs in Fig. 4. Fig. 11b can be used for a simplified evaluation of the reduced cross-section width when a beam is calculated using the "500°C-Isotherm Method".

Figure 12a shows the distance a_Y between the 500°C-isotherm and the bottom side of the section for various cross-section widths against the standard fire duration. The general shape of the diagrams is similar to those shown in Fig. 11a. For relatively wide cross-sections (30, 50 and 60 cm) the diagrams are very close.

Figure 12b shows similar diagrams, but – as in the previous case - the values of a_Y, are rounded to the multiple of 0.5 cm, to the advantage of simplified calculations.

a)   b)
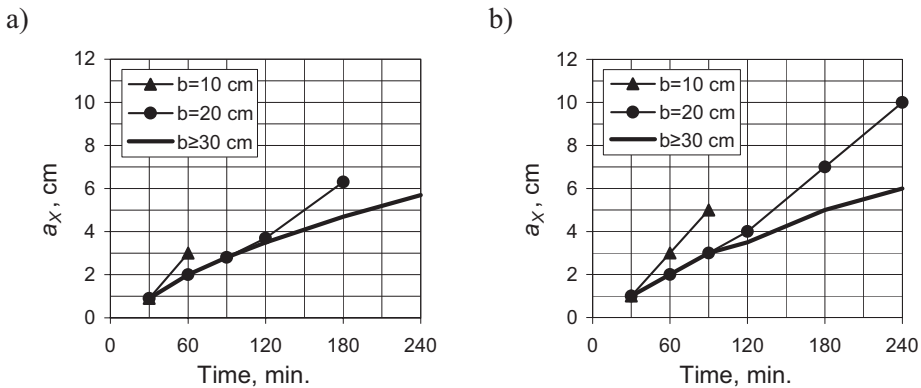
Figure 11 – The distance between the 500°C-isotherm and the vertical side of the section (a_X): (a) numerical results; and (b) proposed simplification.

4.2. Temperature in the reinforcing bars

The calculations described in chapter 4.1 allow to predict the temperature in the reinforcement as a function of the fire duration, for various values of sectional width and for various bar positions.

a)

b)
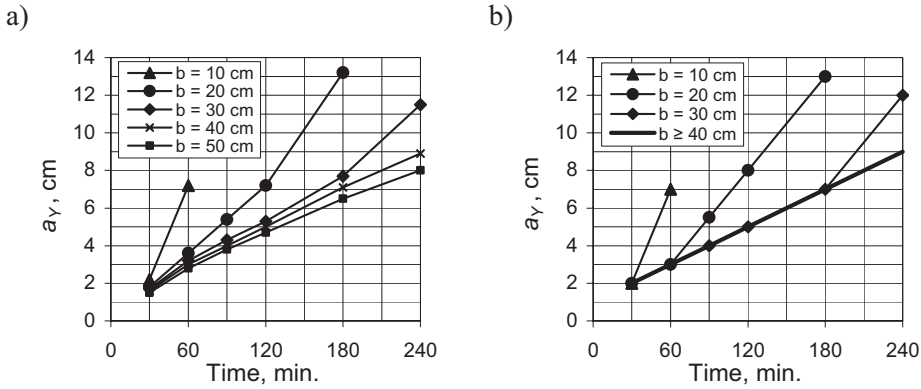
Figure 12 – The distance a_Y between the 500°C-isotherm and the bottom side of the section: (a) numerical results; and (b) proposed simplification.

Figures 13a-e show the thermal field in the corner of a given cross-sections for six values of the fire duration and five values of the width of the section.

Below each pattern of the isotherms, the temperature is plotted horizontally for three values of the concrete cover (from the bottom side to the axes of the bars): $a = 3$, 5, and 7 cm. (These values are commonly found in R/C beams). As should be expected, corner bars are much hotter than intermediate bars.

Figure 15a shows the temperature of the corner bars for a distance between bar axis and cross-section side equal 3, 5 and 7 cm. The vertical axis in Fig. 15a shows the temperature values taken from Fig. 13. The following lines in each figure, starting from the upper side, refer to the cross-section width 20, 30, 40 and 50 cm (some of these lines are situated very close to each other). Additionally, in Fig. 15a referring to $a = 3$ cm the temperature calculated for the cross-section width $b = 10$ cm is shown as a broken line.

Figure 15b shows the diagrams of calculated mean temperature of the bars situated in the middle part of the cross-section (all bars apart from the corner bars). For calculation of the mean temperature the Author took considered only the temperature at the points situated between the distance $a + 3$ cm from left side and the plane of symmetry (see Fig. 14).

For instance, for $a = 5$ cm, the temperatures of point situated between the point at $5+3 = 8$ cm from the left side and plane of symmetry were taken into calculation.
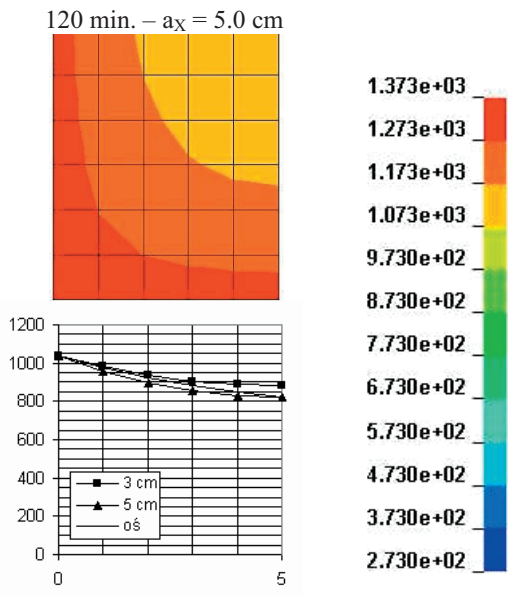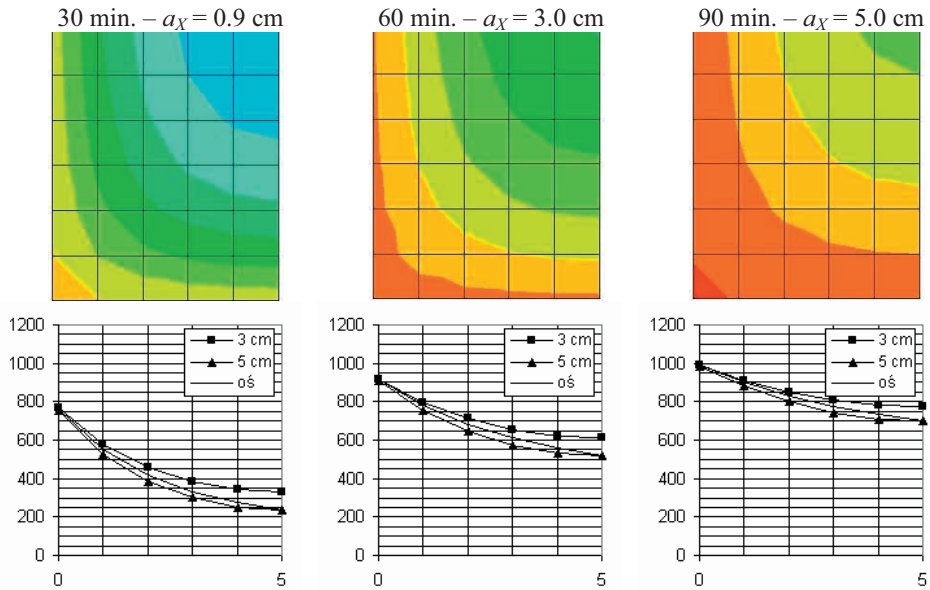
Figure 13a – Section $b \times h = 10 \times 30$ cm ($^1/_2 b \times {}^1/_2 h = 5 \times 15$ cm).): thermal field calculated in the corner; and plots of the temperature in horizontal sections situated at the distance 3, 5, 7 cm from the bottom side.
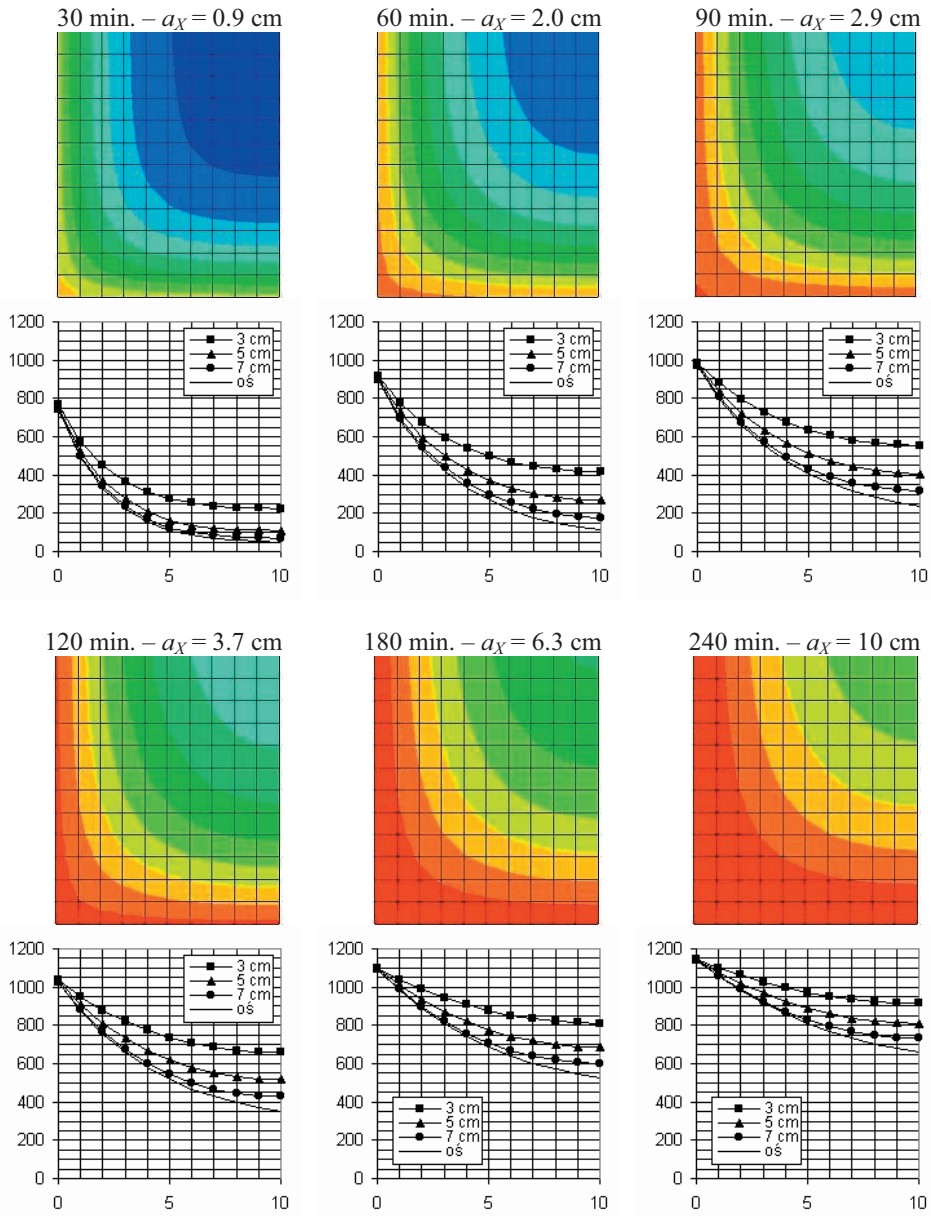
Figure 13b – Cross-section $b{\times}h = 20{\times}60$ cm ($^1/_2b \times {}^1/_2h = 10{\times}30$ cm): thermal field calculated in the corner; and plots of the temperature in horizontal sections situated at the distance 3, 5, 7 cm from the bottom side.
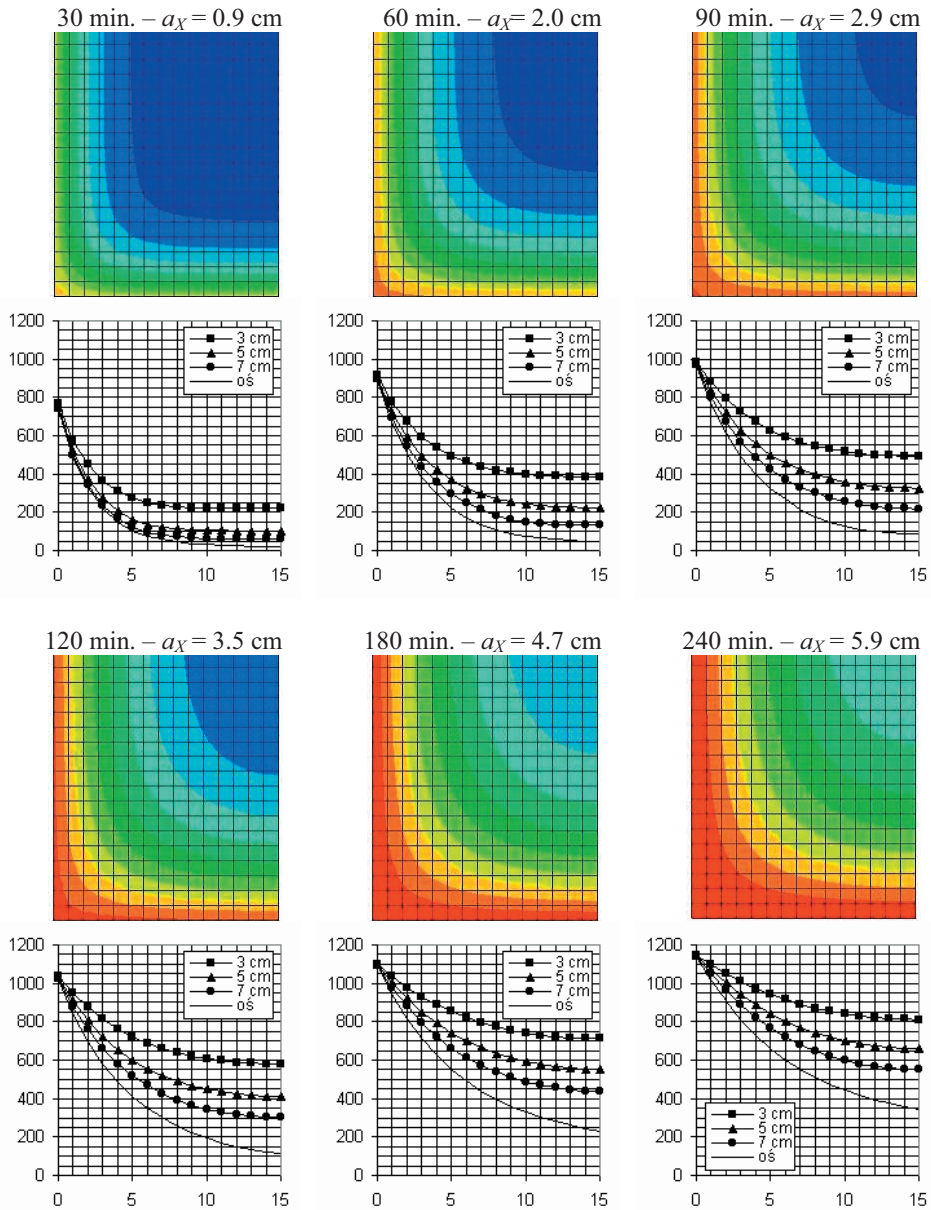
Figure 13c – Cross-section $b{\times}h = 30{\times}90$ cm ($^1/_2 b \times {}^1/_2 h = 15{\times}45$ cm): thermal field calculated in the corner; and plots of the temperature in horizontal sections situated at the distance 3, 5, 7 cm from the bottom side.
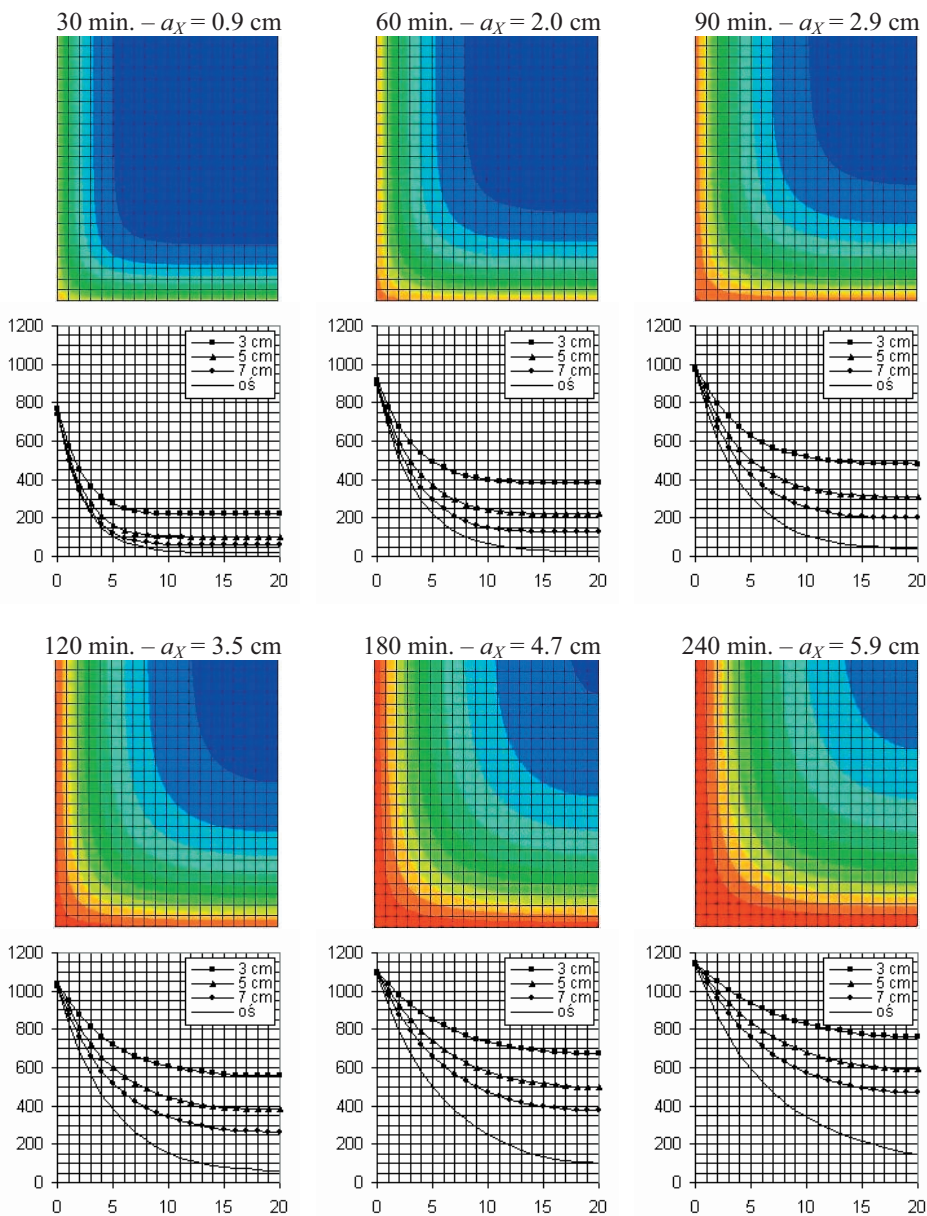
Figure 13d – Cross-section $b \times h = 40 \times 120$ cm ($^1/_2 b \times {}^1/_2 h = 20 \times 60$ cm): thermal field calculated in the corner; and plots of the temperature in horizontal sections situated at the distance 3, 5, 7 cm from the bottom side.
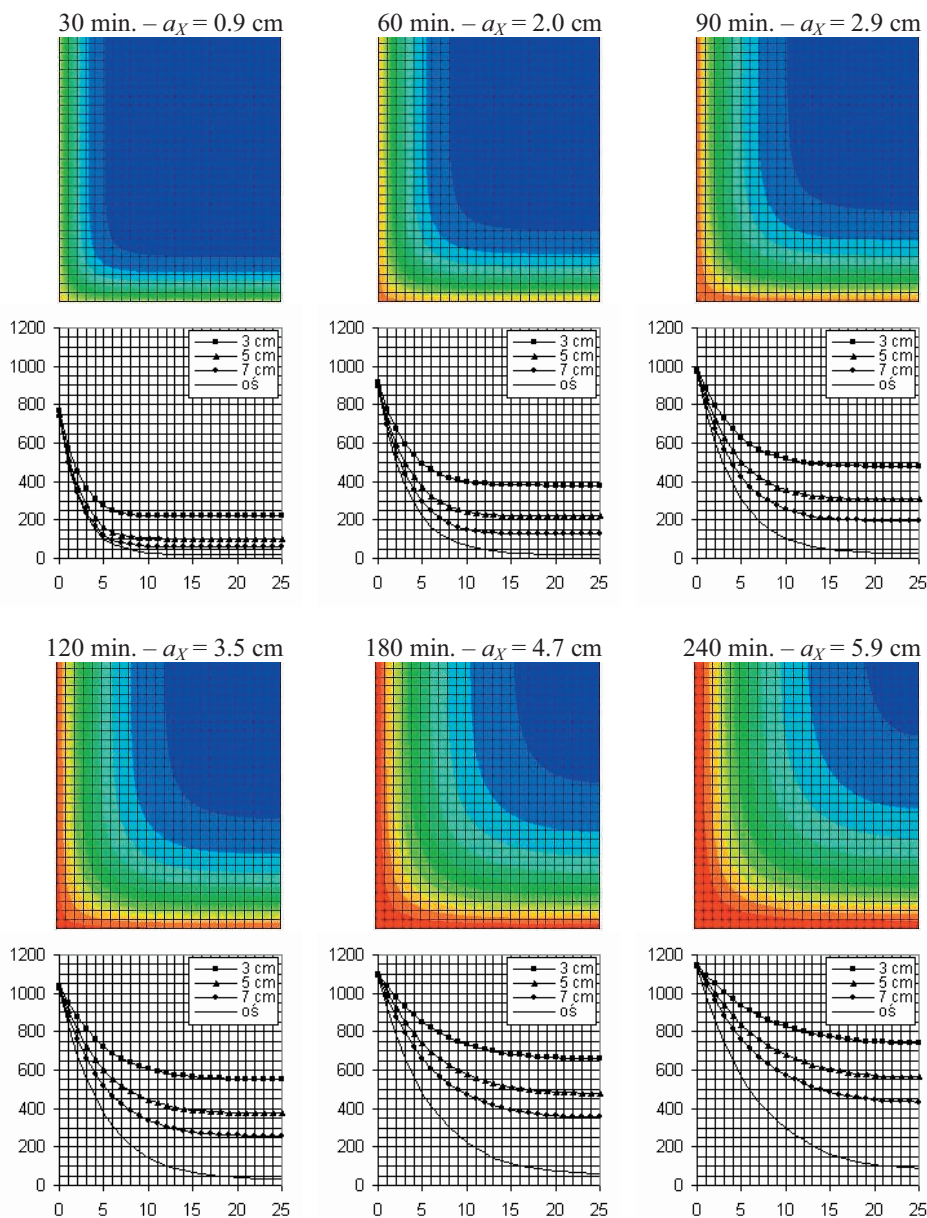
Figure 13e – Cross-section $b{\times}h = 50{\times}150$ cm ($^1/_2b \times {}^1/_2h = 25{\times}75$ cm): thermal field calculated in the corner; and plots of the temperature in horizontal sections situated at the distance 3, 5, 7 cm from the bottom side.
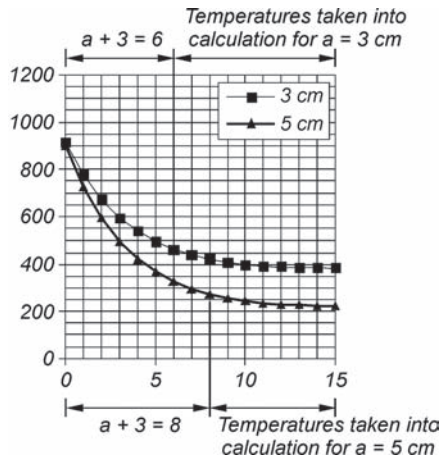
Figure 14 – Temperature considered in the calculation of the mean temperature of middle bars (example with cross-section width b = 30 cm, $^1/_2$b = 15 cm).

Considering Fig. 15a one can observe that for $a = 3$ cm all the curves are very close, except the broken curve for $b = 10$ cm. Similarly for $a = 5$ or 7 cm, where only the curve for $b = 20$ cm, $t \geq 180$ minutes looks different. From a practical point of view, it is useful to replace the curves situated very close to each other with a single curve, as shown in Fig. 16a.

Considering Fig. 15b one can observe that all diagrams are very close, except the diagram referring to $b = 20$ cm. It means that for $b \geq 30$ cm the temperature of bars can be estimated based on one single diagram. Fig. 16b shows these diagrams. Additionally, Fig. 16b shows (broken curves) Author's proposal for evaluating the temperature of the corner bars.

Based on Fig. 16b one can estimate bar temperature against the distance between its axis and the lateral side, as a function of fire duration.

Bold broken curves refer to the temperature of the corner bars. However for $b = 10$ cm the temperature estimated according to Author's proposal is underestimated by about 50°C. Therefore the proposed diagrams can be used only for the values of $b \geq 15$ cm. A smaller cross-section width, however, occurs very rarely.

Bold curves refer to the temperature of the bars situated in the middle part of the cross-section. These curves can be used for any widths b exceeding 30 cm.

For any width $15 \leq b \leq 30$ cm, the temperature of the bars situated in the middle part of the cross-section should be interpolated between the values estimated on the basis of the broken curve (when $b = 15$ cm) and of the solid curve (when $b = 30$ cm). For $a = 3$ cm this proposal gives adequate results. However for $a = 5$ cm the results are a little bit underestimated and for $a = 7$ cm the results are overestimated by about 70-100°C. Hence, a further modification is proposed.
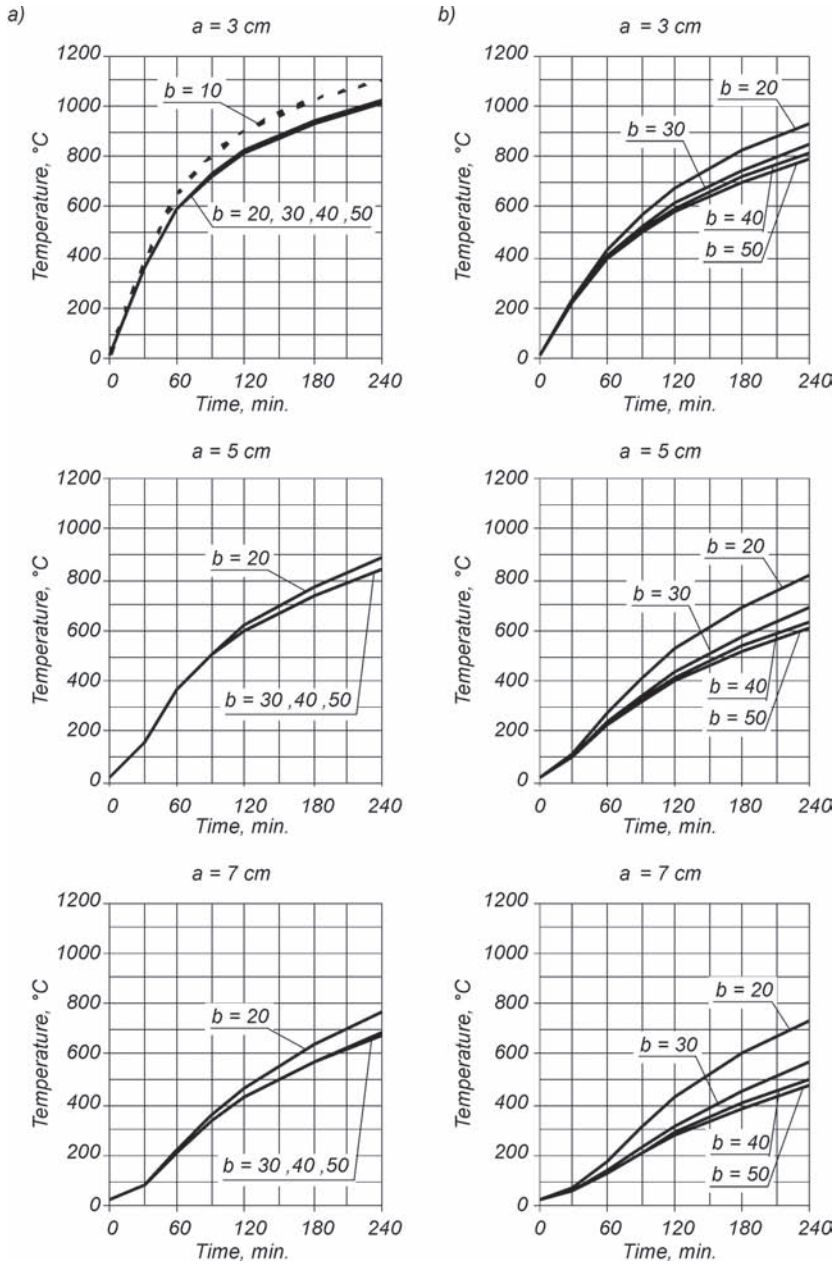
Fig. 15 – Temperature of the bars for various values of the distance *a* between the axis of the bars and the bottom side of the section, and for various values of the sectional width: (a) corner bars; and (b) middle bars (all bars except the corner ones).
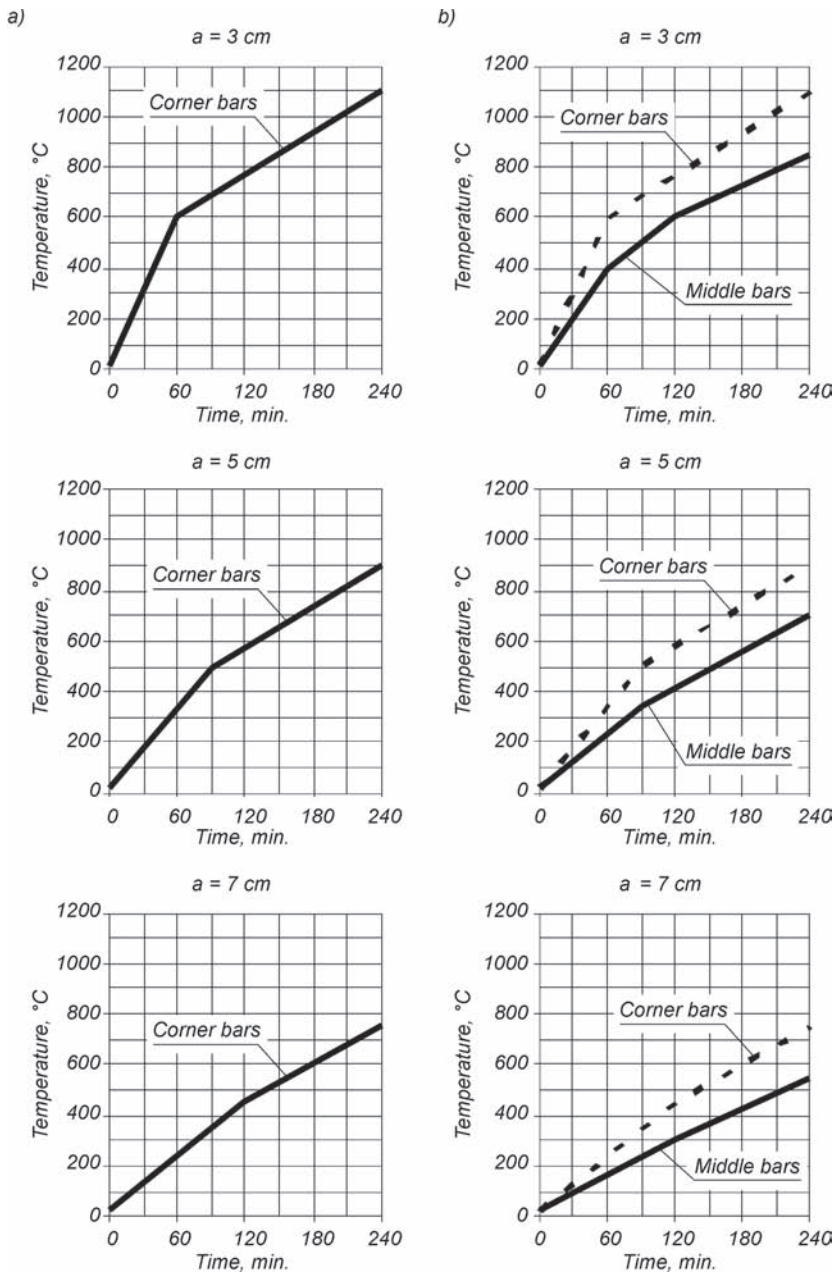
Fig. 16 – Proposed simplified curves for estimating the temperature of the bars for various values of the distance *a* between the axis of the bars and the bottom side of the section, and for various values of the sectional width: (a) corner bars; and (b) middle and corner bars.

For any width of a beam $15 \leq b \leq 20$ cm, the temperature in the intermediate bars should be estimated on the basis of the broken curve. For any value $20 < b < 30$ cm, an interpolation should be made between the broken curve (when $b = 20$ cm) and the solid curve (when $b = 30$ cm). For $b \geq 30$ cm the temperature in the intermediate bars should be estimated on the basis of the solid curve.

5. RECOMMENDATIONS

5.1. R/C Slabs

Recommendations for identifying the "effective" or "reduced" section of concrete and for evaluating the temperature in the reinforcing bars of R/C slabs using the "500°C-Isotherm Method" are given in Fig 4. These recommendations are valid when the slab thickness is:

- $h \geq 5$ cm for standard fire duration t ≤ 60 minutes;,
- $h \geq 10$ cm for standard fire duration t ≤ 120 minutes;
- $h \geq 15$ cm for standard fire duration t ≤ 240 minutes.

5.2. R/C Beams

Recommendations for identifying the "effective" or "reduced" section of concrete and for evaluating the temperature in the reinforcing bars of R/C beams using the "500°C-Isotherm Method" are given in Figs. 11b, 12b and 16b. Alternatively, the simplified curves of Figs.17 and 18 may be used.

In Fig. 17 the parameters a_X and a_Y are plotted as a function of the fire duration; the width and the depth of the reduced cross-section can be obtained as follows.

In the case $h/b \geq 2$:

- width of the reduced cross-section: $b_{red} = b - 2a_X$;
- depth of the reduced cross-section: $h_{red} = h - 2a_Y$.

In the case $h/b \leq 1$, for calculating the reduced cross-section width one should take a_Y instead of a_X (it means that $b_{red} = b - 2a_Y$). In the case $1 < h/b < 2$, an interpolation is necessary in order to obtain the reduced cross-section width.

Figure 18 gives recommendations for evaluating the temperature of the bars at the distance a between the bar axis and the surface of the member ($a = 3, 5, 7$ cm). This recommendation can be used for any beams with a width $b \geq 15$ cm.

6. CONCLUDING REMARKS

The 500°C-Isotherm Method" is based on two clearly-defined assumptions: (1) the part of the concrete section that is enveloped by the 500°C-isotherm is fully active (mechanical properties as in virgin conditions), and the part of the concrete outside the 500°C-isotherm is neglected (totally damaged concrete); and (2) the reinforcement has the mechanical properties corresponding to its actual temperature.
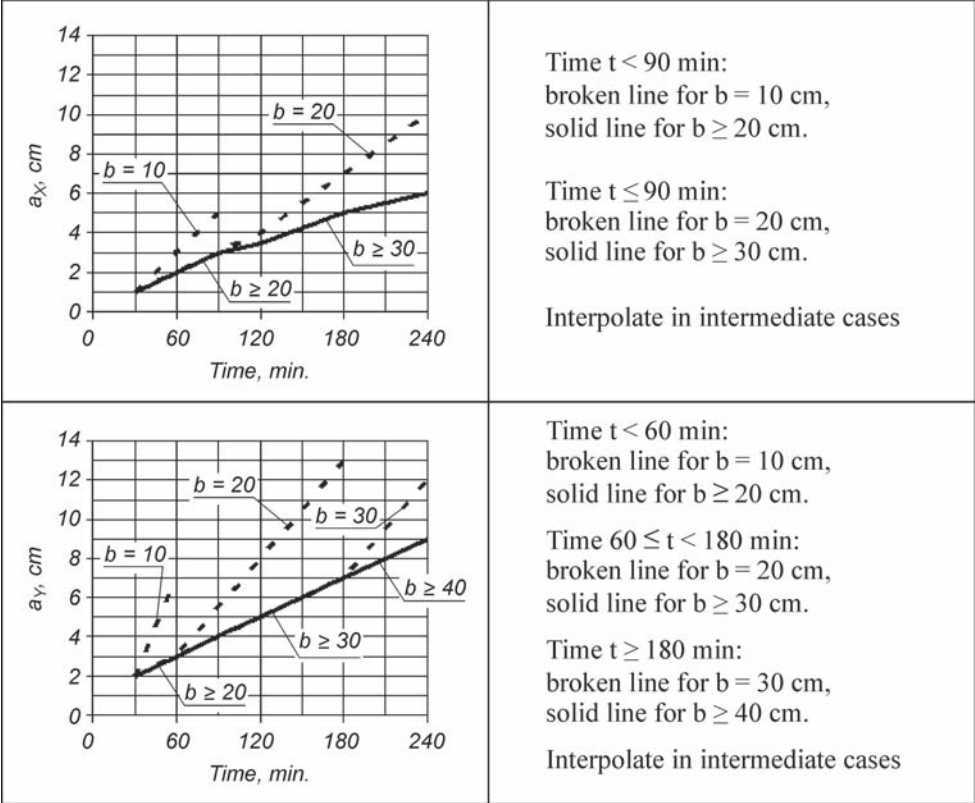
Fig. 17 – Position of the 500°C-isotherm in R/C beams (a_X – measured from the lateral side, and a_Y – measured from the bottom side).

In spite of its conceptual simplicity, the "500°C-Isotherm Method" is not really "simple" because it requires rather time-consuming computational efforts for calculating the thermal field in the cross-section of the given structural member.

In practice, for calculating the thermal field, the materials properties provided by the codes are usually used and the only variable parameters are the dimensions of the cross-section.

The parametric analyses carried out by the Author made it possible to work out a set of diagrams, which simplify the evaluation (1) of the size of the reduced cross-sections, and (2) of the temperature in the reinforcing bars. These diagrams can be useful in the design of R/C beams and slabs using the "500°C-Isotherm Method", as time-consuming calculations are no longer necessary for the assessment of the thermal field in the case of unsteady heat flows.

One should remember, however, that the results presented in this paper refer to the materials properties provided by the Eurocodes, whose values apply to ordinary concrete and are hardly suitable for some of the most recent and innovative cementitious composites.
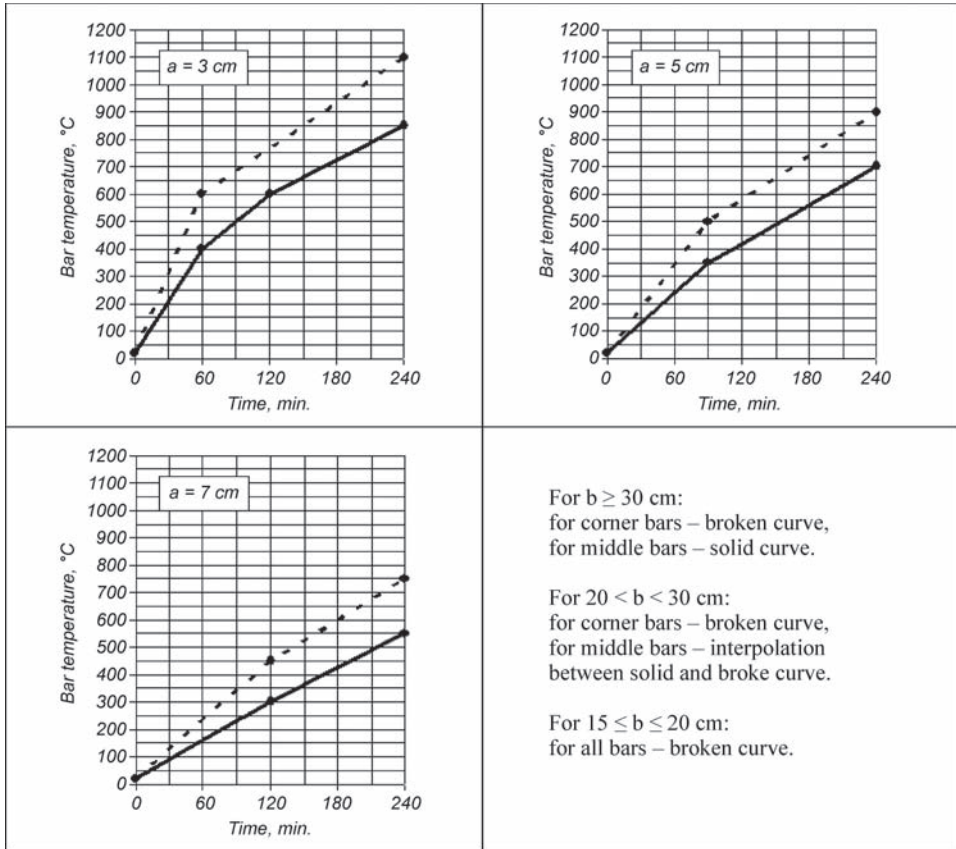
Figure 18 – Temperature of the reinforcing bars in R/C beams (a = distance between bar axis and heated surface from heated surface).

REFERENCES

EN 1992-1-2 (2004). Eurocode 2: *Design of Concrete Structures – Part 1-2: General Rules - Structural Fire Design*.

EN 1991-1-2 (2002). *Eurocode 1: Actions on Structures – Part 1-2: General Actions - Actions on Structures Exposed to Fire.*

fib Bulletins 38 (2007)/46 (2008). *Fire Design of Concrete Structures – Materials, Structures and Modeling / Structural Behaviour and Assessment.*

Bazant Z.P. and Kaplan M.F. (1996). *Concrete at High Temperatures. Material Properties and Mathematical Models*. Longman Group Ltd.

Buchanan A.H. (2002). *Structural Design for Fire Safety*. John Wiley and Sons Ltd.

Khoury G.A., Majorana C.E., Pesavento F. and Schrefler B.A. (2002). "Modelling of Heated Concrete". *Magazine of Concrete Research*, Vol. 54, No. 2, pp. 77-101.

Bamonte P., Gambarova P.G. and Meda A. (2008). "Today's Concretes Exposed to Fire – Test Results and Sectional Analysis. *Structural Concrete*, Journal of the fib, Vol. 9, No 1, pp. 19-29.

ACKNOWLEDGEMENTS

PREPARATION OF MANUSCRIPTS

General

- Size of the volume: 165 x 240 mm.
- Area in which the text must be typed: 129 x 195.
- Upper, lower, left and right margins: 20, 25, 18 and 18 mm.
- Abstract, text, references, captions, titles of the tables: single spaced, left- and right-justified, 11 Times New Roman.
- Figures, tables and captions: skip two lines between the text and each figure or table, skip one line between each figure (table) and its caption (title), skip two lines between each caption (title of the table) and the text.
- Tables: put the title underneath the table.
- Maximum suggested number of pages: 30.

First page

- Top left corner: identification of the volume (3 lines, 11 Times New Roman) as in the papers published in V.26; then skip at least three lines.
- Title: centered, upper-case letters, bold characters, 13 Times New Roman; then skip at least two lines.
- Authors' names: centered, upper and lower case, 11 Times New Roman; then skip at least three lines.
- Abstract: preceded by the heading **ABSTRACT**, left- and right-justified, any length with the only limit of being contained in the 1st page (together with the keywords), 11 Times New Roman.
- Keywords: preceded – on the same line - by **KEYWORDS**, up to 5 keywords should be indicated (left- and right-justified, 11 Times New Roman; skip two lines between the last line of the abstract and the keywords).
- Indentation: 5 spaces at the beginning of each paragraph, except the first paragraph.
- Affiliation: at least two lines below the abstract, preceded by a full straight line, at the foot of the page, with academic or professional position, department or division, employer (university, research center, company, firm ...), city, state.

Following pages

- Indentation: 5 spaces at the beginning of each paragraph, except the first paragraph following the heading or sub-heading of each chapter or sub-chapter.
- Headings:

1. INTRODUCTION	(1st level, chapters)
1.1 Materials	(2nd level, sub-chapters)
1.1.1 Concrete	(3rd level, sub-chapters)

- Skip two lines between the end of a chapter and the heading of the following chapter.
- Skip one line between the end of a sub-chapter and the heading of the following sub-chapter.
- Skip one line between each heading or sub-heading and the following text.
- Fill each page with text/figures/tables/references in order to avoid half-filled pages. If the last page is not full, place the references in two partial columns of similar length.
- Fill each page in such a way that its last line be aligned with the last lines of the other pages, in accordance with the page format.

Captions, quotations, references and appendixes

- Captions and titles (to be placed always under the figures and the tables): short captions or titles (less than one line) should be centered; long captions or titles (two or more lines) should be left- and right-justified.

   Examples:

   Figure 1 – Fracture energy vs. temperature.

   Table 1 – Geometry of the specimens: L = span; b = section width; ΔL = distance between the point loads; and d',t' = depth and thickness of the mid-span notch.

- Quotations within the text: ..... Chopra (1995) or ..... Black and White (1998) or .... Black et al. (2000) or ... (White, 1995; Black, 2002; Gray, 2003a) [add a letter like "a", "b", "c", ... if two or more papers published in the same year by the same author(s) are cited in the references].

- References: should be in alphabetic order (numbered references, like [5], are accepted whenever the references are very numerous and/or cumbersome):

   Black K. and White E. (1998). "Experimental Studies on Concrete". *Journal of Concrete Constructions*, Vol.00, No.00, pp. 0000-0000.

   Black K., Gray C. and White E. (2000). "Concrete Modeling". *Proc. 4th Int. Conf. on Advances in Concrete Mechanics*, ed. by B. Green and W. Brown, City, State, Vol.1, pp. 0000-0000.

   Chopra A.K. (1995). *Dynamics of the Structures.* Pub. by Prentice-Hall, Upper Saddle River, New Jersey (USA).

- Skip 6pt between two successive references.

- Appendixes: the sections "References" and "Notation" should not be indicated as appendixes; any appendix should be placed past the sections "References" and "Notation", and should be indicated with Roman numbers.

- For the quotation of a paper published in Studies and Researches, adhere to the following example:

Regan P.R. and Kennedy Reid I.L. (2009). "Assessment of Concrete Structures Affected by Cover Delamination – Part 1: Effect of Bond Loss". *Studies and Researches – Annual Review of Structural Concrete*. Vol.29, ed. by Politecnico di Milano and Italcementi, pub. by Starrylink (Brescia, Italy), pp.245-275.

Format of the keywords (compulsory from Vol. 31)

KEYWORDS : bond, chlorides, corrosion, reinforced concrete, shear capacity

Paper submission

The papers should be submitted to any member of the Editorial Board, preferably as a word file, within the month of June of the year of publication. Each paper will be reviewed by at least two independent reviewers, and the reviews will be sent back to the author(s) within 5 weeks since the submittal of the paper.

Design-oriented papers, short contributions on specific scientific or professional topics, and experimental or numerical reports are welcome, and will be published in the Section "Technical Notes".

Presidente Prof. Antonio Migliacci – Direttore Prof.ssa Paola Ronca

Scuola Master F.lli Pesenti
Anni accademici
2009-2010 / 2010-2011

La Scuola F.lli Pesenti – Politecnico di Milano

fine anno accademico 2009-2010 ed inizio 2010-2011
decimo anniversario dell'attivazione dei Corsi di Master

La consueta appendice a "Studies and Researches" sulle iniziative di maggior rilievo della Scuola, durante l'anno accademico appena concluso (2009-2010), presenta qui di seguito un ampio quadro del cammino della Scuola, che ha da poco iniziato il <u>decimo anno di attività come Scuola Master (2010-2011).</u>

Si apre infatti con la rassegna di *"fotografie storiche e di attualità", a* testimonianza del lungo e articolato cammino dell'istituzione, seguite poi dalle consuete *notizie* sull'anno appena terminato e dai *sommari* delle migliori tesi discusse all'esame di Diploma del Master.

L'appendice si articola quindi nelle tre seguenti parti:

1. *Storia e attualità della Scuola "F.lli Pesenti": breve rassegna*

2. *Attività collaterali della Scuola, a favore della diffusione internazionale ed all'innovazione dell'offerta didattica*

3. *Tesi di Master discusse nei due appelli, rispettivamente del 27 ottobre e del 16 dicembre 2010, per l'esame di Diploma*

1. Storia e attualità della Scuola F.lli Pesenti

1927: data storica per la R. Scuola d'Ingegneria (R. Politecnico) Milano

• Nuova sede in P.zza Leonardo da Vinci

Sen. prof.
ing.Gaudenzio Fantoli –
Direttore del Politecnico

• **Istituzione della FONDAZIONE F.LLI PESENTI per l'attuazione della**
"Scuola di Specializzazione
per le Costruzioni in Cemento Armato"
presso l'*Istituto di Ponti e Grandi Strutture Speciali*

1931: inizia la pubblicazione dei Volumi "ATTI RICERCHE STUDI"

Pubblicazione curata e impostata dal **prof. Luigi Santarella** (titolare del corso di *Costruzioni Civili – Ponti - Fondazioni*) per la divulgazione delle attività della Scuola, sia da un punto di vista prettamente didattico, sia come centro di ricerca.

La didattica della Scuola viene soddisfatta attraverso l'istituzione di vari Corsi, negli anni <u>continuamente aggiornati e incrementati</u> nell'intento di ottemperare agli scopi e alle necessarie innovazioni che le costruzioni in cemento armato richiedevano.

Si ricordano, tra gli altri, alcuni <u>docenti della Scuola</u> di quegli anni tra cui, oltre al già citato prof. Santarella:

prof. G. Albenga

prof. O. Belluzzi

prof. A. Danusso

prof. E. Giangreco

prof. P. Locatelli

prof. R. Morandi

prof. G. Oberti

prof. L. Stabilini

Arricchimento dei singoli corsi offerti come testimonianza dell'evoluzione della Scuola: già nel '49 il prof. Stabilini affronta il <u>problema del progressivo cambiamento degli scopi della Scuola</u>, da quelli iniziali di <u>divulgazione delle possibilità</u> del cemento armato a quelli sempre più di <u>specifico perfezionamento</u>, in cui devono essere trattati problemi e teorie che non trovano posto negli usuali corsi politecnici.

Questa "<u>mission</u>" viene affrontata anche con una sempre più numerosa offerta di <u>conferenze</u> pubblicate nei volumi degli Atti della Scuola, tenute da personalità di <u>livello internazionale</u> quali:

F. Von Emperger (1937)   **R. Morandi** (1963)

G. Colonnetti (1954)   **V. Franciosi**

Y. Guyon (1951)   **E. Giangreco**

C. Massonet (1963)

E. Torroja (1953)
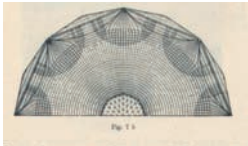
Significato delle conferenze scelte per la **celebrazione del cinquantenario**:

Negli anni '70 si assiste alla "globalizzazione" dei metodi automatici per il calcolo delle strutture, in particolare FEM e FEA; alla fine degli anni '70 vengono proposte le prime applicazioni di tali metodi alle strutture in c.a.

Il prof. SCORDELIS dell'Universita' di Berkeley, in particolare, allora poteva essere considerato pioniere del metodo.

Insieme ai proff. BAZANT (Northwestern Univ.)

e SCHNOBRICH (Urbana-Illinois. Univ.)

Vengono alla Scuola F.lli Pesenti per tenere un ciclo di seminari in occasione del 50° anno della fondazione

POLITECNICO DI MILANO

CORSO DI PERFEZIONAMENTO

PER LE COSTRUZIONI IN CEMENTO ARMATO

"FRATELLI PESENTI"

Cinquantenario della istituzione 1927/28-1977/78

ANALISI DELLE STRUTTURE IN CEMENTO ARMATO MEDIANTE IL METODO DEGLI ELEMENTI FINITI

Seminario 20-23 giugno 1978

Prof. Zdnek P. BAZANT
Northwestern University, Evanston, Illinois
Prof. William C. SCHNOBRICH
University of Illinois, Urbana, Illinois
Prof. Alex C. SCORDELIS
University of California, Berkeley, California

Cammino istituzionale e trasformazioni

della Scuola F.lli Pesenti

Il **Direttore prof. Dei Poli** rafforza l'attivita' di Centro di Studi e Ricerche

• **1987**: D.P.R. - G.U. n°135 - la Scuola viene ufficializzata come

Scuola di Specializzazione nello Statuto del Politecnico

• **1999**: Legge n° 509/99 (Riforma sull'ordinamento degli studi universitari) – vengono abolite su tutto il territorio nazionale le Scuole di Specializzazione e riconosciuta la possibilità di attivare Corsi di Master CFU (60 crediti universitari spendibili a livello europeo)

• **2000- 2001**: si dà avvio all'ultimo ciclo della Scuola di Specializzazione e **viene stipulata una nuova convenzione tra Italcementi e Politecnico-DIS** per l'attivazione di Corsi di Master CFU (prof. A.Migliacci)

• **18 ott. 2001**: il Direttore della Scuola F.lli Pesenti, prof. ing. Antonio Migliacci, all'interno della conferenza da lui tenuta presso il Politecnico di Milano *La Moderna Strategia per la Progettazione Globale delle Grandi Opere* (*fonte :* articolo "A proposito di innovazione" della rivista Politecnico – dic. 2001) annuncia l'attivazione di 3 Corsi di Master CFU.

• Negli anni successivi lo scenario della formazione post-laurea in Italia cambia drasticamente: nel giro di pochi anni vengono attivati oltre duemila Master CFU

La vita e validità della Scuola attingono sempre al binomio

Continuita' e Innovazione

⬇

Ricerca e Formazione Continua

*" History doesn't repeat itself,
But it does rhyme "*

Mark Twain

La Scuola F.lli Pesenti oggi , espressa dall'andamento di alcuni indici

- Grafico degli iscritti
- Numero dei docenti coinvolti
- Corsi di Master Universitari attivati
- Unità Didattiche svolte
- Collaborazioni con enti esterni (*stipula convenzioni*)
- Stage come coop-system

Gli allievi

Grafico numerico degli allievi *stranieri*
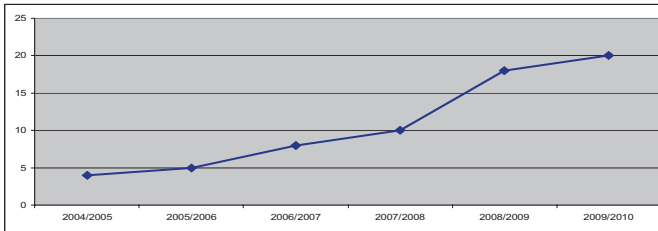
L'andamento del *numero complessivo* degli allievi
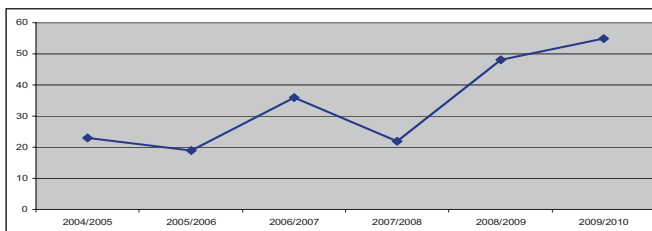
La docenza

- 26 Docenti del DIS
- 20 Docenti di altri Dipartimenti,del Politecnico
  (DIAR, BEST, DIG, DIAP, …)
- 14 Docenti del mondo tecnico-industriale, professionale e gestionale
- 19 Docenti di altri Atenei ,italiani ed internazionali , Centri di Ricerca (Eucenter, Ispra)

- **Excellence in great project participation**, either because the industrial and professional community of Milano and Lombardia region is one of the most propulsive in Europe, either because the faculty members of the F.lli Pesenti School have strong connections with major private and public developers , and, not last, because firms and professional offices recognize the determination and hard working characters of our students.
- **The geographical location** which plays a central role as a link between Europe and the south side-Mediterranean countries .
- **The frequent and welcome job opportunities** , as a consequence of our Master Diploma and the co-operative work experience.
- Possibility of **Continuing and Updating Education, by means of short non-credit courses,** which are held, generally, in no more than one-week and even offered on line.

FLOW CHART UNITA' MASTER 2010/2011 - SCUOLA MASTER F.LLI PESENTI - DIS/CIS-E POLITECNICO DI MILANO

MASTER 1,3,4,5,6 UNITA'1: Materiali da Costruzione (54 ore)

MASTER 1,2,3,4,5 UNITA' 2: sostenibilità nelle costruzioni, materiali, risparmio energetico e fonti di energia rinnovabili (47 ore)

MASTER 2,3,4,5 UNITA' 8: Progettazione Urbana (20 ore)

MASTER 2,3,4,5 UNITA' 9: Il Recupero del Costruito e il controllo del nuovo (16 ore)

MASTER 2,3,4,5 UNITA' 13: Controllo e Gestione del Progetto e del Cantiere (28 ore)

MASTER 1 UNITA' 3.1:le Basi dell'Analisi Strutturale (20 ore) - FEM
UNITA' 3.2: i Programmi di Calcolo FEM/FEA (10 ore)

MASTER 1 UNITA' 4:Strutture in c.a. (70 ore)

MASTER 1 UNITA' 5: Progettazione in Zona Sismica (25 ore)

MASTER 1 UNITA' 6: Strutture Speciali (35 ore)

MASTER 2 UNITA' 12: Rapporto fra Architettura e Tecnologia (24 ore)

MASTER 3 UNITA' 16: Controllo e Gestione del Costruito (20 ore)

MASTER 4 UNITA' 15: Fondamenti del Controllo di Gestione (60 ore)

MASTER 5 UNITA' 15 BIS: Contractor Management (30 ore)

MASTER 2 UNITA' 10: Informatica e Disegno nell'Architettura Scientifica (14 ore)

MASTER 3 UNITA' 10: Informatica e Disegno nell'Architettura Scientifica (14 ore)

MASTER 4 UNITA' 11: Tecnologia, Sicurezza ed Ergonomia della Costruzione (40 ore)

MASTER 5 UNITA' 11: Tecnologia, Sicurezza ed Ergonomia della Costruzione (40 ore)

MASTER 2 UNITA' 11: Tecnologia, Sicurezza ed Ergonomia della Costruzione (40 ore)

MASTER 3 UNITA' 11: Tecnologia, Sicurezza ed Ergonomia della Costruzione (40 ore)

MASTER 4 UNITA' 16: Controllo e Gestione del Costruito (20 ore)

MASTER 5 UNITA' 7 BIS: Long Life Assessment

MASTER: 2 UNITA' DA DEFINIRE

MASTER 3 UNITA' 7: i criteri per la Valutazione delle Costruzioni Sostenibili

MASTER: 5 UNITA' DA DEFINIRE

MASTER 3 UNITA' 14: Strutture per la Protezione dell'Ambiente (40 ore)

TUTTI I MASTER UNITA' 17: società di ingegneria, studi professionali (40 ore)

321

Continuazione

- **Excellence in great project participation**, either because the industrial and professional community of Milano and Lombardia region is one of the most propulsive in Europe, either because the faculty members of the F.lli Pesenti School have strong connections with major private and public developers , and, not last, because firms and professional offices recognize the determination and hard working characters of our students.
- **The geographical location** which plays a central role as a link between Europe and the south side-Mediterranean countries .
- **The frequent and welcome job opportunities** , as a consequence of our Master Diploma and the co-operative work experience.
- Possibility of **Continuing and Updating Education, by means of short non-credit courses,** which are held, generally, in no more than one-week and even offered on line.

FLOW CHART UNITA' MASTER 2010/2011 - SCUOLA MASTER F.LLI PESENTI - DIS/CIS-E POLITECNICO DI MILANO

Gli stage 2009 – 2010 - Esperienza di cooperazione con l'Industria e le Professioni

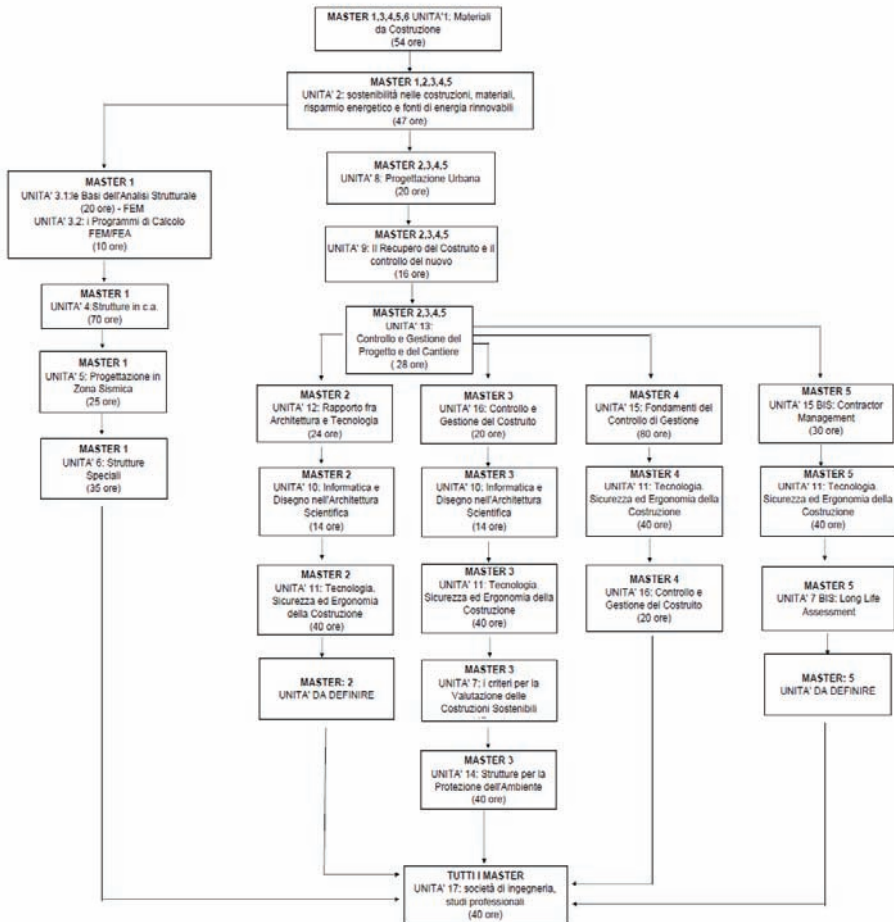| N.	Allievo	Master	Ente stage	Referente univ	Tematica/Progetto
1	Anzani Andrea	Aspetti	NAVIGLI	Ing. Alessandro Zichi	Progettazione paesaggistica e architettonica
2	Assenza Alessandra	Project	FAVERO & MILAN	Prof. Cigolini	Assistenza al coordinamento e alla gestione delle attività di progettazione delle strutture, impianti e faciate nell'ambito della Fondazione Prada - Nuovo museo di arte moderna
3	Bande Linda	Opere	SARNO	Prof.ssa Ronca	Progettazione architettonica
4	Bonacina Sara	Aspetti	ST. ARDEA	Prof.ssa Ronca	Architettura e paesaggio: tipologie abitative e tecnologia in rapporto a contesti ambientali di alto valore
5	Caschili Marcello	Project	FERRETTI	Prof. Franchi	Progetto di un cantiere in Libia
6	Cerav Sibel	Design	CTG	Prof.ssa Ronca	Architectural and Indoor Air Quality (IAQ) aspects of TX Active cements
7	Colombo Roberto	ca	FERRETTI	Prof. Ferrara	Progetto di un cantiere in Libia
8	Crivellaro Luca	Project	PROJECT & DESIGN	Prof. Franchi	Il Project e il Design Management e la loro applicazione nella verifica della progettazione
9	Daw Akram	Project	DIS	Prof.ssa Ronca	Rehabilitation and renewal of 2 Fevrier Hotel in Lome (Togo)
10	De Panfilis Giulio	Project	DIS	Ing. Pietro Crespi	La gestione della commessa di una grande opera infrastrutturale
11	Gallina Francesca	Aspetti	GRASSI	Prof.ssa Ronca	Progetto Antica Cà Litta: ristrutturazione e conversione in residenza di un edificio settecentesco a Milano
12	Gatti Ricardo	Project	DE ECCHER	Prof. Franchi	Analisi e approfondimento dei processi di gestione di uan commessa, a partire dall'acquisizione delle competenze tecniche di base attraverso la gestione della fase progettuale
13	Gomez Mataix G.	Aspetti	da definire	da definire	da definire
14	Grassi Vanessa	Project	GDM	Ing. Bamonte	Programmazione del cantiere di Via Salaino - Milano
15	Guaragna Luca	ca	IMPREGILO	Prof. Franchi	Progetto idroelettrico Ingula (Sud Africa)
16	Ierardi Diego	ca	GDM	Prof. Franchi	Area progettazione
17	Kanberoglu Burak	Design	DIS	Prof. Franchi	Life cycle assessment of a construction project
18	Laricchia Antonella	Aspetti	NAVIGLI	Prof.ssa Ronca	Redazione di elaborati progettuali
19	Lepori Simona	ca	ARUP	Prof. Franchi	Assistenza alla progettazione dell'Aeroporto di Baku
20	Lonardi Alberto	Project	AUOSTRADE BRENNERO	Prof. Franchi	Analisi dei documenti propedeutici al contratto e controllo del costruito
21	Medici Nicola	Project	GDM	Prof. Franchi	Cantiere di Via Varesina - Milano
22	Mentor Balilay	ca	DIS/AQUILA	Prof. Franchi	Prove sperimentali e simulazioni numeriche sul comportamento di ancoraggi nel calcestruzzo fessurato sotto carico ciclico
23	Milanovic Slavko	Aspetti	VGA & PARTNERS (Arch. Grassi)	Prof.ssa Ronca	Analisi e progettazione di modelli isnediativi ecosostenibili e tecnologicamente avanzati
24	Molinari Nicola	Project	da definire	da definire	da definire
25	Moscoso Rocio	Opere	CIS-E	Ing. Alessandro Zichi	Le costruzioni sostenibili, stima dell'impatto ambientale con metodi quantitativi
26	Mustafa Kaya	Design	FERRETTI	Franchi	Progetto di un cantiere in Libia
27	Norouzy Reza	Design	ALISAZ - Quatar	Prof.ssa Ronca	Azienda ALISAZ a Doha (Qatar) -
28	Ozdemir Ozlem	Design	CTG	Prof.ssa Ronca	Architectural and Indoor Air Quality (IAQ) aspects of TX Active cements
29	Ozturk Sakir	Design	CLAUDIO SALINI spa	Prof. Franchi	Project Manager nell'ambito di opere civili
30	Pacheco Eliana	Aspetti	QUAGLIA	Ing. Pietro Crespi	
31	Panizza Simone	Project	ST. PRAU	Prof.ssa Ronca	Affiancamento alla Direzione Lavori per la realizzazione delle opere di urbanizzazione a scomputo di un alottizzazione residenziale
32	Papagianni Evengelia	Aspetti	DIS (Arch. Grassi)	Prof.ssa Ronca	Analisi e progettazione di modelli insediativi ecosostenibili e tecnologicamente evoluti
33	Patteri Chiara	ca	ARUP	Prof.ssa Ronca	Assistenza alla progettazione - Hotel Gallia
34	Pazzola Maria Carla	Opere	DIS	Ing. Alessandro Zichi	Impatto ambientale delle attività di costruzione dei centri urbani e nel territorio: caso emblematico PGT e strumenti attuativi nel comune di Turbigo
35	Perret Richard	ca	AMIS	Prof. Franchi	Indagini sulle strutture e progetto strutturale per l'adeguamento anti-sismico di un complesso scolastico
36	Pitzus Francesco	Aspetti	DIS	Ing. Alessandro Zichi	Progettazione a basso impatto ambientale nel contesto della Darsena, Navigli - Milano
37	Posteraro Nicola	Project	SALINI	Prof. Franchi	Project Manager nell'ambito di opere strutturali e infrastrutturali

38	Tugce Tuncay	Design	DIAP	Prof.ssa G. Fossa	Megaregione: Planning and architectural trends and strategy
39	Tuna Sevi	Design	CLAUDIO SALINI spa	Prof. Franchi	Project Manager nell'ambito di opere civili
40	Yagli Secil	Design	CTG	Prof.ssa Ronca	Architectural and Indoor Air Quality (IAQ) aspects of TX Active cements
41	Yunusogullari Asude	Design	DIAP	Prof.ssa G. Fossa	Megaregione: Planning and architectural trends and strategy
42	Zela Esmeralda	ca	STUDIO ING. MOLA ELENA	Prof. Mola	Assiststenza alla progettazione strutturale edifici in c.a.
43	Zoncheddu Filippo	ca	SINECO	Ing. Pietro Crespi	Gestione e manutenzione ponti autostradali
44	Dal Lago Bruno	sismica	DIS	Prof. Toniolo	Connessioni di strutture prefabbricate in zona sismica
45	Gianni Cristian	sismica	Lombardi - Reico	Ing. Crespi	Progettazione sismica di pareti in c.a. in bassa duttilità
46	Yagli Bora	sismica	CTG	Prof. Franchi	UHPC in structural retrofitting
47	Mariotti Arnaldo	sismica	Studio tecnico di Bari	Prof. Franchi	da definire
48	Palamara Giuseppe	sismica	DIS	Ing. Crespi	Strutture in acciaio in zona sismica
49	Pinato Rossana	sismica	Studio di Ing e Arch	Ing. Crespi	Progettazione di strutture in zona sismica
50	Valle Giovanni	sismica	da definire	da definire	da definire
51	Lenoci Innocenzo	sismica	DIS	Prof. Franchi	Indagine sul rinforzo delle murature di Palazzo Camponeschi de L'Aquila

Nota: - in giallo gli studenti italiani che hanno svolto lo stage all'estero
*   - in azzurro gli studenti stranieri*

Avanzamento procedura e lavori di adeguamento e ristrutturazione locali della Scuola

-La ricerca dei fondi e' andata a buon fine

-L'Odissea dei Permessi si e' conclusa

↓

Finiti i lavori di bonifica (maggio 2010), i locali sono rimasti inagibili; il progetto e la procedura di gara hanno dovuto subire parecchie revisioni

A fine settembre 2010 si è aperto il cantiere, di cui alcune immagini qui di seguito:

- Mantenimento della certificazione in Qualita'

- Lato docenza : eccellenza e innovazione

- Offerta della didattica nella forma e-learning

- Continuo processo di informatizzazione

Per l'eccellenza della Scuola

• Partecipazione e promozione continua di temi di "*Ricerca*"

collegamenti con Scuole di Dottorato

• *Individuare i temi per sviluppare "ricerca applicata"* › acquisizione di "*Contratti di Ricerca*" *o/e "Contratti di Consulenza"*

Fondamentale la collaborazione col Consorzio CIS-E

<u>solo una istituzione come si configura il CIS-E</u>
(come spin-off di un Dipartimento Universitario, tipo DIS)
puo' al meglio fornire :

- Consulenze operative su problemi particolari, richieste direttamente o all'interno di attivita' riservate
- Sviluppo di Linee Guida e loro applicabilita'
- Garanzia del prodotto fornito
- Personale non distratto e impegnato da troppa didattica o carriera in logica universitaria

---

I Master Universitari : indagine condotta dal Consorzio "AlmaLaurea"
(Universita' di Bologna)

- L'offerta post-laurea per l'anno accademico 2010-2011 prevede in Italia l'attivazione di 2100 corsi di MasterUniversitari.

- Dal *Sole 24 ore (articolo 20 sett. 2010)* "…Perche' iscriversi ad un Master, quando e perche' conviene?"

↓

Affidabilita' dell'ente promotore

"La soluzione piu' efficace sarebbe una <u>valutazione di qualita</u>' estesa a tutti i Master"(il Direttore di AlmaLaurea)

- La Scuola Pesenti e' certificata in qualita' da tre anni : la verifica ispettiva di fine luglio si e' conclusa con piena approvazione :
- "… *L'esame condotto ha consentito di rilevare il notevole e proficuo lavoro svolto dalla struttura in termini di razionalizzazione delle attività, riprogettazione e semplificazione di processi…*"

Salvaguardia e Sviluppo

- Nell'immediato : rinnovo della convenzione con Italcementi group

- Ridefinizione e valorizzazione delle caratteristiche della Scuola Pesenti, e dei servizi che fornisce nell'ambito della *long-life education*, alla luce anche della futura nuova gestione del Politecnico e dell'Universita', in seguito alla riforma Gelmini.

- Riconoscibilita' dei Corsi di Master a livello internazionale con la sigla MAS (**M**aster **A**dvanced **S**tudies); cosi' come e' avvenuto per i MSc

- Chiarezza, spendibilita' e utilita' dei 60 CFU (ECTS)

2. Attività collaterali della Scuola a supporto della diffusione internazionale e dell'innovazione dell'offerta didattica

La Scuola, grazie anche alle attività sinergiche con il consorzio CIS-E, ha continuato ad incoraggiare sia attività seminariali (con inviti diretti di esperti o con partecipazione di propri docenti a seminari esterni), sia attività di collaborazione in ambito internazionale (con contatti tuttora in corso), sia infine lo sviluppo di temi di ricerca prenormativa, con partecipazione in commissioni per la ridefinizione dei nuovi standard internazionali.
Di seguito sono riportate alcune immagini ed alcuni commenti riferentisi alle iniziative più significative e recenti (in ordine temporale).

Con l'aiuto economico del "Fondo internazionalizzazione" della Convenzione stipulata tra Italcementi-CIS-E-Scuola F.lli Pesenti, si e' continuato ad approfondire i temi della "Green Economy" nei diversi ambiti delle costruzioni, incoraggiando il lavoro di squadra di alcuni giovani, in ambito LEED.
In particolare Alessandro Zichi - il giovane ingegnere "Senior" del gruppo - ha superato la selezione internazionale, acquisendo il Diploma Internazionale di "LEED A.P.", come di seguito riportato

Grazie al lavoro del gruppo guidato dai professori Franchi (DIS) e Chiesa (BEST), i vari aspetti della progettazione sostenibile in ambito LEED hanno avuto pratica applicazione nel progetto e nel cantiere per l'adeguamento statico e funzionale dell'Ostello della Gioventù P. Rota del Comune di Milano, già in vista dell'EXPO 2015.

 Di seguito una immagine della giornata inaugurale del cantiere LEEDsostenibile dell'Ostello al QT8, presente il Sindaco dott.ssa Moratti.

I lavori presso l'Ostello sono in fase avanzata e l'obiettivo di ottenere la certificazione LEED GOLD sembra essere concretamente raggiungibile.

Come si può leggere nel paragrafo seguente, dedicato alle tesi migliori dei diplomati Master 2010-2011, la procedura sostenibile LEED è stata applicata ad altri edifici e progetti, a riprova della sempre maggiore attenzione che tale procedura sta suscitando negli operatori privati e negli enti pubblici, e della sua grande diffusione nei paesi emergenti.

I giovani del gruppo LEED del CIS-E/Scuola hanno partecipato ai Convegni annuali del Green Building Council, nel 2009 a Boston e nel 2010 a Chicago.
Durante il convegno di Chicago, l'ing. Zichi ha frequentato alcuni corsi tematici, acquisendo crediti GBCI, come di seguito attestato dal GREENBUILDING *Certificate:*

Session Number	Session Name	Date	Hours	LEED Specific
HD12	Municipal Facilities: Methods and Means	2010-12-21	4	
GR19	Systems Thinking for Residential Buildings: prioritizing green building and waste prevention practices with life cycle assessment	2010-11-18	1.5	
SS02	USGBC's Building Performance Partnership	2010-11-18	1.5	BD+C
OF06	Risk Management, Liability and Insurance on Sustainable Construction	2010-11-18	1.5	
OR12	Case Studies: Deconstruction, Reuse, & C&D Recycling to Achieve Reuse and Recycling Rates of 95% and Support Local Community Development	2010-11-17	1.5	
BL02	How to Integrate the OPR, BOD and Commissioning to Optimize Building Performance	2010-11-18	1.5	BD+C
SU10	LEED on a Campus: An Update to the 2005 Application Guide for Multiple Buildings and On-Campus Projects	2010-11-17	1	BD+C
SU53	LEED for Neighborhood Development: The Top Ten Things You Should Know 2	2010-11-19	1	ND
RD05	LEED for Neighborhood Development: Creating Green Affordable Neighborhoods	2010-11-17	1.5	ND
Total Credit Hours Earned			15.0	

L'attivita' in ambito LEED della Scuola/CIS-E e' stata anche presente durante l'esposizione del

MADE EXPO 2010

con l'organizzazione di uno stand autonomo.

Come da tradizione consolidata, l'attività didattica dei Corsi di Master della Scuola è stata caratterizzata da una vivace **attività seminariale**, pubblicizzata a livello nazionale con avvisi specifici e quindi non riservata solo agli allievi della Scuola Master.

Di seguito alcuni temi dei seminari svoltisi presso la Scuola :

Giovedì 4 Febbraio, dalle 11.15 alle 13.15, nell'aula 1 della Scuola di Specializzazione,

il **Dr. Fabrizio GALADINI**, direttore della sezione di Milano-Pavia dell'Istituto Nazionale di Geofisica e Vulcanologia,

terrà il seguente seminario:

CARATTERISTICHE SISMOTETTONICHE DEL TERREMOTO DI L'AQUILA

Nel corso del seminario verranno descritte e discusse le caratteristiche geologiche della faglia che ha causato il terremoto del 6 aprile 2009, e delle faglie del settore appenninico colpito dalla scossa principale e dalle successive scosse di assestamento.

Siete cordialmente invitati a intervenire,

G. Toniolo, E. Faccioli

La Master School F.lli Pesenti

del Dipartimento di Ingegneria Strutturale

del Politecnico di Milano

e il Consorzio CIS-E

HUGO CORRES PEIRETTI

"CONCEPTUAL DESIGN OF BRIDGES. DIFFERENT EXAMPLES."

Il seminario è a partecipazione gratuita

GIOVEDI' 25 MARZO 2010

Ore 9.00/13.00 – 14.00/16.00

Scuola Master F.lli Pesenti
Dipartimento di Ingegneria Strutturale
Politecnico di Milano
P.zza Leonardo da Vinci, 32

POLITECNICO
DI MILANO

La Master School F.lli Pesenti

del Dipartimento di Ingegneria Strutturale

del Politecnico di Milano e

il Consorzio CIS-E

presentano la giornata su:

MIDAS/Gen 2010

Ultima versione del programma di calcolo strutturale ad elementi finiti illustrata dagli esperti di CSPFea

La partecipazione è gratuita

Mercoledi 21 aprile 2010

dalle ore 10,00 alle ore 17,00

Aula Castigliano
Dipartimento di Ingegneria Strutturale
Politecnico di Milano
P.zza Leonardo da Vinci 32

POLITECNICO DI MILANO

La Master School F.lli Pesenti

del Dipartimento di Ingegneria Strutturale

del Politecnico di Milano e

il Consorzio CIS-E

Presentano il Seminario:

PROF. ING. MICHELE CALVI

"ESPERIENZE DI GRANDI REALIZZAZIONI DI PONTI IN ZONA SISMICA"

Il Seminario è a partecipazione gratuita

GIOVEDI' 22 APRILE 2010

ore 11.00/13.00

Aula Castigliano
Dipartimento di Ingegneria Strutturale
Politecnico di Milano
P.zza Leonardo da Vinci, 32

POLITECNICO
DI MILANO

La Master School F.lli Pesenti

del Dipartimento di Ingegneria Strutturale

del Politecnico di Milano

e il Consorzio CIS-E

presentano il Seminario:

PROF. MAURO DOLCE

nell'ambito della tematica

"ISOLAMENTO SISMICO"

all'interno del Master in
"Progettazione sismica delle strutture per costruzioni
sostenibili"

Il Seminario è a partecipazione gratuita

MARTEDI' 11 MAGGIO 2010

ore 9.15/12.15

Aula 243
Dipartimento di Ingegneria Strutturale – II piano
Politecnico di Milano
P.zza Leonardo da Vinci, 32

POLITECNICO
DI MILANO

Ultimo, in ordine temporale, il seminario tenuto **dal prof. Rolf Eligehausen** dell'Universita' di Stoccarda, esteso agli allievi della Scuola di dottorato ed ai giovani assegnisti e ricercatori del DIS,

Nell'immagine, il titolo del seminario

La sempre maggiore diffusione a livello internazionale delle attività della Scuola è stata favorita anche con contatti diretti e personali che alcuni docenti della Scuola mantengono partecipando a seminari, gruppi di lavoro e giornate di studio.
Di seguito alcune di queste iniziative, principalmente svoltesi nella primavera/estate 2010.

Le immagini successive documentano l'intervento della professoressa Ronca al convegno su invito, organizzato a Madrid da CIAS-IABSE il 12/15 maggio 2010,

E' continuata l'attività (tuttora in corso) del programma di **International Research Staff Exchange** fra le 4 Università consorziate, come brevemente di seguito riportato:

SEVENTH FRAMEWORK PROGRAMME
Marie Curie Actions
People
International Research Staff Exchange Scheme

Full Title: Building with Environmentally Sustainable Structural Timber

Partner Number *	Partner name	Partner short name	Country
1 (*beneficiary*)	Politecnico di Milano	POLIMI	IT
2 partner organisation	University of Sassari	UNISS	IT
3 partner organisation	University of Stuttgart	KE	DE
4 partner organisation	University of Canterbury	UoC	NZ

 I responsabili del programma si sono riuniti sia in occasione del WCTE a Riva del Garda, sia a Milano, presso il Politecnico, nel luglio 2010.
Di seguito una foto del gruppo.

Ancora in ambito "**costruzioni sostenibili / social housing**" il prof. del Bo e la prof.ssa Ronca sono intervenuti ad un primo incontro con una delegazione russa, presso la Camera di Commercio Italo-Russa, sede di Milano, sui temi di adeguamento degli edifici di edilizia popolare degli anni '50/60 in Russia.

Di seguito due momenti della giornata.
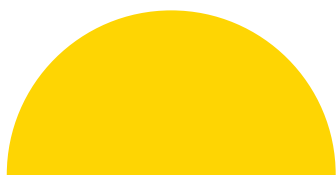
Gli Stage e le Tesi
2009-2010

Gli Stage e le Tesi 2009-2010

Master in "Progettazione delle strutture in c.a."

Allievo: Mentor Balilaj
Relatori: Prof. A. Franchi – Ing. P. Crespi
Titolo: Prove sperimentali sul comportamento di ancoraggi nel calcestruzzo fessurato sotto carico ciclico

In questa tesi si sviluppano interpretazioni, modelli teorico–numerici e prove di laboratorio sul comportamento meccanico di ancoraggi strutturali post-inseriti per strutture soggette a carichi sismici. Questa ricerca permette di migliorare i livelli di sicurezza di tali elementi strutturali, fornisce una base per lo sviluppo di metodi di requisito sismici e criteri di valutazione di prestazioni, e aiuta l'industria del settore a pensare nuovi prodotti più adatti a migliorare le prestazioni meccaniche in zona sismica. All'inizio dello stage, mi è stata offerta dal prof. Franchi la possibilità di inserirmi, nell'ambito di un programma di collaborazione tra la Scuola di Specializzazione F.lli Pesenti (Dipartimento di Ingegneria Strutturale) ed EOTA (European Organisation for Technical Approvals), nel gruppo di lavoro sulla sperimentazione di ancoraggi strutturali meccanici a espansione, post- inseriti in calcestruzzo fortemente fessurato. Si tratta di ricerca prenormativa, con utili ricadute per l'ETAG 001 e gli Eurocodici. Le prove sono state svolte su diciotto provini di calcestruzzo, nel laboratorio prove materiali (LPM) del DIS del Politecnico di Milano. Su tali provini sì e creata la fessura dove sono stati installati degli ancoraggi meccanici a espansione a controllo di coppia del tipo FM-753 crack, prodotti dall'azienda Friulsider. Quindi il provino è stato sottoposto a cicli di carico simulanti un sisma, che ha provocato un'ampiezza della fessura nel calcestruzzo, nello stesso tempo si è proceduto all'estrazione degli ancoraggi. In stretta collaborazione con l'ing.Crespi, ricercatore del DIS, è stato possibile concludere la prima fase di sperimentazione e interpretazione dei dati sperimentali.

Allievo: Luca Guaragna
Relatori: Prof. A. Franchi – Dott. S. Scarpa
Titolo: Ingula pomped-storage scheme

L'Ingula Pumped Storage Scheme, inizialmente denominato Braamhoek Scheme, è situato in Sud Africa, al confine tra il Free State ed il Kwa Zulu-Natal, 350km a sud-est di Johannesburg. Il progetto fa parte del programma di costruzione di nuovi impianti per la produzione e l'immagazzinamento di energia elettrica della Eskom, compagnia sudafricana che ne gestisce la produzione e la distribuzione, per venire incontro all'aumento della domanda nelle ore di picco (si prevede entro il 2025 una richiesta di 40.000 MW di potenza). L'esecuzione dei lavori è stata affidata ad una Joint Venture formata da IMPREGILO, CMC e PG Mavundla, le prime due italiane, l'ultima locale. L'impianto prevede la costruzione di due dighe, due canali sotterranei, una power-house in caverna che alloggerà 4 turbine da 333MW l'una, tunnel e strade di accesso. Il progetto di Ingula funziona come una grande batteria di riserva.

Allievo: Diego Ierardi
Relatori: Prof. Alberto Franchi – Ing. A. Boe
Titolo: Progettazione strutturale dell'ampliamento della sede GDM Costruzioni S.p.A.

Il *primo tema* è quello dell'analisi sismica del muro portante del "Blocco Passerella" in relazione al dimensionamento sismico degli ancoraggi delle travi in acciaio della struttura della passerella facendo riferimento alla normativa americana ACI 318-05, Allegato D, ACI 308-08, Allegato A ed ES Report: 1 Novembre 2007 ESR-2322. Il *secondo tema* è quello relativo alle deformazioni e alle tensioni nel calcestruzzo indotte dal fenomeno di ritiro, esaminato prendendo come base di calcolo l'Eurocodice 2 – Progettazione delle strutture in calcestruzzo UNI EN 1992-1-2:2005, prendendo in esame le componenti dell'autogenous shrinkage e del drying shrinkage.
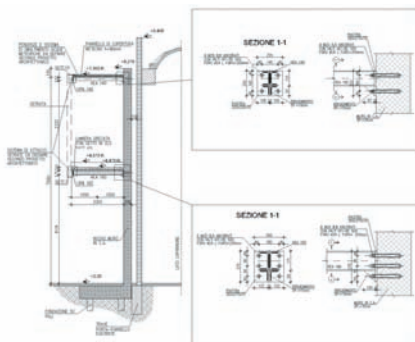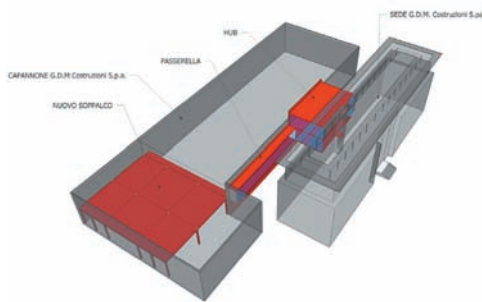
Allievo: Simona Lepori
Relatori: Prof. A. Franchi – Dott. L. Buzzoni
Titolo: Sul ritiro termico del calcestruzzo in strutture massicce – Un caso di studio

Negli ultimi decenni si sta ponendo sempre più attenzione al concetto di durabilità delle strutture in calcestruzzo armato. Tale concetto è strettamente legato al problema della fessurazione del conglomerato. Per prevenire tale problematica la ricerca scientifica approfondito in particolar modo fenomeni che avvengono nella struttura nei suoi primi giorni di vita ossia quelli appena successivi al getto. Lo scopo di questa di tesi è quello di analizzare, in un esempio specifico, il comportamento del calcestruzzo durante la sua fase di vita iniziale. Il problema è stato affrontato prendendo in esame il caso della platea di fondazione dell'edificio E di Porta Nuova Isola a Milano. Si sono analizzati i risultati sperimentali sullo sviluppo di temperatura all'interno della fondazione, monitorati nei primi nove giorni dal getto. In seguito è stato sviluppato un modello ad elementi finiti della platea e del terreno sottostante che simula lo sviluppo della temperatura e dà indicazioni su una possibile fessurazione. Dal confronto dei risultati ottenuti è stato possibile stimare una possibile fessurazione della platea.

Allievo:Chiara Patteri
Relatori: Prof.ssa Paola Ronca – Dott. L. Buzzoni
Titolo: Sul calcestruzzo ad alta resistenza gettato in opera: il calore d'idratazione

In questo lavoro viene preso in esame il calcestruzzo utilizzato per la realizzazione dei pilastri fuori terra di due edifici medio-alti del cantiere delle ex Varesine, a Milano. Viene utilizzato un calcestruzzo ad alta resistenza con Rck 85 MPa. In Italia è possibile realizzare strutture utilizzando calcestruzzi ad alta resistenza sino alla classe di resistenza C 70/85, a patto che 'tutte le grandezze che hanno influenza sulla resistenza e durabilità del conglomerato devono essere accertate prima dell'inizio dei lavori tramite un'apposita sperimentazione preventiva e la produzione deve seguire specifiche procedure per il controllo di qualità' (NTC 2008 p. 4.1)., viene in particolare analizzato il problema dell'alto calore di idratazione che questo tipo di calcestruzzo sviluppa in maniere notevole grazie alla particolare composizione degli elementi che lo compongono e alla sua maggiore compattezza e impermeabilità.

Allievo: Esmeralda Zela
Relatore: Prof. Franco Mola – Dott. P. Zappamiglio
Titolo: Comportamento, analisi e progettazione di travi e pareti in un edificio residenziale

L'edificio in oggetto consiste in una costruzione ad uso civile abitazione da realizzarsi a Milano. La pianta ha una geometria pressoché rettangolare per i piani interrati, in elevazione la geometria è a L. La struttura presenta inoltre un irrigidimento centrale costituito dal vano scale e ascensore, avente funzione di nucleo di controventamento, sono presenti anche due vani ascensore nella posizione laterale. L'edificio, a destinazione commerciale - abitativa, presenta 9 piani fuori terra e 3 piani interrati. Le analisi numeriche sono state condotte con l'ausilio del software agli elementi finiti PRO_SAP e Midas Gen 2010. E' stata condotta un'analisi statica lineare. Tale modellazione è fatta per valutare il comportamento globale della struttura.
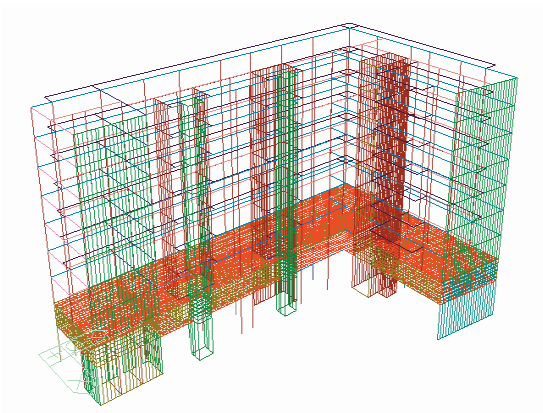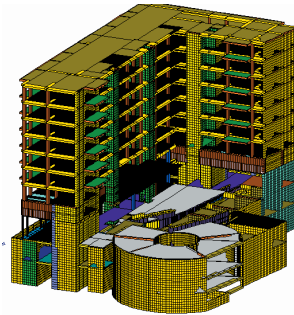
Master in "Architettura : strutture e tecnologia"

Allievo:Francesca Gallina
Relatori: Prof.ssa Paola Ronca - Dott.ssa C. Domenici
Titolo: Il recupero del costruito – Ricerca di un metodo e sua valutazione attraverso un caso studio a Milano

La tesi ha lo scopo di discutere alcune questioni metodologiche relative al tema del recupero edilizio con riferimento ad un esempio pratico di intervento su un edificio del centro storico di Milano del quale saranno valutate scelte e tecniche per l'intervento. La finalità dell'elaborato è quella di inquadrare problemi e strategie per dare luogo ad un intervento rispettoso della materia esistente e della sua connotazione architettonica esente dal timore di intervenire attraverso operazioni di aggiunta, rimozione o ripristino, ovvero atti utili al riuso e alla ri-funzionalizzazione dell'edificio in un contesto di cultura del progetto e di esigenze fruitive contemporanee. Oltre alla valutazione delle scelte metodologiche e tecniche operate, la sintesi propone due suggerimenti alternativi rispetto al progetto elaborato dallo studio di architettura Vittorio Grassi di sistemi volti al risparmio energetico, ovvero di un impianto fotovoltaico e solare termico e un sistema di termo isolamento a cappotto interno. Le scelte operate per l'impostazione delle due proposte saranno valutate tenendo conto di parametri ulteriori rispetto alla performance energetica, come ad esempio l'energia inglobata e la durabilità, al fine di verificarne la compatibilità ambientale e l'integrazione con il contesto di esercizio. Infine verranno verificate le scelte progettuali operate da parte del progettista e le alternative proposte sulla base delle considerazioni di carattere teorico generale formulate nella parte iniziale dell'elaborato.

Allievo:Evangelia Papagianni
Relatore: Prof.ssa Paola Ronca - arch.Vittorio Grassi
Titolo: Development of new settlements through sustainability and technology by applying the standards of LEED for Neighborhood Development

La progettazione urbana sostenibile e l'applicazione delle norme di Sistema di Rating LEED for Neighborhood Development sono i principi base di questa tesi. Il sistema LEED è stato inteso sia come metodo di valutazione che premia lo sviluppo sostenibile delle aree, sia, principalmente, come strumento per fare della sostenibilità una pratica comune. Una panoramica del sistema fornisce indicazioni relativamente alle strategie che contribuiscono a creare uno sviluppo completo e connesso con il territorio in cui esso stesso opera e alle misure che possono contribuire a ridurre gli impatti ambientali causati dalla costruzione e al funzionamento di edifici e infrastrutture. Il caso di studio analizzato si riferisce ad un progetto situato nel Nord Italia, dove, attraverso l'applicazione delle norme del Sistema di Rating citato viene calcolata la classe LEED di riferimento attraverso l'attribuzione di punteggi relativi ai diversi campi di valutazione. L'analisi approfondisce i singoli prerequisiti e le esigenze del programma utilizzando i dati reali del progetto, con riferimento all'attuale normativa locale vigente nell'area di progetto. Infine, utilizzando LEED ND come strumento di progettazione per lo sviluppo urbano, vengono proposte alcune strategie e indicazioni pratiche, anche riferite a questioni relative alle tecnologie *green,* per dimostrare le potenzialità di questo sistema e per verificare la possibilità di applicazione in Italia.

Allievo: Slavko Milanovic
Relatori: Prof.Pietro Crespi – Dott. C. Lodewickx
Titolo: ETFE technology - A case study: the cover of a sport arena

The application of the ETFE technology (Ethylene + Tetrafluoroethylene Technology) to the cover of the new Sport Arena of Lamezia Terme (in Calabria, southern Italy) is presented in this Thesis. Structural analysis shows that the light weight of the proposed structure can reduce the cost significantly. As the own weight of this type of cladding is 1-2 daN/m^2, the overall savings can be sizable indeed. EFTE brings in a better structural behaviour under both static and dynamic loads. EFTE is a demonstration that – contrary to the widespread opinion that more material means more strength – a thin cover system is more efficient, in terms of bearing capacity and safety, because it is more adaptable to the path of the loads. However, it is too early to tell whether EFTE will end up at the margins of the actual architectural practice (as occurred to many too ambitious technologies of the 20th century) or will be successful. What is unquestionable is that EFTE meets today's need for sustainable design and energy saving, thanks to low weight and extremely low maintenance costs. Having just one percent of the weight of glass, EFTE is often described as a material that is nothing for 99%. The remaining 1% makes the difference and may be the future.
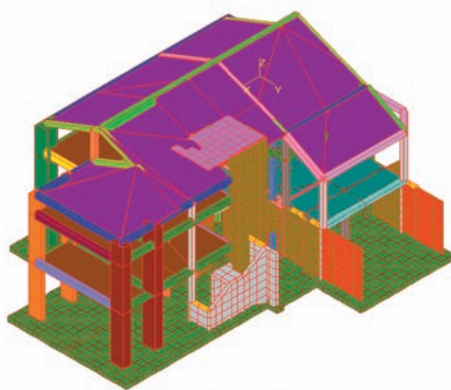
Allievo: Eliana Pacheco
Relatori: Ing. Pietro Crespi - Ing. F. Quaglia
Titolo: Analisi tecnico – comparativa di strutture in c.a. in zone a differente livello di sismicità

Scopo del presente lavoro di ricerca è quello di capire le possibili differenze in termini tecnico – quantitativi eventualmente esistenti per realizzare un edificio in zona a bassa sismicità e lo stesso edificio in zona a maggiore sismicità. Inoltre si vuole capire l'incidenza percentuale delle eventuali variazioni sul costo della struttura. Il lavoro è diviso in due parti: la prima affronta il tema dell'analisi critica delle NTC 2008 con particolare riguardo ai criteri di progettazione in zona sismica, che verranno ripresi e applicati più avanti; la seconda affronta l'analisi comparativa di due edifici a livello strutturale in zona a diversa intensità sismica, partendo da un progetto architettonico reale. L'ubicazione scelta è Rosate (MI) in zona a bassa sismicità e Agnani (FR) per la sismicità maggiore. La tipologia di edificio studiata è un'abitazione monofamiliare a due piani più sottotetto. E' di interesse capire che influenza reale hanno i criteri imposti dalle NTC 2008 su edifici ordinari: in particolare si vuole capire come e quanto può cambiare la progettazione, per uno stesso edificio, a livello strutturale, cercando di mantenere il più possibile invariato il progetto architettonico di base. A conclusione del lavoro, viene fatto un confronto per valutare le variazioni economiche e capire l'influenza dell'intensità sismica sulla progettazione strutturale, attraverso lo sviluppo dei disegni esecutivi per il cantiere, il computo metrico per calcestruzzo e acciaio, tabelle riepilogative dei risultati ottenuti.
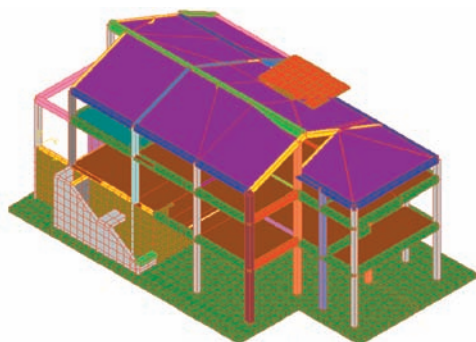
VISTA. EDIFICIO A ROSATE   VISTA. EDIFICIO AD ANAGNI

Allievo: Antonella Laricchia
Relatori: Prof.ssa P. Ronca - Arch. F. Gurrado
Titolo: Interventi di recupero, ed adeguamenti energetici ed impiantistici: il caso della ex-filanda di Malvaglio

In questo lavoro si affrontano quelle che sono le problematiche legate al recupero energetico degli edifici. Da una analisi degli obiettivi e delle strategie di tale tipo di recupero, emerge la necessità di agire sull'involucro edilizio e sulle componenti impiantistiche in modo da raggiungere i livelli di comfort odierni. Esaminando il quadro delle tecnologie attuali di realizzazione dell'involucro esterno e delle componenti impiantistiche ad oggi impiegate, sono state adottate delle soluzioni alle problematiche riscontrate in un caso pratico oggetto dello studio: la riqualificazione della ex-filanda Rusconi presso Malvaglio a Robecchetto con Induno. Il complesso, per volontà della committenza, subirà una riconversione d'uso, divenendo un centro ricreativo in cui troveranno posto una biblioteca, delle sale musica, un piccolo auditorium e alcuni ambienti polivalenti. L'intera opera è completata da un ampliamento ex-novo che accoglierà una scuola di danza. Le scelte progettuali operate, dal punto di vista energetico, consistono nella progettazione di un cappotto interno, che rende l'involucro della ex-filanda conforme rispetto ai valori limite di trasmittanza imposti dalle normative vigenti, e la realizzazione di un involucro con pannelli sandwich e vetri basso emissivi schermati da sistemi frangisole, elementi che permettono al volume di ampliamento di avere una elevata efficienza termica garantendo anche la resa architettonica ricercata. L'analisi delle tecnologie termomeccaniche ha invece portato alla progettazione di un impianto di climatizzazione che sfrutta l'energia geotermica dell'acqua di falda, nonché la realizzazione secondo gli attuali standard degli impianti idrici ed elettrici. È stata inoltre proposta una ulteriore integrazione impiantistica costituita da un impianto fotovoltaico da installare in copertura nel rispetto delle scelte architettoniche eseguite a monte.

Master in "Costruzioni e infrastrutture sostenibili per la protezione e lo sviluppo del territorio"

Allievo: Rocio Moscoso
Relatore: Ing. Alessandro Zichi – Prof. A. Franchi
Titolo: Sustainable Constructions and Infrastructures for the Protection and the Development of the Territory - Integrating LCA into LEED rating system

This thesis deals with the coupling of the LCA approach (Life Cycle Assessment) and the LEED rating system, taking into consideration the mix of materials adopted on the basis of energy, emissions, maintenance, repair and transport needs. Recent research projects have explored buildings performance with reference to their internal environment, in areas such as energy consumption, day lighting, recycled materials and air quality. However, as owners, designers, regulators and occupants increasingly desire a better internal environment, integrating LCA and LEED is becoming a necessity. Nationally and globally, all buildings contribute significantly to energy consumption, as well as to environmental impact (through – for example – the emission of green-house gases and the production of solid waste). Buildings are a very complex industrial product with a lifetime of decades. Emerging health-related issues related to buildings environmental impact (such as the so-called "sick building" syndrome) are increasing the awareness of the role buildings play on our wellbeing. While some efforts are in progress to control individual aspects of buildings environmental qualities, a comprehensive approach is still badly needed, particularly in the design phase of a building. It is, however, in the design phase that the greatest opportunities occur and may bring in long-lasting benefits. A new approach has emerged lately, which considers a building as a system of interrelated environmental impacts, that should be "juggled" to create a more environmentally-benign building. In this thesis, by using the SimaPro software,

the Life-Cycle Assessment approach is applied to a real (albeit rather simple) case, the stairway system of the renovated building of the Master School "F.lli Pesenti" in the Leonardo Campus of Politecnico di Milano. In spite of its simplicity, this example shows to what an extent the life cycle is affected by the different materials, and how LCA and LEED can coexist.

Allievo: Linda Bande
Relatori: Prof.ssa P. Ronca - Ing. Alessandro Zichi
Titolo: A New office building for ATM, Monte Rosa Street Milan – Energy and environmental evaluation according to the LEED Rating System

ATM Office Tower designed by Studio Sarno in Milan for the Public Transportation Agency of Milan - ATM integrates the principles of green buildings. During a stage in the Sarno design bureau, the MS Candidate Linda Bande compared the American rating system LEED with its Italian version and performed a preliminary analisys for the certification of the tower, through a software based on a model that takes into consideration all aspects of energy saving. The ATM tower was examined from different points of view:

- Functional: location, accessibility and relationship among the different functions (offices, auditorium, cafeteria, kindergarten, library/archive, etc.).

- Environmental: solutions for energy saving, and use of eco-friendly materials and technologies, to obtain class A+ according to CENED;

- Architectural: requirement for the tower to be a landmark;

- Constructive: use of materials and technologies that maximize performance, and minimize construction time and maintenance costs.

The tower alignement takes advantage of passive solar contribution and has some "green-building" characters, as green roof and fotovoltaic panels. The urban location, the functional and the typological choices, and the use of low-impact building materials contribute to the high ranking of the tower according to the LEED rating system. The type of software used in the analysis ("dynamic" software) agrees with the American provisions (ASHRAE/IESNA Standard 90,1-2.007). ATM Tower is shown to save 22% of energy compared to similar non-LEED buildings, and gains 6 points in terms of LEED rating.
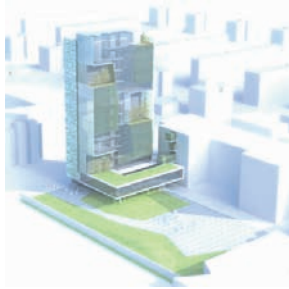
Rendering of the ATM Tower.
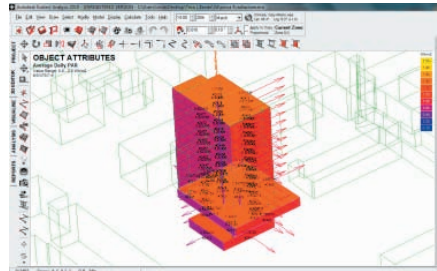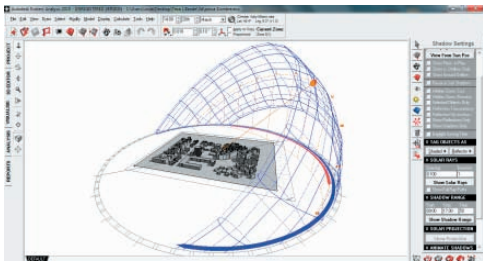
Images of the energy modelling of the tower.

Master in "Project Management delle opere strutturali e infrastrutturali"

Allievo: Nicola Medici
Relatore: Prof. A. Franchi – Dott. Francescantonio Gioia
Titolo: Gestione della commessa: riqualificazione di un'ex acciaieria in un centro polifunzionale, Via Varesina 162 Milano

L'oggetto del lavoro è stata la gestione dei processi operativi e gestionali nel progetto di riqualificazione industriale di un'ex acciaieria in un centro polifunzionale. Il progetto vuole conservare come destinazione d'uso la memoria storica dei luoghi industriali, mantenendo i vecchi capannoni in acciaio e lo stabile usato per contenere la parte amministrativa, dall'altro si propone come un nuovo intervento assolutamente contemporaneo, sia nella concezione strutturale, che nell'uso dei materiali, realizzando un edificio ex novo di otto piani in acciaio – calcestruzzo. Il primo capitolo è stato dedicato alla trattazione teorica delle tecniche, dei metodi e dei modelli propri del project management: WBS, Diagrammi di Gantt, curve ad S ed EVMS (Earned value method system) necessari per la pianificazione ed il controllo delle attività, la gestione dei contratti, degli approvvigionamenti e dei fornitori. Il secondo capitolo è stato invece dedicato interamente alla descrizione del progetto, analizzandolo dal punto di vista gestionale, architettonico e strutturale.

Allievo: Vanessa Grassi
Relatore: Ing. Patrick Bamonte – Dott. M. Comelli
Titolo: Il Project Management nella commessa edilizia

L'ambito d'intervento è compreso nell'isolato delimitato dalle vie Salaino, Solari, Montevideo e Valparaiso (Milano). L'intorno immediato dell'area di intervento è caratterizzato da un addensamento di costruzioni eterogenee che saturano i cortili tra volumetrie di varia natura. L'intervento progettuale consiste nella ristrutturazione di un immobile, la sostituzione del tessuto edilizio preesistente, la modifica parziale della sagoma e della destinazione d'uso, da terziario a residenziale. Il progetto prevede la ristrutturazione urbanistica dell'area, che viene interamente destinata a residenza. L'obiettivo del progetto è stato quello di proporre un edificio del tutto in linea con gli indirizzi dell'architettura contemporanea, in modo da esprimere il proprio carattere residenziale attraverso la composizione apparentemente casuale di pannelli di vetro decorato, e nello stesso tempo di presentare un decoro elegante tale da garantire la *privacy* degli affacci, grazie all'arretramento dei fronti. Il prospetto è completamente ridisegnato grazie ad una facciata in *doppia pelle*, che presenta verso la città una superficie discontinua di pannelli vetrati serigrafati di colore bronzo-dorato (per proteggere le logge) ed un ballatoio continuo su tutto il perimetro dell'edificio.
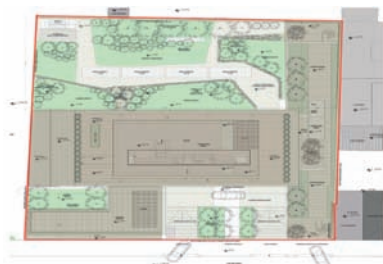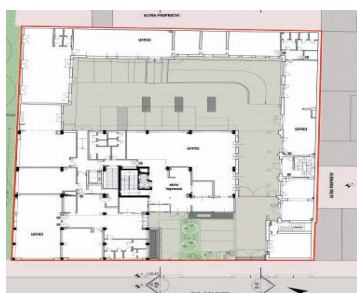
Allievo: Alberto Lonardi
Relatore: Prof. Alberto Franchi – Dott. S. Vivaldelli
Titolo: Le terre rinforzate

Scopo di questa tesi è condurre uno studio delle terre rinforzate da impiegare nei rilevati stradali per capire i vantaggi economici che possono dare. Si è preso un caso modello, si sono fatti i calcoli statici, i tre computi metrici relativi alle soluzioni utilizzate per determinare la differenza in termine di costo e quindi si sono ottenute le soluzioni più vantaggiose per le varie altezze di rilevato possibili. Si sono fatti i crono-programmi delle tre soluzioni per un'altezza di rilevato di dieci metri per determinare la soluzione più veloce. Si sono eseguiti tre crono-programmi, uno per soluzione, prendendo in considerazione un'altezza di rilevato di 10 metri. I crono-programmi sono stati eseguiti in base a situazioni reali che si sono già verificate quindi su dati storici.

ID	Nome attività	Durata	Inizio	Fine
1	**Terre rinforzate H=10 metri Lsup=12 metri Linf= 21 metri**	**35 g**	**lun 04/10/10**	**lun 22/11/10**
2	Scotico piano di campagna fino a 50 cm di profondità	3 g	lun 04/10/10	gio 07/10/10
3	Compattazione e stesa di tessuto non tessuto	3 g	gio 07/10/10	mar 12/10/10
4	Posa casseri metallici e geogriglie	14 g	mar 12/10/10	lun 01/11/10
5	Trasporto, stesa e compattazione di materiale di riporto e geogriglie	14 g	lun 01/11/10	ven 19/11/10
6	Idrosemina	1 g	ven 19/11/10	lun 22/11/10
7				
8	**Riporto 3:2 H=10 metri Lsup=12 metri Linf= 42 metri**	**45 g**	**lun 04/10/10**	**lun 06/12/10**
9	Scotico piano di campagna fino a 50 cm di profondità	3 g	lun 04/10/10	gio 07/10/10
10	Compattazione e stesa di tessuto non tessuto	3 g	gio 07/10/10	mar 12/10/10
11	Trasporto, stesa e compattazione di materiale di riporto	28 g	mar 12/10/10	ven 19/11/10
12	Trasporto, stesa e sistemazione di terreno vegetale sulle scarpate	10 g	ven 19/11/10	ven 03/12/10
13	Posa embrici ed idrosemina	1 g	ven 03/12/10	lun 06/12/10
14				
15	**Soluzione con muri in c.a. H=10 metri**	**65 g**	**lun 04/10/10**	**lun 03/01/11**
16	Scotico piano di campagna fino a 50 cm di profondità	3 g	lun 04/10/10	gio 07/10/10
17	Compattazione	3 g	gio 07/10/10	mar 12/10/10
18	Montaggio ponteggio lato esterno	3 g	mar 12/10/10	ven 15/10/10
19	Stesa di magrone e posa gabbie di fondazione	15 g	ven 15/10/10	ven 05/11/10
20	Montaggio ponteggio lato interno	3 g	ven 05/11/10	mer 10/11/10
21	Casseratura	15 g	mer 10/11/10	mer 01/12/10
22	Getto del cls	3 g	mer 01/12/10	lun 06/12/10
23	Smontaggio casseri	3 g	lun 06/12/10	gio 09/12/10
24	Smontaggio ponteggi	3 g	gio 09/12/10	mar 14/12/10
25	Riempimento a strati del materiale	14 g	mar 14/12/10	lun 03/01/11
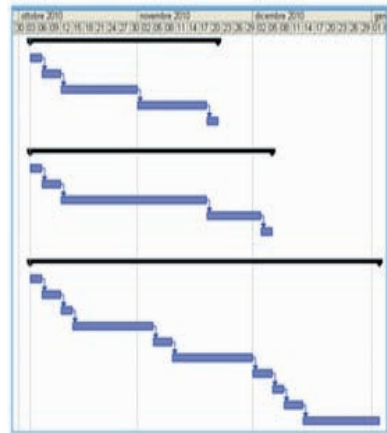
Allievo: Luca Crivellaro
Relatore: Prof. Alberto Franchi – Ing. L. Gaggeri
Titolo: Il Project Management nella verifica della progettazione ai fini della validazione

L'art. 112 del Dlgs 163/2006 ridefinisce il concetto di verifica della progettazione ai fini della validazione, peraltro già introdotto dalla legge Merloni 109/1994 e dal relativo Regolamento di attuazione DPR 554/1999. La verifica della progettazione nasce come richiesta del mondo economico – finanziario che vede in questo strumento la garanzia dell'efficacia in termini di tempi, costi e qualità del processo costruttivo. La verifica della progettazione è un valido strumento per ridurre i rischi di gestione dell' appalto. Le stazioni appaltanti hanno l'obbligo di verificare la progettazione prima della messa in bando della medesima.

Un utile strumento per una corretta evoluzione sia dell'attività di progettazione che di quella di verifica è dato dalle tecniche di project management. Nell'elaborato proposto dallo scrivente è, dapprima, messo in evidenza lo sviluppo delle teorie di project management, a partire dall'evoluzione storica di tale approccio, dalla figura del project manager stesso fino ad arrivare al suo team di lavoro. In seguito, quali strumenti di controllo di gestione del processo progettuale, vengono riportate le principali le tecniche di project management applicabili all'attività di progettazione; solo ad esempio la Work Breakdown Structure (WBS), il Gantt chart, il Critical Path Method (CPM), ecc. Poi, l'elaborazione prosegue nella trattazione della verifica della progettazione ai fini della validazione.

Partendo da un inquadramento dell'attività di verifica nella legislazione storica e cogente degli appalti pubblici vengono, in seguito, definiti gli attori del processo di verifica e la documentazione base obbligatoria per l'attività ispettiva ai sensi della norma UNI CEI EN ISO/IEC 10720. La verifica può essere vista come l'attività "duale" della progettazione, di conseguenza l'applicazione delle stesse metodologie o tecniche di project management utilizzate per il controllo sulla progettazione possono essere riproposte per la gestione e lo svolgimento dell'attività di verifica. La trattazione si conclude con la descrizione dell'esperienza vissuta durante lo stage presso una società di ingegneria di Milano operante nel settore delle infrastrutture, presso la quale è avvenuto il processo di predisposizione documentale, gestione dell'attività di verifica e conseguente accreditamento presso Accredia (ex-Sincert).

Allievo: Nicola Posteraro
Relatori: Prof. Alberto Franchi – Dott. A. Cambruzzi
Titolo: La Gestione e la Programmazione dei Grandi cantieri: Interventi di Riqualificazione dei Complessi Immobiliari delle Stazioni e di Realizzazione delle Opere Infrastrutturali Complementari.

Il lavoro di Stage – Tirocinio è stato svolto presso l'impresa di Costruzioni Generali "Ing. Claudio Salini – Grandi Lavori S.p.A.". La ICS (acronimo di "Ing. Claudio Salini S.p.A.") è una impresa di costruzioni generali che opera, in Italia e all'estero, in tutti i campi delle costruzioni: dalle grandi infrastrutture – strade, ferrovie, autostrade, metropolitane e gallerie – ad ogni settore di specializzazione dell'edilizia civile e industriale._ In particolare, il mio lavoro di stage si è concentrato sull'intervento inerente la commessa n.036 - Lotto Sud che riguarda la riqualificazione funzionale ed impiantistica delle Stazioni Ferroviarie di: Napoli C. le; Bari C. le; Palermo C. le. Nello specifico, mi sono interessato della corrispondenza tecnica tra le figure professionali coinvolte nella riqualificazione della Stazione di Bari Centrale. Tale corrispondenza non è stata di facile attuazione, viste le problematiche esistenti tra le varie parti, non solo di carattere pratico ma anche comunicativo. Dunque, non solo un confronto tecnico sulla progettazione esecutiva, ma soprattutto un confronto umano e diplomatico per avviare una proficua collaborazione. Dopo aver proceduto ad uno studio prima generale e poi puntuale delle tavole di progettazione e del materiale di supporto, è stato possibile focalizzare il mio lavoro sugli aspetti più urgenti che impedivano di fatto il prosieguo dell'intervento sulla Stazione di Bari Centrale. Era necessario riuscire a comunicare tra le parti, al fine di concludere la fase di analisi delle tavole progettuali esecutive e avere l'approvazione degli interventi. Tale obiettivo è stato possibile non solo semplificando le modalità di invio del materiale digitale, che creava una perdita di informazioni; ma soprattutto creando un dialogo positivo e di confronto con gli interlocutori. Inoltre, per avere un quadro generale degli interventi più organizzato e quindi più leggibile, si è proceduto alla suddivisione di un macrointervento in diversi microinterventi (tecnicamente WBS Work Breakdown Structure), suddivisi per tipologia di intervento e identificati da una lettera alfabetica. Il risultato è stato un rilevante miglioramento dell'aspetto comunicativo tra le parti, una semplificazione degli aspetti procedurali e una riduzione della tempistica per l'inizio esecutivo dei lavori.

Allievo: Alessandra Assenza
Relatori: Prof. R. Cigolini – Ing. M. Milan
Titolo: Il Project Management nell'arte - Il caso del Museo della Moda /
Fondazione Prada

È nell'area di un'ex cittadella industriale a sud di Milano, oggi fascinoso sistema di silos e magazzini, che verranno ospitati gli uffici della Fondazione Prada e di Luna Rossa e centinaia di opere imballate in enorme casse di legno come in attesa di essere caricate su un piroscafo. Qui, su un'area di 17 500mq, il guru dello studio di architettura olandese Rem Koolahaas ne costruirà 10 mila ex novo. Le parti nuove saranno la Torre, un magazzino espositore verticale che fungerà da landmark, da riferimento visivo e l'Ideal Museum, spazio espositivo modellato su uno studio delle proporzioni spaziali delle sale di maggior affluenza di alcuni grandi musei mondiali, dal Louvre all'Hermitage. Due corpi saranno abbattuti. Si salveranno la hall a doppia navata, un silos per le installazioni, gli uffici, gli archivi di Prada e di Luna Rossa. Il 20 novembre 2008, l'Office Metropolitan Architecture (OMA) e Prada SPA firmano il contratto per lo sviluppo architettonico del progetto. A seguire il contratto tra OMA e Favero & Milan SPA nell'ambito del MEP systems e l'ingegnerizzazione delle facciate. Il project management nell'arte: dalla ricerca di un innovativo rivestimento in schiuma di alluminio per il Museo alla collocazione strategica delle opere d'arte in funzione del dimensionamento

strutturale della Torre. L'arte diventa la protagonista indiscussa a Largo Isarco e il Project Manager dovrà saper controllare ingegnerizzazione di tutte le proposte architettoniche, nel rispetto dei tempi, costi e qualità del prodotto finale. La tesi approfondisce gli aspetti appena esposti suddividendone il contenuto in tre grandi parti: la presentazione del progetto definitivo (75%), il project management nel corso dell'intera progettazione e la gestione del Sistema Qualità all'interno dell'azienda Favero & Milan Ingegneria tramite l'applicazione della Norma UNI EN ISO.

Master in "Design and Management of structural technologies in construction works"

Allievo: Reza Nozory
Relatore: Prof.ssa Paola Ronca – Dott. Esmaeil Arashfar
Titolo: Construction of a pedestrian bridge between the Sport City Tower and the Villaggio Mall (Doha-Qatar)

The construction of a pedestrian bridge connecting the Sport City Tower to the Villaggio Mall in Doha (Qatar) is examined in this study. This facility makes the pedestrian flow between the two buildings easier, as crossing a heavy-trafficked avenue will be no longer necessary. The construction of the bridge was performed by the contractor ALISAZ, which has a long and valuable experience in Middle-East countries, where it has been active for more than thirty years. After a rather general introduction, the works, the contractor's equipments, the technical procedures, the organization of the project, the legal aspects and the reference design codes are presented and discussed.

The project plans are mainly divided into mobilization, quality and HSE plans. Organization charts and dedicated suppliers and subcontractors are considered as well. In the conclusions, a synthesis of the many aspects concerning a project of this size is presented.

Allievo: Secil Yagli
Relatori: Prof.ssa P. Ronca – Ing. M. Borsa
Titolo: Innovative Cement and Concrete Products in Architectural Works

This study is focused on the effect that innovative cements and concretes have had – and still are having - on the development of Architecture. Firstly the interrelation between Architecture and Materials is discussed, and then the origins, development and different families of innovative materials are presented and discussed.

Technology has transformed Architecture into a tool for social and cultural reform.

Modern Architecture has given an answer to the request for a new life, following the continuously-evolving World's conditions, norms and relationships.

Within this context, cement and concrete have not been merely "new materials", but they have been a ring of the "chain" of Modernism.

Becoming one of the main actors in the field of materials, concrete has contributed – unsurprisingly - to the ideology of innovation in Architecture.

During his stage at Italcementi in Bergamo, MS Eng. Yagli had the opportunity to improve his knowledge of the problems and achievements of one of the largest cement and concrete producer in Europe, and one of the most active players in cement and concrete innovation.

The challenge of innovation is brought forward under the brand "i.nova®", that puts together all Italcementi's activities in the area of innovation, in order to achieve excellence in the construction domain, while preserving the environment and improving life quality.

TX Active®, effix Design®, i.light®, i.clime®, Alipre® cements are the basic innovative products of Italcementi Group, that are examined in this study, to point out their potential in contributing to structural design and architectural values.

Allievo: Sakir Ozturk
Relatore: Prof. Alberto Franchi – Dott. G. Ragnetti
Titolo: Il Cantiere di Leoncavallo – The Building Site of Leoncavallo

The building site of an underground parking lot and the construction process are described in this thesis. The 4-storey underground construction has a capacity of 282 cars; the contractor is Ing.Claudio Salini Construction Company of Milan.

When MS Candidate Ozturk started his stage in the building site (May-September 2010), the construction was 80% complete. Hence it was still possible for the Candidate to become acquainted with all major operations, from concrete casting to final finishing, under the supervision of MS Eng. Ali Seyed. Eng. Ozturk cooperated also in performing a static test under the supervision of Professor Alberto Castellani of Politecnico di Milano.

Notes

Notes

Notes